Semi-Analytical Model to Study Vibrations of High-Speed, Rotating Axisymmetric Bodies Coupled to Other Rotating/ Stationary Structures

Kedar S. Vaidya

Dissertation submitted to the Faculty of the
Virginia Polytechnic Institute and State University
in partial fulfillment of the requirements for the degree of

Doctor of Philosophy
in
Engineering Mechanics

Robert G. Parker, Chair
Nicole T. Abaid
Mark P. Embree
Saad A. Ragab
Surot Thangjitham

May 6, 2021
Blacksburg, Virginia

Keywords: Finite element method, Fourier series, coupling constraints, rotationally periodic, parametric resonance

Semi-Analytical Model to Study Vibrations of High-Speed, Rotating Axisymmetric Bodies Coupled to Other Rotating/ Stationary Structures

Kedar S. Vaidya

(ABSTRACT)

The vibration of complex mechanical systems that include coupled rotating and stationary bodies motivates this work. A semi-analytical model is developed for high-speed, compliant, rotating bodies. Exploiting the axisymmetry of the rotating body, the developed semi-analytical model only discretizes the two-dimensional radial cross-section; Fourier series are used in the circumferential direction. The corresponding formulation for thin-walled, axisymmetric shells is given. Even though the body is axisymmetric, its deflection as well as external forces, constraints, and supports acting on the body are allowed to be asymmetric. These asymmetric elements can be stationary or rotating. The model includes Coriolis and centripetal effects. The prestress (or geometric) stiffness matrix that arises from external forces and constant centripetal acceleration has additional terms compared to the literature, and these terms can significantly change the natural frequencies.

Discrete stiffness-damper elements, elastic foundations, and constraint equations are used to couple the rotating body to other rotating and stationary bodies. The model is developed in a stationary reference frame to avoid time-dependent coefficients in the equations of motion when coupled to stationary components. Surface constraints are developed using equivalent force relations between multiple points on the surface and a reference node.

Discrete stiffness-dampers, asymmetric elastic foundation, and asymmetric constraints introduce non-axisymmetry in the system. The speed-dependent natural frequencies and complex-valued vibration modes, presence of multiple Fourier harmonics in each mode, changes to critical speeds, divergence and flutter instability phenomena, and eigenvalue veering are investigated for spinning systems with asymmetric features.

The developed semi-analytical model is used for rotationally periodic systems, for example, planetary gears. Rotationally periodic systems consist of multiple vibrating, rotating central components and substructures. The model is developed in a reference frame rotating with the central component that supports the substructures. Structured modal properties of the cyclically symmetric systems and diametrically opposed systems are investigated. The modes of the spinning system are categorized into translational-tilting, rotational-axial, and substructure modes.

Time-varying coupling elements act as parametric excitation in the system. Large strain energy in the coupling elements lead to large parametric instability regions. The analytical closed-form expression of the parametric instability bandwidth obtained using a perturbation method compares well with numerical results from Floquet theory.

Semi-Analytical Model to Study Vibrations of High-Speed, Rotating Axisymmetric Bodies Coupled to Other Rotating/ Stationary Structures

Kedar S. Vaidya

(GENERAL AUDIENCE ABSTRACT)

Complex mechanical systems, for example, mechanical transmission, consist of coupled rotating and stationary bodies. The vibrations of rotating bodies are transmitted to the other bodies through coupling elements. To reduce weight of the system, the rotating bodies are made thin-walled resulting in increased flexibility of the body. The existing lumped parameter/rigid body models do not account for the flexibility of these rotating bodies. Conventional three-dimensional finite element models lead to a large number of degrees of freedom in the system, increasing the computational cost. We aim to develop a computationally efficient model to analyze the dynamics and vibration of complex mechanical systems. Most rotating bodies can be approximated as axisymmetric. The axisymmetric property of the rotating body is harnessed to reduce the three-dimensional model of the body to a two-dimensional radial cross-section using Fourier series in the circumferential direction. This reduces the system degrees of freedom. Coriolis, centripetal, and prestress effects are included in the model. Discrete stiffness-dampers, elastic foundations, and constraint equations couple the rotating body to other rotating and stationary bodies. Non-axisymmetric coupling elements and forces introduce asymmetry in the system. The system model for these asymmetric systems are developed in a stationary reference frame to avoid time-dependent coefficient equations of motion. Flexible stationary bodies alter the natural frequencies and

vibration modes of the system. Instabilities, critical speeds, effects of asymmetry on the natural frequencies and vibration modes of the system are investigated. The model is extended for rotationally periodic systems, for examples, planetary gears and bearings. This model is developed in the reference frame that rotates with the central component that supports substructures. Structured modal characteristics are observed for the rotationally periodic systems. Changing contact conditions act as a source of parametric excitation in systems. Parametric resonances occur when natural frequencies of vibration with large strain energy in the coupling elements sum to the excitation frequency. Parametric instability regions obtained using an analytical equation compare well with numerical results.

Acknowledgments

My sincere thanks to Prof. Robert Parker for giving me the opportunity to explore this field and to guide me throughout my Ph.D. process. Ph.D. is about 'learning how to learn' was his first advice and he indeed kept me on the path to learn the process. I am grateful to him for the support both in research and advice in personal life. His 'good work' after every meeting, allowing me to make mistakes, and take my time to dig deeper and understand has led to better learning of the subject. He surely has been one of the best teachers, a great advisor, and a friend. Thank you, Rob, for this experience.

I will also like to thank Prof. Mark Embree, Prof. Saad Ragab, Dr. Nicole Abaid, Dr. Surot Thangjitham, and Dr. James Hanna for serving on my doctoral committee. Prof. Embree's class on Numerical analysis has been one of the best courses and teaching I have experienced. His quick suggestions on dealing with matrix problems have helped me progress faster through some problems I was stuck. Prof. Ragab's course on Finite element laid the foundation of FEM knowledge for me. Dr. Abaid's courses on Nonlinear Systems and Perturbation helped me with fundamentals in the field. Dr. Thangjitham's course on Plate and Shell theory and Dr. Hanna's course on Solid Mechanics formed the basics of mechanics required for my doctoral research.

I will like to extend my gratitude to Luca Ronchiato and other engineers at Avio Aero for trusting me with this project and guiding me through the project to make it better. I am glad that my work will be useful to the engineers.

My friends have been a source of continuous encouragement. I am thankful to them for bearing with all my mood swings and quirks. I am really grateful to have Nandita NH, Sandeep Hatte, Sankha, Aakash Gautam, RY Srikar, Vinnakota Sai Rakshit, Jenil Shah,

Divya Shree, Suraj Rao, Aditya Shahi, Sanchit Ingale, Aamir Khan, Shardul Adkar, Dhruv Sharma, Nishant Shirodkar, Soumya, Abhiyani, and others as my friends to whom I can approach with all my highs and lows.

I am grateful to my labmates who have been a source of encouragement and guidance at every step of my doctoral journey. Thanks to Bin Dong, Chenxin Wang, Martin Grasic, Fabio Bruzzone, Zi Wang, Xiaoqi Li, Xiang Dai, Zakia Ahmed, Faris Alsaedi, Thomas Roberts, Li Tan, Yan Song, and Zehua Hu for a memorable time in the lab and dinner outings. Without discussions with you all, the journey would have been more difficult.

Lastly and most importantly, I thank my family for their love and support. My parents, Snehal Vaidya and Sanjay Vaidya, have been a source of inspiration and motivation. I love you both for all the sacrifices you made to bring me where I am. I am sorry for not being there for you when you needed me the most. Thanks to my sister Karishma Kothare and brother-in-law Vaibhav Kothare who have supported me, inspired me, and been there for the family always. Thank you, Mai, Vijay Jawlekar, Arnav, Prashant Vaidya, Sharvari Vaidya, Yogita Dand, and others for your love, support, and for being there for mom and dad always. I am lucky to have such an amazing extended family.

Without all these wonderful people, this wouldn't have been possible. Thank you for shaping me, guiding me, inspiring me, motivating me, and supporting me through the years.

Contents

List of Figures

List of Tables

Chapter 1

Introduction

1.1 Motivation

From small rotating gears in our watches to large rotating turbines in aircraft engines, rotating systems are everywhere. Complex systems such as turbomachinery, transmission systems, guided cutting saws, brake disks, and hard drives consist of flexible, rotating bodies interacting with other rotating and stationary bodies. The vibrations due to high-speed rotating, deformable bodies and their interactions with other structures can lead to failures in the system that makes the study of rotating, deformable bodies important. Many rotating systems are analyzed as rigid bodies, for examples, lumped parameter models are used for gears and disks in transmission systems. To make systems lightweight and compact, the rotating bodies are made thinner and more compliant. Rigid body models cannot be used to model compliant systems. This work aims to develop a semi-analytical model for high-speed, rotating, compliant bodies interacting with other rotating and stationary bodies in a complex system. This model is used to study the natural frequencies and vibration modes, static deformation, dynamics, nonlinearities, and instabilities in the system. The model is applied to some example systems that include a rotating brake-disk in contact with the disk pads, coaxial rotors in a turbine-compression system enclosed in a stationary casing, and coupled rotating gears.

Rotating bodies have complex geometries. It is difficult to obtain an analytical

equation of motion for complex systems. Thus, numerical methods, for example, the finite element method, are used to model these rotating bodies. Conventional finite element method for rotating bodies require: (a) a highly refined mesh at the interface to model contact between the rotating and rotating/stationary bodies, (b) remeshing with rotation to model the changing contact surface between the bodies, (c) a large number of degrees of freedom, and (d) large computational expense. This makes the use of conventional finite element method inefficient. Also, gyroscopic and centripetal effects due to rotation are absent in most conventional finite element models. Gyroscopic effects can have substantial effect on the dynamics of structures and thus, it is important to consider the gyroscopic effects.

Rotating bodies are usually axisymmetric about their rotation axis, or can be approximated as axisymmetric. The axisymmetric property of the body coupled with the power of the finite element method to model complex-geometry systems is used to model rotating bodies. The axisymmetric property is harnessed to reduce the three-dimensional conventional finite element structure to a two dimensional cross-sectional finite element model. The body, its deflections, and other parameters are periodic in the circumferential direction. Thus, Fourier series approximate the body displacements in the circumferential direction. This reduces the number of elements and nodes in the finite element model and thereby, reduces the number of degrees of freedom and the computational cost. This model is called a 'semi-analytical finite element method.' Fig. 1.1(a) shows a schematic of an example three-dimensional axisymmetric body reduced to its two-dimensional cross-section. Thin-walled, shell-type bodies can be further reduced to one-dimensional finite elements in the cross-section, as shown in Fig. 1.1(b).

A rotating, axisymmetric body coupled to a non-axisymmetric body results in time-dependent coefficient equations of motion. This occurs because the material point on the rotating body in contact with other bodies changes as the body rotates. The time-dependent

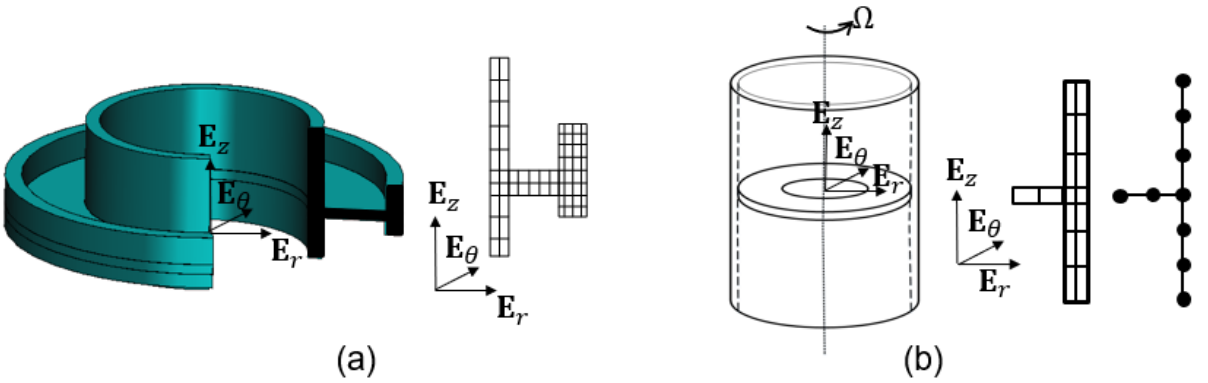

Figure 1.1: (a) Three-dimensional rotating, axisymmetric, deformable body with its two-dimensional radial-axial cross-section and (b) Three-dimensional rotating axisymmetric plate-cylinder structure with its two-dimensional cross-section and a shell model.

coefficients act as parametric excitation in the system, resulting in complicated mathematical analysis as compared to the constant coefficient equations of motion. The axisymmetry of the rotating body allows for the model to be developed in a stationary reference frame to avoid time-dependent coefficient/matrices equations of motion.

The model in the stationary reference frame allows one to easily couple other non-axisymmetric stationary bodies. The rotating bodies in mechanical systems are coupled to other bodies through bearings, splines, couplings, and joints. Spring-damper elements are commonly used to model these coupling elements. Coupling mechanisms such as discrete stiffness-damper elements, continuous elements, constraint equations, and elastic foundations are used to model the coupling elements between different bodies. These coupling elements are usually fixed in space, resulting in easy assembly to the semi-analytical finite element model of the bodies in the system.

Rotationally periodic systems, such as planetary/epicyclic gears are commonly used in automobiles, helicopters, and aircraft engines for their compactness and relatively low weights. Roller or ball bearings and harmonic drives are other rotationally periodic systems with axisymmetric central components and substructures. These models are widely analyzed

using lumped parameter models or elastic-discrete models. The developed semi-analytical model is extended to model these rotationally periodic systems in a central component rotating reference frame. This allows one to include compliance in all components and yields better system dynamic prediction compared to the lumped parameter models.

Time-varying coupling elements model the changing contact between meshing gears, the contact between races and rolling elements in a bearing, and other periodic components in the system. These time-varying elements are a major source of vibration in rotating component systems. These elements can result in large vibrations due to parametric instabilities that can damage the components. In this work, parametric instability caused by time-varying coupling components between the semi-analytical finite element model of the rotating body and other bodies is studied.

One can assemble complex systems that include rotating bodies using the semi-analytical finite element model and coupling element models developed in this work. The system frequencies, vibration modes, and dynamics can be analyzed using the obtained system equation of motion.

1.2 Literature Review

1.2.1 Modeling of rotating axisymmetric bodies

Rotating bodies are often cyclic symmetric or axisymmetric about their axis of rotation. The axisymmetry of the body allows for reduction of the model to a two-dimensional cross-section for analysis. Clough and Rashid [25] were the first to study stationary axisymmetric solids subjected to axisymmetric loads using axisymmetric elements of triangular cross-section. Due to the symmetry in the system and loading, displacements of the system

were developed only in the radial and axial directions. Wilson [154] extended the model to include stationary axisymmetric bodies subjected to non-axisymmetric loads. They used Fourier series in the circumferential direction. The non-axisymmetric loads demanded inclusion of the circumferential displacement in addition to the radial and axial displacements [25]. Finite element models for axisymmetric solids have since been discussed in books such as [26, 159].

Rotating bodies are often analyzed in the rotating reference frame. Geradin and Kill [46] developed a three-dimensional formalism of flexible rotors in a rotating and an inertial reference frame. They proposed an axisymmetric finite element model. The centripetal effects and rotational stress stiffening effects were absent in the equations of motion obtained in the inertial reference frame. Genta and Tonoli [45] applied the semi-analytical finite element method for the analysis of flexural, torsional, and axial rotordynamic behavior of discs. Fayos et al. [38] developed an Eulerian coordinate-based method for rotating bodies using vibration modes of the system as basis functions. Many rotordynamics textbooks [43, 44, 83, 117] have analyzed rotating systems using analytical and numerical methods.

The rotation-induced centripetal acceleration and stationary external forces acting on a rotating body lead to prestress in the body affecting its stiffness. Genta [44], Friswell [43], and Hu et al. [57] derived the prestress effects assuming the prestress is known *apriori* from a static analysis. A systematic approach to obtain the prestress stiffness from the steady deflections of the system and linearization of the nonlinear equations of motion is discussed in this work.

Thin-walled, rotating bodies (rotating shells of revolution) have been widely used to reduce weight. Many shell theories have been developed over the years [3, 103, 124]. Chen et al. [22] studied vibrations of high-speed, rotating, axisymmetric shells using Novozhilov's shell theory [103]. Rotating, conical shells have been studied by [24, 59, 86, 87, 129, 149].

Different numerical methods such as the Galerkin method, finite element method, discrete singular convolution method, and generalized differential quadrature methods were used by the authors. Cylindrical shells are a special case of conical shells. Refs. [48, 50, 58, 80, 133, 134] studied the effect of rotation and boundary conditions on the frequencies of rotating, cylindrical shells using the above methods.

Thin rotating disks are analyzed independent of the shell theory, but disks can be assumed to be a particular case of general shells. Linear plate theories lead to uncoupled out-of-plane (transverse) and in-plane vibrations. The transverse and in-plane vibrations of the rotating disks are analyzed in [20, 32, 65, 78, 79, 82], to name a few. In this work, a general nonlinear shell theory [124] will be utilized to build a semi-analytical finite element model for rotating shells of revolution that can also model classical shells like cylinders, cones, and disks.

Rotating bodies may experience loads that are stationary in space. For example, cutting circular saws experience a constant force at the cutting edge, rotating computer disks experience a stationary force due to its contact with the recording pinhead, and rotating gear pairs experience force at the contact due to the gear meshing. Renshaw and Mote [122] performed a perturbation analysis to model a rotating disk subjected to a transverse load and compared the results with experiments. The vibration and stability of rotating disks subjected to in-plane edge loads was studied in [18, 19, 126]. Tian and Hutton [139] developed a general approach to study the instabilities due to interactions between rotating disks and a stationary constraining system. Liew et al. [89] studied dynamic stability of a rotating cylindrical shell subjected to periodic axial loads. Spelsberg-Korspeter et al. [131] investigated the coupling of in-plane and transverse vibration of a rotating annular disk in the presence of a distributed friction load on the surface depicting the brake-squeal phenomenon. Ono et al. [105] analyzed a flexible rotating disk with a pair of head and suspension systems

at opposing points on its two sides. The prestress stiffness effect on the natural frequencies and vibration modes of rotating shells and bodies of revolution due to nonaxisymmetric, stationary loads are analyzed in this work.

1.2.2 Rotating axisymmetric bodies coupled to other rotating/ stationary structures

Interaction between a rotating, axisymmetric body and other rotating or stationary structures can result in vibration of the entire system. Examples of systems with rotor-rotor or rotor-stator coupling include guided circular sawblades, coupled gears in a stationary housing, washing machines, turbine-compressor coaxial rotors in an aircraft engine, a rotating brake disk coupled to stationary pads, and others. Stationary stiffness-damper elements, stationary loads, and other coupling elements model the coupling between the bodies.

Jacquet et al. [67] reviewed literature on rotor to stator contacts in turbomachines, concluding that most studies on rotor-stator contact are based on simplified models, for example, the Jeffcott type rotor and rigid bearings. Lee [88] developed a mathematical model using vibration modes of uncoupled bodies as a basis to obtain the equations of motion. Shen et al. [127] also used general modal coordinates to study the vibration of a rotating disk/spindle system coupled to flexible housing/stator assembly via bearings modeled as spring-damper systems. Tseng et al. [141] used a similar approach to study the vibrations of rotating axisymmetric structures in contact with stationary parts. The modal coordinate approach in [127, 141] requires a complex volume integral of the mode shapes and its derivatives to obtain the rotational effects of the body. In this work, the rotational gyroscopic and centripetal effects are obtained from the material velocity of the body without requiring any additional complex volume integral.

Discrete stiffness-damper elements are commonly used to couple different bodies in the system, for example, guides in a circular sawblade, read/write pinhead in HDD drivers, and mesh stiffness in coupled rotating gears. Tadeo and Cavalca [136] compared Kramer [84] and Nelson and Crandall [102] flexible coupling stiffness-damper models. Iwan and Moeller [66] studied the transverse vibration of a spinning elastic disk with a transverse mass-spring-damper loading system. Hutton et al. [65] modeled the guides on a circular sawblade with stationary point loads and springs. Huang and Hsu [61, 63] used the theory of receptance to study the vibration of rotating disks with interior multi-point supports and multi-circular guides. Refs. [10, 28, 29, 118] analyzed the vibrations of rotating rings on elastic foundations and space-fixed stiffnesses. Huang and Hsu [62] used the receptance theory for modal analysis of a spinning cylindrical shell with stiffness supports. Firouz-Abadi et al. [40] investigated the whirling frequencies of a rotating cylindrical shell surrounded by an elastic foundation.

Complex systems with coupling between multiple rotating bodies and stationary structures is analyzed with the semi-analytical finite element model developed in this work. Rotating brake disks coupled to rigid or flexible brake pads via elastic foundations and friction are analyzed in [51, 56, 75, 76, 106, 107]. Coaxially rotating turbine-compressor systems coupled via intercoupling bearing stiffness and enclosed in a casing via bearings are analyzed in [15, 151, 152, 157]. The coupling elements can model bearings, nonlinearities due to rotor-stator rub, pedestal looseness, and time-varying intershaft bearings in the system.

1.2.3 Modeling of rotationally periodic systems

Rotationally periodic systems, such as planetary/epicyclic gears, bearings, and strain wave gearing (harmonic drives) are compact and widely used in automobile and aerospace applications. Roller or ball bearings are present in all mechanical systems to

provide the required coupling between moving parts. Most of these systems are cyclically symmetric with equally spaced substructures. Refs. [33, 104, 128] mathematically proved the modal characteristics for general cyclically symmetric systems.

Lumped parameter models are commonly used for these rotationally periodic systems. Refs. [11, 31, 68, 90, 92] used lumped-parameter planetary gear models to study the modal characteristics and dynamics of planetary gears. Eritenel and Parker [37] mathematically developed a three-dimensional lumped parameter model for helical planetary gears. Kiracofe and Parker [81] extended the lumped-parameter single planetary gear model to compound planetary gears.

The elastic vibration of gear components is important for compliant systems rotating at high speeds. The importance of ring gear elastic deformation in a planetary gear was concluded by Hidaka et al. [52, 53]. Abousleiman and Velex [1] developed a three-dimensional lumped-parameter planetary gear model with a finite element model for the deformable ring gear. To account for carrier vibration, Abousleiman et al. [2] extended the model to include a finite element model of the carrier. Wu and Parker [155] established an elastic-discrete planetary gear model with discrete planetary degrees of freedom and an elastic ring to investigate the modal properties of the system. Wang and Parker [147] included bending and shear deformations in the analytical ring model.

A finite element/contact mechanics (FE/CM) model [146] includes finite element models for all components, thereby accounting for the system deformation. Refs. [5, 72, 112] investigated the dynamics of planetary gears using the FE/CM model. The dynamic analysis using the FE/CM model is computationally expensive. It neglects the gyroscopic effects that are important for compliant gears at high-speeds. The semi-analytical finite element model for rotationally periodic systems in this work includes gyroscopic effects and is computationally efficient for dynamic analysis.

The modal properties of planetary gears are categorized into translational, rotational, and substructure modes. The modal characteristics of planetary gears were analytically analyzed in [27, 37, 90, 148, 155] using lumped-parameter and elastic-discrete models. The effect of gyroscopic effects on the modal properties was analytically investigated by [27, 148].

Strain wave gearing (harmonic drives) are used in applications that have space and weight constraints. Harmonic drives are light weight, compact in size, have high reduction ratios, zero backlash, and high accuracy. These find applications in robot joints, satellites, and other aerospace equipment. The harmonic drive consists of an elliptical central component called wave generator that supports the ball-bearing assembly, and this is in contact with an axisymmetric flexspline, and enclosed in a circular spline. The flexsplines produce elastic deformations via the wave generator and engage with the circular spline to transmit motion and power. Tuttle and Seering [143] used experimental observations to guide the development of a lumped-parameter model for harmonic-drives. [54, 77, 150] are some other references that have analyzed harmonic drive systems.

1.2.4 Parametric instability and dynamics in rotating systems

Gears are an important part of mechanical transmission systems. The contact between the meshing gears is usually fixed in space. The gear meshing teeth are modeled as space-fixed stiffnesses. The number of teeth in the contact meshing changes between one tooth and two teeth. This changing contact conditions due to change in the number of teeth in contact is the primary source of vibration in gears. This change in contact conditions is modeled by periodically varying mesh stiffnesses. The dynamic analysis of gear pairs using lumped-parameter gear models with time-varying mesh stiffnesses were studied by [4, 7, 140].

Lin and Parker [92] investigated parametric instability due to the fluctuating mesh stiffness in a two-mesh, multiple-gear system. The need for light-weight gears in aerospace applications has made the gears more flexible. Vangipuram Canchi and Parker [12] studied the parametric instabilities of in-plane bending vibrations of an elastic, rotating ring subjected to moving, time-varying springs. Liu et al. [93] also studied the parametric instabilities of spinning elastic rings excited by fluctuating time-varying stiffnesses.

Large vibrations and backlash in the gears can lead to tooth contact loss in the meshing gear. This introduces a nonlinearity in the rotating, coupled gear system. Kahraman and Singh [70] investigated the nonlinear dynamics of a gear pair modeled by two degrees of freedom using a harmonic balance method. Theodossiades and Natsiavas [138] investigated the dynamics of a gear pair with backlash and time-dependent mesh stiffness using a two degrees of freedom torsional gear model. Liu and Parker [94] examined the nonlinear, parametrically excited dynamics of idler gear sets using a lumped parameter model. Eritenel and Parker [35] developed a three-dimensional helical gear lumped parameter model to study the nonlinear vibrations due to tooth contact loss. Light-weight, deformable gears require a model that considers the deformations in the gears. The conventional finite element model of rotating gear pairs requires highly refined elements at the contact region with remeshing at every time instant. Thus, the conventional finite element method is computationally inefficient to deal with such problems. Vijayakar [146] developed a finite element model in conjunction with a surface integral contact model that captures the effects at the contact. The model developed includes the effects of changing tooth contact and contact loss and thus, an external excitation or nonlinearity is not required. Parker et al. [113] used the finite element/contact mechanics model developed by [146] to study the nonlinear dynamic response of a spur gear pair. Cooley et al. [30] developed an efficient frequency domain method using the finite element/ contact mechanics model to reduce the time taken

for dynamic analysis of gears. Even though the contact model is accurate, the dynamic analysis takes a long computation time.

1.3 Scope and organization of the work

Chapter 2 develops a semi-analytical finite element model of high-speed rotating, flexible, axisymmetric bodies. Exploiting the axisymmetry of the body, the developed model only discretizes the two-dimensional radial cross-section with global or local shape functions and uses Fourier series in the circumferential direction. This formulation is further reduced to a one-dimensional radial cross-sectional mesh for thin-walled, axisymmetric shells. Even though the body is axisymmetric, external forces, constraints, and elastic supports acting on the body are allowed to be asymmetric. The model is developed in the stationary reference frame to easily couple stationary components to the axisymmetric rotating body and to avoid time-dependent coefficient equations of motion. The model includes Coriolis, centripetal effects, and prestress due to external forces and constant centripetal acceleration. The prestress stiffness in the current formulation has additional terms as compared to methods in the literature and these terms have a significant effect on the natural frequencies. The splitting of degenerate natural frequencies from rotation, change in critical speeds due to rotational prestress, presence of divergence and flutter instabilities, and the effects of rotation on the complex-valued vibration modes are investigated. Asymmetric stationary components break the axisymmetry of the system leading to distinct stationary eigenvalues, eigenvalue veering, and vibration modes with multiple Fourier harmonic contributions. The semi-analytical model of rotating, axisymmetric bodies forms the basis for further chapters.

Chapter 3 develops coupling models to couple the rotating, axisymmetric body to other rotating and stationary bodies in a complex system. Component equations of mo-

tion for all bodies are obtained in their respective local, stationary reference frames. The semi-analytical model from Chapter 2 is used for all rotating, axisymmetric bodies in the system. The space-fixed formulation simplifies the inclusion of space-fixed coupling elements resulting in constant coefficient equations of motion. Discrete stiffness-damper elements, elastic foundations, and constraint equations are used as coupling elements in the system. Surface constraint equations based on the transfer of equivalent loads between points on the surface and a reference node are developed for the axisymmetric body formulation from Chapter 2 and for conventional finite element models. The coupling models are demonstrated for a brake disk-pad system coupled via non-axisymmetric elastic foundation and non-conservative friction. A turbine-compressor coaxially rotating system enclosed in a casing is also developed. The rotors are coupled via a time-varying bearing stiffness. Discrete stiffnesses, surface constraints, and elastic foundations couple the rotor to the outer casing. Distinct stationary eigenvalues, eigenvalue veering, parametric excitation due to fluctuating coupling elements, and other effects are observed for the system.

In Chapter 4, the models developed in the previous chapters are used to model rotationally periodic systems, such as planetary/epicyclic gears, roller/ ball bearings, and harmonic drives. The rotationally periodic system consists of P central components and N substructures. The model is developed in a rotating reference frame of the central component that supports all the substructures. Only this central component is allowed to be non-axisymmetric. All the remaining central components and substructures are either axisymmetric or rigid bodies. The coupling between the central components and substructures is space-fixed when viewed in the rotating reference frame of the central component with the substructures. This results in a constant coefficient equation of motion. Gyroscopic and centripetal effects due to relative velocities of the bodies are included in the model. Cyclically symmetric systems possess structured modal properties. The developed, general

model is used to validate the structured modal characteristics of cyclically symmetric and diametrically opposed systems. The modes for the stationary system are categorized into translational-tilting, rotational-axial, and substructure modes. Pure component modes are an additional mode type observed for systems with specific couplings. The effect of gyroscopic effect on the mode types is verified with the literature.

Parametrically excited systems are analyzed in Chapter 5. The source of parametric excitation is the time-varying coupling elements. The changing contact between rotating gears and between bearing races and rolling elements lead to periodically changing coupling elements. The governing equations are cast into a state space form and reduced using eigenvectors of the system. A closed-form expression obtained using method of multiple scales is used to obtain the parametric instability regions. The analytical results compare well with numerical results from Floquet theory.

Chapter 2

Semi-analytical model to study vibrations of high-speed, rotating axisymmetric bodies coupled to other rotating/stationary structures

2.1 Introduction

The vibration of rotating, axisymmetric bodies coupled to stationary structures, for example, high-speed gear pairs with space-fixed stiffness representing the meshing tooth, rolling wheels with ground contact, guided circular sawblades, and disk brakes, motivates this study. Rotating structures are frequently axisymmetric about their rotation axes, or can be approximated as axisymmetric. This feature is exploited to accomplish multiple objectives: a) handle arbitary axisymmetric geometry, b) formulate the model in a stationary reference frame that simplifies coupling the rotating body to space-fixed bodies, constraints, or elastic supports, c) avoid time-dependent matrices that arise when a rotating body coupled to stationary components is analyzed in a rotating reference frame, d) include Coriolis and centripetal effects, e) include prestress (or geometric) stiffening effects, and f) reduce the computational cost compared to full three-dimensional models.

The semi-analytical formulation of a three-dimensional, rotating, axisymmetric body allows reduction of the model to a two-dimensional radial cross-section. Clough and Rashid [25] modeled stationary axisymmetric structures subjected to axisymmetric loads with triangular cross-sectional finite elements. Because of the symmetry in the system and loading, they only considered radial and axial displacements. Wilson [154] extended the study to include stationary axisymmetric bodies subjected to non-axisymmetric loads. Finite element models for axisymmetric bodies have been discussed in books such as [9, 26, 159].

A rotating axisymmetric body coupled to non-axisymmetric, stationary structures or supports leads to time-dependent coefficient equations of motion in the rotating reference frame. This arises because the space-fixed component, such as the ground contact in a rotating tire, the caliper acting on a disk brake, the fixed guide on a circular sawblade, or the tooth contact in a spinning gear, appears as a moving component when viewed in a rotating reference frame. These time-dependent coefficients act as parametric excitation. Mathematical analysis of parametrically excited systems is complicated compared to more familiar methods for constant coefficient systems. Numerical solutions for parametrically excited systems are computationally expensive. We model rotating bodies in a stationary reference frame to avoid time-dependent coefficients/matrices in the equations of motion.

Geradin and Kill [46] developed a finite element model of an axisymmetric rotor in rotating and stationary reference frames. The centripetal and rotational stress stiffening effects are absent in the stationary reference frame model. Genta and Tonoli [45] applied a semi-analytical finite element method to analyze rotordynamic behavior of discs. Additional methods to analyze the rotating systems are discussed in articles and books [39, 43, 44, 83, 117].

The rotation-induced constant centripetal acceleration and external forces acting on a rotating body lead to prestress that affects the stiffness. Genta [44] derives a prestress

(or geometric) stiffness matrix assuming the prestress is known *a priori* from a separate analysis. He neglects strain energy terms that are cubic in total displacement, but such terms contribute to the equations of motion when the displacements of the prestressed state are moderate, as shown later. Consequently his prestress (or geometric) stiffness matrix has missing terms compared to the current approach. Other references [43, 57] follow the same approach as Genta [44] and thus result in prestress stiffness that differs from the current model.

Thin-walled, rotating bodies can be modeled using shell theories [3, 103, 124]. Chen et al. [22] analyzed the vibration of high-speed, rotating, axisymmetric shells using Novozhilov's shell theory [103]. In [22], the rotational prestress arising from the centripetal acceleration is obtained analytically for shells with free-free boundary conditions. Other researchers [24, 50, 59, 86, 87] studied the vibrations of conical shells with different boundary conditions, yet they used the rotational prestress obtained in [22] for the free-free case. Similarly, [58, 133, 134] studied rotating cylindrical shells with different boundary conditions, but they used the rotational prestress obtained in [22] for the free-free case. These studies neglect the effect of boundary conditions on the rotational prestress by incorrectly using the rotational prestress for the free-free shell obtained by Chen [22]. This problem does not arise in the current formulation.

Penzes and Kraus [114] and Padovan [108] analyzed cylindrical shells prestressed due to uniform loading. Sivadas [129] analyzed thick, rotating, conical shells with prestress due to centripetal acceleration and external torque. Carrera and Filippi [13] analyzed spinning cylindrical shells with prestress due to rotation-induced force using refined beam models. Guo et al. [47] studied vibrations of rotating cylindrical shells under stationary point loads with prestress using equations of motion in Guo et al. [48]. They obtain the dynamic response of the system, but they do not discuss the effects of prestress. In this work, the

prestress stiffness for rotating, axisymmetric shells with general loading is derived similar to that obtained for axisymmetric bodies as described above. The references discussed above have missing terms in the prestress stiffness when compared to the prestress stiffness in this work.

The present semi-analytical formulation uses a two-dimensional finite element mesh of the radial cross-section for general axisymmetric solid bodies. For axisymmetric shells, this formulation reduces to one-dimensional finite elements to mesh the cross-section. Constraints on the motion, coupling to elastic supports, and applied forces are included, and these are not restricted to be axisymmetric. Rotational effects, rotational prestress, and prestress due to external forces are included. The model results validate well with commercial software and literature. The splitting of degenerate natural frequencies from rotation, stress stiffening due to rotational prestress, and effects of rotation on the complex-valued (i.e., traveling wave) vibration modes are investigated. Symmetry breaking effects of prestress due to non-axisymmetric forces lead to distinct stationary frequencies, eigenvalue veering, and vibration modes with multiple nodal diameter components.

2.2 Rotating axisymmetric body

2.2.1 Model description

Fig. 2.1 shows an axisymmetric, flexible body rotating at constant speed Ω about its symmetry axis. The body has an arbitrary two-dimensional radial cross-section. The total cross-sectional area is A. The geometry is uniform circumferentially (i.e., axisymmetric). The material properties are uniform circumferentially but can vary within the cross-section. The Young's modulus, density, and Poisson's ratio are E, ρ, and ν, respectively.

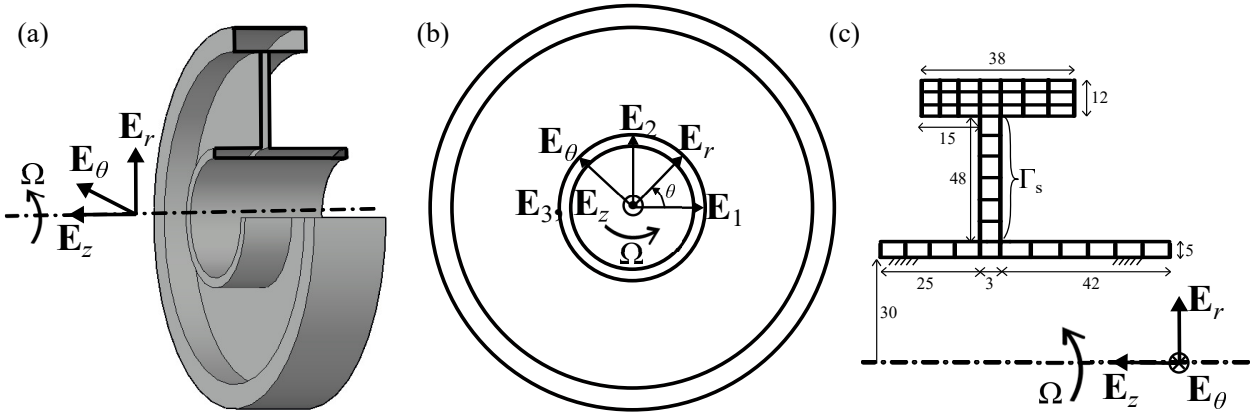

Figure 2.1: (a) Three-dimensional axisymmetric, rotor–disk with radial cross-section marked in solid black lines, (b) front view of the rotor–disk, and (c) two-dimensional discretized finite element cross-section (dimensions in millimeters). A circumferential elastic foundation supports the body along the edge Γ_s.

An elastic foundation with radial (k_u), tangential (k_v), and axial (k_w) stiffnesses per unit of surface area supports the body along any portion of its $r-z$ plane boundary (denoted by Γ_s and shown in Fig. 2.1(c)). The elastic foundation can vary circumferentially so is not necessarily axisymmetric. External forces $\mathbf{F}$ with arbitrary spatial and temporal variation act on the body. These external forces can be asymmetric and can be moving. Constraints may restrict the motion of the rotating body. Like the external forces, these constraints can be asymmetric, vary circumferentially, and be stationary or rotating. Boundary conditions must be specified at points on the boundary in the $r-z$ plane. The boundary conditions are uniform circumferentially.

The basis $\{\mathbf{E}_1, \mathbf{E}_2, \mathbf{E}_3\}$ shown in Fig. 2.1(b) is stationary. The basis $\{\mathbf{E}_r, \mathbf{E}_\theta, \mathbf{E}_z\}$ is also fixed but oriented by the angle θ as shown, where θ defines a spatially fixed angle relative to the stationary base vector $\mathbf{E}_1$. Because the body rotates while the basis $\{\mathbf{E}_r, \mathbf{E}_\theta, \mathbf{E}_z\}$ is fixed, θ does not identify a cross-section of material points on the body. Instead, the cross-section of material points at a given θ changes with time as the body rotates. Similarly, the angle θ identifying the location of a given cross-section of material points changes with

time according to $\theta(t) = \Omega t + \theta_0$.

The elastic deflections of a material point instantaneously at a specified θ are represented by radial $u(r, z, \theta, t)$, tangential $v(r, z, \theta, t)$, and axial $w(r, z, \theta, t)$ displacement degrees of freedom aligned with the $\{\mathbf{E}_r, \mathbf{E}_\theta, \mathbf{E}_z\}$ basis.

The dynamic model of a three-dimensional, rotating, axisymmetric body is derived first. Thin-walled shell structures are considered subsequently.

2.2.2 Dynamic model of a rotating axisymmetric body

Kinetic energy

The position vector of a material point on the rotating axisymmetric body instantaneously rotating past the angle θ before deformation is $\mathbf{r}_0 = r\mathbf{E}_r + z\mathbf{E}_z$. The position vector after deformation is

$$\mathbf{r} = [r + u(r, z, \theta, t)]\,\mathbf{E}_r + v(r, z, \theta, t)\mathbf{E}_\theta + [z + w(r, z, \theta, t)]\,\mathbf{E}_z. \tag{2.1}$$

The velocity of a material point is obtained by the material time derivative of $\mathbf{r}$ that combines: (a) convective velocity terms arising because the angle θ associated with a material particle changes with time according to $\partial\theta/\partial t = \Omega$, and (b) partial derivatives of elastic deflections with respect to time. The material time derivatives are

$$\frac{\mathrm{d}u}{\mathrm{d}t} = \frac{\partial u}{\partial t} + \frac{\partial u}{\partial r}\frac{\partial r}{\partial t} + \frac{\partial u}{\partial \theta}\frac{\partial \theta}{\partial t} + \frac{\partial u}{\partial z}\frac{\partial z}{\partial t} = u_{,t} + \Omega u_{,\theta} \tag{2.2a}$$

$$\frac{\mathrm{d}\mathbf{E}_r}{\mathrm{d}t} = \frac{\partial \mathbf{E}_r}{\partial t} + \frac{\partial \mathbf{E}_r}{\partial \theta}\frac{\partial \theta}{\partial t} = \Omega\mathbf{E}_\theta; \quad \frac{\mathrm{d}\mathbf{E}_\theta}{\mathrm{d}t} = -\Omega\mathbf{E}_r; \quad \frac{\mathrm{d}\mathbf{E}_z}{\mathrm{d}t} = 0, \tag{2.2b}$$

where $(\cdot)_{,t}$ and $(\cdot)_{,\theta}$ are partial derivatives with respect to t and θ. The material time derivatives of displacements v and w are similar to Eq. (2.2a). The particle velocity from the material derivative of $\mathbf{r}$ in Eq. (2.1) is

$$\dot{\mathbf{r}} = \left[u_{,t} + \Omega\left(u_{,\theta} - v\right)\right]\mathbf{E}_r + \left[v_{,t} + \Omega\left(v_{,\theta} + r + u\right)\right]\mathbf{E}_\theta + \left[w_{,t} + \Omega w_{,\theta}\right]\mathbf{E}_z. \tag{2.3}$$

The kinetic energy of the body is

$$T = \frac{1}{2}\int_A \int_0^{2\pi} \rho\dot{\mathbf{r}}\cdot\dot{\mathbf{r}} r \mathrm{d}\theta \mathrm{d}A. \tag{2.4}$$

Strain energy

The elastic strain energy is obtained from Green's nonlinear strain-displacement relations [3]. The strains are expressed as a sum of the linear (L) and nonlinear (NL) terms as

$$\boldsymbol{\epsilon} = \{\epsilon_{rr}, \epsilon_{\theta\theta}, \epsilon_{zz}, \gamma_{r\theta}, \gamma_{\theta z}, \gamma_{rz}\}^T = \boldsymbol{\epsilon}^{\mathrm{L}} + \boldsymbol{\epsilon}^{\mathrm{NL}}, \tag{2.5a}$$

$$\boldsymbol{\epsilon}^{\mathrm{L}} = \begin{Bmatrix} \frac{\partial u}{\partial r} \\ \frac{1}{r}\left(\frac{\partial v}{\partial \theta} + u\right) \\ \frac{\partial w}{\partial z} \\ \left(\frac{1}{r}\frac{\partial u}{\partial \theta} + \frac{\partial v}{\partial r} - \frac{v}{r}\right) \\ \left(\frac{1}{r}\frac{\partial w}{\partial \theta} + \frac{\partial v}{\partial z}\right) \\ \left(\frac{\partial w}{\partial r} + \frac{\partial u}{\partial z}\right) \end{Bmatrix}, \quad \boldsymbol{\epsilon}^{\mathrm{NL}} = \begin{Bmatrix} \frac{1}{2}\left[\left(\frac{\partial u}{\partial r}\right)^2 + \left(\frac{\partial v}{\partial r}\right)^2 + \left(\frac{\partial w}{\partial r}\right)^2\right] \\ \frac{1}{2r^2}\left[\left(\frac{\partial v}{\partial \theta} + u\right)^2 + \left(\frac{\partial u}{\partial \theta} - v\right)^2 + \left(\frac{\partial w}{\partial \theta}\right)^2\right] \\ \frac{1}{2}\left[\left(\frac{\partial u}{\partial z}\right)^2 + \left(\frac{\partial v}{\partial z}\right)^2 + \left(\frac{\partial w}{\partial z}\right)^2\right] \\ \frac{1}{r}\left[\frac{\partial u}{\partial r}\left(\frac{\partial u}{\partial \theta} - v\right) + \frac{\partial v}{\partial r}\left(\frac{\partial v}{\partial \theta} + u\right) + \frac{\partial w}{\partial r}\frac{\partial w}{\partial \theta}\right] \\ \frac{1}{r}\left[\frac{\partial v}{\partial z}\left(\frac{\partial v}{\partial \theta} + u\right) + \frac{\partial u}{\partial z}\left(\frac{\partial u}{\partial \theta} - v\right) + \frac{\partial w}{\partial z}\frac{\partial w}{\partial \theta}\right] \\ \left(\frac{\partial u}{\partial r}\frac{\partial u}{\partial z} + \frac{\partial v}{\partial r}\frac{\partial v}{\partial z} + \frac{\partial w}{\partial r}\frac{\partial w}{\partial z}\right) \end{Bmatrix}. \tag{2.5b}$$

The stresses are obtained from the constitutive relation $\boldsymbol{\sigma} = \mathbf{D}\boldsymbol{\epsilon}$, where $\mathbf{D}$ is the elasticity tensor. The elastic strain energy of the body is

$$\Pi = \frac{1}{2}\int_A \int_0^{2\pi} \boldsymbol{\epsilon}^T \boldsymbol{\sigma} r \mathrm{d}\theta \mathrm{d}A. \tag{2.6}$$

Terms up to the third order of displacement are retained in the elastic strain energy.

The strain energy in the elastic foundation is

$$\Pi_f = \frac{1}{2}\int_{\Gamma_s} \int_0^{2\pi} \left(k_u u^2 + k_v v^2 + k_w w^2\right) r \mathrm{d}\theta \mathrm{d}\Gamma_s. \tag{2.7}$$

While the elastic foundation can vary circumferentially, a circumferentially varying foundation that is fixed relative to the rotating body results in time-dependent foundation stiffness terms in the equations of motion.

External forces

Rotating bodies can experience space-fixed or rotating external forces. Examples of space-fixed forces are the stationary contact force acting on a rotating tire in contact with the ground, a tooth meshing force at a fixed contact location in a coupled gear pair, and a stationary braking force on a spinning brake rotor. Whether stationary or moving, the external forces may vary circumferentially, in which case the system response may lack symmetry despite the rotating body being axisymmetric.

An external force distribution $\mathbf{F} = F_u \mathbf{E}_r + F_v \mathbf{E}_\theta + F_w \mathbf{E}_z$ per unit volume acts on the body. The forces can arise from nonlinearity such that, in general, they are functions of displacements and velocities as well as the spatial coordinates and time. The virtual work

expression is

$$\delta W = \int_A \int_0^{2\pi} \left(F_u \delta u + F_v \delta v + F_w \delta w\right) r \mathrm{d}\theta \mathrm{d}A, \tag{2.8}$$

where $\delta u, \delta v$, and δw are virtual displacements.

Constraints

Constraints that restrict the motion of a rotating body are admitted. Such constraints are, most likely, either fixed in space or moving with the rotating body, but the formulation is not limited to these cases. The constraints can be asymmetric. Examples include zero axial displacement at a guide location on a circular sawblade or hard disk drive and a brake-rotor area constrained by a brake pad. A set of N_c constraints, whether holonomic or non-holonomic, can be represented by the N_c-dimensional vector expression

$$\mathbf{f}(u, v, w, u_{,t}, v_{,t}, w_{,t}, t) = \mathbf{0}. \tag{2.9}$$

The constraints are assumed to be at most linear in the velocities.

The constraints are mathematically imposed using Lagrange multipliers collected in an N_c-dimensional vector $\mathbf{\Lambda}$ [26, 97]. Alternatively, the penalty method [8, 26] can impose the constraint equations. Boundary conditions can be treated as constraints and imposed using Lagrange multipliers, which yields the forces needed to impose the boundary conditions.

Because the present method formulates the governing equations in the stationary $\{\mathbf{E}_r, \mathbf{E}_\theta, \mathbf{E}_z\}$ reference frame, asymmetric constraints fixed to the rotating body lead to time-dependent coefficients in the equations of motion. Constraints fixed in space, whether axisymmetric or asymmetric, and axisymmetric constraints fixed to the rotating body result in constant coefficient equations of motion.

2.2.3 Displacement field approximation

The displacement fields required to calculate the foregoing kinetic and strain energies are spatially discretized. A key point of the formulation is that, because of axisymmetry of the body, the discretization is carried out only on a radial cross-section of the body. The choice of discretization method depends on whether the geometry of the cross-section has a simple form (such as a circle or rectangle) or a more complex form. If the cross-section has a simple form where one can identify discretization basis functions that define the entire cross-section (e.g., polynomials or Bessel functions combined with trigonometric functions for circular cross-sections like in a torus), then these are the most computationally efficient and convenient. We call these global basis functions. If, however, the cross-section has a complex shape, then a local discretization such as finite element is required (other local discretization approaches such as finite differences are also possible). We discuss both global and local discretizations below.

For either of global or local discretization, the essential point is that, because of axisymmetry of the body, the basis functions are the same for any value of the space-fixed angular coordinate θ; they only depend on the cross-sectional coordinates r and z. Circumferential variations of the displacement fields, which are not restricted to be axisymmetric, are captured by dependence of the basis function coefficients on θ.

Considering first the case of simple cross-sectional geometry and global discretization, the displacement field at a given space-fixed angular location θ is expressed as

$$u(r,z,\theta,t) = \sum_l \sum_m \Phi_u^{lm}(r,z) U^{lm}(\theta,t). \tag{2.10}$$

The basis functions $\Phi_u^{lm}(r,z)$ form a complete set that satisfy, at a minimum, the geometric boundary conditions in the (r,z) plane of the cross-section. The unknown coefficients

$U^{lm}(\theta,t)$ are to be determined. Axisymmetry of the body means that, even as the body rotates, the undeflected shape of the cross-section (but not the displacement fields) is the same at any angular orientation θ and at any moment in time. Thus, the basis functions $\Phi_u^{lm}(r,z)$ in Eq. (2.10) do not depend on either θ or t. The dependence of the displacement field on θ and t is captured through the basis function coefficients.

The basis functions $\Phi_u^{lm}(r,z)$ depend on the cross-sectional geometry. For example, the cross-section of the outer cylindrical body of the system in Fig. 2.1 is rectangular with length a and thickness b. For the case of simply supported boundaries on all sides, a suitable choice of basis functions is

$$\Phi_u^{lm}(r,z) = \sin\frac{l\pi r}{b}\sin\frac{m\pi z}{a}, \qquad l,m = 1,2,...,\infty. \tag{2.11}$$

For other boundary conditions or other cross-sectional shapes (e.g., circular), one would choose the basis functions to be polynomials, other trigonometric functions, Bessel functions, and the like.

Because the body and its displacement fields are continuous in θ and 2π periodic, so are the θ-dependent coefficients $U^{lm}(\theta,t)$ in Eq. (2.10). Thus, they can be expanded using Fourier series as

$$U^{lm}(\theta,t) = U_0^{lm}(t) + \sum_{n=1}^{\infty}\left[U_{nc}^{lm}(t)\cos n\theta + U_{ns}^{lm}(t)\sin n\theta\right]. \tag{2.12}$$

The coefficients $U_{nc}^{lm}(t), U_{ns}^{lm}(t)$ determine the amplitude of the n^{th} Fourier harmonic of the radial displacement, also referred to as the n^{th} nodal diameter component of radial displacement. The displacements represented by $U_0^{lm}(t)$ correspond to circumferentially uniform 0^{th} harmonic axisymmetric deflections.

Following a similar process for the tangential and axial displacements, the three displacement fields for an axisymmetric body are

$$u(r,z,\theta,t) = \sum_l \sum_m \Phi_u^{lm}(r,z) \left[U_0^{lm}(t) + \sum_{n=1}^{\infty} \left(U_{nc}^{lm}(t) \cos n\theta + U_{ns}^{lm}(t) \sin n\theta \right) \right], \quad (2.13a)$$

$$v(r,z,\theta,t) = \sum_l \sum_m \Phi_v^{lm}(r,z) \left[V_0^{lm}(t) + \sum_{n=1}^{\infty} \left(V_{nc}^{lm}(t) \cos n\theta - V_{ns}^{lm}(t) \sin n\theta \right) \right], \quad (2.13b)$$

$$w(r,z,\theta,t) = \sum_l \sum_m \Phi_w^{lm}(r,z) \left[W_0^{lm}(t) + \sum_{n=1}^{\infty} \left(W_{nc}^{lm}(t) \cos n\theta + W_{ns}^{lm}(t) \sin n\theta \right) \right], \quad (2.13c)$$

where $\Phi_u^{lm}(r,z)$, $\Phi_v^{lm}(r,z)$, and $\Phi_w^{lm}(r,z)$ are global basis functions for the radial, tangential, and axial displacement fields, respectively.

These displacement fields admit non-axisymmetric deformations of the axisymmetric body.

The negative sign in Eq. (2.13b) is used for convenience to result in identical stiffness matrices corresponding to the symmetric and antisymmetric components [26].

We now consider complex cross-sectional geometries, like in Fig. 2.1, that require local discretization. For an axisymmetric body with a complex cross-section, obtaining global basis functions that span the entire cross-section is typically not possible. Thus, the cross-section is discretized locally using the finite element method with two-dimensional (e.g., triangular or quadrilateral) elements as shown in Fig. 2.1(c). Anticipating the use of Fourier series to extend each cross-sectional finite element in the θ direction, as done above with global basis functions, one can visualize each individual finite element as defining a

three-dimensional elemental ring. These multiple elemental rings collectively constitute the full axisymmetric body.

The displacement field within a finite element e at any given angular location θ is expressed similarly to Eq. (2.10) as

$$u_e(r, z, \theta, t) = \mathbf{\Psi}_u^{e\,T}(r, z)\mathbf{U}_e(\theta, t), \tag{2.14}$$

where $\mathbf{\Psi}_u^e(r, z)$ is a vector of local shape functions within an element e that defines the radial displacement field. The as yet unknown $\mathbf{U}_e(\theta, t)$ is a vector of the nodal deflections of an element. The local shape functions $\mathbf{\Psi}_u^e(r, z)$ are analogous to the global basis function $\Phi_u^{lm}(r, z)$ in Eq. (2.13). Axisymmetry of the body allows the use of an identical cross-sectional mesh at any angular position θ and at any time t. Thus, $\mathbf{\Psi}_u^e(r, z)$ is not a function of θ or t. The nodal deflections of each element $\mathbf{U}_e(\theta, t)$ vary circumferentially such that they are functions of θ.

The local shape functions $\mathbf{\Psi}_u^e(r, z)$ are standard finite element shape functions such as Lagrange polynomials, Legendre polynomials, or Chebyshev polynomials [9, 26, 119, 159]. To accommodate elements of general polygonal shape, an isoparametric form of shape functions is used on the isoparametric space defined by coordinates (ξ, η). The standard finite element approach [9, 26, 159] is used to convert between physical coordinates (r, z) and isoparametric coordinates (ξ, η).

The nodal deflections $\mathbf{U}_e(\theta, t)$ are periodic and so expanded in Fourier series as done in Eq. (2.12). Consequently, the displacement fields for an axisymmetric body with

complex radial cross-section locally discretized into finite elements are

$$u_e(r,z,\theta,t) = \boldsymbol{\Psi}_u^{eT}(r,z)\left[\mathbf{U}_0^e(t) + \sum_{n=1}^{\infty}\left(\mathbf{U}_{nc}^e(t)\cos n\theta + \mathbf{U}_{ns}^e(t)\sin n\theta\right)\right], \tag{2.15a}$$

$$v_e(r,z,\theta,t) = \boldsymbol{\Psi}_v^{eT}(r,z)\left[\mathbf{V}_0^e(t) + \sum_{n=1}^{\infty}\left(\mathbf{V}_{nc}^e(t)\cos n\theta - \mathbf{V}_{ns}^e(t)\sin n\theta\right)\right], \tag{2.15b}$$

$$w_e(r,z,\theta,t) = \boldsymbol{\Psi}_w^{e\,T}(r,z)\left[\mathbf{W}_0^e(t) + \sum_{n=1}^{\infty}\left(\mathbf{W}_{nc}^e(t)\cos n\theta + \mathbf{W}_{ns}^e(t)\sin n\theta\right)\right]. \tag{2.15c}$$

2.2.4 Matrix form

For a simple cross-section defined using global basis functions, substitution of Eq. (2.13) into strain-displacement Eq. (2.5) results in

$$\boldsymbol{\epsilon} = \boldsymbol{\epsilon}^{\mathrm{L}} + \boldsymbol{\epsilon}^{\mathrm{NL}} = \mathbf{B}\mathbf{q} + \frac{1}{2}\mathbf{S}(\mathbf{q})\boldsymbol{\beta}\mathbf{q}. \tag{2.16}$$

The matrices $\mathbf{B}$, $\mathbf{S}(\mathbf{q})$, and $\boldsymbol{\beta}$ are analogous to elemental matrices discussed later and are described in Appendix A.1. $\mathbf{q}$ is the vector of unknown time-dependent coefficients defined in Eq. (2.13) for all harmonics given as

$$\mathbf{q} = \left\{\mathbf{q}_0^T \quad \mathbf{q}_1^T \quad \ldots \quad \mathbf{q}_n^T\right\}^T, \tag{2.17}$$

$$\mathbf{q}_n = \left\{U_{nc} \quad U_{ns} \quad V_{ns} \quad V_{nc} \quad W_{nc} \quad W_{ns}\right\}^T.$$

Substitution of Eq. (2.16) and $\boldsymbol{\sigma} = \mathbf{D}\boldsymbol{\epsilon}$ into the strain energy Eq. (2.6) and retaining up to cubic orders of displacement $\mathbf{q}$ leads to

$$\Pi = \frac{1}{2}\left[\mathbf{q}^T\mathbf{K}\mathbf{q} + \mathbf{N}(\mathbf{q})\right], \tag{2.18a}$$

$$\mathbf{K} = \int_A \int_0^{2\pi} \mathbf{B}^T\mathbf{D}\mathbf{B}\, r\mathrm{d}\theta\mathrm{d}A, \tag{2.18b}$$

$$\mathbf{N}(\mathbf{q}) = \frac{1}{2}\mathbf{q}^T\left[\int_A \int_0^{2\pi} \left(\mathbf{P}(\mathbf{q}) + \mathbf{P}^T(\mathbf{q})\right) r\mathrm{d}\theta\mathrm{d}A\right]\mathbf{q}, \tag{2.18c}$$

$$\mathbf{P}(\mathbf{q}) = \boldsymbol{\beta}^T\mathbf{S}^T(\mathbf{q})\mathbf{D}\mathbf{B}. \tag{2.18d}$$

The first term of Eq. (2.18a) will yield the constant linear elastic stiffness matrix $\mathbf{K}$ in the equations of motion; the term $\mathbf{N}(\mathbf{q})$ containing cubic orders of displacement will contribute to the prestress stiffness matrix.

Similarly, substitution of Eq. (2.13) into Eqs. (2.4), (2.7), (2.8), and (2.9), leads to

$$T = \frac{1}{2}(\dot{\mathbf{q}}^T\mathbf{M}\dot{\mathbf{q}} + \Omega\dot{\mathbf{q}}^T\mathbf{G}\mathbf{q} + \Omega^2\mathbf{q}^T\mathbf{C}\mathbf{q} + \Omega^2 r^2) + \Omega^2\mathbf{F}_\Omega^T\mathbf{q}, \tag{2.19a}$$

$$\Pi_f = \frac{1}{2}\mathbf{q}^T\mathbf{K}_f\mathbf{q}, \tag{2.19b}$$

$$\delta W = \mathbf{F}(\mathbf{q}, \dot{\mathbf{q}}, t) \cdot \delta \mathbf{q}, \tag{2.19c}$$

$$\mathbf{f}(u, v, w, u_{,t}, v_{,t}, w_{,t}, t) = \mathbf{f}(\mathbf{q}, \dot{\mathbf{q}}, t) = \mathbf{0}. \tag{2.19d}$$

$\mathbf{M}, \mathbf{G}$, and $\mathbf{C}$ are the mass, gyroscopic, and centripetal matrices, respectively. $\mathbf{F}_\Omega$ is a constant, rotation-induced vector due to centripetal acceleration. $\mathbf{K}_f$ is the elastic foundation stiffness matrix. All of the matrix components are analogous to the matrix components of the elemental matrices that are discussed next and are described in Appendix A.1.

For a complex geometric cross-section divided into two-dimensional finite elements, the matrix forms of a single elemental ring of cross-sectional area A_e are obtained by substitution of Eq. (2.15) into Eqs. (2.4), (2.6), (2.7), and (2.8), leading to

$$T_e = \frac{1}{2}(\dot{\mathbf{q}}_e^T \mathbf{m}_e \dot{\mathbf{q}}_e + \Omega \dot{\mathbf{q}}_e^T \mathbf{g}_e \mathbf{q}_e + \Omega^2 \mathbf{q}_e^T \mathbf{c}_e \mathbf{q}_e + \Omega^2 r^2) + \Omega^2 \mathbf{f}_\Omega^T \mathbf{q}_e, \tag{2.20a}$$

$$\Pi_e = \frac{1}{2}\left[\mathbf{q}_e^T \mathbf{k}_e \mathbf{q}_e + \mathbf{n}_e(\mathbf{q}_e)\right], \tag{2.20b}$$

$$\Pi_{f_e} = \frac{1}{2}\mathbf{q}_e^T \mathbf{k}_{f_e} \mathbf{q}_e, \tag{2.20c}$$

$$\delta W_e = \mathbf{F}_e(\mathbf{q}_e, \dot{\mathbf{q}}_e, t) \cdot \delta \mathbf{q}_e, \tag{2.20d}$$

where $\mathbf{m}_e, \mathbf{g}_e$, and $\mathbf{c}_e$ are the elemental mass, gyroscopic, and centripetal matrices, and $\mathbf{f}_\Omega$ is a constant rotation-induced vector. $\mathbf{k}_{f_e}$ is the elemental elastic foundation matrix. $\mathbf{k}_e$ and

$\mathbf{n}_e(\mathbf{q}_e)$ are analogous to corresponding terms in Eq. (2.18) and given as

$$\mathbf{k}_e = \int_{A_e} \int_0^{2\pi} \mathbf{B}_e^T \mathbf{D} \mathbf{B}_e \, r \mathrm{d}\theta \mathrm{d}A_e, \tag{2.21a}$$

$$\mathbf{n}_e(\mathbf{q}_e) = \frac{1}{2} \mathbf{q}_e^T \left[\int_{A_e} \int_0^{2\pi} \left(\mathbf{p}_e(\mathbf{q}_e) + \mathbf{p}_e^T(\mathbf{q}_e) \right) r \mathrm{d}\theta \mathrm{d}A_e \right] \mathbf{q}_e, \tag{2.21b}$$

$$\mathbf{p}_e(\mathbf{q}_e) = \boldsymbol{\beta}_e^T \mathbf{S}_e^T(\mathbf{q}_e) \mathbf{D} \mathbf{B}_e, \tag{2.21c}$$

where $\mathbf{B}_e$, $\mathbf{S}_e(\mathbf{q}_e)$, and $\boldsymbol{\beta}_e$ are given in Appendix A.1. $\mathbf{q}_e$ is the vector of time-dependent nodal deflections for all harmonics associated with a single finite element (i.e., a single elemental ring) given as

$$\begin{aligned} \mathbf{q}_e &= \left\{ \mathbf{q}_{0_e}^T \quad \mathbf{q}_{1_e}^T \quad \dots \quad \mathbf{q}_{n_e}^T \right\}^T, \\ \mathbf{q}_{n_e} &= \left\{ \mathbf{U}_{nc}^e \quad \mathbf{U}_{ns}^e \quad \mathbf{V}_{ns}^e \quad \mathbf{V}_{nc}^e \quad \mathbf{W}_{nc}^e \quad \mathbf{W}_{ns}^e \right\}^T. \end{aligned} \tag{2.22}$$

The sum of the energies of all elemental rings yields the total energy of the axisymmetric body as $T = \sum_{e=1}^{N_e} T_e$, with similar summations for Π, Π_f, and δW, where N_e is the number of elements in the cross-section. The summation of elemental energies leads to the assembly of elemental matrices into global matrices in such a way that nodal degrees of freedom for nodes that are common to adjacent elements are set equal. This is a standard finite element assembly process that results in global matrices analogous in form to Eq. (2.19) and a global time-dependent coefficient vector $\mathbf{q}$ analogous to Eq. (2.17). The terms "global matrices" and "global coefficient vector" used in this context are standard finite element terminologies and should not be confused with global discretization defined previously.

The constraint in Eq. (2.19d) applies to the global assembled system. This constraint (holonomic or non-holonomic) in terms of the nodal coefficients $\mathbf{q}$ in Eq. (2.17) is of the form

$$\mathbf{A}_{\mathbf{q}}(\mathbf{q},t)\dot{\mathbf{q}} + \mathbf{a}_t(\mathbf{q},t) = \mathbf{0}. \tag{2.23}$$

For a holonomic constraint, $\mathbf{A}_{\mathbf{q}} = \partial\mathbf{f}/\partial\mathbf{q}$.

The generalized constraint forces $\mathbf{F}_c(\mathbf{q},t)$ [97] required to impose the constraint are obtained using Lagrange multipliers $\mathbf{\Lambda}$ as

$$\mathbf{F}_c(\mathbf{q},t) = \mathbf{A}_{\mathbf{q}}^T(\mathbf{q},t)\mathbf{\Lambda}. \tag{2.24}$$

No work is performed by the constraint forces in a virtual displacement ($\mathbf{F}_c(\mathbf{q},t)\cdot\delta\mathbf{q} = 0$).

2.2.5 Equation of motion

Lagrange's equations of motion with respect to the unknown nodal coefficients $\mathbf{q}(t)$ in Eq. (2.17) are

$$\frac{\mathrm{d}}{\mathrm{d}t}\left(\frac{\partial T}{\partial\dot{\mathbf{q}}}\right) - \frac{\partial T}{\partial\mathbf{q}} + \frac{\partial\Pi}{\partial\mathbf{q}} + \frac{\partial\Pi_f}{\partial\mathbf{q}} = \mathbf{F}(\mathbf{q},t) + \mathbf{F}_c(\mathbf{q},t). \tag{2.25}$$

The energies from Eqs. (2.18) and (2.19) or the global assembled energies of elemental energies from Eq. (2.20) and constraint force $\mathbf{F}_c(\mathbf{q},t)$ from Eq. (2.24) are substituted into Eq. (2.25). Applying variation with respect to the unknown nodal coefficients, the equations of motion with constraints are

$$\mathbf{M}\ddot{\mathbf{q}} + \Omega\mathbf{G}\dot{\mathbf{q}} + (\mathbf{K} + \mathbf{K}_f - \Omega^2\mathbf{C})\mathbf{q} + \frac{1}{2}\frac{\partial\mathbf{N}(\mathbf{q})}{\partial\mathbf{q}} + \mathbf{A}_{\mathbf{q}}^T\mathbf{\Lambda} = \Omega^2\mathbf{F}_\Omega + \mathbf{F}(\mathbf{q},t), \tag{2.26a}$$

$$\mathbf{A}_\mathbf{q}\mathbf{q} = \mathbf{0}. \tag{2.26b}$$

Prestress in a rotating axisymmetric body

The rotating body is prestressed by $\mathbf{F}_\Omega$ due to the constant, rotation-induced acceleration and the mean values of any external forces $\mathbf{F}$. Our goal is to determine a steady prestressed state defined by steady deflection $\overline{\mathbf{q}}$ that can have moderate amplitude; small vibratory displacements $\tilde{\mathbf{q}}(t)$ occur relative to the prestressed state. Prestress from the steady deflection generates a prestress (or geometric) stiffness matrix in the equations of motion for vibration relative to the steady deflected state.

First, the steady state deflection of the body is obtained by elimination of the time derivatives from Eq. (2.26), resulting in

$$(\mathbf{K} + \mathbf{K}_f - \Omega^2\mathbf{C})\overline{\mathbf{q}} + \frac{1}{2}\frac{\partial \mathbf{N}(\overline{\mathbf{q}})}{\partial \overline{\mathbf{q}}} + \mathbf{A}_\mathbf{q}^T\overline{\mathbf{\Lambda}} = \Omega^2\mathbf{F}_\Omega + \mathbf{F}(\overline{\mathbf{q}}), \tag{2.27a}$$

$$\mathbf{A}_\mathbf{q}\overline{\mathbf{q}} = \mathbf{0}, \tag{2.27b}$$

where $\overline{(\cdot)}$ denotes a steady term. This nonlinear algebraic problem is solved numerically for $\overline{\mathbf{q}}$.

Eq. (2.27) can be linearized for small steady deflection. Assuming no constraints in Eq. (2.27) for simplicity, the linearized steady state deflection is

$$\overline{\mathbf{q}} = (\mathbf{K} + \mathbf{K}_f - \Omega^2\mathbf{C})^{-1}(\Omega^2\mathbf{F}_\Omega + \mathbf{F}(\overline{\mathbf{q}})). \tag{2.28}$$

This solution is substantially easier to compute than using Eq. (2.27). Later results show it

can yield excellent results.

Further reduction of computational expense is possible for the combination of low to moderate speeds and negligible steady deflection arising from $\mathbf{F}(\overline{\mathbf{q}})$. In such cases, $\mathbf{F}(\overline{\mathbf{q}})$ is omitted in Eq. (2.28), and Taylor series approximation in Ω gives

$$\overline{\mathbf{q}} = \Omega^2[(\mathbf{K}+\mathbf{K}_f)^{-1}\mathbf{F}_\Omega] + O(\Omega^4) \approx \Omega^2\overline{\mathbf{q}}_a. \tag{2.29}$$

Significant computational savings arise from Eq. (2.29) because $\overline{\mathbf{q}}_a = (\mathbf{K}+\mathbf{K}_f)^{-1}\mathbf{F}_\Omega$ is independent of speed. It is calculated once, and thus calculation of $\overline{\mathbf{q}}$ from Eq. (2.29) for any given Ω is trivial. In contrast, either of Eqs. (2.27) or (2.28) involve much greater computational expense to solve for $\overline{\mathbf{q}}$ at each rotation speed. An example comparing the effects of steady deflection obtained from Eqs. (2.27) and (2.29) on natural frequencies is given later. One can readily extend Eqs. (2.28) and (2.29) if constraints $\mathbf{A}_\mathbf{q}$ are present.

With $\overline{\mathbf{q}}$ determined, the equations governing the small vibrations $\tilde{\mathbf{q}}(t)$ about the steady deflected state are obtained by substitution of $\mathbf{q}(t) = \overline{\mathbf{q}} + \tilde{\mathbf{q}}(t)$ into Eq. (2.26). Linearizing the nonlinear term $\frac{\partial \mathbf{N}(\mathbf{q})}{\partial \mathbf{q}}$ in Eq. (2.26a) for small $\tilde{\mathbf{q}}(t)$, the linear prestress stiffness matrix is

$$\mathbf{K}_p(\overline{\mathbf{q}}) = \int_A \int_0^{2\pi} \left[\boldsymbol{\beta}^{\mathrm{T}}\boldsymbol{\Sigma}(\overline{\mathbf{q}})\boldsymbol{\beta} + \mathbf{P}(\overline{\mathbf{q}}) + \mathbf{P}^T(\overline{\mathbf{q}})\right] r\mathrm{d}\theta\mathrm{d}A, \tag{2.30a}$$

$$\boldsymbol{\Sigma}(\overline{\mathbf{q}}) = \begin{bmatrix} \overline{\sigma}_{rr}\mathbf{I}_3 & \overline{\sigma}_{r\theta}\mathbf{I}_3 & \overline{\sigma}_{rz}\mathbf{I}_3 \\ \overline{\sigma}_{r\theta}\mathbf{I}_3 & \overline{\sigma}_{\theta\theta}\mathbf{I}_3 & \overline{\sigma}_{\theta z}\mathbf{I}_3 \\ \overline{\sigma}_{rz}\mathbf{I}_3 & \overline{\sigma}_{\theta z}\mathbf{I}_3 & \overline{\sigma}_{zz}\mathbf{I}_3 \end{bmatrix}, \tag{2.30b}$$

where $\mathbf{I}_3$ is the 3×3 identity matrix and $\mathbf{P}(\overline{\mathbf{q}})$ is from Eq. (2.18d). The equations $\mathbf{S}(\tilde{\mathbf{q}})\boldsymbol{\beta}\overline{\mathbf{q}} =$

$\mathbf{S}(\overline{\mathbf{q}})\boldsymbol{\beta}\tilde{\mathbf{q}}$ and $\mathbf{S}^T(\tilde{\mathbf{q}})\mathbf{D}\mathbf{B}\overline{\mathbf{q}} = \boldsymbol{\Sigma}(\overline{\mathbf{q}})\boldsymbol{\beta}\tilde{\mathbf{q}}$ are applied in obtaining Eq. (2.30). Also, $\mathbf{D}\mathbf{B}\overline{\mathbf{q}} = \{\overline{\sigma}_{rr}, \overline{\sigma}_{\theta\theta}, \overline{\sigma}_{zz}, \overline{\sigma}_{r\theta}, \overline{\sigma}_{\theta z}, \overline{\sigma}_{rz}\}$ is used.

For the conditions where Eq. (2.29) applies, the prestress stiffness matrix is

$$\mathbf{K}_p(\overline{\mathbf{q}}) = \Omega^2 \int_A \int_0^{2\pi} \left[\boldsymbol{\beta}^{\mathrm{T}}\boldsymbol{\Sigma}(\overline{\mathbf{q}}_a)\boldsymbol{\beta} + \mathbf{P}(\overline{\mathbf{q}}_a) + \mathbf{P}^T(\overline{\mathbf{q}}_a)\right] r\mathrm{d}\theta\mathrm{d}A = \Omega^2\mathbf{K}_{pa}(\overline{\mathbf{q}}_a). \tag{2.31}$$

The matrix $\mathbf{K}_{pa}$ is calculated only once rather than at each speed, which substantially reduces computational cost.

The linearized equation of motion including the effects of prestress is

$$\mathbf{M}\ddot{\tilde{\mathbf{q}}} + \Omega\mathbf{G}\dot{\tilde{\mathbf{q}}} + [\mathbf{K} + \mathbf{K}_f + \mathbf{K}_p(\overline{\mathbf{q}}) - \Omega^2\mathbf{C}]\tilde{\mathbf{q}} + \mathbf{A}_{\mathbf{q}}^T\tilde{\boldsymbol{\Lambda}} = \tilde{\mathbf{F}}(t), \tag{2.32a}$$

$$\mathbf{A}_{\mathbf{q}}\tilde{\mathbf{q}} = \mathbf{0}. \tag{2.32b}$$

Eq. (2.32) is in the standard form of a conservative, gyroscopic system where $\mathbf{M}$, $\mathbf{K}$, $\mathbf{K}_f$, $\mathbf{K}_p(\overline{\mathbf{q}})$, and $\mathbf{C}$ are symmetric (note the sum $\mathbf{P}(\overline{\mathbf{q}}) + \mathbf{P}^T(\overline{\mathbf{q}})$ in Eq. (2.30a) is symmetric), and $\mathbf{G}$ is skew-symmetric.

The prestress (or geometric) stiffness matrix derived in Eq. (2.30) has terms that are absent in the prestress stiffness matrix in Refs. [43, 44, 57]. Only the first term ($\boldsymbol{\beta}^T\boldsymbol{\Sigma}(\overline{\mathbf{q}})\boldsymbol{\beta}$) in Eq. (2.30a) is present in the prestress stiffness matrix in the above references. The differences, discussed below, can substantially impact natural frequencies and vibration modes, as shown later for the system in Fig. 2.3(a).

The prestressed state of the body is defined by the steady deflection $\overline{\mathbf{q}}$ relative to the unstressed state that results in prestrain $\overline{\boldsymbol{\epsilon}}$ and corresponding prestress $\overline{\boldsymbol{\sigma}} = \mathbf{D}\overline{\boldsymbol{\epsilon}}$. These

steady deflections are assumed to be moderate such that $\overline{\mathbf{q}}^2$ is small but not negligible (*i.e.*, $\overline{\mathbf{q}}^2$ is the same order as $\tilde{\mathbf{q}}(t)$). The vibratory state of the body is defined by small, time-dependent deflections $\tilde{\mathbf{q}}(t)$ measured relative to the prestressed state. The total deflection of the body relative to its unstressed state is $\mathbf{q}(t) = \overline{\mathbf{q}} + \tilde{\mathbf{q}}(t)$. The total strain and total stress of the vibratory state relative to the unstressed state are $\boldsymbol{\epsilon}$ and $\boldsymbol{\sigma} = \mathbf{D}\boldsymbol{\epsilon}$, respectively.

Because it captures what is done in similar references, including [43, 57], we discuss prestress in relation to [44]. The strain energy differential from Eq. (15.53) of [44] using the notation of the present dissertation is

$$\mathrm{d}\Pi = \int \boldsymbol{\sigma}^T \mathrm{d}\boldsymbol{\epsilon} = \int [\overline{\boldsymbol{\sigma}}^T + (\boldsymbol{\epsilon}^T - \overline{\boldsymbol{\epsilon}}^T)\mathbf{D}]\mathrm{d}\boldsymbol{\epsilon} = \overline{\boldsymbol{\sigma}}^T\boldsymbol{\epsilon} + \frac{1}{2}\boldsymbol{\epsilon}^T\mathbf{D}\boldsymbol{\epsilon} - \overline{\boldsymbol{\epsilon}}^T\mathbf{D}\boldsymbol{\epsilon}. \tag{2.33}$$

According to [44], the prestress $\overline{\boldsymbol{\sigma}}$ and prestrain $\overline{\boldsymbol{\epsilon}}$ are determined *a priori*, for example from a finite element analysis. The use of vibratory strain $(\boldsymbol{\epsilon} - \overline{\boldsymbol{\epsilon}})$ in Eq. (2.33) from [44] indicates that $\boldsymbol{\epsilon}$ is the total strain relative to the unstressed state. One draws the same conclusion after substitution of $\overline{\boldsymbol{\sigma}} = \mathbf{D}\overline{\boldsymbol{\epsilon}}$ in the last expression of Eq. (2.33) that leaves only the classical strain energy per unit volume $\frac{1}{2}\boldsymbol{\epsilon}^T\mathbf{D}\boldsymbol{\epsilon}$. The total strain $\boldsymbol{\epsilon}$ depends on the total deflection $\mathbf{q}(t)$; thus, $\boldsymbol{\epsilon}$ is a function of both $\overline{\mathbf{q}}$ and $\tilde{\mathbf{q}}(t)$ rather than only $\tilde{\mathbf{q}}(t)$. This is important below.

Substitution of the nonlinear strain-displacement relation $(\boldsymbol{\epsilon} = \boldsymbol{\epsilon}^{\mathrm{L}} + \boldsymbol{\epsilon}^{\mathrm{NL}})$ from Eq. (2.5) (same as Eq. (15.55) in [44]) into Eq. (2.33) integrated over the volume results in

$$\begin{aligned}\Pi = \tfrac{1}{2}\int_A\int_0^{2\pi} \boldsymbol{\epsilon}^{\mathrm{L}T}\mathbf{D}\boldsymbol{\epsilon}^{\mathrm{L}}\, r\mathrm{d}\theta\mathrm{d}A + \tfrac{1}{2}\int_A\int_0^{2\pi} (\boldsymbol{\epsilon}^{\mathrm{L}T}\mathbf{D}\boldsymbol{\epsilon}^{\mathrm{NL}} + \boldsymbol{\epsilon}^{\mathrm{NL}T}\mathbf{D}\boldsymbol{\epsilon}^{\mathrm{L}})\, r\mathrm{d}\theta\mathrm{d}A + \\ \int_A\int_0^{2\pi} (\overline{\boldsymbol{\sigma}}^T\boldsymbol{\epsilon}^{\mathrm{L}} + \overline{\boldsymbol{\sigma}}^T\boldsymbol{\epsilon}^{\mathrm{NL}} - \overline{\boldsymbol{\epsilon}}^T\mathbf{D}\boldsymbol{\epsilon}^{\mathrm{L}} - \overline{\boldsymbol{\epsilon}}^T\mathbf{D}\boldsymbol{\epsilon}^{\mathrm{NL}})\, r\mathrm{d}\theta\mathrm{d}A.\end{aligned} \tag{2.34}$$

The term that is quadratic in $\boldsymbol{\epsilon}^{\mathrm{NL}}$ has been discarded. The terms it would contribute to the linearized (for small $\tilde{\mathbf{q}}(t)$) vibratory equations of motion are of the form $\overline{\mathbf{q}}^2\tilde{\mathbf{q}}$, which are

negligible when $\overline{\mathbf{q}}$ is moderate in magnitude. The strain energy in Eq. (2.34) is identical to Eq. (15.56) in [44] except we retain the second integral that Genta [44] neglects. The first integral in Eq. (2.34) leads to the linear elastic stiffness matrix $\mathbf{K}$ in Eq. (2.26a). The following discussion concerns the differing treatments of the second and third integrals in Eq. (2.34) that yield the different prestress stiffness matrices.

Evidently Genta neglects the second integral in Eq. (2.34) because all terms are cubic in displacement, when it is known that linear terms in the equations of motion on application of Lagrange's equations derive only from terms that are quadratic in displacement. Because $\boldsymbol{\epsilon}^{\mathrm{L}}$ and $\boldsymbol{\epsilon}^{\mathrm{NL}}$ are functions of both $\overline{\mathbf{q}}$ and $\tilde{\mathbf{q}}(t)$, however, the second integral generates terms of the form $\overline{\mathbf{q}}\tilde{\mathbf{q}}^2(t)$. Being quadratic in $\tilde{\mathbf{q}}(t)$, such terms contribute terms linear in $\tilde{\mathbf{q}}(t)$ to the prestress stiffness matrix after application of Lagrange's equations with $\tilde{\mathbf{q}}(t)$ as the generalized coordinates. Thus, the second integral that Genta neglects is necessary. In fact, it is the sole source of the prestress stiffness matrix in our formulation.

In contrast, Genta derives the prestress stiffness matrix entirely from the third integral of Eq. (2.34). The first and third terms of this integral are linear in $\tilde{\mathbf{q}}(t)$ and only lead to constant "right-hand side" terms in the equations of motion after application of Lagrange's equations. Genta [44] neglects the fourth term of this integral on the basis that the prestrain $\overline{\boldsymbol{\epsilon}}$ is small. That Genta [44] intends to neglect prestrain is indicated by his statement that "In most cases, no prestrain $\overline{\boldsymbol{\epsilon}}$ is present." The only remaining term that, in Genta's formulation, contributes to prestress stiffness is the second term of the third integral in Eq. (2.34), namely, $\overline{\boldsymbol{\sigma}}^T\boldsymbol{\epsilon}^{\mathrm{NL}}$. This is confirmed by the expression for geometric strain energy on p. 573 of [44]. Substitution of $\boldsymbol{\epsilon}^{\mathrm{NL}}$ from Eq. (2.16) as a function of $\overline{\mathbf{q}}$ and $\tilde{\mathbf{q}}(t)$ in the $\overline{\boldsymbol{\sigma}}^T\boldsymbol{\epsilon}^{\mathrm{NL}}$ term and retaining terms quadratic in $\tilde{\mathbf{q}}(t)$ results in prestress strain energy in

Genta [44] as

$$\Pi_p^G = \int_A \int_0^{2\pi} \overline{\boldsymbol{\sigma}}^T \boldsymbol{\epsilon}^{\mathrm{NL}} \, r \mathrm{d}\theta \mathrm{d}A = \frac{1}{2} \left(\int_A \int_0^{2\pi} \overline{\boldsymbol{\sigma}}^T \mathbf{S}(\tilde{\mathbf{q}}) \boldsymbol{\beta} \, r \mathrm{d}\theta \mathrm{d}A \right) \tilde{\mathbf{q}} = \frac{1}{2} \tilde{\mathbf{q}}^T \mathbf{K}_p^G(\overline{\mathbf{q}}) \tilde{\mathbf{q}}, \tag{2.35a}$$

$$\mathbf{K}_p^G(\overline{\mathbf{q}}) = \int_A \int_0^{2\pi} \boldsymbol{\beta}^T \boldsymbol{\Sigma}(\overline{\mathbf{q}}) \boldsymbol{\beta} \, r \mathrm{d}\theta \mathrm{d}A, \tag{2.35b}$$

where $\mathbf{K}_p^G(\overline{\mathbf{q}})$ is the prestress (or geometric) stiffness matrix in Genta [44] and $\boldsymbol{\Sigma}(\overline{\mathbf{q}})$ is the same as Eq. (2.30b).

In the present model, however, the third integral in Eq. (2.34) vanishes because $\overline{\boldsymbol{\sigma}} = \mathbf{D}\overline{\boldsymbol{\epsilon}}$. The prestress stiffness derives only from the second integral. Substitution of the strain-displacement relations of Eq. (2.16) and $\mathbf{q}(t) = \overline{\mathbf{q}} + \tilde{\mathbf{q}}(t)$ in the second integral of Eq. (2.34) results in the prestress strain energy as

$$\Pi_p = \frac{1}{2} \tilde{\mathbf{q}}^T \mathbf{K}_p(\overline{\mathbf{q}}) \tilde{\mathbf{q}}, \tag{2.36}$$

where $\mathbf{K}_p(\overline{\mathbf{q}})$ is the prestress stiffness matrix in Eq. (2.30a). The first term in $\mathbf{K}_p(\overline{\mathbf{q}})$ in Eq. (2.30a) is same as the prestress stiffness $\mathbf{K}_p^G(\overline{\mathbf{q}})$ in Eq. (2.35b) based on [44], but the second and third terms in $\mathbf{K}_p(\overline{\mathbf{q}})$ are missing in $\mathbf{K}_p^G(\overline{\mathbf{q}})$ because of the differences in approach.

In the earlier formulation leading to Eq. (2.30a), the prestress stiffness matrix was obtained by linearizing the nonlinear stiffness term $\frac{\partial \mathbf{N}(\mathbf{q})}{\partial \mathbf{q}}$ in the equation of motion Eq. (2.26a) for small vibrations $\tilde{\mathbf{q}}(t)$ relative to the steady deflection $\overline{\mathbf{q}}$, but that process yields the identical prestress stiffness matrix as in Eq. (2.36).

Friswell et al. [43] follows a similar procedure as Genta [44] to obtain the prestress/geometric stiffness, but additionally diagonalizes the stress tensor and considers dis-

placements along the principal directions. Thus, the differences observed with Genta [44] also occur for Friswell et al. [43].

Elimination of Lagrange multiplier

$\mathbf{A_q}$ may not be a full rank matrix. For a rank-deficient $\mathbf{A_q}$, Eq. (2.32b) can have a non-trivial solution expressed in the general form

$$\tilde{\mathbf{q}} = \mathbf{R}\tilde{\mathbf{Q}}, \tag{2.37}$$

where the columns of $\mathbf{R}$ form the basis of the null space of $\mathbf{A_q}$. $\mathbf{R}$ can be obtained from a singular value decomposition of $\mathbf{A}_\mathbf{q}^T$. Substitution of Eq. (2.37) into Eq. (2.32a), pre-multiplication by $\mathbf{R}^T$, and use of $\mathbf{A_q R} = \mathbf{0} \implies \mathbf{R}^T\mathbf{A}_\mathbf{q}^T = \mathbf{0}$ eliminates the term involving $\tilde{\mathbf{\Lambda}}$ in Eq. (2.32a). The result is

$$\begin{gathered}\mathbf{M}_s\ddot{\tilde{\mathbf{Q}}} + \Omega\mathbf{G}_s\dot{\tilde{\mathbf{Q}}} + \mathbf{L}_s\tilde{\mathbf{Q}} = \mathbf{f}(t), \\ \mathbf{M}_s = \mathbf{R}^T\mathbf{M}\mathbf{R}, \quad \mathbf{G}_s = \mathbf{R}^T\mathbf{G}\mathbf{R}, \\ \mathbf{L}_s = \mathbf{R}^T(\mathbf{K} + \mathbf{K}_f + \mathbf{K}_p(\overline{\mathbf{q}}) - \Omega^2\mathbf{C})\mathbf{R}, \quad \mathbf{f}(t) = \mathbf{R}^T\tilde{\mathbf{F}}(t).\end{gathered} \tag{2.38}$$

The free vibration eigenvalue problem from use of $\tilde{\mathbf{Q}} = \boldsymbol{\chi}e^{\lambda t}$ in Eq. (2.38) is

$$\lambda^2\mathbf{M}_s\boldsymbol{\chi} + \lambda\Omega\mathbf{G}_s\boldsymbol{\chi} + \mathbf{L}_s\boldsymbol{\chi} = \mathbf{0}. \tag{2.39}$$

This polynomial eigenvalue problem can be converted to a state-space form [98].

System properties

In the absence of deviations from axisymmetry (e.g., asymmetric space-fixed elements, constraints, elastic foundation, or prestress), substitution of the displacement fields in Eqs. (2.13) or (2.15) into Eqs. (2.4), (2.6), and (2.7) leads to integrals of trigonometric products (such as $\int_0^{2\pi} \cos m\theta \cos n\theta \mathrm{d}\theta$). The vanishing of such integrals for $m \neq n$ leads to block diagonal matrices $\mathbf{M}$, $\mathbf{G}$, $\mathbf{C}$, $\mathbf{K}$, and $\mathbf{K}_f$ in Eq. (2.26a) that decouple the harmonics. For example, $\mathbf{M}$ is of the form

$$\mathbf{M} = \begin{bmatrix} \mathbf{M}_0 & & & \\ & \mathbf{M}_1 & & \\ & & \ddots & \\ & & & \mathbf{M}_n \end{bmatrix}, \tag{2.40}$$

where $\mathbf{M}_n$ corresponds to the n^{th} harmonic coefficient $\mathbf{q}_n$ in Eq. (2.17) or Eq. (2.22). Similarly, $\mathbf{F}_\Omega$ consists of trigonometric integrals such that partitions of $\mathbf{F}_\Omega$ for non-zero harmonics ($n \neq 0$) vanish; only the 0^{th} harmonic partition of $\mathbf{F}_\Omega$ is non-zero.

Thus, in the axisymmetric case, the full $ND \times ND$ eigenvalue problem in Eq. (2.39) decouples into N eigenvalue problems of size $D \times D$, where D is the number of unknown nodal coefficients in the cross-section (i.e., the size of $\mathbf{q}_n$ in Eq. (2.17) or global assembled Eq. (2.22)). Consequently, all vibration modes of an axisymmetric system involve a single Fourier harmonic, that is, they occur strictly as n-nodal diameter modes for a single integer n determined from a single reduced eigenvalue problem of order D. The system response using Eqs. (2.38) and (2.39) also decouples into multiple reduced problems associated with each harmonic n. Solving N reduced problems is less computational cost than solving the full $ND \times ND$ system.

In the evaluation of the cubically nonlinear strain energy $\mathbf{N}(\mathbf{q})$ that results in the prestress stiffness matrix $\mathbf{K}_p(\overline{\mathbf{q}})$ in Eq. (2.30), the following expressions simplify evaluation of the integrals

$$\int_0^{2\pi} \cos m\theta \cos n\theta \cos p\theta \mathrm{d}\theta = \begin{cases} \frac{\pi}{2}, & m+n=p; \\ 0 & \text{otherwise}; \end{cases},$$

$$\int_0^{2\pi} \cos m\theta \sin n\theta \sin p\theta \mathrm{d}\theta = \begin{cases} \frac{\pi}{2}, & n=m+p \quad \text{and} \quad p=m+n; \\ -\frac{\pi}{2}, & m=n+p; \\ 0 & \text{otherwise} \end{cases}, \tag{2.41}$$

$$\int_0^{2\pi} \cos m\theta \cos n\theta \sin p\theta \mathrm{d}\theta = 0 \quad m,n,p \text{ are arbitrary integers},$$

$$\int_0^{2\pi} \sin m\theta \sin n\theta \sin p\theta \mathrm{d}\theta = 0 \quad m,n,p \text{ are arbitrary integers}.$$

The presence of an asymmetric feature disrupts the block-diagonal form of one or more system matrices and couples the Fourier harmonics in Eqs. (2.38) and (2.39). For example, asymmetric forces lead to an asymmetric stress field and coupled Fourier harmonics in the prestress stiffness matrix $\mathbf{K}_p(\overline{\mathbf{q}})$. An asymmetric constraint leads to harmonic coupling in $\mathbf{A}_\mathbf{q}$ in Eq. (2.26a). This couples the matrices in Eq. (2.38) through the basis of the null space $\mathbf{R}$ used to eliminate the Lagrange multipliers. An asymmetric elastic foundation results in harmonically coupled $\mathbf{K}_f$.

Coupling of the Fourier harmonics necessitates solution of the full $ND \times ND$ eigenvalue problem with all harmonics. In general, each mode contains multiple Fourier harmonics (i.e., multiple nodal diameter components), in contrast to the single Fourier harmonic/nodal diameter modes of axisymmetric systems. The Fourier coefficients in Eqs. (2.17) or (2.22) give the magnitudes of the various Fourier harmonics in a mode.

Because a full system solution is computationally expensive, one can use a Krylov-Schur algorithm [132] to obtain a smaller number of eigensolutions. A vibration mode may be influenced by modes with close natural frequencies, so it is recommended to obtain more eigensolutions than only in the natural frequency range of interest. In addition, a model order reduction using appropriate basis functions (the stationary system modes, for example) can be performed on the full system to reduce the computational cost.

2.3 Rotating axisymmetric thin-walled body

Rotating axisymmetric bodies are often thin-walled, particularly for weight reduction, including the examples of bearing cages and races, ring gears of epicyclic/planetary gear systems, circular saw blades, and brake rotors. Shells of revolution can model these thin-walled, axisymmetric bodies. Extension of the formulation above to such cases allows the cross-section of the thin-walled bodies to be modeled with one-dimensional finite elements rather than the two-dimensional elements for a general body.

2.3.1 Model description

Fig. 2.2 shows a general shell of revolution rotating at constant speed Ω. The radial cross-section of the shell is called the meridional section. The middle line of the meridional section is the meridian. The arbitrarily shaped meridian, when rotated about its rotation axis, traces the middle surface of the shell. The displacements of the meridian describe the dynamics of the shell based on the Kirchhoff-Love assumptions. The thickness $h(\alpha)$ of the meridional section can vary within the cross-section, but the shell is uniform circumferentially.

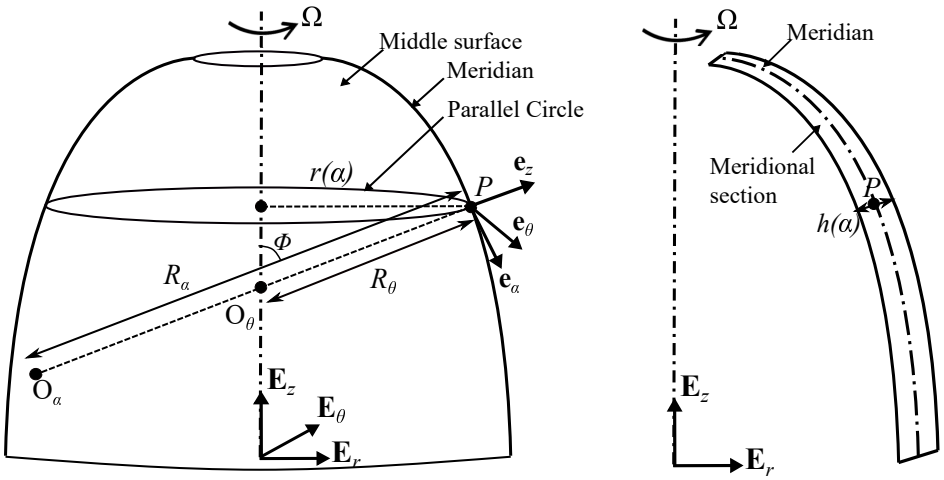

Figure 2.2: Schematic of a rotating, general shell of revolution.

We adopt the conventional shell terminologies described in [3, 103, 145]. The curvilinear coordinates α and θ define the middle surface of the shell. P is a point on the meridian shown in Fig. 2.2. The outward normals to two neighboring points on the meridian intersect at O_α. The segment length PO_α is the radius of curvature of the meridian denoted by R_α. A point on the meridian traces a circle of radius $r(\alpha)$ perpendicular to the rotation axis (shown in Fig. 2.2). The outward normals to two neighboring points on the circle intersect at O_θ on the rotation axis. The segment length PO_θ is the second radius of curvature denoted by R_θ. Lame' parameters A_α and A_θ relate the change in length of an infinitesimal arc ds to changes in the curvilinear coordinates dα and dθ according to $\mathrm{d}s^2 = (A_\alpha)^2\mathrm{d}\alpha^2 + (A_\theta)^2\mathrm{d}\theta^2$. The curvilinear coordinate α depends on the type of shell. Straight-line meridian shells (cylindrical and conical shells) can be defined by $\alpha = s$, where s is the distance of a point along the meridian. A spherical coordinate $\alpha = \phi$ can define spherical shells as shown in Fig. 2.2.

The material properties are uniform circumferentially and defined as above for general, non-shell structures. An elastic foundation attaches to the middle surface of the shell. External forces that can have arbitrary spatial and temporal variation and are not

necessarily axisymmetric act on the shell.

The stationary bases $\{\mathbf{E}_1, \mathbf{E}_2, \mathbf{E}_3\}$ and $\{\mathbf{E}_r, \mathbf{E}_\theta, \mathbf{E}_z\}$ defined by coordinate θ are as described previously for non-shell structures. θ defines a spatially fixed angular location and not a material point on the shell. A local orthonormal basis $\{\mathbf{e}_\alpha, \mathbf{e}_\theta, \mathbf{e}_z\}$ is defined at a point P on the meridian such that $\mathbf{e}_\alpha$ is directed along the tangent to the meridian, $\mathbf{e}_\theta$ is along $\mathbf{E}_\theta$, and $\mathbf{e}_z$ is along the outward normal to the meridian at P. ϕ is the angle between $\mathbf{e}_z$ and $\mathbf{E}_z$.

The elastic deflections of a material point P on the meridian at time t and instantaneously at circumferential location θ are $u(\alpha, \theta, t)$, $v(\alpha, \theta, t)$, and $w(\alpha, \theta, t)$ along $\mathbf{e}_\alpha, \mathbf{e}_\theta$, and $\mathbf{e}_z$, respectively. The deflections at a point P_z located at a distance z from P along $\mathbf{e}_z$ are $u_z(\alpha, \theta, z, t)$, $v_z(\alpha, \theta, z, t)$, and $w_z(\alpha, \theta, z, t)$.

2.3.2 Dynamic model of a rotating axisymmetric shell

Kinetic energy

According to the Kirchhoff-Love assumptions, the deflections of P_z are related to the deflections of P as

$$u_z(\alpha, \theta, z, t) = u(\alpha, \theta, t) - z\omega_1(\alpha, \theta, t), \quad v_z(\alpha, \theta, z, t) = v(\alpha, \theta, t) - z\omega_2(\alpha, \theta, t),$$
$$w_z(\alpha, \theta, z, t) = w(\alpha, \theta, t), \tag{2.42}$$

where ω_1 and ω_2 are the angles of rotation about tangents to the curvilinear coordinates θ and α, respectively, described in [3, 103, 145] and given as

$$\omega_1 = \frac{u}{R_\alpha} + \frac{1}{A_\alpha}\frac{\partial w}{\partial \alpha}, \quad \omega_2 = \frac{v}{R_\theta} + \frac{1}{A_\theta}\frac{\partial w}{\partial \theta}. \tag{2.43}$$

The position vector of an undeflected point P_z instantaneously rotating past θ before deformation is $\mathbf{r}_0 = r(\alpha)\mathbf{E}_r + Z\mathbf{E}_z$, and its deflected position is

$$\begin{aligned}\mathbf{r} = &\left[r(\alpha) + u_z(\alpha,\theta,z,t)\cos\phi + w_z(\alpha,\theta,z,t)\sin\phi\right]\mathbf{E}_r + v_z(\alpha,\theta,z,t)\mathbf{E}_\theta \\ &+ \left[Z - u_z(\alpha,\theta,z,t)\sin\phi + w_z(\alpha,\theta,z,t)\cos\phi\right]\mathbf{E}_z. \end{aligned} \tag{2.44}$$

The material time derivatives of Eq. (2.44) using Eq. (2.2) result in the velocity of the material point as

$$\begin{aligned}\dot{\mathbf{r}} = &\left[u_{z,t}\cos\phi + w_{z,t}\sin\phi + \Omega\left(u_{z,\theta}\cos\phi + w_{z,\theta}\sin\phi - v_z\right)\right]\mathbf{E}_r \\ &+ \left[v_{z,t} + \Omega\left(v_{z,\theta} + r + u_z\cos\phi + w_z\sin\phi\right)\right]\mathbf{E}_\theta \\ &+ \left[-u_{z,t}\sin\phi + w_{z,t}\cos\phi + \Omega\left(-u_{z,\theta}\sin\phi + w_{z,\theta}\cos\phi\right)\right]\mathbf{E}_z. \end{aligned} \tag{2.45}$$

The kinetic energy in terms of displacements of the meridian is obtained by substituting Eqs. (2.42) and (2.45) into

$$T = \frac{1}{2}\int_\alpha \int_0^{2\pi} \int_{-h/2}^{h/2} \rho\dot{\mathbf{r}}\cdot\dot{\mathbf{r}} r \mathrm{d}z\mathrm{d}\theta\mathrm{d}\alpha. \tag{2.46}$$

Strain energy

The strain energy of a shell is obtained from Sanders' nonlinear general shell theory [124]. The total strains $\boldsymbol{\epsilon}^z$ at a distance z from the meridian are

$$\boldsymbol{\epsilon}^z = \boldsymbol{\epsilon} + z\boldsymbol{\kappa}, \tag{2.47a}$$

$$\boldsymbol{\epsilon} = \{\epsilon_{\alpha\alpha}, \epsilon_{\theta\theta}, \gamma_{\alpha\theta}\}^T = \boldsymbol{\epsilon}^{\mathrm{L}} + \boldsymbol{\epsilon}^{\mathrm{NL}}, \quad \boldsymbol{\kappa} = \{\kappa_{\alpha\alpha}, \kappa_{\theta\theta}, \kappa_{\alpha\theta}\}^T, \tag{2.47b}$$

where $\boldsymbol{\epsilon}$ are the strains of the middle surface and $\boldsymbol{\kappa}$ are the changes in bending curvatures and twisting of the middle surface. The strains ($\boldsymbol{\epsilon}$) are decomposed into linear (L) and nonlinear (NL) terms. The strain-displacement relationships are obtained from [124].

The stresses are $\boldsymbol{\sigma} = \mathbf{D}\boldsymbol{\epsilon}^z$, where $\mathbf{D}$ is the elasticity tensor for plane stress [145]. The strain energy of the shell is

$$\Pi = \frac{1}{2}\int_{\alpha}\int_{0}^{2\pi}\int_{-h/2}^{h/2} \boldsymbol{\epsilon}^T\boldsymbol{\sigma} r \mathrm{d}z\mathrm{d}\theta\mathrm{d}\alpha. \tag{2.48}$$

A circumferential elastic foundation supports the middle surface. Viewed in the radial cross-section, this foundation runs along the meridian. The elastic foundation stiffnesses per unit area are $k_u(\alpha,\theta,t)$, $k_v(\alpha,\theta,t)$, and $k_w(\alpha,\theta,t)$, and these can vary circumferentially. The strain energy in the elastic foundation is

$$\Pi_f = \frac{1}{2}\int_{\alpha}\int_{0}^{2\pi} \left(k_u u^2 + k_v v^2 + k_w w^2\right) r\mathrm{d}\theta\mathrm{d}\alpha. \tag{2.49}$$

The external force components are F_u, F_v, and F_w along $\mathbf{e}_\alpha$, $\mathbf{e}_\theta$, and $\mathbf{e}_z$, respectively. The virtual work expression is

$$\delta W = \int_{\alpha}\int_{0}^{2\pi}\int_{-h/2}^{h/2} \left(F_u\delta u + F_v\delta v + F_w\delta w\right) r\mathrm{d}z\mathrm{d}\theta\mathrm{d}\alpha. \tag{2.50}$$

General constraint equations (holonomic or non-holonomic) analogous to Eq. (2.9) model the constraints on the motion of the shell.

2.3.3 Displacement field approximation

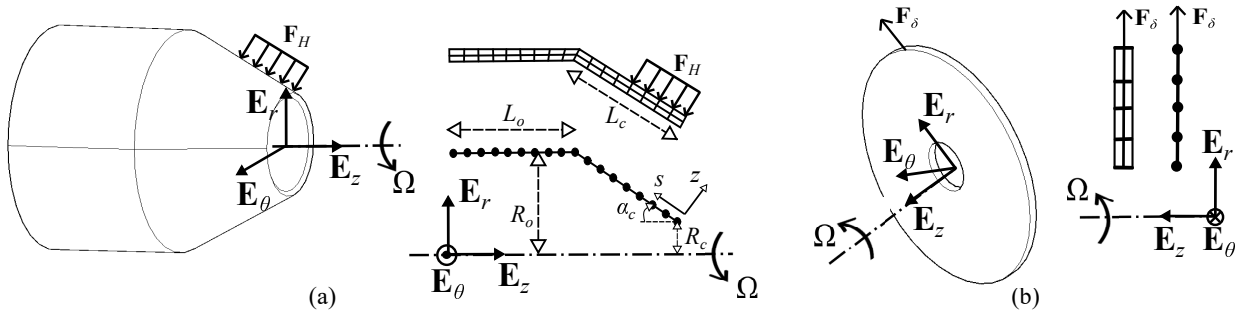

Figure 2.3: Three-dimensional, rotating, axisymmetric body reduced to two-dimensional and one-dimensional discretized finite element cross-sections: (a) Conical-cylindrical body with space-fixed, uniformly distributed force $\mathbf{F}_H$ perpendicular to the conical section at a specified angle β, and (b) Annular plate with a space-fixed, radial point force $\mathbf{F}_\delta$.

Because of Eqs. (2.42) and (2.43), the shell motion is described by the motion of the meridian. Because of axisymmetry, discretization is carried out along the one-dimensional curve within a radial cross-section that defines the meridian. Displacements of a shell with simple meridian geometry (for example, a plate with a single straight-line meridian as shown in Fig. 2.3(b)) can be defined using global basis functions over the entire meridian, analogous to the general, non-shell body case with the two-dimensional global basis functions replaced by one-dimensional basis functions. A complex meridian shape (for example, the cylinder-cone shown in Fig. 2.3(a)) for which global basis functions cannot be identified is approximated using local discretization (i.e., finite elements along the meridian). In this section, only local discretization is discussed.

The meridian of the shell is divided into one-dimensional finite elements, as shown for the two example structures in Fig. 2.3 (where two-dimensional elements are also shown for each body). Axisymmetry of the shell means the cross-sectional discretization and the associated local basis functions do not depend on the angular coordinate θ. The nodal deflections, however, do depend on θ. The displacement field within a line element at any

space-fixed angular location θ and at time t is

$$u_e(\alpha,\theta,t) = \boldsymbol{\Psi}_u^{eT}(\alpha)\mathbf{U}_e(\theta,t), \tag{2.51}$$

where (analogous to Eq. (2.14) for a non-shell body) $\boldsymbol{\Psi}_u^e(\alpha)$ is a vector of shape functions within an element e and $\mathbf{U}_e(\theta,t)$ is a vector of the nodal deflections of the element. Displacements $v_e(\alpha,\theta,t)$ and $w_e(\alpha,\theta,t)$ are expressed similarly with one-dimensional shape functions $\boldsymbol{\Psi}_v^e(\alpha)$ and $\boldsymbol{\Psi}_w^e(\alpha)$. The deformation must satisfy continuity conditions between adjacent elements. At least displacement continuity is required for displacements $u_e(\alpha,\theta,t)$ and $v_e(\alpha,\theta,t)$ along $\mathbf{e}_\alpha$ and $\mathbf{e}_\theta$, respectively, and at least displacement and slope continuity are required for $w_e(\alpha,\theta,t)$. Thus, linear Lagrange polynomials can define $\boldsymbol{\Psi}_u^e(\alpha)$ and $\boldsymbol{\Psi}_v^e(\alpha)$ and Hermite cubic functions can define $\boldsymbol{\Psi}_w^e(\alpha)$ [9, 26, 159]. The shape functions can be defined using alternate sets of functions, provided they satisfy the necessary continuity conditions.

Periodicity of the body and the displacement fields allows Fourier expansion of the nodal deflections $\mathbf{U}_e(\theta,t)$ in Eq. (2.51), and similarly for $v_e(\alpha,\theta,t)$ and $w_e(\alpha,\theta,t)$. Thus, the local displacement fields within a cross-sectional finite element are

$$u_e(\alpha,\theta,t) = \boldsymbol{\Psi}_u^{eT}(\alpha)\left[\mathbf{U}_0^e(t) + \sum_{n=1}^{\infty}\left(\mathbf{U}_{nc}^e(t)\cos n\theta + \mathbf{U}_{ns}^e(t)\sin n\theta\right)\right], \tag{2.52a}$$

$$v_e(\alpha,\theta,t) = \boldsymbol{\Psi}_v^{eT}(\alpha)\left[\mathbf{V}_0^e(t) + \sum_{n=1}^{\infty}\left(\mathbf{V}_{nc}^e(t)\cos n\theta - \mathbf{V}_{ns}^e(t)\sin n\theta\right)\right], \tag{2.52b}$$

$$w_e(\alpha,\theta,t) = \mathbf{\Psi}_w^{e\,T}(\alpha)\left[\mathbf{W}_0^e(t) + \sum_{n=1}^{\infty}\left(\mathbf{W}_{nc}^e(t)\cos n\theta + \mathbf{W}_{ns}^e(t)\sin n\theta\right)\right], \tag{2.52c}$$

where $\mathbf{U}_{nc}^e(t), \mathbf{U}_{ns}^e(t), \ldots$ are coefficients that associate with the n^{th} Fourier harmonic.

2.3.4 Matrix form

Substitution of Eq. (2.52) into Eqs. (2.46) and (2.48)–(2.50) gives the matrix form of the kinetic and strain energies of an element. These matrix forms and the time-dependent nodal deflections vector $\mathbf{q}_e$ for the shell element are analogous to Eqs. (2.20) and (2.22). The constraint equations are analogous to Eq. (2.19d).

The elemental energies are summed to obtain the total energies of the axisymmetric shell resulting in finite element global matrices obtained by the usual process of assembling elemental matrices.

2.3.5 Equation of motion

Lagrange's equation in Eq. (2.25) is applied with respect to the nodal coefficients $\mathbf{q}(t)$ resulting in the equation of motion for a rotating axisymmetric shell analogous to Eq. (2.26) as

$$\mathbf{M}\ddot{\mathbf{q}} + \Omega\mathbf{G}\dot{\mathbf{q}} + (\mathbf{K} + \mathbf{K}_f - \Omega^2\mathbf{C})\mathbf{q} + \frac{1}{2}\frac{\partial \mathbf{N}(\mathbf{q})}{\partial \mathbf{q}} = \mathbf{f}(\mathbf{q},t), \tag{2.53}$$

where $\mathbf{f}(\mathbf{q},t)$ is the sum of the constant, rotation-induced loading $\mathbf{F}_\Omega$ and external forces $\mathbf{F}(\mathbf{q},t)$. For an axisymmetric shell element,

$$\mathbf{F}_\Omega = (\mathbf{f}_\Omega^0, \mathbf{0}, ..., \mathbf{0})^T, \tag{2.54a}$$

$$\mathbf{f}_\Omega^0 = 2\pi \int_\alpha \rho h \begin{Bmatrix} \boldsymbol{\Psi}_u \cos\phi & \mathbf{0} & \boldsymbol{\Psi}_w \sin\phi \end{Bmatrix} r^2 \mathrm{d}\alpha. \tag{2.54b}$$

Constraint equations are modeled similar to the non-shell structures in Eq. (2.26a). They are dropped in the shell formulation for simplicity.

Prestress in rotating axisymmetric shell

The constant, rotation-induced loading $\mathbf{F}_\Omega$ and constant mean values of the external forces $\mathbf{F}$ result in prestress in a thin-walled body. The steady deflection $\overline{\mathbf{q}}$ obtained by elimination of the time derivatives in the equation of motion Eq. (2.53) leads to equations similar to Eq. (2.27). Geometric boundary conditions are applied to the steady state equations (Eq. (2.27)) when the steady deflection is calculated. Substitution of $\mathbf{q}(t) = \overline{\mathbf{q}} + \tilde{\mathbf{q}}(t)$ into Eq. (2.53) and linearization for small $\tilde{\mathbf{q}}(t)$ results in the linear prestress stiffness matrix $\mathbf{K}_p(\overline{\mathbf{q}})$ from $\frac{\partial \mathbf{N}(\mathbf{q})}{\partial \mathbf{q}}$ as

$$\mathbf{K}_p(\overline{\mathbf{q}}) = \int_\alpha \int_0^{2\pi} h \left[\boldsymbol{\beta}^T \boldsymbol{\Sigma}(\overline{\mathbf{q}}) \boldsymbol{\beta} + \mathbf{P}(\overline{\mathbf{q}}) + \mathbf{P}^T(\overline{\mathbf{q}}) \right] r \mathrm{d}\theta \mathrm{d}\alpha, \tag{2.55a}$$

$$\boldsymbol{\Sigma}(\overline{\mathbf{q}}) = \begin{bmatrix} \overline{\sigma}_{\alpha\alpha} & \overline{\sigma}_{\alpha\theta} & 0 \\ \overline{\sigma}_{\alpha\theta} & \overline{\sigma}_{\theta\theta} & 0 \\ 0 & 0 & (\overline{\sigma}_{\alpha\alpha} + \overline{\sigma}_{\theta\theta}) \end{bmatrix}, \tag{2.55b}$$

where $\mathbf{P}(\overline{\mathbf{q}})$ is analogous to Eq. (2.18d) with $\mathbf{B}, \mathbf{S}(\mathbf{q})$, and $\boldsymbol{\beta}$ for an axisymmetric shell element shown in Appendix A.2. The expression $\mathbf{DB}\overline{\mathbf{q}} = \{\overline{\sigma}_{\alpha\alpha}, \overline{\sigma}_{\theta\theta}, \overline{\sigma}_{\alpha\theta}\}$ is used to obtain Eq. (2.55).

Chen et al. [22] included rotational prestress due to $\mathbf{F}_\Omega$ in conical and cylindri-

cal shells. They analytically solved the steady state equations for conical and cylindrical shells with free-free boundary conditions, which yields $\overline{\sigma}_{\theta\theta} = \rho h r(\alpha)^2 \Omega^2$ as the only non-zero rotational prestress. Other references [24, 50, 86, 87, 133, 134] studied the vibration of rotating cylindrical and conical shells with other boundary conditions. These references, however, used the above rotational prestress from [22] despite the differing boundary conditions. This leads to incorrect rotational prestress. The prestress stiffness matrix/operator is not symmetric/self-adjoint in Refs. [24, 50, 86, 87, 133, 134]. A rotating, axisymmetric shell is a conservative system where the differential operators or their discretized matrices, including the prestress operator, should be self-adjoint, except for the skew-self-adjoint gyroscopic operator. $\mathbf{K}_p(\overline{\mathbf{q}})$ in Eq. (2.55a) is symmetric, as expected, because $\mathbf{P}(\overline{\mathbf{q}}) + \mathbf{P}^T(\overline{\mathbf{q}})$ is symmetric.

The prestress stiffness in Guo et al. [48] consists of only the first term ($\boldsymbol{\beta}^T \boldsymbol{\Sigma}(\overline{\mathbf{q}})\boldsymbol{\beta}$) from Eq. (2.55a), similar to the differences in the prestress stiffness expression discussed earlier for general, non-shell bodies.

The equation of motion for an axisymmetric shell including the prestress stiffness is analogous to the solid body equation of motion in Eq. (2.38). The shell equation of motion is conservative and gyroscopic, similar to the solid body model.

As for general, non-shell structures, the matrices in the shell equation of motion are block diagonal with decoupled Fourier harmonics in the absence of asymmetric features (giving reduced eigenvalue problems that yield only single nodal diameter modes). Asymmetric features (forces, constraints, and elastic foundation) lead to Fourier harmonic coupling, similar to general, solid bodies.

2.4 Numerical Results

2.4.1 Validation of the solid and shell models

Table 2.1: Non-dimensional natural frequencies $\hat{\lambda} = \lambda R_o\sqrt{\rho(1-\nu^2)/E}$ of the stationary, free-clamped conical-cylindrical body (Fig. 2.3(a)) are compared with Nastran and Refs. [73, 125] for Fourier harmonics 0 ND to 4 ND (ND = nodal diameter). The geometric parameters are: $R_c/R_o = 0.4226$, $h/R_o = 0.01$, $L_o/R_o = 1$, $\alpha_c = 30^\circ$.

ND	Present Model		3D FE Nastran		Kang et al. [73]	Sarkheil [125]
	Shell	Solid	Shell	Solid		
0 ND	0.504	0.505	0.498	0.511	0.510	0.504
	0.610	0.599	0.610	0.599	0.610	0.610
	0.931	0.931	0.930	0.934	0.931	0.935
	0.957	0.958	0.956	0.962	0.956	0.959
1 ND	0.293	0.289	0.292	0.290	0.295	0.295
	0.636	0.637	0.631	0.645	0.637	0.633
	0.812	0.816	0.813	0.819	0.811	0.812
	0.933	0.934	0.930	0.938	0.932	0.931
2 ND	0.100	0.099	0.100	0.100	0.101	0.105
	0.503	0.507	0.501	0.515	0.503	0.504
	0.692	0.693	0.697	0.702	0.691	0.692
	0.859	0.861	0.865	0.875	0.859	0.859
3 ND	0.087	0.088	0.088	0.090	0.087	0.087
	0.392	0.395	0.392	0.404	0.392	0.392
	0.515	0.517	0.522	0.528	0.514	0.514
	0.754	0.757	0.765	0.780	0.754	0.753
4 ND	0.145	0.147	0.147	0.153	0.143	0.142
	0.330	0.333	0.334	0.344	0.331	0.329
	0.396	0.398	0.404	0.411	0.396	0.393
	0.648	0.651	0.663	0.680	0.647	0.644

The present solid (i.e., non-shell) and shell models are validated against commercial finite element software for the stationary, conical-cylindrical body shown in Fig. 2.3(a). The cross-sectional thickness and material properties are uniform. The conical end is free and the cylindrical end is clamped. The natural frequencies are non-dimensionalized as $\hat{\lambda} = \lambda R_o\sqrt{\rho(1-\nu^2)/E}$.

Because the system is axisymmetric, all vibration modes involve a single Fourier harmonic. These are determined from reduced eigenvalue problems associated with each

block of the block-diagonal matrices. Table 2.1 shows that natural frequencies for the first five Fourier harmonics compare well with three-dimensional solid and shell models developed in Nastran. Because the body is thin-walled, the natural frequencies obtained from the solid and shell models are close. In addition, the natural frequencies agree well with the shell models in Refs. [73, 125].

Because the Fourier harmonics are uncoupled based on axisymmetry, convergence of the natural frequencies for a given harmonic is unaffected by the number of Fourier harmonics in Eqs. (2.15) or (2.52), and modes of each harmonic are analyzed separately with no loss of accuracy. Convergence depends only on the cross-sectional mesh. This contrasts with three-dimensional finite element models where accuracy of higher Fourier harmonics requires a fine mesh in the circumferential direction. The present models do not require any mesh in the circumferential direction, improving computational efficiency.

Fig. 2.4 compares the presented solid and shell models for an increasing ratio of thickness to outer radius (h/R_o) of the conical-cylindrical body. The plot indicates the mean (symbols) and standard deviation (tick marks) of the percentage differences between the natural frequencies from the solid and shell models. The first 10 natural frequencies for each harmonic are used to obtain the mean and standard deviation. The percentage difference between the solid and shell models increases with thickness ratio and with harmonic number. The errors from the shell model increase much more sharply for higher Fourier harmonics when the thickness ratio increases.

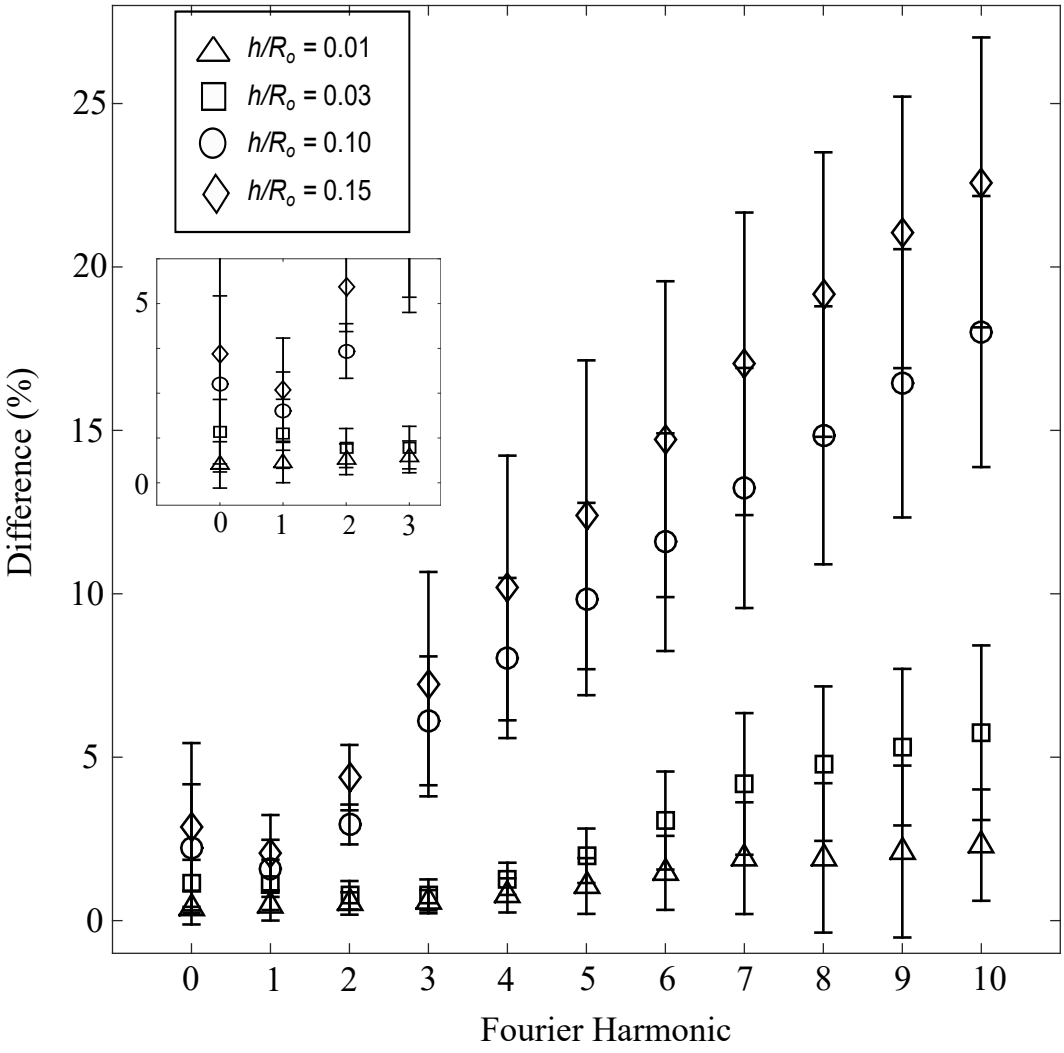

Figure 2.4: Mean (symbols) and standard deviation (tick marks) of percentage differences of the natural frequencies obtained from the solid and shell models. Difference (%) = $\frac{|\lambda^{shell}-\lambda^{solid}|}{\lambda^{solid}} \times 100$ for varying thickness and increasing harmonics of the stationary conical-cylindrical body. The inset shows enlarged view of the differences for harmonics 0 to 3.

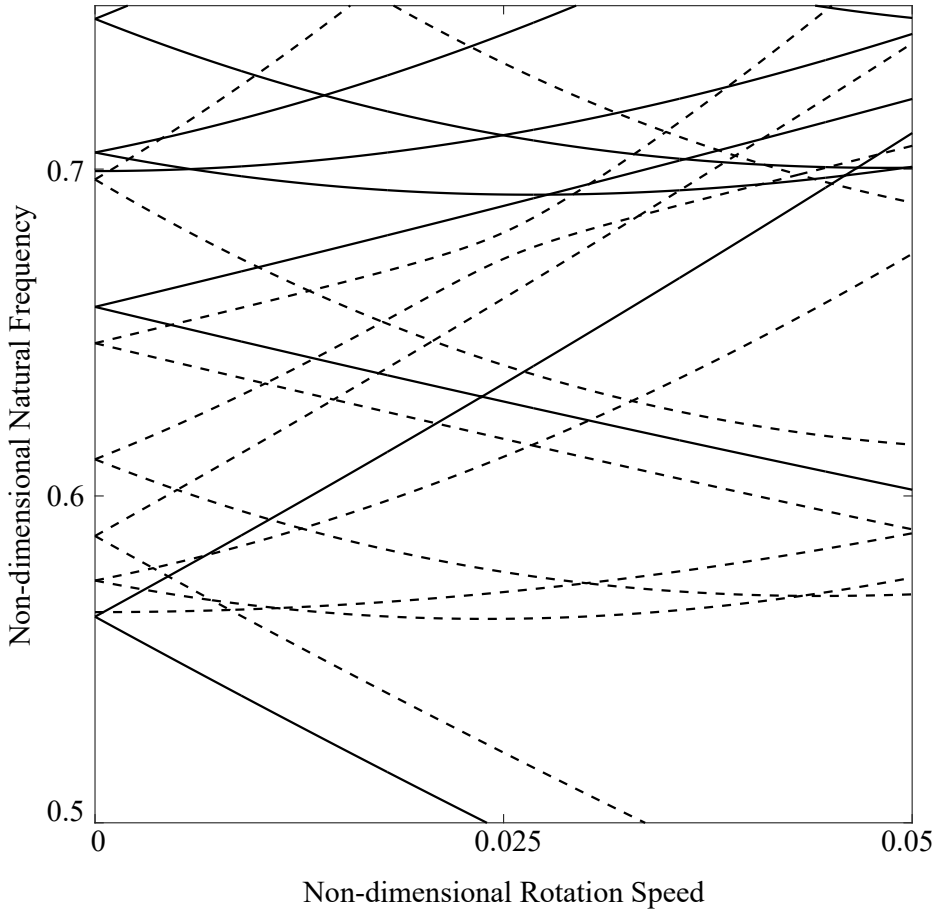

Figure 2.5: Non-dimensional natural frequencies ($\hat{\lambda} = \lambda R_o\sqrt{\rho(1-\nu^2)/E}$) for the rotor-disk in Fig. 2.1 obtained using the presented solid model (solid lines) and shell model (dashed lines). The dimensions of the rotor-disk are shown in Fig. 2.1(c).

2.4.2 Solid and shell models applied to complex cross-sectional body

The presented solid and shell models are applied to the axisymmetric rotor-disk body with the cross-sectional geometry in Fig. 2.1. The shell cross-section is developed by joining the middle lines of the two-dimensional cross-section in Fig. 2.1(c). The rotation speed and natural frequencies are non-dimensionalized as $\hat{\Omega} = \Omega R_o\sqrt{\rho(1-\nu^2)/E}$ and $\hat{\lambda} =$

$\lambda R_o\sqrt{\rho(1-\nu^2)/E}$, where R_o is the outer radius.

Fig. 2.5 shows the natural frequencies obtained using the solid (solid lines) and shell (dashed lines) models for a range of rotation speeds. Both models capture the gyroscopic and centripetal effects that lead to eigenvalue splitting and curvature of eigenvalue loci as rotation speed increases from zero. The solid and shell model eigenvalues do not compare well because the outer cylindrical section of the body has a relatively large thickness to outer radius ratio of 0.13. Differences in the eigenvalues for vibration modes dominated by the outer cylindrical section and by the middle plate section (section parallel to the $\mathbf{E}_z$ axis) are within 10% and 17%, respectively. These differences drop to within 5% and 6% on reducing the thickness ratio of the outer cylindrical section to 0.03. Other modes are much less affected by thickness of the outer cylindrical section.

A mixed solid-shell formulation can be used for bodies that have combinations of thick and thin portions of the cross-section. As presented above, the solid model has only translational degrees of freedom whereas the shell model involves rotational (slope) and translational degrees of freedom. A solid-shell transition element [135] at the solid-shell coupling edge can account for this change in degrees of freedom. Alternatively, multipoint constraints [130] can be used.

2.4.3 Effects of rotational prestress on natural frequencies

While a great deal of literature includes the effects of rotational prestress on the natural frequencies of out-of-plane (transverse) circular plate vibration, we have not seen results for in-plane vibration of circular and annular plates that include rotational prestress. Fig. 2.6 compares the in-plane natural frequencies for a clamped-free annular plate (Fig. 2.3(b)) without rotational prestress (dashed lines), with prestress using the nonlinear steady

deflection from Eq. (2.27) (solid lines), and with prestress from the linearized, moderate speed steady deflection from Eqs. (2.29) and (2.31) (dotted lines). Use of the linearized steady deflection from Eq. (2.28) yields results that are indistinguishable from the solid lines throughout the speed range. The results in Fig. 2.6 are obtained using the previously presented shell model that, for flat plates, results in uncoupled in-plane and out-of-plane vibration modes. The rotational prestress is axisymmetric, so the Fourier harmonics are decoupled and all modes have only a single nodal diameter component. This allows use of reduced eigenvalue problems instead of the full system formulation.

Although the eigenvalue loci without prestress (dashed lines) in Fig. 2.6 compare well with Chen and Jhu [20] (comparison not shown), the eigenvalues with prestress (solid and dotted lines) differ significantly from those without prestress. The differences between results from the nonlinear (solid lines) versus linearized, moderate speed (dotted lines) steady deflection are much smaller. The linearized, moderate speed steady deflection in Eq. (2.29) (and implemented in Eq. (2.31)) works well except for especially high speeds. Prestress stiffens the system and increases all natural frequencies. The model using nonlinear steady deflection is slightly stiffer than the model with linearized, moderate speed steady deflection. Eigenvalues from the linearized steady deflection from Eq. (2.28) overlay those from the nonlinear steady deflection results (solid lines).

The rotational prestress increases the critical speeds (where an eigenvalue vanishes) that correspond to potential instabilities [109, 123]. For example, the critical speed for the (3,0) mode increases from $\hat{\Omega} = 0.77$ to $\hat{\Omega} = 0.91$ and $\hat{\Omega} = 0.95$, respectively, for prestress using the linearized and nonlinear steady deflections. Some critical speeds that are present when neglecting the prestress vanish when prestress is included, for example, the (0,0) mode as circled in Fig. 2.6. When rotational prestress is omitted, a flutter instability (two imaginary eigenvalues merge into complex eigenvalues with one having a positive real part) occurs for

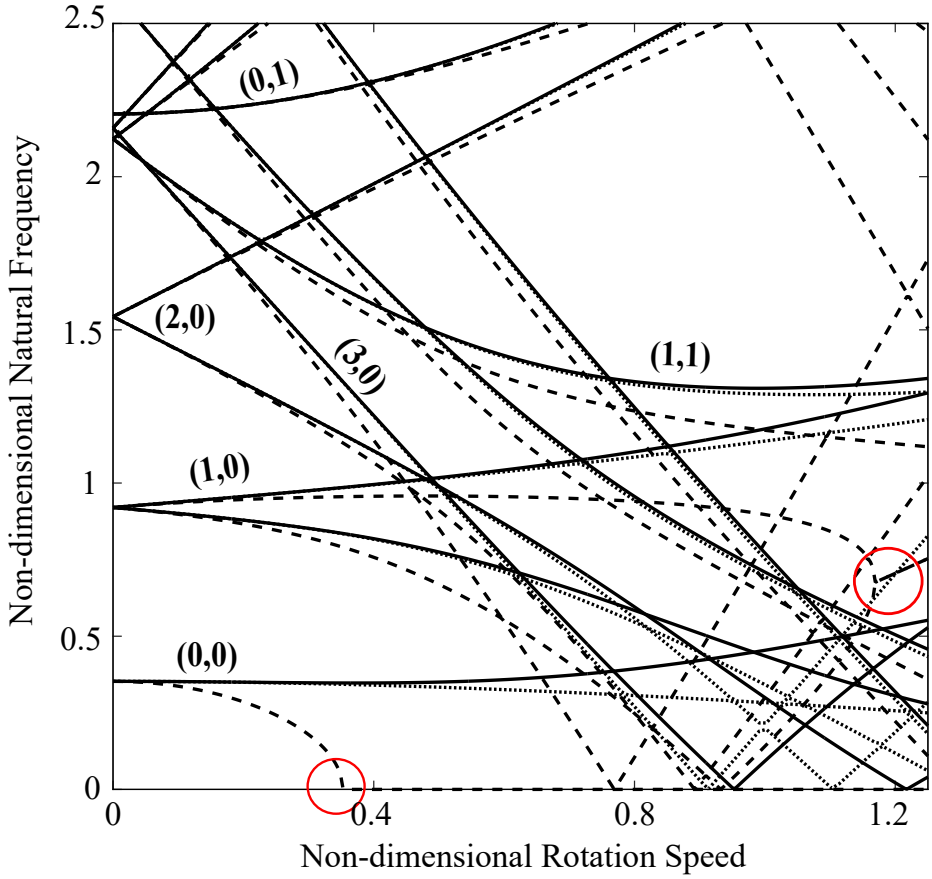

Figure 2.6: Non-dimensional in-plane natural frequencies of a rotating, annular, clamped-free plate (clamping ratio $R_i/R_o = 0.2$ and $h/R_o = 0.01$) without rotational prestress (dashed lines), with prestress using the nonlinear steady deflection from Eq. (2.27) (solid lines), and with prestress from the linearized, moderate speed steady deflection from Eq. (2.29) (dotted lines). The vibration modes are labeled as (ND, NC), where ND and NC are the number of nodal diameters and nodal circles.

the (1,0) mode at $\hat{\Omega} = 1.16$ as circled in Fig. 2.6 (the real part of the unstable eigenvalue is not shown). This instability vanishes on inclusion of the rotational prestress as shown by following the monotonically increasing solid line for the (1,0) mode starting from 0.92 at zero speed. Some practical systems, for example, thin, high-speed spur gears and tires, have dominant in-plane vibrations where the large prestress from high-speed rotation is important.

The out-of-plane natural frequencies for the example plate are not shown in Fig. 2.6, but we obtained excellent agreement with results from Hutton et al. [65] for out-of-plane

natural frequencies with and without rotational prestress.

2.4.4 Constrained rotating axisymmetric body

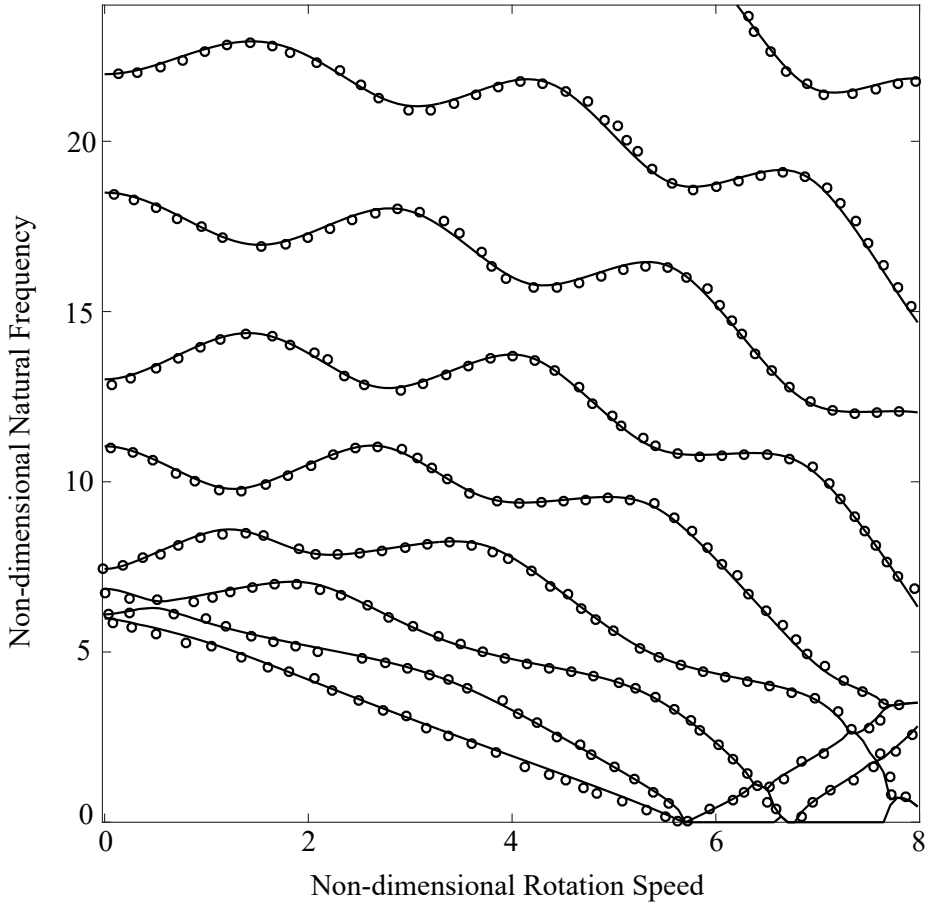

Figure 2.7: Non-dimensional natural frequencies $\hat{\lambda} = \lambda R_o\sqrt{\rho(1-\nu^2)/E}$ of an annular, clamped-free plate with clamping ratio of 0.268 and a zero axial displacement constraint at a point on the outer edge ($w(R_o, h, 0, t) = 0$). Results using the presented solid model are the solid lines, and the guided sawblade results from Hutton et al. [65] are the circles.

We demonstrate the treatment of constraints by considering a spinning, annular, clamped-free plate constrained to have zero transverse displacement at a point on its outer edge. While the spinning plate is axisymmetric the constraint is not, which is permitted by the current approach. Hutton et al. [65] studied this system with an analytical circular plate

model in the context of a guided circular sawblade.

The axial displacement ($w(r, z, \theta, t)$) at the space-fixed point on the outer radius ($r = R_o, z = h, \theta = \beta$) is constrained to be zero. This yields a constraint equation obtained from the displacement approximation (Eq. (2.15c)) as

$$w_e(R_o, h, \beta, t) = \boldsymbol{\Psi}_w^{e\,T}(R_o, h) \left[\mathbf{W}_0^e(t) + \sum_{n=1}^{\infty} (\mathbf{W}_{nc}^e(t) \cos n\beta + \mathbf{W}_{ns}^e(t) \sin n\beta) \right] = 0. \quad (2.56)$$

The axial constraint is holonomic and in the form described in Eq. (2.9). This constraint is converted to a matrix form ($\mathbf{A_q}$ in Eq. (2.23)), resulting in $\mathbf{A_q} = \partial w_e(R_o, h, \beta, t)/\partial \mathbf{q}$ as a single row vector with the Fourier harmonics ($\cos n\beta$ and $\sin n\beta$) from Eq. (2.56) as its entries. $\mathbf{A_q}$ is a full rank matrix. The constraint can be applied by reducing out one of the Fourier coefficients using the other coefficients or by using a Lagrange multiplier (Λ).

The asymmetric constraint leads to Fourier harmonic coupling, where such coupling is absent without the constraint. The Fourier harmonics at the constrained node are linearly related through the constraint equation in Eq. (2.56) and the matrix $\mathbf{A_q}$. The basis of the null space ($\mathbf{R}$ in Eq. (2.37)) used to eliminate the Lagrange multiplier couples the Fourier harmonics in the matrices in Eq. (2.38). Because of this constraint, the matrices are not block-diagonalized into individual Fourier harmonics as in Eq. (2.40). One must solve the full system eigenvalue problem in Eq. (2.39), and each mode involves multiple Fourier harmonics.

Fig. 2.7 shows non-dimensional natural frequencies of the constrained, rotating annular plate obtained from the present solid model (solid lines). The natural frequencies closely match those from Hutton et al. [65], who investigated a guided sawblade modeled analytically as a thin plate-spring system with a high stiffness to approximate a rigid constraint (circles).

2.4.5 Effect of prestress due to stationary external force

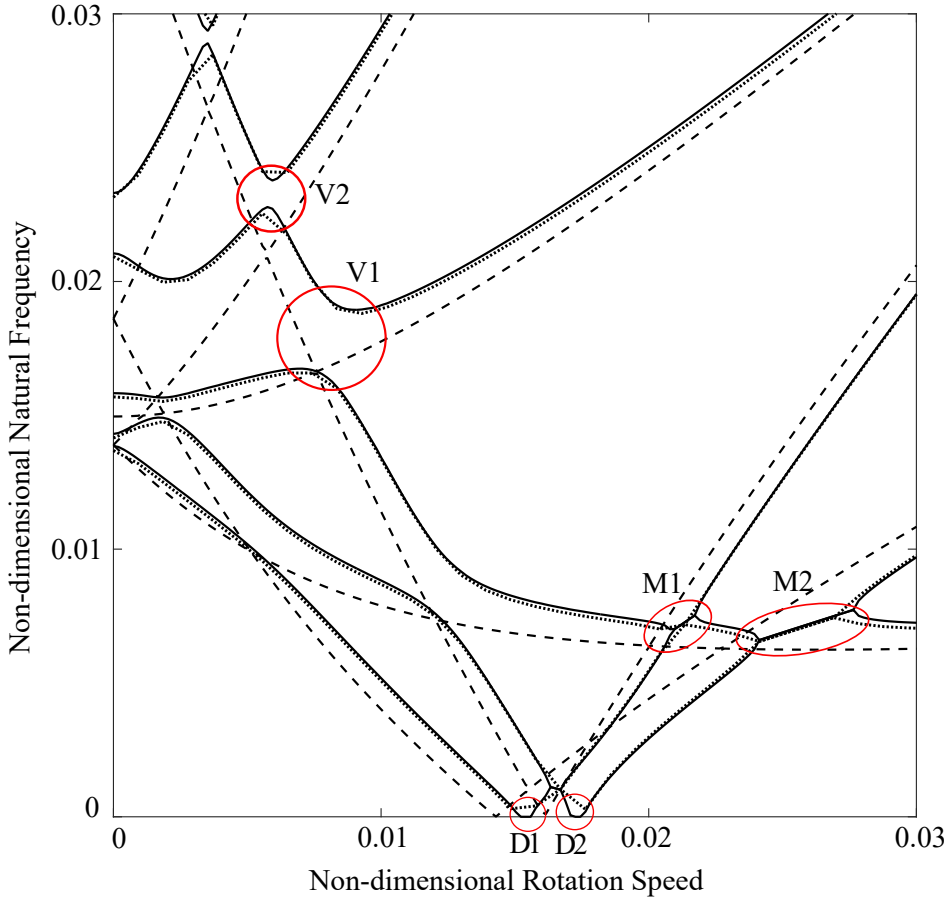

Figure 2.8: Non-dimensional natural frequencies $\hat{\lambda} = \lambda R_o\sqrt{\rho(1-\nu^2)/E}$ of a rotating, annular plate with a clamping ratio of 0.2, $h/R_o = 0.01$, and a space-fixed, radial point force $\hat{\mathbf{F}}_\delta = 5.52 \times 10^{-7}\delta(\hat{r}-1)\frac{\delta(\theta)}{\hat{r}}\delta(\hat{z})\mathbf{E}_r$. The natural frequencies without prestress due to the external force obtained using the solid model (dashed lines) are compared to the body with prestress obtained using the solid model (solid lines) and shell model (dotted lines).

The formulation includes the influence of prestress on the vibration, where that prestress may arise from rotation and/or steady components of externally applied forces. The prestress is captured through $\mathbf{K}_p(\overline{\mathbf{q}})$ in Eqs. (2.30) and (2.55).

We consider the example of a stationary, radial point force acting on a spinning, clamped-free, annular plate such that the prestress field arises from both the external force and rotation. A force per unit volume $\mathbf{F}$ is non-dimensionalized as $\hat{\mathbf{F}} = \frac{\mathbf{F}}{F^*}$, where

$F^* = \frac{E}{R_o(1-\nu^2)}$. The spatial coordinates are non-dimensionalized as $\hat{r}, \hat{z} = \frac{r,z}{R_o}$. The non-dimensionalized stationary point force $\hat{\mathbf{F}}_\delta$ applied to the annular plate is $\hat{\mathbf{F}}_\delta = \hat{F}_\delta \delta(\hat{r} - 1)\frac{\delta(\theta)}{\hat{r}}\delta(\hat{z})\mathbf{E}_r$, where $\hat{F}_\delta = \frac{F_\delta}{F^* R_o^3} = 5.52 \times 10^{-7}$ and F_δ is the amplitude of the point force. Substitution of the force in the virtual work Eqs. (2.8) or (2.50) and use of Lagrange's equations gives the force vector $\mathbf{F}$ in the equation of motion Eq. (2.26a). Because the force acts at a single node, only the force terms corresponding to the nodal harmonic coefficients of the node at which the force acts are non-zero in $\mathbf{F}$ in Eq. (2.26a).

Fig. 2.8 shows the imaginary parts of the eigenvalues, where the non-dimensional rotation speed is $\hat{\Omega} = \Omega R_o \sqrt{\rho(1-\nu^2)/E}$. All eigenvalues in Fig. 2.8 include rotational prestress. The eigenvalues without the external force prestress using the solid model (dashed lines) are compared to those with prestress due to the external force using the solid (solid lines) and shell (dotted lines) models. The solid and shell model eigenvalues including prestress nearly overlap.

The eigenvalues for the cases with and without prestress from the stationary point force differ substantially because the stress field from the point force is asymmetric. The asymmetric stress field leads to Fourier harmonic coupling in the prestress stiffness matrix $\mathbf{K}_p(\overline{\mathbf{q}})$ in Eqs. (2.30) and (2.55). As a result, the stationary system eigenvalues are no longer degenerate, as they are for the system where the point force prestress is neglected (dashed lines). The asymmetric stress field from the point force introduces speed ranges of divergence instability (purely imaginary eigenvalues become real-valued) at D1 and D2. Divergence instability does not occur when only rotational prestress is considered. Similarly, the asymmetric stress field generates speed regions of flutter instability at M1 and M2 that are not present with only rotational prestress. At the left boundaries of these regions, two imaginary eigenvalues merge and diverge off the imaginary axis as a complex conjugate pair. At the right boundaries that terminate the flutter instability regions, the complex eigenvalues

merge and return to stable, imaginary eigenvalues.

Whether asymmetry arises from constraints (Fig. 2.7), prestress (Fig. 2.8), or other sources of asymmetry, it couples the various Fourier harmonics in the equation of motion Eq. (2.38). In addition to the computational expense of analyzing the full matrix problem in Eqs. (2.38) or (2.39), rather than analyzing each Fourier harmonic independently using the block-diagonal form of matrices, asymmetry introduces qualitative differences with the corresponding axisymmetric system. Three of these are mentioned above, namely, modes with multiple Fourier harmonic components, splitting of degenerate eigenvalues at zero speed, and creation of divergence and flutter instability regions.

A fourth difference is eigenvalue veering, where two eigenvalues approach each other as a parameter is varied but then veer away without crossing [115]. Two such veering regions are marked as V1 and V2 in Fig. 2.8, and others are present there and in Fig. 2.7. Despite the absence of intersection of the loci, the vibration modes are exchanged between the two loci as the varying parameter increases or decreases across the veering region. The sharpness of the veering depends on the extent to which the modes of the two veering eigenvalues have common Fourier harmonics. If the modes of the two approaching eigenvalues have one or more common Fourier harmonic coefficients with large amplitude in both modes, then the veering region is broad without sharp changes (e.g., most of the veering regions in Fig. 2.7 and the region V1 in Fig. 2.8). If, however, all of the common Fourier harmonics that are present in both of the two modes make small contributions to their respective modes, the veering region is narrow and sharp like in V2 of Fig. 2.8. If the two modes have no common Fourier harmonics, then the eigenvalues intersect each other and no veering occurs.

The prestress stiffness in Genta [44] and shown in Eq. (2.35b) consists of only the first term ($\boldsymbol{\beta}^T \boldsymbol{\Sigma}(\overline{\mathbf{q}})\boldsymbol{\beta}$) in the prestress stiffness derived in Eq. (2.30). This creates substantial differences, which we discuss using Fig. 2.9. This figure compares the natural frequencies of

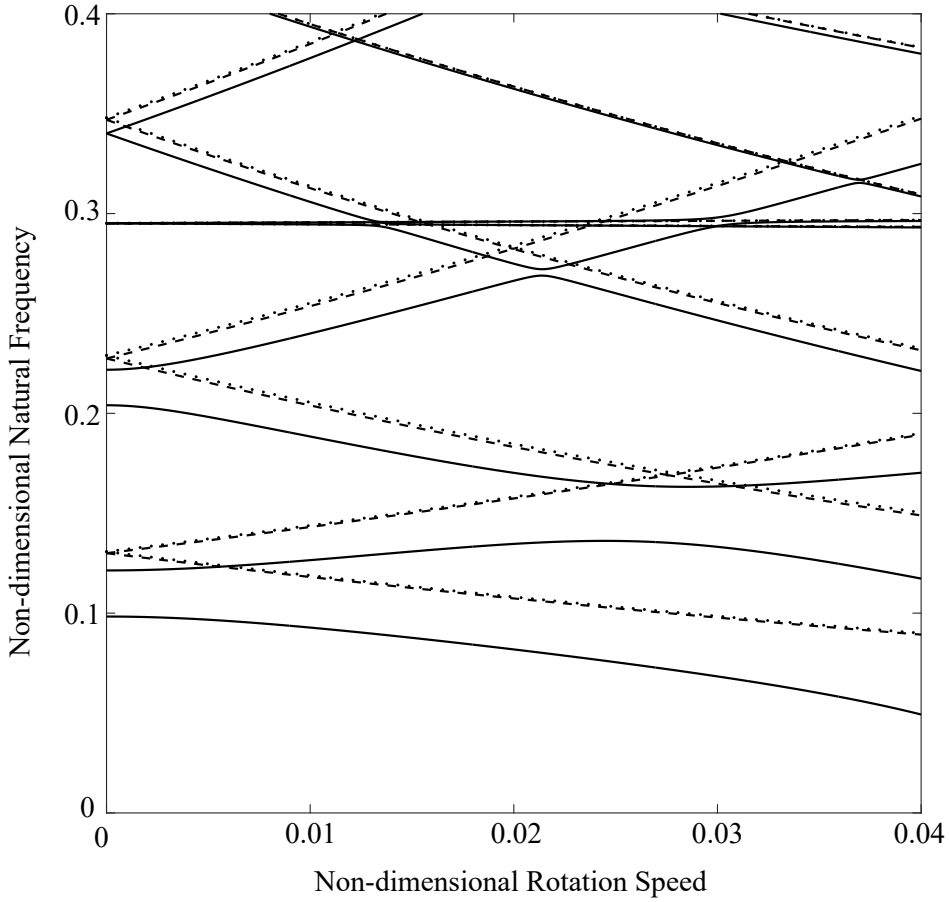

Figure 2.9: Non-dimensional natural frequencies of a free-clamped conical-cylinder shown in Fig. 2.3(a) with dimensions: $R_c/R_o = 0.4226$, $h/R_o = 0.03$, $L_o/R_o = 1$ and $\alpha_c = 30°$. A uniformly distributed force $\hat{\mathbf{F}}_H = 1.49\times10^{-5}\frac{\delta(\theta)}{\hat{r}}\delta(\hat{z}-0.015)H(1.155-\hat{s})(\cos\alpha_c\mathbf{E}_r+\sin\alpha_c\mathbf{E}_z)$ is acting on half the conical length at $\theta = 0$. The natural frequencies obtained using the present solid model are shown for the cases with (solid lines) and without (dashed lines) prestress due to the external force, where the prestress influence is captured as in Eq. (2.30). The frequencies using the solid model and including prestress according to Ref. [44] as given in Eq. (2.35b) are shown by dotted lines that essentially overlap with the dashed lines.

a system that includes prestress stiffness as obtained in this work (solid lines) to the prestress stiffness in [44] (dotted lines). The system is the free-clamped conical-cylinder shown in Fig. 2.3(a). A space-fixed force is uniformly distributed over half the cone length ($L_c/2$, where L_c is the cone length). The slant cone length is denoted by s with the free cone end as $s = 0$ and the cone-cylinder junction as $s = L_c$. The lengths are non-dimensionalized as $\hat{r}, \hat{z}, \hat{s} = \frac{r,z,s}{R_o}$.

In this case, z is considered normal to the cone. The non-dimensional uniform force is $\hat{\mathbf{F}}_H = \hat{F}_H \frac{\delta(\theta)}{\hat{r}} \delta(\hat{z} - 0.015) H(1.155 - \hat{s})(\cos\alpha_c \mathbf{E}_r + \sin\alpha_c \mathbf{E}_z)$, where $\hat{F}_H = \frac{F_H}{F_H^*} = 1.49 \times 10^{-5}$, F_H is the force per unit length, $F_H^* = \frac{ER_o}{(1-\nu^2)}$, and $H(\cdot)$ is a step function.

The eigenvalue loci from the present solid model with prestress (solid lines) differ significantly from those from the present model without prestress (dashed lines). The prestress generates the expected asymmetry features of splitting of the degenerate eigenvalues, multiple Fourier harmonic contributions in each mode, and eigenvalue veering, as discussed above. These features are absent when the prestress is ignored (dashed lines). When implementing the prestress as done in [44] (dotted lines) and given in Eq. (2.35b), the results are essentially identical to those from the present model when prestress is neglected. The expected features from the prestress field asymmetry are not captured. Thus, the second and third terms of the prestress stiffness matrix in Eqs. (2.30) and (2.55) are necessary.

2.5 Conclusions

High-speed, rotating, axisymmetric bodies with arbitrary radial cross-section are modeled with a semi-analytical method that discretizes only a radial cross-section and uses Fourier series in the circumferential direction. While the body geometry and material properties must be axisymmetric, the overall system may not be as a result of: coupling with space-fixed, asymmetric components as well as asymmetric external forces, constraints, prestress fields, and elastic foundations. The model developed in a stationary reference frame allows straightforward inclusion of these stationary asymmetric features. The displacement fields use global basis functions or local shape functions (finite elements) in the radial cross-section depending on the cross-sectional geometry. Fourier series model the θ-dependence of the displacement fields. The model includes Coriolis (i.e., gyroscopic), centripetal, and

prestress effects. Holonomic or nonholonomic constraints on the motion of the rotating body, which are not restricted to be axisymmetric and can be space-fixed or rotating, are modeled in a general way.

The presented solid (non-shell) model has no restrictions on the thickness of any portions of its cross-section, while thin-walled axisymmetric bodies can be analyzed using the presented shell model. These models that take advantage of axisymmetry are computationally more efficient than three-dimensional finite element models that require meshing along the circumferential direction.

The derived prestress stiffness matrix due to rotation-induced centripetal acceleration and steady components of the external forces has additional terms compared to the literature. An example shows these additional terms are important.

Asymmetric space-fixed components, forces, constraints, prestress, components like discrete stiffnesses, and the like that break the axisymmetry of the overall system result in vibration modes with multiple Fourier harmonic contributions (i.e., multiple nodal diameter components) and significantly changes the qualitative eigenvalue and instability behavior of otherwise axisymmetric systems: degenerate eigenvalues split, eigenvalue veering arises, critical speeds change, and speed ranges of divergence and flutter instability materialize.

Chapter 3

Coupling of rotating body to other rotating/stationary bodies for vibration study

Modeling systems comprising of flexible, rotating bodies coupled via bearings, splines, and other mechanical elements to other rotating or stationary flexible bodies motivates this study. Examples of systems that involve interaction between rotating bodies include gear trains, coaxial rotors, and dual rotor gas turbines. Systems with coupled rotating and stationary bodies include a gear train enclosed in a housing, rotating guided sawblades, and brake disk-pads. The mechanical elements that couple these flexible bodies can be discrete or continuous, rigid or flexible, linear or nonlinear, and time-invariant or time-varying. Discrete stiffness-damper elements, elastic foundations, and constraint equations can model these coupling elements. This work focuses on developing coupling models to couple rotating and stationary bodies in a system.

A rotating body coupled to non-axisymmetric, stationary structures leads to time-dependent coefficient equations of motion in the rotating reference frame. This occurs because the stationary body appears as a moving contact in the rotating reference frame. These time-dependent coefficients act as parametric excitation in the system. Mathematical analysis of parametrically excited equations of motion is complex as compared to constant

coefficient equations of motion.

Rotating bodies are frequently axisymmetric about their rotation axis, or can be approximated as axisymmetric. Because of axisymmetry, the three-dimensional, rotating, axisymmetric body allows for the reduction of the model to a two-dimensional radial cross-section [144, 154, 159]. The model of the axisymmetric, rotating body coupled to non-axisymmetric, stationary bodies developed in a stationary reference frame results in constant coefficient equations of motion. This arises because the cross-sectional location of the contact remains space-fixed in the stationary reference frame. The space-fixed formulation of axisymmetric, rotating bodies from Chapter 2 is adopted to model the rotating bodies. Axisymmetry of the rotating body greatly simplifies coupling the rotating body to other rotating and stationary bodies in the space-fixed formulation.

Geradin and Kill [46] proposed an axisymmetric finite element model for flexible rotors in rotating and stationary reference frames. The centripetal and rotational stress stiffening effects are absent in the stationary reference frame model because of the Lagrangian formulation. Fayos et al. [38] developed an Eulerian coordinate-based method for rotating bodies using the vibration modes of the body as basis functions to approximate its displacements. Refs. [43, 44, 117] discuss rigid body models, beam finite element models, and other analytical methods to analyze rotating bodies.

Jacquet et al. [67] in their review paper concluded that most rotor-stator contact studies are based on simplified models, for example, Jeffcott type rotors and rigid bearings. Vibration modes of the uncoupled bodies are commonly used as basis functions to approximate the motion of the system. Lee [88] developed a model using the vibration modes of individual bodies to study the dynamics of elastic structures interacting with rotating machinery. Shen et al. [127] used the vibration modes of individual stator and disks as basis functions to approximate the motion of a rotating disk/spindle system coupled to a flexible

housing via stiffness-damper bearing model. Tseng et al. [141] used a similar model for axisymmetric, rotating bodies in contact with a stationary body. Because the displacements of the body were approximated with the vibration modes, the coefficients of the gyroscopic term [141] required a complex algorithm to obtain the volume integral of the mode shapes and their spatial derivatives. In this work, the rotational effects obtained from the velocity expression of the body do not require any synthesized, complex volume integrals.

Discrete stiffness-dampers and elastic foundations are commonly used as coupling elements, for example, guides in a circular sawblade [65], read/write pinhead in HDD drives, and contact mesh in coupled gears [29]. Tadeo and Cavalca [136] compared the flexible stiffness-damper coupling models of Kramer [84] and Nelson and Crandall [102]. Iwan and Moeller [66] studied the vibrations of a spinning elastic disk with a transverse mass-spring-damper loading system. Hutton et al. [65] modeled the guides on a circular sawblade with stationary point loads and spring elements. Huang and Hsu [62] analyzed the vibration of a spinning cylindrical shell with point or line stiffness supports. Hmida et al. [55] studied the effects of rigid and elastic coupling [102] on the modal characteristics of a spur gearbox with time-varying mesh stiffness. Cooley and Parker [29] analytically investigated the vibration of rotating ring gears coupled via space-fixed stiffnesses. Other researchers [21, 28, 61, 63, 118] have studied vibrations of rotating disks, rings, and shells in contact with stationary mass-spring-damper supports. Refs. [40, 64] analyzed the vibrations of rotating rings and cylindrical shells with elastic foundation supports. Discrete or continuous stiffness-dampers, elastic foundations, and constraint models are developed in this work to couple multiple bodies in a system.

The coupling methods in this work are used to model complex systems consisting of a rotating, axisymmetric body coupled to other rotating or stationary bodies. The axisymmetric, rotating bodies in the system can have arbitrary cross-sectional geometries. The

space-fixed formulation [144] models the axisymmetric rotating bodies. Coriolis, centripetal, and prestress effects due to rotation-induced constant centripetal acceleration and external forces are included. Stiffness-damper, elastic foundation, point constraint, and surface constraints are used to model the coupling elements between multiple bodies. We demonstrate the simplicity and the ease of using the coupling elements in a brake disk-pad system [51, 56, 75, 76, 106, 107] and a dual rotor-casing system [15, 151, 152, 157]. A rotating brake disk is coupled to a rigid brake pad via an asymmetric elastic foundation and non-conservative friction force. The asymmetric coupling results in Fourier harmonic coupling in the vibration modes and the friction results in squeal onset. A dual rotor-casing system consists of coaxial, flexible rotating bodies enclosed in a flexible stationary casing. Elastic foundation, surface constraints, discrete stiffnesses, and a time-varying intershaft bearing couple the dual rotors and the stationary casing. The effects of a flexible stationary casing on the system frequencies, and the effects of a fluctuating coupling element on the system dynamics are investigated.

3.1 Analytical Model

Fig. 3.1 shows an example system with two rotating bodies and a stationary body. The rotation speeds of the rotating bodies are Ω_i, $i = 1, 2$ about their respective rotation axis $\mathbf{E}^i_z$. An asymmetric, elastic foundation $\mathbf{k}_f$ couples the two rotating bodies. The rotating body 1 couples to the stationary body with a discrete stiffness ($\mathbf{k}_d$) - damper ($\mathbf{d}_d$) element.

The cylindrical basis $\{\mathbf{E}^i_r, \mathbf{E}^i_\theta, \mathbf{E}^i_z\}$ of the rotating bodies and Cartesian basis $\{\mathbf{E}_x, \mathbf{E}_y, \mathbf{E}_z\}$ of the stationary body in Fig. 3.1 are fixed in space. The equations of motion for each flexible body are obtained in their respective local, stationary basis, for example, rotating, axisymmetric bodies are defined in their local cylindrical basis $\{\mathbf{E}^i_r, \mathbf{E}^i_\theta, \mathbf{E}^i_z\}$ in Fig. 3.1. Using

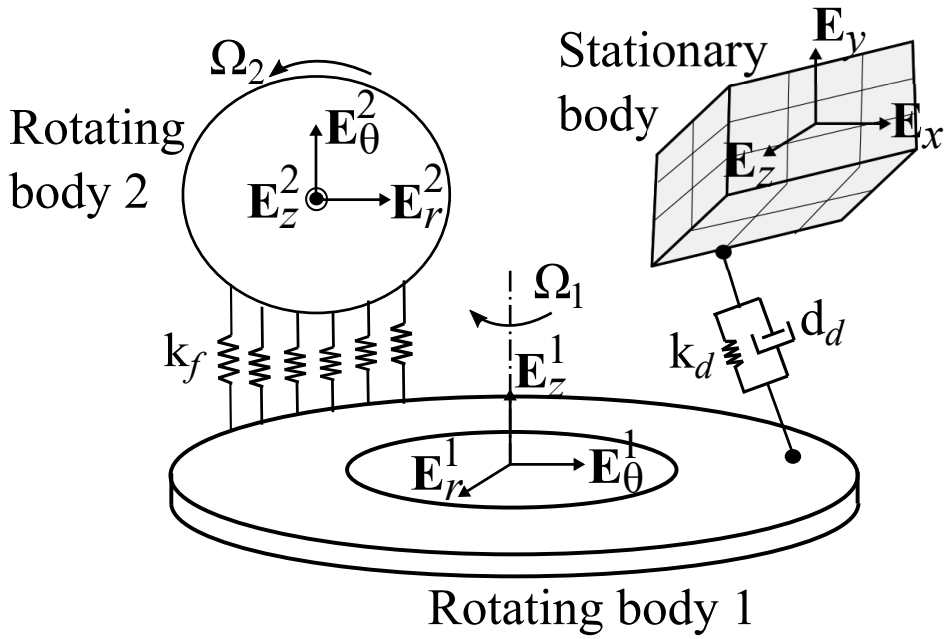

Figure 3.1: Schematic of a system that consists of an axisymmetric, rotating body 1 coupled to an axisymmetric, rotating body 2 via an elastic foundation $\mathbf{k}_f$ and coupled to a stationary body via a discrete stiffness ($\mathbf{k}_d$) - damper ($\mathbf{d}_d$) element. The rotating bodies rotate at Ω_1 and Ω_2 about their rotation axes $\mathbf{E}_z^1$ and $\mathbf{E}_z^2$, respectively.

space-fixed formulation for the rotating bodies [144] and the finite element method (or other numerical methods) for the stationary body, the equations of motion for uncoupled bodies in the system are first obtained. Coupling element models couple the degrees of freedom of the bodies in the system equation of motion.

3.1.1 Axisymmetric, rotating body

Fig. 3.2 shows an axisymmetric, flexible body rotating at speed Ω about its symmetry axis. The axisymmetric body has an arbitrary two-dimensional radial cross-section, shown by the crosshatching in Fig. 3.2. The material properties are uniform in the circumferential direction, but they are allowed to vary within the cross-section. The total cross-sectional area, Young's modulus, density, and Poisson's ratio are A, E, ρ, and ν, re-

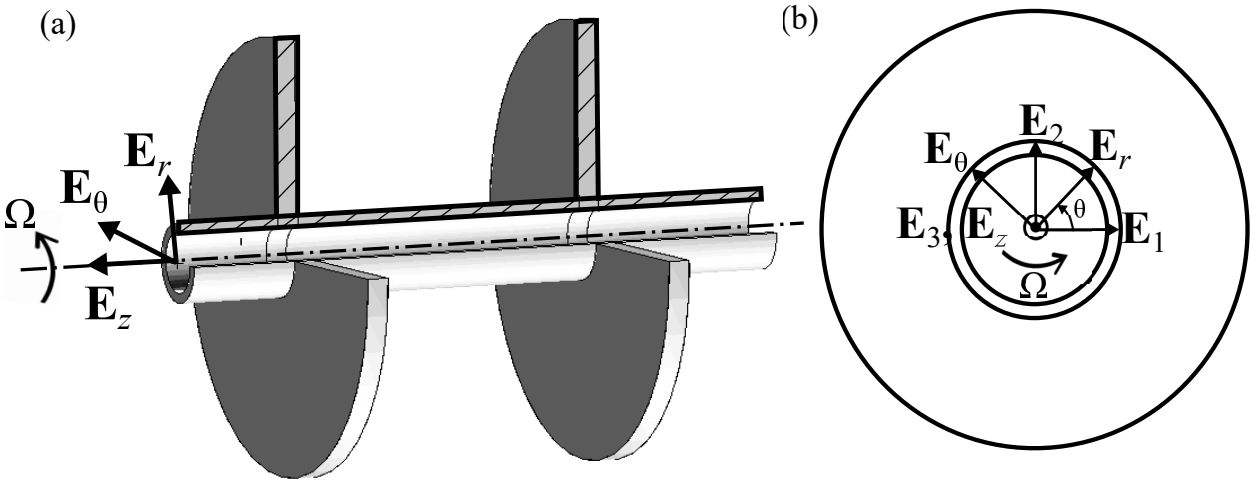

Figure 3.2: (a) Three-dimensional axisymmetric, rotor-disk body with crosshatched radial cross-section and (b) the front view of the rotor-disk.

spectively. External forces $\mathbf{F}$ act on the body.

The basis $\{\mathbf{E}_1, \mathbf{E}_2, \mathbf{E}_3\}$ shown in Fig. 3.2(b) is stationary. The basis $\{\mathbf{E}_r, \mathbf{E}_\theta, \mathbf{E}_z\}$ is also fixed but oriented by a spatially fixed angle θ relative to $\mathbf{E}_1$. The cross-section of material points at a given θ changes with time because the body rotates while the basis $\{\mathbf{E}_r, \mathbf{E}_\theta, \mathbf{E}_z\}$ is fixed. Similarly, the angle θ identifying a material point changes with time according to $\theta(t) = \Omega t + \theta_0$.

The elastic deflections of a material point on the rotating body instantaneously at a specified θ along its local, fixed $\{\mathbf{E}_r, \mathbf{E}_\theta, \mathbf{E}_z\}$ basis are $u(r, z, \theta, t)$, $v(r, z, \theta, t)$, and $w(r, z, \theta, t)$, respectively.

The velocity of a material point is obtained from the material time derivative of the position vector that combines (a) convective velocity terms arising because the angle θ associated with a material particle changes with time according to $\partial\theta/\partial t = \Omega$, and (b) partial derivatives of elastic deflections with respect to time. The material time derivatives

are

$$\frac{\mathrm{d}u}{\mathrm{d}t} = \frac{\partial u}{\partial t} + \frac{\partial u}{\partial r}\frac{\partial r}{\partial t} + \frac{\partial u}{\partial \theta}\frac{\partial \theta}{\partial t} + \frac{\partial u}{\partial z}\frac{\partial z}{\partial t} = u_{,t} + \Omega u_{,\theta} \tag{3.1a}$$

$$\frac{\mathrm{d}\mathbf{E}_r}{\mathrm{d}t} = \frac{\partial \mathbf{E}_r}{\partial t} + \frac{\partial \mathbf{E}_r}{\partial \theta}\frac{\partial \theta}{\partial t} = \Omega \mathbf{E}_\theta; \quad \frac{\mathrm{d}\mathbf{E}_\theta}{\mathrm{d}t} = -\Omega \mathbf{E}_r; \quad \frac{d\mathbf{E}_z}{dt} = 0, \tag{3.1b}$$

where $(\cdot)_{,t}$ and $(\cdot)_{,\theta}$ are partial derivatives with respect to time t and θ. The material time derivatives of displacements v and w are similar to Eq. (3.1a). The particle velocity from the material time derivative is

$$\dot{\mathbf{r}} = \left[u_{,t} + \Omega\left(u_{,\theta} - v\right)\right]\mathbf{E}_r + \left[v_{,t} + \Omega\left(v_{,\theta} + r + u\right)\right]\mathbf{E}_\theta + \left[w_{,t} + \Omega w_{,\theta}\right]\mathbf{E}_z. \tag{3.2}$$

The kinetic and strain energies of the rotating body are obtained from the particle velocity Eq. (3.2) and nonlinear strain-displacement relations [3]. The rotating body energies and virtual work expression due to external forces are obtained from [144].

The kinetic and strain energies depend on the displacement fields. Axisymmetry of the rotating body allows for the discretization of the displacement fields to be carried out only in the radial cross-section of the body. Because of axisymmetry, the basis (shape) functions are the same for any space-fixed angular location θ and depend only on the cross-sectional coordinates r and z. The radial displacement field within a finite element e at any angular location θ is

$$u_e(r, z, \theta, t) = \mathbf{\Psi}_u^{e\,T}(r, z)\mathbf{U}_e(\theta, t), \tag{3.3}$$

where $\mathbf{\Psi}_u^e(r, z)$ is a vector of shape functions within a finite element and $\mathbf{U}_e(\theta, t)$ is the time-dependent nodal coefficient vector.

The body and its displacement fields are continuous in θ and 2π periodic. Thus, the θ-dependent nodal coefficients can be expanded in Fourier series [144]. The displacement fields for an axisymmetric body locally discretized into finite elements are

$$u_e(r,z,\theta,t) = \boldsymbol{\Psi}_u^{eT}(r,z)\left[\mathbf{U}_0^e(t) + \sum_{n=1}^{\infty}\left(\mathbf{U}_{nc}^e(t)\cos n\theta + \mathbf{U}_{ns}^e(t)\sin n\theta\right)\right], \tag{3.4a}$$

$$v_e(r,z,\theta,t) = \boldsymbol{\Psi}_v^{eT}(r,z)\left[\mathbf{V}_0^e(t) + \sum_{n=1}^{\infty}\left(\mathbf{V}_{nc}^e(t)\cos n\theta - \mathbf{V}_{ns}^e(t)\sin n\theta\right)\right], \tag{3.4b}$$

$$w_e(r,z,\theta,t) = \boldsymbol{\Psi}_w^{eT}(r,z)\left[\mathbf{W}_0^e(t) + \sum_{n=1}^{\infty}\left(\mathbf{W}_{nc}^e(t)\cos n\theta + \mathbf{W}_{ns}^e(t)\sin n\theta\right)\right], \tag{3.4c}$$

where $\boldsymbol{\Psi}_u^e(r,z)$, $\boldsymbol{\Psi}_v^e(r,z)$, and $\boldsymbol{\Psi}_w^e(r,z)$ are the shape functions for the radial, tangential, and axial displacement fields. The time-dependent coefficients $\mathbf{U}_{nc}^e(t)$, $\mathbf{U}_{ns}^e(t)$, $\mathbf{V}_{ns}^e(t)$, $\mathbf{V}_{nc}^e(t)$, $\mathbf{W}_{nc}^e(t)$, $\mathbf{W}_{ns}^e(t)$ are the nth Fourier harmonics of the displacements of the element, also referred to as n nodal diameter components of displacement.

The displacement fields in Eq. (3.4) can admit non-axisymmetric deformations for an axisymmetric body.

Substitution of the displacement field Eq. (3.4) into the energy and work done expressions results in energies in terms of the elemental matrices and time-dependent coefficient vector. A standard finite element assembly process results in global matrices and a global coefficient vector from the elemental components. Applying Lagrange's equation with respect to the time-dependent, coefficient vector ($\mathbf{q}_r$) results in the rotating body equations

of motion as

$$\mathbf{M}_r\ddot{\mathbf{q}}_r + \Omega\mathbf{G}_r\dot{\mathbf{q}}_r + (\mathbf{K}_r - \Omega^2\mathbf{C}_r)\mathbf{q}_r + \frac{\partial\mathbf{N}(\mathbf{q}_r)}{\partial\mathbf{q}_r} = \Omega^2\mathbf{F}_\Omega + \mathbf{F}_r, \tag{3.5a}$$

$$\mathbf{q}_r = \left\{\mathbf{q}_0 \quad \mathbf{q}_1 \quad \ldots \quad \mathbf{q}_n\right\}^T, \tag{3.5b}$$

$$\mathbf{q}_n = \left\{\mathbf{q}_n^1 \quad \mathbf{q}_n^2 \quad \ldots \quad \mathbf{q}_n^j \quad \ldots\right\}, \tag{3.5c}$$

$$\mathbf{q}_n^j = \left\{U_{nc}^j \quad U_{ns}^j \quad V_{ns}^j \quad V_{nc}^j \quad W_{nc}^j \quad W_{ns}^j\right\}, \tag{3.5d}$$

where superscript j is the node number. $\mathbf{M}_r$, $\mathbf{G}_r$, $\mathbf{C}_r$, and $\mathbf{K}_r$ are the mass, gyroscopic, centripetal, and linear elastic stiffness matrices, respectively. $\mathbf{F}_\Omega$ and $\mathbf{F}_r$ are the rotation-induced vector due to centripetal acceleration and external force vector, respectively. $\mathbf{N}(\mathbf{q}_r)$ is the nonlinear component of the elastic stiffness that is retained to obtain the prestress stiffness due to $\mathbf{F}_\Omega$ and $\mathbf{F}_r$. The elemental matrix components are shown in Vaidya and Parker [144].

3.1.2 Arbitrary-shaped, stationary body

Stationary bodies coupled to a rotating body, for example, the casing in the dual rotor system, the stationary housing of a gear train, and the brake pads in a brake rotor system, can have arbitrary shapes. These stationary bodies are not necessarily axisymmetric. They can be rigid or flexible, solid or thin-walled, etc. Material properties can vary in the

stationary body.

Depending on the shape and flexibility of the stationary body, one can use analytical equations, rigid body models, or numerical methods (for example, finite element methods) to model the stationary body. Analytical equations of motion can model simple (for example, circular or rectangular) geometric bodies. Shell equations of motion or shell finite element method can model thin-walled bodies. Numerical methods can be used to model complex-shaped bodies.

The stationary body is defined in the local, stationary basis $\{\mathbf{E}_x, \mathbf{E}_y, \mathbf{E}_z\}$ as shown in Fig. 3.1. Depending on the geometry of the body, other bases can be used. One can use a stationary, cylindrical basis to model an axisymmetric, stationary body.

The stationary body deflections are $\zeta(x, y, z, t)$, $\eta(x, y, z, t)$, and $\xi(x, y, z, t)$ along $\mathbf{E}_x, \mathbf{E}_y$, and $\mathbf{E}_z$, respectively.

Conventional three-dimensional finite elements [9, 26, 159] discretize the complex-shaped, stationary body. Three-dimensional shape functions form the basis for the displacements within an element. Time-varying nodal coefficients are the unknowns. The elemental matrices are obtained following the standard finite element method [9, 26, 159]. Assembling the elemental matrices using the standard finite element assembly process results in the equations of motion of the stationary body as

$$\mathbf{M}_s\ddot{\mathbf{q}}_s + \mathbf{D}_s\dot{\mathbf{q}}_s + \mathbf{K}_s\mathbf{q}_s + \frac{\partial \mathbf{N}(\mathbf{q}_s)}{\partial \mathbf{q}_s} = \mathbf{F}_s, \tag{3.6a}$$

$$\mathbf{q}_s = \left\{ \mathbf{q}_s^1 \quad \mathbf{q}_s^2 \quad \dots \quad \mathbf{q}_s^j \quad \dots \right\}^T, \quad \mathbf{q}_s^j = \left\{ \boldsymbol{\zeta}^j \quad \boldsymbol{\eta}^j \quad \boldsymbol{\xi}^j \right\}, \tag{3.6b}$$

where $\boldsymbol{\zeta}^j$, $\boldsymbol{\eta}^j$, and $\boldsymbol{\xi}^j$ are the unknown, time-dependent nodal coefficients of the jth node.

$\mathbf{M}_s$, $\mathbf{D}_s$, and $\mathbf{K}_s$ are the mass, damping, and stiffness matrices of the body. $\mathbf{F}_s$ is the external force acting on the stationary body. The nonlinear elastic stiffness $\mathbf{N}(\mathbf{q}_s)$ is retained to obtain the prestress stiffness matrix, following the process described in Chapter 2.

A commercial finite element software can be used to extract the mass, damping, and stiffness finite element matrices.

Rigid body equations of motion can define rigid stationary bodies. The time-dependent, nodal coefficients ($\mathbf{q}_s$) in Eq. (3.6) are replaced by the translational and rotational degrees of freedom for rigid body equations of motion.

3.1.3 Coupling models

Discrete stiffness-damper elements (Fig. 3.3(a)), continuous elastic foundations (Fig. 3.3(b)), and constraints (Fig. 3.4) can couple a rotating body to other rotating or stationary bodies in the system. These elements couple the degrees of freedom (or nodal coefficients) in Eqs. (3.5) and (3.6) for the rotating and stationary bodies. We next obtain the coupling models for different coupling elements.

Discrete stiffness-damper elements

Discrete stiffness-dampers are commonly used to couple bodies in a system. Bearing pedestals in contact with rotating bearing races [96, 157], the contact between rotating brake disk and stationary brake pads [51, 106], the read/write pinhead coupled to a hard-disk drive [66] and the guides on a rotating sawblade [65] are some examples that use stiffness-dampers to model contact with rotating bodies. Examples of stiffness-dampers between two coupled, rotating bodies include tooth mesh stiffnesses in coupled gear pairs [29, 71] and the intershaft bearing in a dual rotor system [15, 151].

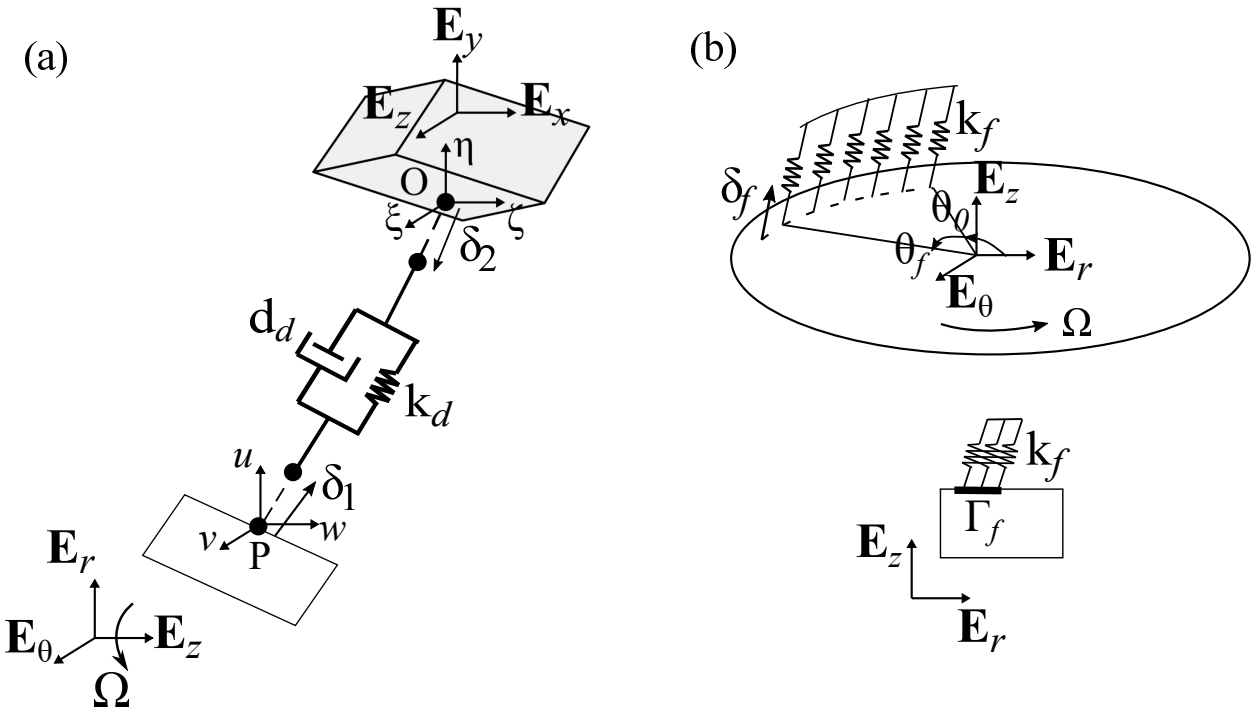

Figure 3.3: (a) Discrete stiffness ($\mathbf{k}_d$) - damper ($\mathbf{d}_d$) element that couples node P on a rotating body to node O on a stationary body, (b) elastic foundation $\mathbf{k}_f$ that spans from θ_0 to θ_f in the circumferential direction and along path $\mathbf{\Gamma}_f$ in the radial cross-section of the rotating body.

The discrete elements can be a function of displacements and time. This allows for the inclusion of time-varying stiffnesses between coupled gears [71] and between bearing races and rolling elements [152]. Dependence of the coupling stiffnesses on the contact deflections [36, 69] and an initial clearance introduces displacement-based nonlinearity in the stiffness element.

In the space-fixed formulation, the contact location of the stationary, discrete element remains fixed in space. The material point on the rotating body at the contact location changes as the body rotates, but the location of the cross-sectional contact point is space-fixed. Thus, the deformation at the discrete element contact location is obtained at a space-fixed point.

The stiffness and damping constants of the coupling element are k_d and d_d, respectively. The deflections at the two ends of the stiffness-damper element along the direction of the coupling element force are δ_1 and δ_2 as shown in Fig. 3.3(a). These deflections depend on the nodal coefficients of the bodies. For example, the deflections in the stiffness-damper element between a rotating and a stationary body are $\delta_1 = \mathbf{R}_r\mathbf{q}_r$ and $\delta_2 = \mathbf{R}_s\mathbf{q}_s$, where $\mathbf{q}_r$ and $\mathbf{q}_s$ are the nodal coefficients from Eqs. (3.5b) and (3.6b), and $\mathbf{R}_r$ and $\mathbf{R}_s$ are the transformation matrices.

The total deflection in the coupling element is $\delta = \delta_1 + \delta_2$. The damping and stiffness energy in the nonlinear stiffness-damper element is

$$C_d = \frac{1}{2}d_d(\mathbf{q},t)\dot{\delta}^2, \quad \Pi_d = \frac{1}{2}k_d(\mathbf{q},t)\delta^2, \tag{3.7}$$

where the nodal coefficient vector $\mathbf{q}$ consists of the degrees of freedom of the two coupled bodies. For a discrete element between a rotating and stationary body shown in Fig. 3.3(a), the nodal coefficient vector $\mathbf{q} = \left\{ \mathbf{q}_r^T \quad \mathbf{q}_s^T \right\}^T$.

The element deflections (δ) in terms of nodal coefficients are substituted into the energy Eq. (3.7). Applying variation with respect to the nodal coefficients results in the discrete stiffness-damper element equation as

$$\mathbf{D}_d(\mathbf{q},t)\dot{\mathbf{q}} + \mathbf{K}_d(\mathbf{q},t)\mathbf{q} = \mathbf{F}_d, \tag{3.8}$$

where $\mathbf{D}_d(\mathbf{q})$ and $\mathbf{K}_d(\mathbf{q})$ are the damping and stiffness matrices and $\mathbf{F}_d$ is the force in the discrete element. Only the components in the matrices that correspond to the degrees of freedom of the two end points of the discrete element are non-zero.

Some bodies can deform in one direction with an applied force in another direction.

The scalar stiffness-damper element can be converted to a general stiffness-damper matrix element to account for these cross-couplings. Guo and Parker [49] converted rolling element bearing to a 6×6-dimensional bearing stiffness matrix. The off-diagonal cross-coupling terms couple the deflections and angular tilting of the bearing. Nonlinear relations between the contact force and deflections are converted to bearing stiffness using $\mathbf{K}_d = \frac{\partial \mathbf{F}_d}{\partial \mathbf{q}}$. The direct stiffness method [159] converts the truss and beam coupling components into stiffness matrix elements. The matrix form of stiffness ($\mathbf{k}_d$) and damping ($\mathbf{d}_d$) constants can be used in Eq. (3.7). In this case, the deflection $\boldsymbol{\delta}$ represents the displacement vector in the reference frame that defines the coupling stiffness-damper matrix. The final equation of the coupling stiffness-damper component obtained by applying variation to the energies with respect to the nodal coefficients is similar to Eq. (3.8).

Elastic foundation

Elastic foundations can model distributed fluid, elastic, magnetic, or acoustic media between two coupled bodies. The friction material between brake disk and pads [75, 76] is an example. The foundation stiffness can be non-axisymmetric as shown in Fig. 3.3(b).

The foundation stiffness is k_f per unit of surface area. It can be a function of the spatial coordinates, displacements, and time. The deflection in the elastic foundation is $\delta_f = \mathbf{R}_f \mathbf{q}$, where $\mathbf{q}$ is the vector of the nodal coefficients and $\mathbf{R}_f$ is the transformation matrix. The elastic foundation energy is

$$\Pi_f = \frac{1}{2} \int_{A_f} k_f(\mathbf{s}, \mathbf{q}) \delta_f^2 \, \mathrm{d}A_f, \tag{3.9}$$

where A_f is the surface area spanned by the elastic foundation and $\mathbf{s}$ is the spatial coordinate.

Variation of the energy Eq. (3.9) with respect to the nodal coefficients results in

the foundation stiffness matrix as $\mathbf{K}_f(\mathbf{s}, \mathbf{q})\mathbf{q}$. Only the elements of $\mathbf{K}_f$ that correspond to the nodes connected to the elastic foundation are non-zero.

Trigonometric orthogonality results in decoupled Fourier harmonics of the rotating body for an axisymmetric elastic foundation. For a non-axisymmetric foundation, the Fourier harmonics are coupled in $\mathbf{K}_f$.

Constraint Equations

Constraints can restrict or couple the motion of different bodies in the system by constraining two points, surfaces, or a surface and a point. A point constraint describes the motion of a single point or relates the motion between two points. Zero axial displacement at a guide location on a circular sawblade [144] is an example of a point constraint. A surface constraint is a multi-point constraint that describes the motion of a surface relative to a point or another surface. The surface area on a brake disk constrained to the flexible brake pad surface and bearing races constrained to rotating shafts are some examples of surface (or multi-point) constraints.

The constraints can be asymmetric. The space-fixed constraints, whether axisymmetric or asymmetric, will result in constant coefficients in the constraint equation. This arises because of the stationary reference frame formulation. For an asymmetric constraint fixed to the rotating body, the points of contact with the stationary body change as the body rotates. This result in constraint equations with time-dependent coefficients.

A set of N constraints that depend on the nodal coefficients $\mathbf{q}$ through the displacements and velocities (at most linear) of the body are represented by the N-dimensional vector expression

$$\mathbf{f}(\mathbf{q}, \dot{\mathbf{q}}, t) = 0. \tag{3.10}$$

Generalized constraint forces $\mathbf{F}_c(\mathbf{q},t)$ are required to impose the constraint Eq. (3.10). Lagrange multipliers are used to apply these constraint forces. The matrix form of the constraint Eq. (3.10) and the generalized constraint forces $\mathbf{F}_c(\mathbf{q},t)$ are of the form

$$\mathbf{A}_q(\mathbf{q},t)\dot{\mathbf{q}} + \mathbf{a}_t(\mathbf{q},t) = 0, \tag{3.11a}$$

$$\mathbf{F}_c(\mathbf{q},t) = \mathbf{A}_q^T(\mathbf{q},t)\mathbf{\Lambda}, \tag{3.11b}$$

respectively, where $\mathbf{\Lambda}$ is the N-dimensional Lagrange multiplier vector.

Constraint relations between two points on the coupled bodies is a point-to-point constraint. For example, the axial displacement $(w(R,Z,\beta,t))$ at a point (R,Z,β) on a rotating hard disk drive equals the axial rigid body motion $(\xi(t))$ of the stationary pinhead as

$$w(R,Z,\beta,t) - \xi(t) = 0. \tag{3.12}$$

The point-to-point constraint in Eq. (3.12) is equivalent to an infinite stiffness element between the two contacting points. The infinite stiffness rigidly constrains the motion of the two points.

Substitution of the displacement field from Eq. (3.4) into Eq. (3.12) results in the matrix form of the constraint equation. The matrix $\mathbf{A}_q$ in Eq. (3.11a) is a row vector given as

$$\mathbf{A}_q = \left\{ 1 \quad \cos\beta \quad \sin\beta \quad \ldots \quad \cos n\beta \quad \sin n\beta \quad -1 \right\}, \tag{3.13a}$$

$$\mathbf{q} = \left\{ W_0 \quad W_{1c} \quad W_{1s} \quad \dots \quad W_{nc} \quad W_{ns} \quad \xi \right\}^T . \tag{3.13b}$$

A single Lagrange multiplier Λ imposes the single constraint equation.

Coupling between two surfaces requires a surface constraint to relate the motion of multiple points on the surface. This is performed by constraining the motion of all points on the surface to a reference point. The weighted summation of all these point-to-point constraints result in a surface constraint equation. The reference point can be located at the center of mass of the body, on a symmetry line, or at an arbitrary point depending on the coupling mechanism.

Forces and moments at the points on the surface can be converted to an equivalent single force and moment at the reference point that is statically equivalent to the original forces and moments. These equivalent resultant force and moment relations between the points on the surface and the reference point are used to obtain the surface constraint equation. The surface constraint equations obtained are in form similar to Eq. (3.11).

The surface constraint does not rigidly constrain the motion of the contact surface points and the reference point. It does not artificially add stiffness to the system as in Eq. (3.12). This surface constraint between finite element nodes and a reference node is similar to the RBE3 element in Nastran [100, 120].

Fig. 3.4 shows a schematic of surface constraints between multiple stationary body and rotating body nodes and their respective reference nodes O_s and O_r. A point-to-point constraint or a discrete stiffness-damper element couples the reference nodes. A discrete stiffness matrix element ($\mathbf{k}_b$) couple the reference nodes O_s and O_r in Fig. 3.4.

Each reference node has six rigid body degrees of freedom. The stationary body finite element nodes have three translational degrees of freedom.

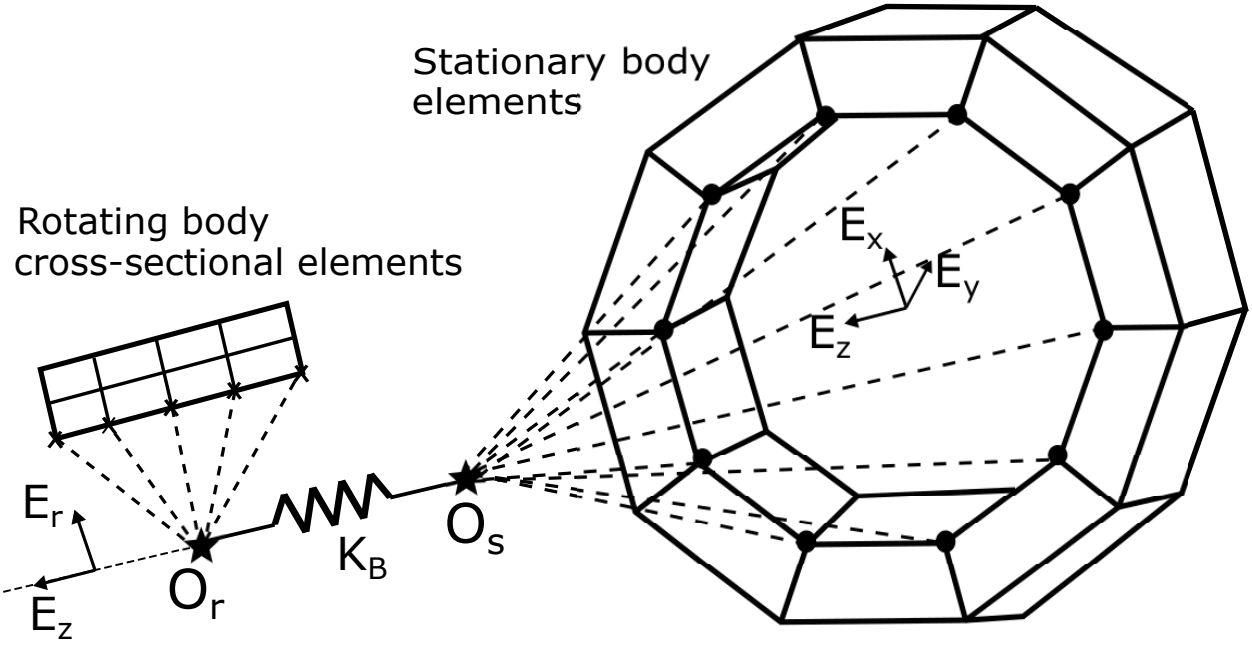

Figure 3.4: Surface constraints (dashed lines) constrain the rotating body cross-sectional nodes (cross-marked) and stationary body nodes (dots) to their respective reference nodes O_r and O_s. The discrete bearing stiffness $\mathbf{k}_b$ couples the reference nodes.

Fig. 3.4 shows nodes (marked as dots) on the surface of the stationary body connected to the reference node O_s. The surface constraint equation is obtained from the equivalent force and moment relation between the contact surface nodes and the reference node. The relations between the forces and moments $\mathbf{P}_i$ at the i^{th} contact surface node and the equivalent force and moment $\mathbf{P}_o$ at O_s due to $\mathbf{P}_i$ are

$$\mathbf{P}_o = \mathbf{L}_{io}^T \mathbf{P}_i, \tag{3.14a}$$

$$\mathbf{P}_o = \begin{Bmatrix} F_{ox} \\ F_{oy} \\ F_{oz} \\ M_{ox} \\ M_{oy} \\ M_{oz} \end{Bmatrix}, \quad \mathbf{P}_i = \begin{Bmatrix} F_{ix} \\ F_{iy} \\ F_{iz} \\ M_{ix} \\ M_{iy} \\ M_{iz} \end{Bmatrix}, \quad \mathbf{L}_{io} = \begin{bmatrix} 1 & 0 & 0 & 0 & L_{iz} & -L_{iy} \\ 0 & 1 & 0 & -L_{iz} & 0 & L_{ix} \\ 0 & 0 & 1 & L_{iy} & -L_{ix} & 0 \\ 0 & 0 & 0 & 1 & 0 & 0 \\ 0 & 0 & 0 & 0 & 1 & 0 \\ 0 & 0 & 0 & 0 & 0 & 1 \end{bmatrix}, \tag{3.14b}$$

$$L_{ix} = x_i - x_o, \quad L_{iy} = y_i - y_o, \quad L_{iz} = z_i - z_o, \tag{3.14c}$$

where $\{x_o, y_o, z_o\}$ and $\{x_i, y_i, z_i\}$ are the coordinates of the reference node O_s and i^{th} contact surface node. With $q = x, y, z$, F_{oq} and F_{iq} are the forces and M_{oq} and M_{iq} are the moments at O_s and the i^{th} node along the $\{\mathbf{E}_x, \mathbf{E}_y, \mathbf{E}_z\}$ basis.

A force at the reference node can be distributed to multiple surface contact points using the equivalent force relation in Eq. (3.14). Weights $\mathbf{W}_i$ can be used to define the fraction of the force at the reference node being transferred to the i^{th} contact surface node. The weighted force $\mathbf{P}_i$ due to an input force $\mathbf{P}_{in}$ at the reference node is

$$\mathbf{P}_i = \mathbf{W}_i \mathbf{L}_{io} \mathbf{A}_s \mathbf{P}_{in} = \mathbf{H}_{si} \mathbf{P}_{in}, \tag{3.15a}$$

$$\mathbf{W}_i = \mathrm{diag}(l_1, l_2, l_3, l_4, l_5, l_6), \tag{3.15b}$$

where $l_1, ..., l_6$ are the weights for the force and moment transfer. The customized weighting in Eq. (3.15) results in an unknown matrix $\mathbf{A}_s$. The matrix $\mathbf{A}_s$ is used to satisfy the equivalent force and moment relation between forces at multiple contact points and the

equivalent input force $\mathbf{P}_{in}$. $\mathbf{H}_{si}$ is a 6×6 - dimensional constraint matrix that relates the forces at the i^{th} contact point due to a force $\mathbf{P}_{in}$ at the reference node.

To obtain the unknown matrix $\mathbf{A}_s$, an equivalent force at the reference node due to forces $\mathbf{P}_i$ in Eq. (3.15) is obtained. The equivalent force is same as the input force $\mathbf{P}_{in}$ that gets distributed at all contact points given as

$$\mathbf{P}_{in} = \sum_{i=1}^{n} \mathbf{L}_{io}^T \mathbf{P}_i = \mathbf{L}^T \mathbf{W} \mathbf{L} \mathbf{A}_s \mathbf{P}_{in}, \tag{3.16a}$$

$$\mathbf{L} = \begin{Bmatrix} \mathbf{L}_{1o} & \mathbf{L}_{2o} & ... & \mathbf{L}_{no} \end{Bmatrix}, \quad \mathbf{W} = \text{blkdiag}(\mathbf{W}_1, \mathbf{W}_2, ..., \mathbf{W}_n). \tag{3.16b}$$

The unknown $\mathbf{A}_s$ is obtained from Eq. (3.16a) as $\mathbf{A}_s = (\mathbf{L}^T \mathbf{W} \mathbf{L})^{-1}$.

The constraint relations defined in Eq. (3.15) are used to constrain the displacements of the surface contact nodes to the reference node. The degrees of freedom ($\mathbf{Q}_s$) of the reference node are constrained to the contact surface node degrees of freedom ($\mathbf{q}_s$) as

$$\mathbf{Q}_s = \mathbf{H}_s \mathbf{q}_s, \tag{3.17a}$$

$$\mathbf{Q}_s = \{x_s, y_s, z_s, \gamma_{xs}, \gamma_{ys}, \gamma_{zs}\}, \quad \mathbf{H}_s = \{\mathbf{H}_{s1}\ \mathbf{H}_{s2}\ \ldots \mathbf{H}_{si}\ \ldots \mathbf{H}_{sN}\}, \tag{3.17b}$$

where $\mathbf{H}_s$ is the constraint matrix with dimension $6 \times 3N$. The nodal degrees of freedom vector $\mathbf{q}_s$ is identical to Eq. (3.6b) with dimension $3N \times 1$. Only the components of $\mathbf{H}_s$ corresponding to the contact surface nodes are non-zero. The surface constraint in Eq. (3.17) constrains the three displacement degrees of freedom of the finite element nodes on the surface to the reference node.

The rotating body is defined using Fourier harmonic nodal coefficients in Eq. (3.5b). A different set of constraint equations constrain the Fourier harmonic nodal coefficients of the rotating body to the reference node degrees of freedom.

Fig. 3.4 shows the cross-sectional nodes of the rotating body coupled to the reference node O_r on the rotation axis with surface constraints. The constraint surface of the rotating body is along a path Γ_f in the $r-z$ cross-section and spans circumferentially from θ_0 to θ_f. The rigid body motion of the constraint surface is

$$\begin{aligned} x_r &= \tfrac{1}{A_r}\int_{\theta_0}^{\theta_f}\int_{\Gamma_f}(u\cos\theta - v\sin\theta)r\,\mathrm{d}\Gamma_f\mathrm{d}\theta, \quad y_r = \tfrac{1}{A_r}\int_{\theta_0}^{\theta_f}\int_{\Gamma_f}(u\sin\theta + v\cos\theta)r\,\mathrm{d}\Gamma_f\mathrm{d}\theta, \\ z_r &= \tfrac{1}{A_r}\int_{\theta_0}^{\theta_f}\int_{\Gamma_f} w\,r\,\mathrm{d}\Gamma_f\mathrm{d}\theta, \quad \gamma_{xr} = \tfrac{1}{A_r R}\int_{\theta_0}^{\theta_f}\int_{\Gamma_f} w\sin\theta\,r\,\mathrm{d}\Gamma_f\mathrm{d}\theta, \\ \gamma_{yr} &= -\tfrac{1}{A_r R}\int_{\theta_0}^{\theta_f}\int_{\Gamma_f} w\cos\theta\,r\,\mathrm{d}\Gamma_f\mathrm{d}\theta, \quad \gamma_{zr} = \tfrac{1}{A_r R}\int_{\theta_0}^{\theta_f}\int_{\Gamma_f} v\,r\,\mathrm{d}\Gamma_f\mathrm{d}\theta, \end{aligned} \tag{3.18}$$

where $A_r = \displaystyle\int_{\theta_0}^{\theta_f}\int_{\Gamma_f} r\mathrm{d}\Gamma_f\mathrm{d}\theta$ is the contact surface area and R is the average radius of the contact surface. Substitution of the displacement fields from Eq. (3.4) into Eq. (3.18) results in

$$\mathbf{Q}_r = \mathbf{H}_r\mathbf{q}_r, \tag{3.19a}$$

$$\mathbf{Q}_r = \{x_r, y_r, z_r, \gamma_{xr}, \gamma_{yr}, \gamma_{zr}\}, \tag{3.19b}$$

where $\mathbf{q}_r$ is the vector of the unknown nodal Fourier coefficients from Eq. (3.5b) and $\mathbf{H}_r$ is the constraint matrix. Only the components of $\mathbf{H}_r$ corresponding to the nodes on the path Γ_f are non-zero.

For an axisymmetric constraint surface with $\theta_0 = 0$ and $\theta_f = 2\pi$, only the compo-

nents in $\mathbf{H}_r$ in Eq. (3.19) that correspond to the zeroth and first Fourier harmonics of the nodes are non-zero. A circumferentially asymmetric constraint surface couples all Fourier harmonics.

The surface constraint for conventional finite element nodes in Eq. (3.17) can be applied to the rotating body nodes along with the rotating body constraints in Eq. (3.18). Eq. (3.18) for a single node without the integral over Γ_f results in a relation between Fourier harmonic nodal coefficients of the cross-sectional node to the translations and rotations of that node along the rotation axis. These translational and rotational degrees of freedom of multiple rotating body cross-sectional nodes can be constrained to a reference node using $\mathbf{H}_{si}$ in Eq. (3.15). The resulting constraint equation between the rotating body cross-sectional nodes and the reference node is

$$\mathbf{Q}_r = \mathbf{H}_s \mathbf{H}_r \mathbf{q}_r, \tag{3.20a}$$

$$\mathbf{H}_r = \text{blkdiag}(\mathbf{H}_{r1}, \mathbf{H}_{r2}, \ldots, \mathbf{H}_{rn}), \tag{3.20b}$$

where $\mathbf{H}_s$ is obtained from the 6×6-dimensional $\mathbf{H}_{si}$ matrix from Eq. (3.15). The matrix $\mathbf{H}_{rj}$, where $j = 1, 2, \ldots, n$, is obtained from Eq. (3.19) for each cross-sectional node.

Lagrange multipliers and constraint forces in Eq. (3.11b) are used to apply constraint Eqs. (3.17), (3.19), and (3.20). Each constraint equation increases the system degrees of freedom by twelve (six reference node degrees of freedom and six Lagrange multipliers).

A point-to-point constraint or a discrete element couples the reference nodes of the two coupled surfaces. In Fig. 3.4, a stiffness element $\mathbf{k}_b$ connects the reference nodes O_s and O_r. The stiffness element $\mathbf{k}_b$ is a 6×6-dimensional matrix. The strain energy in the stiffness

element is

$$\Pi_B = \frac{1}{2}(\mathbf{Q}_r - \mathbf{Q}_s)^T \mathbf{k}_b (\mathbf{Q}_r - \mathbf{Q}_s). \tag{3.21}$$

Using Lagrange's equations, the constraint and stiffness matrices for the system in Fig. 3.4 are obtained from Eqs. (3.17), (3.19), and (3.21) as

$$(\mathbf{S} + \mathbf{K}_b)\mathbf{q} = \begin{bmatrix} \mathbf{0} & \mathbf{0} & \mathbf{0} & \mathbf{0} & \mathbf{H}_r^T & \mathbf{0} \\ \mathbf{0} & \mathbf{0} & \mathbf{0} & \mathbf{0} & \mathbf{0} & \mathbf{H}_s^T \\ \mathbf{0} & \mathbf{0} & \mathbf{k}_b & -\mathbf{k}_b & -\mathbf{I}_6 & \mathbf{0} \\ \mathbf{0} & \mathbf{0} & -\mathbf{k}_b & \mathbf{k}_b & \mathbf{0} & -\mathbf{I}_6 \\ \mathbf{H}_r & \mathbf{0} & -\mathbf{I}_6 & \mathbf{0} & \mathbf{0} & \mathbf{0} \\ \mathbf{0} & \mathbf{H}_s & \mathbf{0} & -\mathbf{I}_6 & \mathbf{0} & \mathbf{0} \end{bmatrix} \begin{Bmatrix} \mathbf{q}_r \\ \mathbf{q}_s \\ \mathbf{Q}_r \\ \mathbf{Q}_s \\ \mathbf{\Lambda}_r \\ \mathbf{\Lambda}_s \end{Bmatrix}, \tag{3.22}$$

where $\mathbf{I}_6$ is a 6×6 identity matrix, $\mathbf{S}$ is the constraint matrix, and $\mathbf{K}_b$ is the stiffness matrix coupling the two reference nodes.

One can couple two rotating bodies using the surface constraints in Eqs. (3.18) or (3.20) and a stiffness-damper element.

The constraints in Eq. (3.18) can also constrain a flexible, rotating body to a rigid body. The rigid body is defined at the reference node with the reference node degrees of freedom.

3.2 System equation of motion

The rotating and stationary body equations of motion from Eqs. (3.5) and (3.6) and the coupling element equations are assembled into a global system equation of motion.

The final equation of motion is

$$\mathbf{M}\ddot{\mathbf{q}} + (\mathbf{D}+\mathbf{G})\dot{\mathbf{q}} + (\mathbf{K}-\mathbf{C})\mathbf{q} + (\mathbf{K}_d+\mathbf{K}_f+\mathbf{K}_b+\mathbf{S})\mathbf{q} + \frac{\partial \mathbf{N}(\mathbf{q})}{\partial \mathbf{q}} = \mathbf{F}_\Omega + \mathbf{F}(\mathbf{q},t), \quad (3.23a)$$

$$\mathbf{q} = \{\mathbf{q}_r, \mathbf{q}_s, \mathbf{Q}_r, \mathbf{Q}_s, \mathbf{\Lambda}_r, \mathbf{\Lambda}_s\}^T, \quad (3.23b)$$

where $\mathbf{M}$, $\mathbf{D}$, $\mathbf{G}$, $\mathbf{K}$, $\mathbf{C}$ are the mass, damping, gyroscopic, elastic stiffness, and centripetal matrices, respectively. The nonlinear elastic stiffness component is $\partial\mathbf{N}(\mathbf{q})/\partial\mathbf{q}$. The vectors $\mathbf{F}_\Omega$ and $\mathbf{F}(\mathbf{q},t)$ are the rotation-induced force and external forces, respectively. The matrices $\mathbf{K}_d$, $\mathbf{K}_f$, and $(\mathbf{K}_b+\mathbf{S})$ are the discrete stiffness-damper, elastic foundation, and constraint coupling matrices from Eqs. (3.8), (3.9), and (3.22), respectively.

The matrix components in the equation of motion Eq. (3.23) are system-specific. These matrix components are obtained for a brake disk-pad system and a dual rotor system.

3.2.1 Prestress

Rotation-induced force $\mathbf{F}_\Omega$ and the mean values of external forces $\mathbf{F}(\mathbf{q},t)$ prestress the system. The steady prestressed state defined by steady deflections $\overline{\mathbf{q}}$ generates a linear prestress stiffness matrix for small vibrations defined by $\tilde{\mathbf{q}}(t)$ relative to the steady deflected state. Linearizing the nonlinear elastic stiffness term in Eq. (3.23a) about the steady deflected state of the system results in the linear prestress stiffness matrix.

The steady state deflection is obtained by elimination of the time derivatives from Eq. (3.23a) as

$$(\mathbf{K}-\mathbf{C}+\mathbf{K}_d+\mathbf{K}_f+\mathbf{K}_b+\mathbf{S})\overline{\mathbf{q}} + \frac{\partial \mathbf{N}(\overline{\mathbf{q}})}{\partial \overline{\mathbf{q}}} = \mathbf{F}_\Omega + \mathbf{F}(\overline{\mathbf{q}}). \quad (3.24)$$

This nonlinear algebraic problem is solved numerically for $\overline{\mathbf{q}}$. For small steady deflections, the linearized steady state problem can be solved for $\overline{\mathbf{q}}$.

The equations governing the small vibrations $\tilde{\mathbf{q}}(t)$ about the steady deflected state are obtained by substitution of $\mathbf{q}(t) \rightarrow \overline{\mathbf{q}} + \tilde{\mathbf{q}}(t)$ into Eq. (3.23). Linearizing the nonlinear term $\frac{\partial \mathbf{N}(\mathbf{q})}{\partial \mathbf{q}}$ in Eq. (3.23) for small $\tilde{\mathbf{q}}(t)$ yields the linear prestress (or geometric) stiffness matrix $\mathbf{K}_p(\overline{\mathbf{q}})$.

Because the nonlinear elastic stiffness term is not coupled between different bodies, the prestress stiffness matrix components for each body are uncoupled and obtained independently. Assembling the component prestress stiffness terms results in a global prestress stiffness matrix $\mathbf{K}_p(\overline{\mathbf{q}})$. The detailed derivation and expression of $\mathbf{K}_p(\overline{\mathbf{q}})$ for a rotating body is given in Vaidya and Parker [144]. Following the derivation in [144], the prestress stiffness matrix for a conventional finite element body is obtained.

The equation of motion of the system including prestress is

$$\mathbf{M}\ddot{\tilde{\mathbf{q}}} + (\mathbf{D} + \mathbf{G})\dot{\tilde{\mathbf{q}}} + (\mathbf{K} - \mathbf{C})\tilde{\mathbf{q}} + (\mathbf{K}_d + \mathbf{K}_f + \mathbf{K}_b + \mathbf{S})\tilde{\mathbf{q}} + \mathbf{K}_p(\overline{\mathbf{q}})\tilde{\mathbf{q}} = \mathbf{F}(t). \tag{3.25}$$

The free vibration eigenvalue problem from use of $\tilde{\mathbf{q}} = \boldsymbol{\chi} e^{\lambda t}$ in Eq. (3.25) is

$$\lambda^2 \mathbf{M}\boldsymbol{\chi} + \lambda(\mathbf{D} + \mathbf{G})\boldsymbol{\chi} + (\mathbf{K} - \mathbf{C} + \mathbf{K}_d + \mathbf{K}_f + \mathbf{K}_b + \mathbf{S} + \mathbf{K}_p(\overline{\mathbf{q}}))\boldsymbol{\chi} = \mathbf{0}. \tag{3.26}$$

Model reduction techniques [6, 41, 42], for example, static condensation, can be used to eliminate the reference node degrees of freedom $(\mathbf{Q}_r, \mathbf{Q}_s)$ and Lagrange multipliers $(\boldsymbol{\Lambda}_r, \boldsymbol{\Lambda}_s)$ in Eq. (3.25).

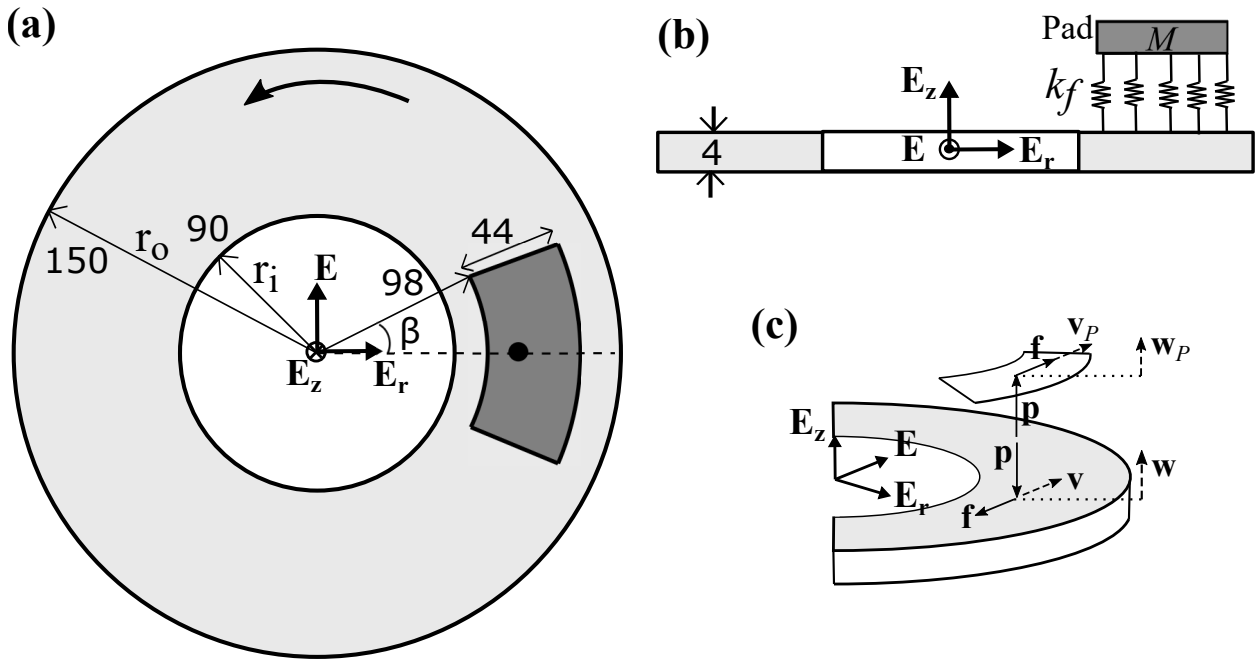

Figure 3.5: (a) Schematic of a clamped-free brake disk rotating with speed Ω and coupled to a stationary, rigid body brake pad with an elastic foundation. The dimensions are in millimeters. (b) The $\mathbf{E}_r - \mathbf{E}_z$ cross-sectional view of the system with an elastic foundation k_f per unit surface area couples the disk and the pad. (c) The elastic force in the contact stiffness $\mathbf{p}$ and the friction force $\mathbf{f}$ acting on the brake disk and the pad.

3.3 Brake disk-pad

A brake disk coupled to stationary brake pads is an example of a system with a rotating body coupled to a stationary body, analyzed in [51, 56, 75, 76, 106, 107]. Analytical rotating disk equations commonly model the brake disks. A rigid body model, analytical equations, or finite element methods model the stationary brake pads [51, 56, 75, 76, 106, 107]. An elastic foundation couples the brake disk and pads.

Fig. 3.5 shows a brake disk-pad system. The clamped-free brake disk rotates with speed Ω about its symmetry axis $\mathbf{E}_z$. A stationary, rigid body with mass M models the brake pad. The contact area between the brake disk and the pad spans radially from r_i to r_o and circumferentially from $-\beta$ to β. An elastic foundation k_f per unit of surface area

models the contact. A non-conservative frictional force with constant friction coefficient μ acts at the contact surface.

The space-fixed formulation in Section 3.1.1 with two-dimensional, cross-sectional finite elements and Fourier series models the rotating brake disk. The equations of motion of the axisymmetric, rotating brake disk are identical to Eq. (3.5).

The brake pad is a two degree of freedom rigid body with tangential (v_p) and axial (w_p) displacements. The brake pad equation of motion is

$$\mathbf{M}_p\ddot{\mathbf{q}}_p + \mathbf{K}_p\mathbf{q}_p = \mathbf{F}_p, \tag{3.27a}$$

$$\mathbf{M}_p = \begin{bmatrix} M & 0 \\ 0 & M \end{bmatrix}, \quad \mathbf{K}_p = \begin{bmatrix} k_t & 0 \\ 0 & k_a \end{bmatrix}, \quad \mathbf{q} = \begin{Bmatrix} v_p \\ w_p \end{Bmatrix}, \tag{3.27b}$$

where k_t and k_a are pad stiffnesses along tangential and axial directions, respectively, and $\mathbf{F}_p$ is an external force on the brake pad.

The contact location of the stationary elastic foundation and the friction force remain fixed in space as the disk rotates. This results in constant coefficient equations for the coupling elements.

The elastic foundation is assumed to act perpendicular to the undeformed disk surface (i.e., in the direction of $\mathbf{E}_z$). The deformation in the elastic foundation is $\boldsymbol{\delta}_f = [w_p - w(r, \theta, Z_p/2, t)]\,\mathbf{E}_z$, where Z_p is the thickness of the disk. The elastic foundation is along path $\Gamma_f = r$ from r_i to r_o and circumferentially from $\theta_0 = -\beta$, and $\theta_f = \beta$. The displacement field Eq. (3.4) and integration limits are substituted into the foundation energy Eq. (3.9). Applying variation with respect to the nodal coefficients results in the following

foundation stiffness matrix:

$$\mathbf{k}_f \mathbf{q}_w = \begin{bmatrix} \mathbf{k}_{rr} & \mathbf{k}_{rp} \\ \mathbf{k}_{rp}^T & k_{pp} \end{bmatrix} \begin{Bmatrix} \mathbf{W} \\ w_p \end{Bmatrix}, \tag{3.28a}$$

$$\mathbf{k}_{rr} = k_f \int_{r_i}^{r_o} \mathbf{\Psi}_w^T \mathbf{\Psi}_w r \, \mathrm{d}r \int_{-\beta}^{\beta} \mathbf{P}_w^T \mathbf{P}_w \mathrm{d}\theta, \qquad \mathbf{k}_{rp} = k_f \int_{r_i}^{r_o} \mathbf{\Psi}_w \, \mathrm{d}r \int_{-\beta}^{\beta} \mathbf{P}_w \mathrm{d}\theta,$$

$$k_{pp} = k_f \beta (r_o^2 - r_i^2), \tag{3.28b}$$

$$\mathbf{P}_w = \{1 \;\; \cos\theta \;\; \sin\theta \;\; ... \;\; \cos n\theta \;\; \sin n\theta\}, \tag{3.28c}$$

where $\mathbf{\Psi}_w$ are the cross-sectional shape functions of the disk from Eq. (3.4) and $\mathbf{W}$ is the vector of axial Fourier harmonic nodal coefficients ($\mathbf{W}_{nc}$ and $\mathbf{W}_{ns}$ from Eq. (3.4)) of the disk.

Friction force acts in the direction of the relative motion between the disk and the pad. The friction force results in a frictional follower force and a friction coupling in the brake-disk system. The frictional follower force has a negligible effect on the system dynamics [51, 76]. Thus, the frictional follower force is neglected in this analysis.

The friction force $\mathbf{f}$ is assumed to act tangentially, given as

$$\mathbf{f} = -\mu k_f (w_p - w(r, \theta, Z_p/2)) \mathbf{E}_\theta. \tag{3.29}$$

The virtual work done by the non-conservative frictional force is

$$\delta W = -\mu k_f \int_{r_i}^{r_o} \int_{-\beta}^{\beta} (w_p - w)(\delta v_p - \delta v) r \, \mathrm{d}\theta \mathrm{d}r. \tag{3.30}$$

The disk displacement field Eq. (3.4) is substituted into Eq. (3.30). Applying variation to the virtual work expression with respect to the nodal coefficients results in the non-symmetric friction coupling matrix as

$$\mathbf{k}_c \mathbf{q}_c = \begin{bmatrix} \mathbf{0} & \mathbf{k}_{crr} & \mathbf{0} & \mathbf{k}_{crp} \\ \mathbf{0} & \mathbf{0} & \mathbf{0} & \mathbf{0} \\ \mathbf{0} & \mathbf{k}_{cpr} & 0 & k_{cpp} \\ \mathbf{0} & \mathbf{0} & 0 & 0 \end{bmatrix} \begin{Bmatrix} \mathbf{V} \\ \mathbf{W} \\ v_p \\ w_p \end{Bmatrix}, \tag{3.31a}$$

$$\mathbf{k}_{crr} = \mu k_f \int_{r_i}^{r_o} \mathbf{\Psi}_v^T \mathbf{\Psi}_w r \, \mathrm{d}r \int_{-\beta}^{\beta} \mathbf{P}_v^T \mathbf{P}_w \mathrm{d}\theta, \quad \mathbf{k}_{crp} = \mu k_f \int_{r_i}^{r_o} \mathbf{\Psi}_v^T \, \mathrm{d}r \int_{-\beta}^{\beta} \mathbf{P}_v^T \mathrm{d}\theta, \tag{3.31b}$$

$$\mathbf{k}_{cpr} = \mu k_f \int_{r_i}^{r_o} \mathbf{\Psi}_w \, \mathrm{d}r \int_{-\beta}^{\beta} \mathbf{P}_w \mathrm{d}\theta, \quad k_{cpp} = \mu k_f \beta (r_o^2 - r_i^2), \tag{3.31c}$$

where $\mathbf{V}$ and $\mathbf{W}$ are the tangential and axial Fourier harmonic nodal coefficients of the disk from Eq. (3.4).

The elastic foundation and the friction force components in Eqs. (3.28) and (3.31) are non-zero only for the disk cross-sectional nodes between $(r_i, Z_p/2)$ and $(r_o, Z_p/2)$.

The brake disk and brake pad equations of motion Eqs. (3.5), (3.27), elastic foundation stiffness matrix Eq. (3.28), and friction coupling matrix Eq. (3.31) are assembled to

obtain the equation of motion of the brake disk-pad system as

$$\mathbf{M}\ddot{\mathbf{q}} + \mathbf{G}\dot{\mathbf{q}} + (\mathbf{K} + \mathbf{K}_c + \mathbf{K}_f - \mathbf{C})\mathbf{q} + \mathbf{K}_p\mathbf{q} = \mathbf{0}, \tag{3.32a}$$

$$\mathbf{q} = \{\mathbf{q}_r, v_p, w_p\}, \tag{3.32b}$$

$$\mathbf{M} = \text{blkdiag}(\mathbf{M}_r, M, M), \quad \mathbf{K} = \text{blkdiag}(\mathbf{K}_r, k_t, k_a),$$

$$\mathbf{G} = \text{blkdiag}(\mathbf{G}_r, 0, 0), \quad \mathbf{C} = \text{blkdiag}(\mathbf{C}_r, 0, 0), \tag{3.32c}$$

where $\mathbf{M}_r$, $\mathbf{G}_r$, $\mathbf{K}_r$, and $\mathbf{C}_r$ are the rotating disk matrices obtained from Eq. (3.5). The elastic foundation stiffness $\mathbf{K}_f$ and friction coupling $\mathbf{K}_c$ matrices are assembled from the components in Eqs. (3.28) and (3.31), respectively. The prestress stiffness matrix $\mathbf{K}_p$ resulting from the rotation-induced force $\mathbf{F}_\Omega$ in Eq. (3.5) is obtained by linearization of the nonlinear equation of motion about the steady deformation of the body [144].

The mass $\mathbf{M}$, elastic stiffness $\mathbf{K}$, centripetal $\mathbf{C}$, contact stiffness $\mathbf{K}_f$, and prestress stiffness $\mathbf{K}_p$ matrices are symmetric whereas the gyroscopic $\mathbf{G}$ matrix is skew-symmetric. The friction coupling matrix $\mathbf{K}_c$ is non-symmetric. The coupling between the brake disk and the pad occurs in the $\mathbf{K}_f$ and $\mathbf{K}_c$ matrices.

The free vibration eigenvalue problem in Eq. (3.26) is solved for the brake disk-pad system natural frequencies and vibration modes.

Fig. 3.6 compares the non-dimensional natural frequencies $\hat{\lambda} = \lambda R_o\sqrt{\rho(1-\nu^2)/E}$ of the brake disk-pad obtained from Eq. (3.26) and those of a clamped-free rotating disk.

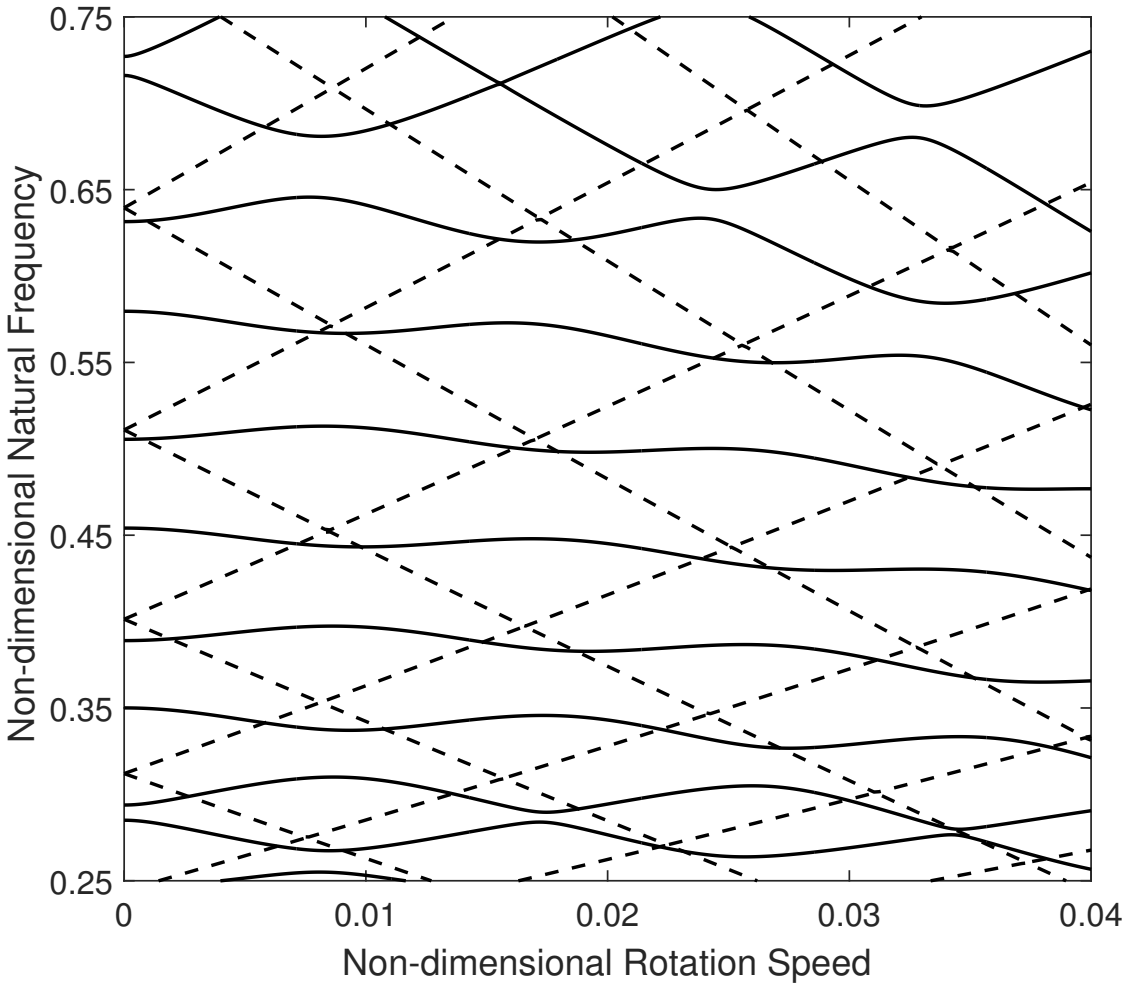

Figure 3.6: Non-dimensional natural frequencies $\hat{\lambda} = \lambda R_o \sqrt{\rho(1-\nu^2)/E}$ of the clamped-free rotating brake disk with dimensions in Fig. 3.5 coupled to a rigid pad via an elastic foundation and friction coupling (solid lines) is compared to the non-dimensional natural frequencies of the clamped-free rotating disk in Fig. 3.5 without brake pad and coupling (dashed lines). The pad and contact model parameters are in Table 3.1.

Table 3.1: Parameters of the brake disk-pad system

Inner radius of the pad (r_i)	98 mm
Outer radius of the pad (r_o)	142 mm
Half-angle of the pad (β)	31°
Mass of the pad (M)	0.22 kg
Tangential stiffness of the pad (k_t)	1.15 $\times 10^9$ N/m
Axial stiffness of the pad (k_a)	4.15 $\times 10^5$ N/m
Elastic foundation stiffness (k_f)	3.5 $\times 10^{10}$ N/m^3
Friction coefficient (μ)	0.5

The brake pad parameters, elastic foundation stiffness, and the friction coefficient are given in Table 3.1.

An asymmetric elastic foundation breaks the axisymmetry of the rotating disk. The degenerate eigenvalues of the stationary, uniform disk split into distinct eigenvalues for the non-axisymmetric brake disk-pad system as observed in Fig. 3.6. The asymmetric foundation also leads to Fourier harmonic coupling in the foundation stiffness $\mathbf{K}_f$ and friction coupling $\mathbf{K}_c$ matrices. This Fourier harmonic coupling is absent in a uniform, axisymmetric body. Vibration modes of the asymmetric system consist of multiple Fourier harmonic components, whereas the axisymmetric body has pure, single, non-zero Fourier components.

Eigenvalue veering occurs when two eigenvalues approach each other as a parameter is varied but then veer away without crossing [115]. Vibration modes are exchanged between two veering eigenvalue loci as the parameter increases or decreases within the veering region. If the modes of the two approaching eigenvalues have common Fourier harmonic coefficients, then veering occurs. If no common Fourier harmonic coefficients exist between the modes of the two approaching eigenvalues, then the eigenvalue loci cross each other. The sharpness of the veering depends on the extent of Fourier harmonic coupling between the approaching eigenvalues. Large amplitudes of the common Fourier harmonic coefficients lead to broad veering regions. Most veering regions in Fig. 3.6 are broad.

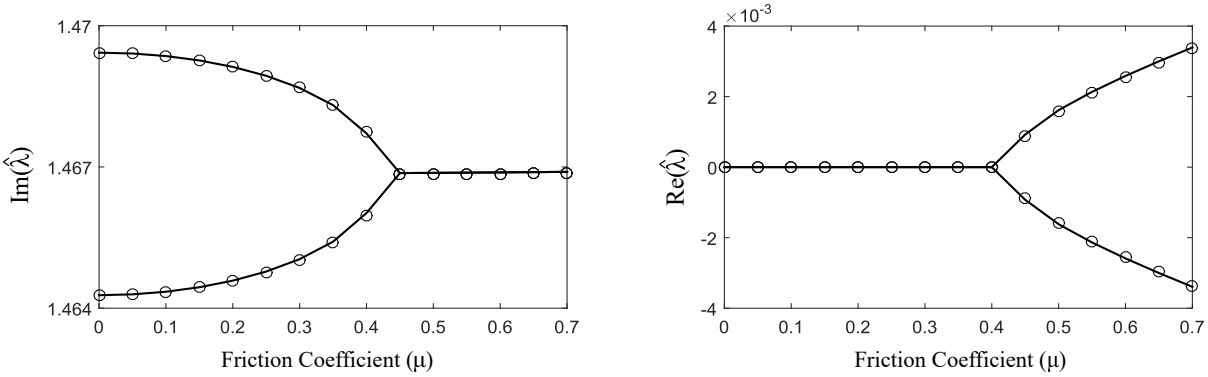

Figure 3.7: Non-dimensional, stationary natural frequencies $\hat{\lambda} = \lambda R_o \sqrt{\rho(1-\nu^2)/E}$ of the clamped-free rotating brake disk-pad system with varying friction coefficient for a full eigenvalue problem in Eq. (3.32) (solid lines) and two-mode (modes 34 and 35) reduced order model in [60, 76] (circles). The system parameters are given in Table. 3.1.

The symmetric elastic foundation stiffness matrix $\mathbf{K}_f$ influences the system frequencies and the non-symmetric friction matrix $\mathbf{K}_c$ produces dynamic instability [76]. Neglecting $\mathbf{K}_c$ in the eigenvalue problem in Eq. (3.26) results in eigenvalues that almost overlap with the solid lines in Fig. 3.6. The effect of frictional coupling on the imaginary part of the eigenvalues is negligible.

The non-conservative friction plays a key role in dynamic instability of the disk-pad system. Disk brake squeal is one of the mode merging (flutter) instabilities that arises when two modes merge on varying a parameter. The brake squeal occurs at low speeds, and thus, rotational effects are ignored in brake squeal analysis [76, 107]. The point of transition of imaginary eigenvalues into complex eigenvalues (mode-merging point) indicates squeal onset [75, 76]. Kang et al. [75] derived an analytical relationship between frequency separation and squeal occurrence. Huang et al. [60] obtained a reduced-order model with modes of two closely spaced eigenvalues. Using eigenvalue perturbation theory, they estimated the critical value of the friction coefficient that results in complex eigenvalues and squeal onset. Fig. 3.7 shows the imaginary and real parts of modes 34 and 35 of the brake disk-pad on varying the friction coefficient. The eigenvalues obtained from a full system eigenvalue problem in Eq.

(3.32) compares well with the analytical expression for the two-mode reduced-order friction coupling model in [60, 76]. This indicates the present model can be used to study the squeal onset, similar to the existing models.

In brake disk-pad systems, a velocity dependent friction is a major destabilizing factor. The rotation speed influences the severity of the instability [76, 85, 106]. The above developed model in Eq. (3.32) can be used to study the effects of a velocity-dependent friction coefficient on the instability.

The friction follower force directed along the deformable surface of the disk may be important in some applications, for example, thin hard-disk drive systems [142]. The model in Eq. (3.32) can be modified to include the friction force as

$$\mathbf{f} = -\mu k_c (w_p - w) \frac{\mathbf{V}_r}{|\mathbf{V}_r|}, \tag{3.33}$$

where $\mathbf{V}_r$ is the relative velocity between the two contacting surfaces. This friction force leads to additional non-symmetric friction follower stiffness term and a symmetric radial dissipative term in the equation of motion Eq. (3.32).

A finite element method can be used to model the brake pad. The vibration modes of a brake pad can be used as basis functions to approximate the brake pad displacements [74].

3.4 Coupled, dual rotors enclosed in a casing

A dual rotor-casing system includes two rotating bodies and a stationary casing. The bodies are coupled via bearings. Refs. [15, 151, 152, 157] analyzed the dual rotor-casing system with beam element rotors, mass-stiffness-damper supports, and nonlinear contact

models. In this work, semi-analytical model in Section 3.1.1 models the rotating bodies and three-dimensional finite elements model the stationary casing. The rotating bodies can have arbitrary radial cross-sectional shape without restricting the system to be composed of beam-type elements. Different coupling methods model the bearings in the system.

Fig. 3.8 shows a dual rotor-casing system with inner low-pressure (LP) and outer high-pressure (HP) rotating systems. Each rotating body has a shaft (LP and HP), a compressor (LPC and HPC), and a turbine disk (LPT and HPT). The LP and HP bodies rotate with speeds Ω_L and Ω_H, respectively, about their rotation axis $\mathbf{E}_z$. The two bodies can rotate in the same or opposite directions.

Two-dimensional, cross-sectional finite elements with Fourier series displacement fields in Eq. (3.4) are used to model the axisymmetric, rotating LP and HP bodies. The equations of motion for the LP and HP rotating bodies with Fourier harmonic nodal degrees of freedom $\mathbf{q}_L$ and $\mathbf{q}_H$, respectively, are obtained from Eq. (3.5). The subscripts 'L' and 'H' will be used to denote 'LP' and 'HP' systems.

The rotating system is enclosed in a stationary, outer cylinder casing. The ground-based casing is fixed at the base from $z = 25$ to 40mm and 560 to 575mm, as marked in Fig. 3.8. Conventional, three-dimensional finite elements are used to model the stationary casing. The stationary casing equation of motion is obtained from Eq. (3.6) with $\mathbf{q}_S$ as the nodal degrees of freedom. The subscript 'S' will be used to indicate the stationary casing.

Assembling the equations of motion of the three independent bodies (rotating LP system, HP system, and a stationary casing) gives the full system equation of motion.

An elastic foundation B_1, surface constraints with a bearing stiffness matrix B_2, intershaft time-varying stiffness B_3, and discrete stiffnesses B_4 shown in Fig. 3.8 couple the bodies in the dual rotor-casing system.

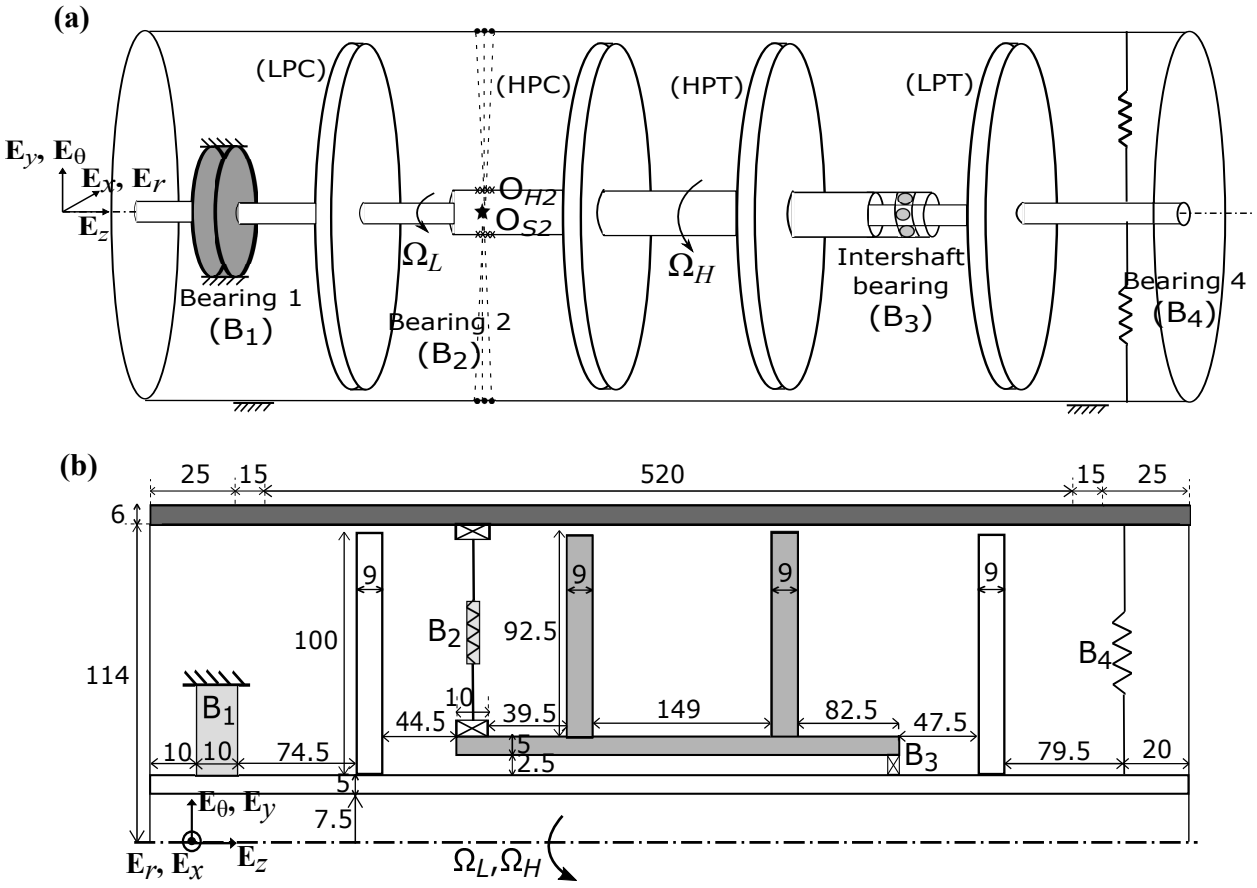

Figure 3.8: (a) Schematic and (b) Cross-section of the dual rotor-casing model with dimesions in millimeters. The low-pressure (LP) and high-pressure (HP) systems consists of a shaft, a compressor disk (LPC, HPC), and a turbine disk (LPT, HPT). The rotation speeds of the LP and HP systems are Ω_L and Ω_H, respectively. The LP shaft is supported by an elastic foundation bearing B_1 and two discrete stiffnesses shown by B_4. The HP shaft is coupled to the casing through surface constraints and a bearing stiffness model B_2. The radial, time-varying stiffness element B_3 couples the LP and HP shafts.

A space-fixed, axisymmetric, grounded elastic foundation B_1 with stiffnesses k_{u1}, k_{v1}, and k_{w1} per unit of surface area in the radial, tangential, and axial directions supports the LP shaft. The elastic foundation is along the path $\Gamma_f = z$ from $z_0 = 10\text{mm}$ to $z_f = 20\text{mm}$ on the LP shaft. The deflection in the elastic foundation is

$$\boldsymbol{\delta}_f = u_L(R_L, z, \theta)\mathbf{E}_r + v_L(R_L, z, \theta)\mathbf{E}_\theta + w_L(R_L, z, \theta)\mathbf{E}_z. \tag{3.34}$$

Substituting the displacement fields from Eq. (3.4) into Eqs. (3.34) and (3.9) with $\mathbf{k}_f = \mathrm{diag}(k_{u1}, k_{v1}, k_{w1})$ and applying variation with respect to $\mathbf{q}_L$ gives the stiffness matrix component $\mathbf{K}_1$ due to bearing B_1 as

$$\mathbf{K}_1\mathbf{q}_L = \begin{bmatrix} \mathbf{k}_{u1} & & \\ & \mathbf{k}_{v1} & \\ & & \mathbf{k}_{w1} \end{bmatrix} \begin{Bmatrix} \mathbf{U}_L \\ \mathbf{V}_L \\ \mathbf{W}_L \end{Bmatrix}, \tag{3.35a}$$

$$\mathbf{k}_{q1} = \left(k_{q1} R_L \int_{z_0}^{z_f} \boldsymbol{\Psi}_q^T \boldsymbol{\Psi}_q \, \mathrm{d}z \right) \mathrm{blkdiag}(2\pi\mathbf{I}_n, \pi\mathbf{I}_n, \pi\mathbf{I}_n, \ldots, \pi\mathbf{I}_n), \tag{3.35b}$$

$$\mathbf{U}_L^T = \{\mathbf{U}_0^T \ \mathbf{U}_{1c}^T \ \mathbf{U}_{1s}^T \ \ldots \ \mathbf{U}_{nc}^T \ \mathbf{U}_{ns}^T\}, \tag{3.35c}$$

where the subscript $q = u, v, w$, and $\mathbf{U}_{nc}, \mathbf{U}_{ns}$ are the radial Fourier harmonic coefficients of the LP body nodes. The vectors $\mathbf{V}_L$ and $\mathbf{W}_L$ are similar to Eq. (3.35c). The size of the identity matrix $\mathbf{I}_n$ is $n \times n$, where n is the number of LP system nodes. Only the matrix components of the LP shaft nodes between coordinates (R_L, z_0) and (R_L, z_f) are non-zero in $\mathbf{K}_1$ matrix.

Bearing 2 (B_2) in Fig. 3.8 couples the HP shaft to the inner surface of the casing using surface constraints in Eqs. (3.17) and (3.18), and a bearing stiffness matrix. The axisymmetric bearing spans axially from $z_1 = 148$mm to $z_h = 158$mm. The constraint Eq. (3.18) constrains the HP shaft cross-sectional nodes between z_1 and z_h to the reference node O_{H2} and Eq. (3.17) constrains the casing nodes to O_{S2}. The reference nodes are located on the rotation axis. An isotropic bearing stiffness matrix $\mathbf{k}_{B2} = k_{b2}\,\mathrm{diag}(1, 1, 1, 10^{-3}, 10^{-3}, 10^{-4})$ couples the reference nodes O_{H2} and O_{S2}. Only the zeroth and first Fourier harmonic components of the HP shaft are non-zero in Eq. (3.18) because of the orthogonality of the trigonometric functions. The surface constraints and the bearing stiffness matrix gives the bearing B_2 stiffness matrix component as $(\mathbf{S} + \mathbf{K}_2)\mathbf{q}$ from Eq. (3.22).

Bearing B_4 couples the LP shaft to the casing via two space-fixed, discrete stiffnesses as shown in Fig. 3.8(a). The stiffnesses are located at the same LP shaft cross-sectional node $(r_4, z_4) = (12.5, 580)$mm and at different circumferential locations $\beta_{1-2} = \frac{\pi}{2}, \frac{3\pi}{2}$ with respect to the $\mathbf{E}_x$ axis. The other ends of the stiffnesses are at $(x_4, y_4, z_4) = (0, \pm 114, 580)$mm. The discrete stiffnesses have radial and tangential components k_{r4} and k_{t4}. The strain energy in the discrete stiffnesses is

$$\begin{aligned}\Pi_4 = \tfrac{1}{2}\sum_{j=1}^{2} \big[&k_{r4}\left(u_L(r_4, z_4, \beta_j) - \zeta_j(x_4, y_4, z_4)\cos\beta_j - \eta_j(x_4, y_4, z_4)\sin\beta_j\right)^2 + \\ &k_{t4}\left(v_L(r_4, z_4, \beta_j) + \zeta_j(x_4, y_4, z_4)\sin\beta_j - \eta_j(x_4, y_4, z_4)\cos\beta_j\right)^2\big]\,, \end{aligned} \tag{3.36}$$

where $u_L(r_4, z_4, \beta)$ and $v_L(r_4, z_4, \beta)$ are the radial and tangential LP shaft displacements from Eq. (3.4), and $\zeta(x_4, y_4, z_4)$ and $\eta(x_4, y_4, z_4)$ are the casing finite element displacements. Substituting the displacement fields into the strain energy Eq. (3.36) and applying variation

with respect to the nodal degrees of freedom results in the stiffness matrix of bearing B_4 as

$$\mathbf{K}_4\mathbf{q}_4 = \begin{bmatrix} \mathbf{k}_{Lr} & \mathbf{0} & -\mathbf{k}_{r1} & -\mathbf{k}_{r2} \\ & \mathbf{k}_{Lt} & -\mathbf{k}_{t1} & -\mathbf{k}_{t2} \\ & & \mathbf{k}_{S1} & \mathbf{0} \\ & \text{symmetric} & & \mathbf{k}_{S2} \end{bmatrix} \begin{Bmatrix} \mathbf{U}_{L4} \\ \mathbf{V}_{L4} \\ \mathbf{q}_{S1} \\ \mathbf{q}_{S2} \end{Bmatrix}, \tag{3.37a}$$

$$\mathbf{k}_{Lr} = k_{r4}\sum_{j=1}^{2}\mathbf{P}_{rj}^T\mathbf{P}_{rj}, \quad \mathbf{k}_{Lt} = k_{t4}\sum_{j=1}^{2}\mathbf{P}_{tj}^T\mathbf{P}_{tj},$$

$$\mathbf{k}_{rj} = k_{r4}\mathbf{P}_{rj}^T\mathbf{P}_{uj}, \quad \mathbf{k}_{tj} = k_{t4}\mathbf{P}_{tj}^T\mathbf{P}_{vj}, \quad \mathbf{k}_{Sj} = (k_{r4}\mathbf{P}_{uj}^T\mathbf{P}_{uj} + k_{t4}\mathbf{P}_{vj}^T\mathbf{P}_{vj}), \quad j = 1, 2 \tag{3.37b}$$

$$\mathbf{P}_{rj} = \{1 \;\; \cos\beta_j \;\; \sin\beta_j \;\; ... \;\; \cos n\beta_j \;\; \sin n\beta_j\},$$

$$\mathbf{P}_{tj} = \{1 \;\; -\sin\beta_j \;\; \cos\beta_j \;\; ... \;\; -\sin n\beta_j \;\; \cos n\beta_j\},$$

$$\mathbf{P}_{uj} = \{\cos\beta_j \;\; \sin\beta_j \;\; 0\}, \quad \mathbf{P}_{vj} = \{-\sin\beta_j \;\; \cos\beta_j \;\; 0\}, \tag{3.37c}$$

$$\mathbf{U}_{L4} = \{U_0 \; U_{1c} \; U_{1s} \; ... \; U_{nc} \; U_{ns}\}, \quad \mathbf{V}_{L4} = \{V_0 \; V_{1s} \; V_{1c} \; ... \; V_{ns} \; V_{nc}\}, \quad \mathbf{q}_{Sj} = \{\boldsymbol{\zeta}^j \; \boldsymbol{\eta}^j \; \boldsymbol{\xi}^j\}, \tag{3.37d}$$

where $\mathbf{U}_{L4}$ and $\mathbf{V}_{L4}$ are the Fourier harmonics of the single LP shaft node connected to the discrete stiffnesses. The Fourier harmonics of the LP shaft node are coupled in $\mathbf{k}_{Lr}$ and

$\mathbf{k}_{Lt}$ in Eq. (3.37a) because of vectors in Eq. (3.37c). The non-diagonal terms of $\mathbf{K}_4$ in Eq. (3.37a) couple the rotating and stationary casing degrees of freedom.

A radial, time-varying stiffness $k_3(t)$ models the intershaft bearing B_3 between the LP and HP shafts. Time-varying stiffness captures the changing number of rolling elements in contact with the bearing races. The space-fixed stiffness connects the LP shaft node (R_L, β_3, z_3) and HP shaft node (R_H, β_3, z_3), where $R_L = 12.5$mm, $R_H = 15$mm, $\beta_3 = 3\pi/2$, and $z_3 = 444$mm. The deformation in the intershaft stiffness is

$$\boldsymbol{\delta}_3 = \left[u_H(R_H, z_3, \beta_3) - u_L(R_L, z_3, \beta_3)\right] \mathbf{E}_r. \tag{3.38}$$

Substituting the displacement field Eq. (3.4) into deformation $\boldsymbol{\delta}_3$ and strain energy Eq. (3.7) and applying variation with respect to the Fourier nodal coefficients results in the stiffness matrix component of bearing B_3 as

$$\mathbf{K}_3\mathbf{q}_3 = k_3(t) \begin{bmatrix} \mathbf{k}_{L3} & -\mathbf{k}_{L3} \\ -\mathbf{k}_{L3}^T & \mathbf{k}_{L3} \end{bmatrix} \begin{Bmatrix} \mathbf{U}_L \\ \mathbf{U}_H \end{Bmatrix}, \quad \mathbf{k}_{L3} = \mathbf{P}_r^T \mathbf{P}_r \tag{3.39}$$

where $\mathbf{U}_L$ and $\mathbf{U}_H$ are the radial Fourier harmonic degrees of freedom of the LP and HP shaft nodes, respectively. The vector $\mathbf{P}_r$ is similar in form to $\mathbf{P}_{rj}$ in Eq. (3.37c).

The stiffness matrix components of the elastic foundation bearing B_1, constraint bearing B_2, intershaft, time-varying stiffness B_3, and discrete stiffnesses B_4 from Eqs. (3.35), (3.22), (3.39), and (3.36) are assembled into a coupling stiffness matrix $\mathbf{K}_B(t)$. The constraint bearing B_2 results in additional reference node ($\mathbf{O}_{S2}$ and $\mathbf{O}_{H2}$) degrees of freedom and Lagrange multipliers as described in Eq. (3.22).

Assembling the equations of motion of the rotating bodies, stationary casing, and

the coupling matrix, the full dual rotor-casing system equation of motion is obtained as

$$\mathbf{M}\ddot{\mathbf{q}} + \mathbf{G}\dot{\mathbf{q}} + (\mathbf{K} + \mathbf{K}_B(t) - \mathbf{C})\mathbf{q} + \mathbf{K}_p\mathbf{q} = \mathbf{F}(t), \tag{3.40a}$$

$$\mathbf{q} = \{\mathbf{q}_L, \mathbf{q}_H, \mathbf{q}_S, \mathbf{Q}_{H2}, \mathbf{Q}_{S2}, \mathbf{\Lambda}_{H2}, \mathbf{\Lambda}_{S2}\}, \tag{3.40b}$$

where $\mathbf{M}$, $\mathbf{G}$, $\mathbf{K}$, $\mathbf{C}$, and $\mathbf{K}_p$ are the mass, gyroscopic, elastic stiffness, centripetal, and prestress stiffness matrices, respectively. The matrices $\mathbf{M}$, $\mathbf{G}$, $\mathbf{K}$, $\mathbf{C}$, and $\mathbf{K}_p$ are similar to those in Eq. (3.25). $\mathbf{F}(t)$ are the external forces.

The matrices $\mathbf{M}$, $\mathbf{G}$, $\mathbf{K}$, $\mathbf{C}$, and $\mathbf{K}_p$ are decoupled between different bodies. The mass matrix $\mathbf{M}$ is of the form

$$\mathbf{M} = \text{blkdiag}(\mathbf{M}_L, \mathbf{M}_H, \mathbf{M}_S, \mathbf{0}, \mathbf{0}, \mathbf{0}, \mathbf{0}), \tag{3.41}$$

where $\mathbf{M}_L$ and $\mathbf{M}_H$ are the LP and HP rotating body mass matrices from Eq. (3.5), and $\mathbf{M}_S$ is the stationary casing mass matrix from Eq. (3.6). The $\mathbf{G}$, $\mathbf{K}$, $\mathbf{C}$, and $\mathbf{K}_p$ matrices are similar in form to Eq. (3.41).

The non-zero components in the gyroscopic $\mathbf{G}$ and centripetal $\mathbf{C}$ matrices correspond only to the rotating body degrees of freedom $\mathbf{q}_L$ and $\mathbf{q}_H$ and are obtained from Eq. (3.5).

The bearing stiffness term assembled from Eqs. (3.35), (3.22), (3.37a), and (3.39)

is

$$\mathbf{K}_B(t)\mathbf{q} = \begin{pmatrix} \mathbf{K}_1+\mathbf{K}_{L3}+\mathbf{K}_{L4} & -\mathbf{K}_{L3} & -\mathbf{K}_{LS4} & \mathbf{0} & \mathbf{0} & \mathbf{0} & \mathbf{0} \\ & \mathbf{K}_{L3} & \mathbf{0} & \mathbf{0} & \mathbf{0} & \mathbf{H}_{H2}^T & \mathbf{0} \\ & & -\mathbf{K}_{S4} & \mathbf{0} & \mathbf{0} & \mathbf{0} & \mathbf{H}_{S2}^T \\ & & & \mathbf{k}_{B2} & -\mathbf{k}_{B2} & -\mathbf{I}_6 & \mathbf{0} \\ & \text{symmetric} & & & \mathbf{k}_{B2} & \mathbf{0} & -\mathbf{I}_6 \\ & & & & & \mathbf{0} & \mathbf{0} \\ & & & & & & \mathbf{0} \end{pmatrix} \begin{Bmatrix} \mathbf{q}_L \\ \mathbf{q}_H \\ \mathbf{q}_S \\ \mathbf{Q}_{H2} \\ \mathbf{Q}_{S2} \\ \mathbf{\Lambda}_{H2} \\ \mathbf{\Lambda}_{S2} \end{Bmatrix}, \tag{3.42}$$

where $\mathbf{k}_{B2}$ is the bearing B_2 stiffness matrix component, and $\mathbf{H}_{H2}$ and $\mathbf{H}_{S2}$ are the surface constraint relation matrices. The intershaft time-varying stiffness component is $\mathbf{K}_{L3}$. The matrices $\mathbf{K}_{i4}$, where $i = L, S, LS$, are the components of the discrete stiffnesses of bearing B_4 from Eq. (3.37a). The bearing stiffness matrix $\mathbf{K}_B(t)$ is symmetric.

Static condensation [41, 42] eliminates the reference node degrees of freedom ($\mathbf{Q}_{H2}$, $\mathbf{Q}_{S2}$) and the corresponding Lagrange multipliers ($\mathbf{\Lambda}_{H2}$ and $\mathbf{\Lambda}_{S2}$). Only the rotating and stationary body degrees of freedom $\mathbf{q}_L$, $\mathbf{q}_H$, and $\mathbf{q}_S$ are retained.

Table 3.2: Parameters of the dual rotor-casing system

Elastic foundation B_1 stiffness, k_{u1}, k_{v1}, k_{w1} (N/m^3)	6.67×10^8
Bearing B_2 stiffness, k_{b2} (N/m) or (Nm/rad)	2×10^7
Intershaft bearing B_3: Average stiffness, k_{a3} (N/m)	11.67×10^5
Intershaft bearing B_3: Peak-to-peak stiffness, k_{p3} (N/m)	3×10^5
Intershaft bearing B_3: Frequency relation	$\hat{f}_m = 30\hat{\Omega}_L$
Discrete bearing B_4 stiffness, k_{r4}, k_{t4} (N/m)	2.6×10^6
Ratio of rotation speeds, Ω_L/Ω_H	1.5

The eigenvalue problem of the dual-rotor casing system Eq. (3.40a) obtained is similar to Eq. (3.26).

Fig. 3.9 shows the effects of the flexible, stationary casing on the eigenvalues of

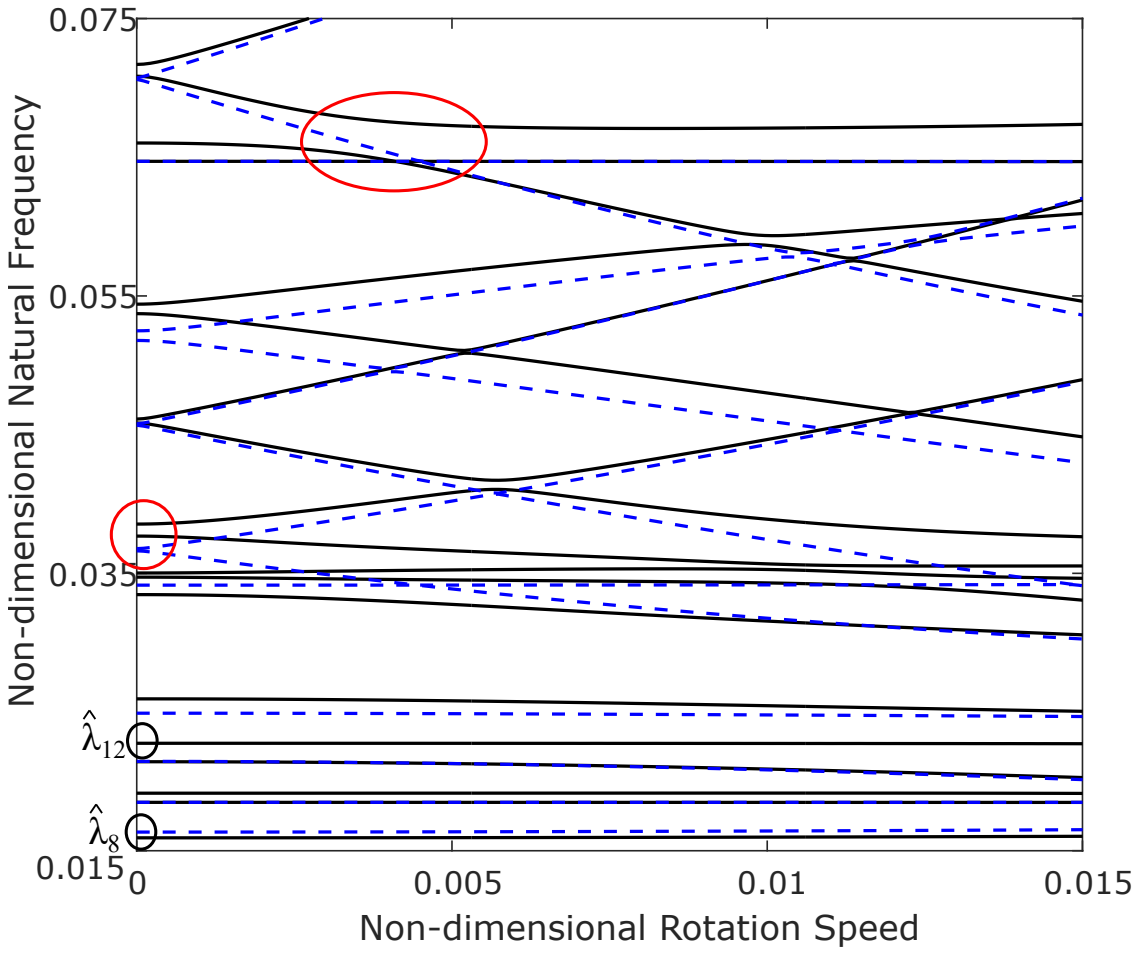

Figure 3.9: Non-dimensional natural frequencies $\hat{\lambda} = \lambda R_d \sqrt{\rho(1-\nu^2)/E}$ of the dual rotor-casing system (solid lines) compared to dual rotor-casing system with a non-vibrating casing (dashed lines). Fig. 3.8 and Table 3.2 show the dimensions and stiffness parameters of the system.

the dual rotor system. The bearing parameters are shown in Table 3.2. The eigenvalues of the complete dual rotor-casing system (solid lines) differ significantly to the eigenvalues of the dual rotors with non-vibrating stationary casing (dashed lines). Degenerate eigenvalues of the dual rotor-only system at $\hat{\lambda} = 0.037$ and $\hat{\lambda} = 0.071$ in Fig. 3.9 split into distinct eigenvalues on inclusion of the stationary casing.

Lower eigenvalues are sensitive to the coupling between different bodies and thus show major changes on the inclusion of casing in the system. The higher frequencies of the system (not shown in Fig. 3.9) are associated with individual bodies and compare well with the uncoupled body natural frequencies.

The asymmetric coupling components couple the Fourier harmonics of the rotating bodies. Thus, vibration modes of the system consist of multiple Fourier harmonic components. When the eigenvalue loci of two modes with common Fourier coefficients approach each other, veering occurs. Some eigenvalue loci that cross without veering on excluding the casing, show veering on inclusion of the casing, for example, the veering region near speed $\hat{\Omega} = 0.004$ marked with a red circle in Fig. 3.9. A flexible, stationary body changes the vibration modes of the system.

The time-varying intershaft bearing stiffness is $k_3(t) = k_{a3} + k_{p3} \tanh(f_m t)$. It acts as a parametric excitation with frequency f_m in the system. k_{a3} and k_{p3} are the average and peak-to-peak values of the stiffness over a contact cycle. The excitation frequency is non-dimensionalized as $\hat{f}_m = f_m R_d \sqrt{\rho(1-\nu^2)/E}$.

The equation of motion Eq. (3.40a) is solved using the Newmark method for the dynamics of the system. Fig. 3.10 shows the non-dimensional radial displacement at the LP shaft node (R_L, z_3) for a range of non-dimensional excitation frequencies $\hat{f}_m$. Resonance is observed at the bearing excitation frequencies $\hat{f}_{m1} = 0.032$, $\hat{f}_{m2} = 0.037$, and $\hat{f}_{m3} = 0.042$.

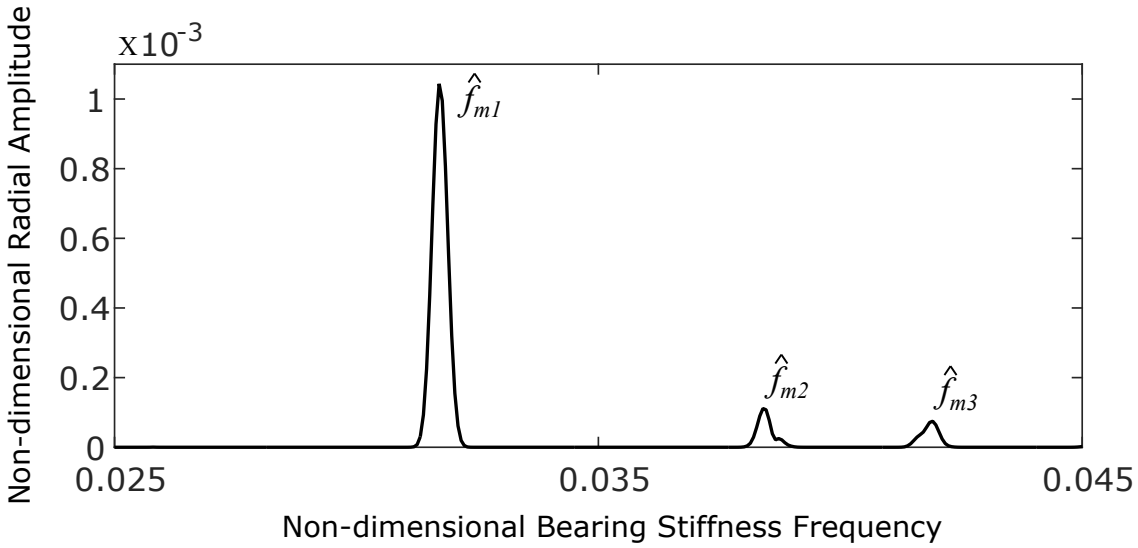

Figure 3.10: Non-dimensional radial displacement amplitude at LP shaft node $(R_L, 3\pi/2, z_3)$ with non-dimensional excitation frequency of the intershaft bearing $\hat{f}_m$.

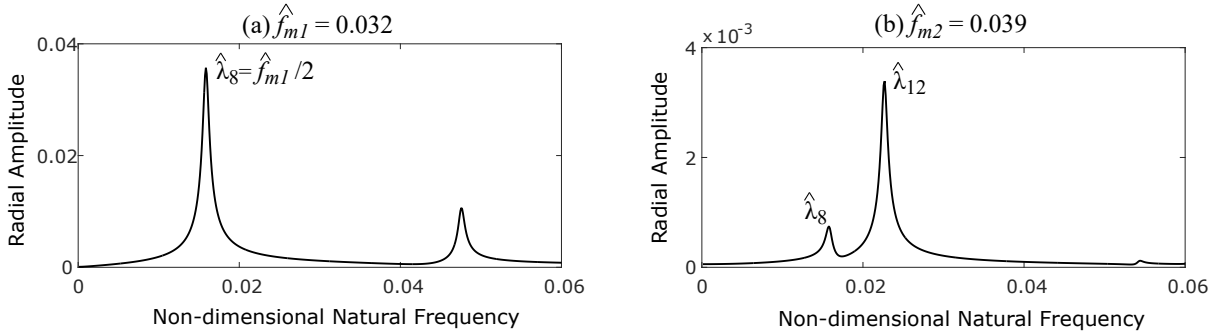

Figure 3.11: Non-dimensional radial displacement amplitude at LP shaft node $(R_L, 3\pi/2, Z_3)$ at the intershaft bearing frequencies of (a) $\hat{f}_{m1} = 0.032$ and (b) $\hat{f}_{m2} = 0.037$, obtained from Fig. 3.10.

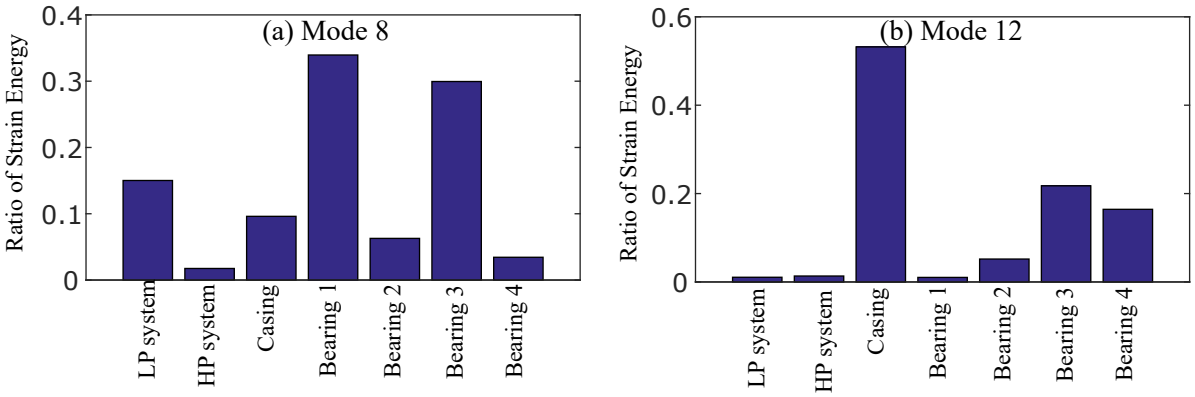

Figure 3.12: Ratio of strain energy in each component to the total strain energy in the system for (a) mode 8 ($\hat{\lambda}_8$)and (b) mode 12 ($\hat{\lambda}_{12}$) of the dual rotor-casing system in Fig. 3.9.

Parametric resonance occurs when the system is excited by a time varying parameter, for example, the intershaft bearing stiffness $k_3(t)$. The dual rotor system is parametrically excited at the intershaft bearing stiffness frequency $\hat{f}_m$. A combination parametric resonance occurs when the sum of two natural frequencies equals the excitation frequency. Fig. 3.11 shows the system response at the two resonant frequencies $\hat{f}_{m1} = 0.032$ and $\hat{f}_{m2} = 0.037$ in Fig. 3.10. At $\hat{f}_{m1}$ in Fig. 3.11(a), the amplitudes are larger at the eighth natural frequency ($\hat{\lambda}_8$), where $\hat{f}_{m1} = 2\hat{\lambda}_8$. Fig. 3.11(b) shows that the eighth and twelfth natural frequencies experience parametric resonance at $\hat{f}_{m2}$ with $\hat{f}_{m2} = \hat{\lambda}_8 + \hat{\lambda}_{12}$. The amplitude of resonance is larger at the two natural frequencies as compared to the amplitude at the excitation frequency.

Vibration modes with significant intershaft bearing strain energy are more likely to experience parametric resonance. Fig. 3.12 shows the distribution of strain energies in all the components for the eighth and twelfth modes. The strain energy in the intershaft bearing (Bearing 3) for modes 8 and 12 are 30% and 22%, respectively, of the total strain energy of the system. The thirteenth mode has 20% bearing 3 strain energy. Parametric resonance is also observed at $\hat{f}_{m3} = 0.042$ in Fig. 3.10 where $\hat{f}_{m3} = \hat{\lambda}_8 + \hat{\lambda}_{13}$.

A rotating stiffness can be included to model a rolling element bearing [14, 17]. These rotating stiffnesses introduce time-dependence in the displacement fields with θ varying as $\theta = \theta_0 + \Omega t$. A rotating intershaft bearing will result in time-varying $\mathbf{k}_{L3}$ component in Eq. (3.39).

The stiffness model can be extended to include nonlinear effects (results not shown). For example, when relative displacement of the rolling elements exceed a specified clearance, bearing forces are generated. This occurrence of bearing forces introduces nonlinearity in the bearing stiffness. The nonlinear stiffness of the rolling element [14, 17] depends on the deformation (δ_3) as

$$k_3^N(\mathbf{q}, t) = H(\delta_3(\mathbf{q}))k_3(f_m t), \tag{3.43a}$$

$$\delta_3 = (u_{Hj}(R_H, Z_H, \theta_j) - u_{Lj}(R_L, Z_L, \theta_j)), \tag{3.43b}$$

$$\theta_j = \Omega_c t + \frac{2\pi}{N_b}(j-1), \quad \Omega_c = \frac{\Omega_L R_L + \Omega_H R_H}{R_L + R_H}, \quad H(\delta_3) = \begin{cases} 1, & \text{if } \delta_3 > \delta_0; \\ 0, & \text{if } \delta_3 < \delta_0, \end{cases} \tag{3.43c}$$

where N_b is the total number of rolling elements and δ_0 is the bearing clearance.

Blade-casing rub is a major source of vibration in the dual rotor systems [151, 156]. Nonlinear discrete stiffnesses in Eq. (3.43) can model the blade-casing rub between rotor disks and the casing.

3.5 Conclusions

Discrete stiffness-damper elements, elastic foundations, and constraint equations model the bearings, splines, couplings, fluid media, rigid constraints, and other components that couple rotating and stationary bodies to an axisymmetric, rotating body in a system. The space-fixed formulation of the flexible, axisymmetric, rotating body allows for space-fixed, axisymmetric or asymmetric elements to couple with the rotating body. The space-fixed couplings result in constant coefficient equations of motion of the system that simplify further mathematical analysis. The coupling elements can nonlinearly depend on the spatial coordinates, displacements, and can vary in time.

An asymmetric elastic foundation and non-conservative friction force couples the brake disk to a stationary, rigid brake pad. A change in the friction coefficient results in the splitting of the real part of closely-spaced eigenvalues, resulting in the squeal onset.

The coupling elements model bearings in a dual rotor-casing to couple two rotating bodies and a stationary body. The flexible, stationary casing alters the low frequencies of the dual rotor system and increases the Fourier harmonic coupling in the modes, resulting in higher number of broad veering regions. A parametrically excited system because of a time-varying intershaft coupling results in parametric resonances of vibration modes with high intershaft coupling strain energy. The models developed allow one to analyze the dynamics of complex, linear/nonlinear, constant/parametric, coupled systems that involve rotating bodies with fewer degrees of freedom for the bodies, as compared to conventional three-dimensional finite element models.

Chapter 4

A semi-analytical finite element model and modal properties of rotationally periodic systems with flexible, vibrating components

4.1 Introduction

Rotationally periodic systems, such as planetary/epicyclic gears, bearings, and harmonic drives are widely used in automobiles, aircraft engines, helicopters, and other industrial applications. To reduce weight, these systems are made light-weight and more flexible. The flexibility of the components increases the elastic deformations in the components. Lumped parameter models do not capture the flexibility of the components. A finite element/contact mechanics model [146] for planetary gears and bearings considers all components deformable, but the dynamic analysis using this tool is computationally expensive. In this work, we develop a semi-analytical model for rotationally periodic systems with vibrating central components and substructures. Application of this model is exhibited for planetary gears.

Lumped-parameter models [11, 31, 68, 90, 92] were widely used to study modal characteristics, quasi-static and dynamic behavior of planetary gears. Hidaka et al. [52, 53] observed the ring gear elastic deformation in a planetary gear, resulting in subsequent models for planetary gears with an elastic model of the ring. Abousleiman and Velex [1] developed a three-dimensional lumped-parameter planetary gear with finite element model for the deformable ring gear. Abousleiman et al. [2] extended the model to include a finite element carrier. Wu and Parker [155] established an analytical elastic-discrete planetary gear model with discrete sun, planet, and carrier and an elastic ring. Wang and Parker [147] developed an analytical planetary gear model with an elastic ring that includes bending, extensional, and shear deformations.

A finite element/contact mechanics (FE/CM) model [146] uses finite element models of gears and bearings. This model has been widely used for gear and bearing research. Parker et al. [112] analyzed the dynamic response of planetary gears using the FE/CM model. Kahraman et al. [72] investigated the dynamic effects of a planetary gear with thin rims using the FE/CM model. Ambarisha and Parker [5] used a lumped parameter model and the FE/CM model to study planetary gear systems with tooth contact loss and periodically varying mesh stiffness. The FE/CM model neglects the gyroscopic effects that are important for compliant gears at high-speeds. The model in this work includes the rotational gyroscopic, centripetal, and prestress effects that are important for better system dynamics. The semi-analytical developed model is computationally efficient for dynamic analysis, as compared to the FE/CM model.

Rotationally periodic systems with equally spaced substructures (cyclic symmetric systems) possess structured modal properties. Olson [104] described the fundamental modal structure of cyclic symmetric bodies. Shi and Parker [128] categorized the modal properties of planar cyclic symmetric systems into translational, rotational, and substructure modes.

Lin and Parker [90] described the translational, rotational, and planet modes for planar spur planetary gears using a three degree of freedom lumped model for each component. Ericson and Parker [34] experimentally validated the modal structure for spur planetary gears. Kiracofe and Parker [81] extended the lumped-parameter single planetary gear model to compound planetary gears and proved that all modes can be classified into one of the same three categories. Cooley and Parker [27] proved the modal structure is retained for high-speed planetary gears with gyroscopic effects. Wu and Parker [155] verified the modal structure persists for an elastic-discrete planetary gear model with elastic continuum ring gear and lumped sun gear, planets, and carrier. In addition to the three known categories of translational, rotational, and substructure modes, they identified pure ring modes for the stationary system. Wang and Parker [148] investigated the modal properties of the elastic-discrete spur planetary gear model with gyroscopic effects. They proved that the stationary pure ring modes transition to either rotational or substructure modes on inclusion of gyroscopic effects. All complex-valued, traveling modes of cyclic symmetric systems with gyroscopic effects exhibit characteristics of rotational, translational, or substructure (planet) modes.

The structured modal characteristics are preserved for three-dimensional cyclic symmetric systems as well. Eritenel and Parker [37] mathematically proved and categorized the modes of three-dimensional, lumped-parameter helical planetary gears. All modes of the three-dimensional cyclic system exhibit characteristics of one of the three mode types: translational-tilting modes, rotational-axial modes, and substructure modes. Dong and Parker [33] obtained the modal characteristics of general three-dimensional cyclically symmetric systems with vibrating central components.

A semi-analytical finite element model for general rotationally periodic systems is developed in this work. The central components and substructures are considered ax-

isymmetric. The semi-analytical model by the authors in [144] models the axisymmetric components. One of the central components that supports the substructures is allowed to be non-axisymmetric. The model is developed in a rotating reference frame fixed to the non-axisymmetic or cyclically symmetric central component. The substructures are at fixed angular locations in the central component rotating reference frame. This leads to a constant coefficient equation of motion for the configuration. All components are allowed to rotate. Gyroscopic, centripetal, and prestress effects are included in the model. The structured modal characteristics of a cyclically symmetric system and a diametrically opposed system are validated with known literature.

4.2 Analytical Model

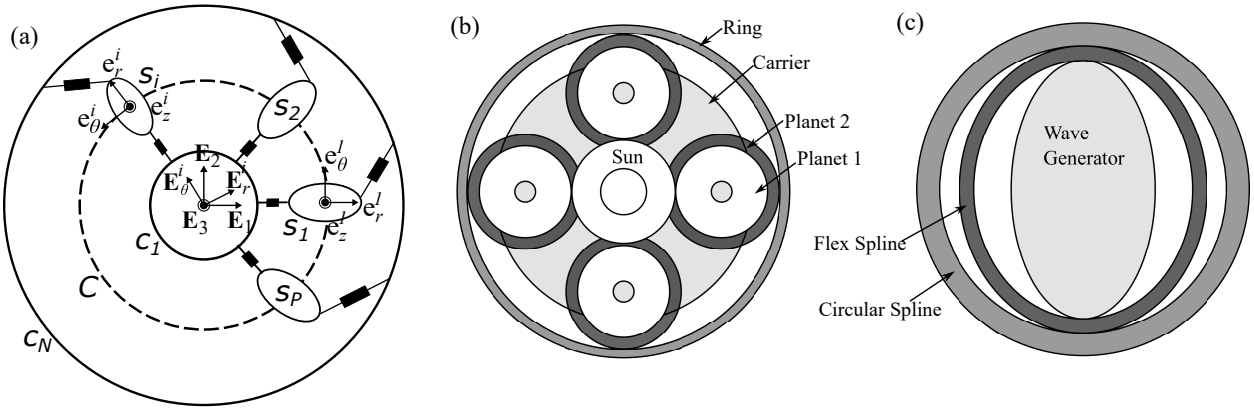

Figure 4.1: (a) A system with multiple rotating central components and substructures. The circles represent the central components, and the ovals are substructures. The central component shown in dashed lines supports the substructures. Solid rectangles are the couplings between the central components and the substructures. (b) Stepped planet compound planetary gear, (c) Harmonic drive/ strain wave generator.

The class of rotationally periodic systems considered in this chapter consists of N rotating, elastically deformable central components and P substructures. The substructures (shown as ovals) are supported on a central component C shown by a dashed circle in Fig.

4.1. This central component is not necessarily axisymmetric. For example, in a planetary gear system, the planet gears (substructures) are supported on a carrier (central component) that is usually cyclically symmetric.

The reference frame $\{\mathbf{E}_1, \mathbf{E}_2, \mathbf{E}_3\}$ in Fig. 4.1 is attached to the central component C. The basis $\mathbf{E}_3$ is oriented about the system axis of rotation. The reference frame $\{\mathbf{E}_1, \mathbf{E}_2, \mathbf{E}_3\}$ rotates at a constant speed Ω_C that is also the rotation speed of the substructures. The system model is derived in the $\{\mathbf{E}_1, \mathbf{E}_2, \mathbf{E}_3\}$ rotating reference frame.

All other central components (solid circles in Fig. 4.1) in the system are assumed to be axisymmetric. These central components are denoted by c_i, where $i = 1, ..., N-1$. The basis $\{\mathbf{E}_r^i, \mathbf{E}_\theta^i, \mathbf{E}_z^i\}$ is associated with the c_ith central component. These bases have a fixed angular orientation θ_i relative to the $\{\mathbf{E}_1, \mathbf{E}_2, \mathbf{E}_3\}$ reference frame. The angle θ_i does not define a material point on the c_ith central component. It defines a fixed angle relative to the reference frame rotating at Ω_c. The cross-section of material points on the c_ith central component that passes a fixed angular location θ_i changes with time as the c_ith body rotates with respect to the basis $\{\mathbf{E}_r^i, \mathbf{E}_\theta^i, \mathbf{E}_z^i\}$.

The central components rotate at speeds Ω_{c_i}. The speeds of different central components are related by kinematic relations. In planetary gears, for example, the kinematic relation between the rotation speeds of the three central components - sun gear (Ω_s), ring gear (Ω_r), and carrier (Ω_C) is

$$\Omega_s = \Omega_C - \frac{Z_r}{Z_s}(\Omega_r - \Omega_C) = \Omega_C - Z_{rs}\Omega_{rC}, \tag{4.1}$$

where Z_r and Z_s are the number of teeth on the ring and sun gears, respectively. The relative velocity of the ring gear with respect to the carrier-fixed reference frame that rotates at speed Ω_C is $\Omega_{rC} = \Omega_r - \Omega_C$.

The P substructures are supported on the central component C. These substructures are not necessarily equally spaced circumferentially. The system can have diametrically opposed or unequally spaced substructures [91, 110]. The substructures are at an angle ψ_i with respect to $\mathbf{E}_1$ in the counter-clockwise direction. Without loss of generality, the first substructure is at $\psi_1 = 0$. The reference frame $\{\mathbf{e}_r^i, \mathbf{e}_\theta^i, \mathbf{e}_z^i\}$ shown in Fig. 4.1 is associated with the ith substructure and at an angular orientation ψ_i with $\mathbf{E}_1$. The axis $\mathbf{e}_r^i$ is directed radially along the line connecting the center of the central component to the substructure center at angle ψ_i. The substructures rotate at Ω_{s_i} about their rotation axis $\mathbf{e}_z^i$. In planetary gears, the planet gear rotation speed is

$$\Omega_p = \Omega_C + \frac{Z_r}{Z_p}(\Omega_r - \Omega_C) = \Omega_C + Z_{rp}\Omega_{rC}, \tag{4.2}$$

where Z_p is the number of teeth in the planet gear.

The substructures are axisymmetric about their rotation axes. These axisymmetric substructures may not necessarily be identical. In compound planetary gears [81], for example, two sets of planet gears have distinct cross-sectional geometries. The axisymmetric substructures are connected to the central component C using rigid body constraint equations and stiffness elements. These substructures couple to other central components via coupling elements (solid rectangles in Fig. 4.1). The coupling elements are spatially fixed relative to the $\{\mathbf{E}_1, \mathbf{E}_2, \mathbf{E}_3\}$ rotating reference frame. The sun-planet and ring-planet mesh stiffnesses are examples of coupling elements in a planetary gear system that couple the planet gears (substructures) to the sun and ring gears (central components). In the carrier-fixed rotating frame, the locations of the mesh stiffnesses is spatially fixed.

The axisymmetric central components and substructures can have arbitrary two-dimensional geometry in the radial cross-section. The semi-analytical finite element method

with two-dimensional finite elements in the radial cross-section and Fourier series in the circumferential direction [144] models the axisymmetric components. The central component C that supports the substructures can have an arbitrary geometry. Conventional three-dimensional finite elements model this central component.

The material properties of the axisymmetric components is uniform in the circumferential direction, but they are allowed to vary in the cross-section. The density, modulus of elasticity, and Poisson's ratio are ρ_i, E_i, and ν_i, respectively for the ith component.

The elastic deflections of the central components are $u_i(r_i, \theta_i, z_i, t)$, $v_i(r_i, \theta_i, z_i, t)$, and $w_i(r_i, \theta_i, z_i, t)$ in their respective local reference frame $\{\mathbf{E}_r^i, \mathbf{E}_\theta^i, \mathbf{E}_z^i\}$. The elastic deflections of the substructures is $\zeta_i(r_i, \theta_i, z_i, t)$, $\eta_i(r_i, \theta_i, z_i, t)$, and $\xi_i(r_i, \theta_i, z_i, t)$ in the reference basis $\{\mathbf{e}_r^i, \mathbf{e}_\theta^i, \mathbf{e}_z^i\}$.

Energy expressions for the central components and the substructures are obtained in the rotating reference frame $\{\mathbf{E}_r^i, \mathbf{E}_\theta^i, \mathbf{E}_z^i\}$. Lagrange's equations are used to obtain the system equation of motion from the energy expressions.

4.2.1 Kinetic energy of the central components

The kinetic energy of the Cth and the c_ith central components is obtained in their respective reference frames that rotate at Ω_C with the reference frame $\{\mathbf{E}_1, \mathbf{E}_2, \mathbf{E}_3\}$.

The position vector of a cross-sectional material point on the central component c_i before deformation is $\mathbf{r}_o = r_i\mathbf{E}_r^i + z_i\mathbf{E}_z^i$. The deformed position vector of the point in the component basis $\{\mathbf{E}_r^i, \mathbf{E}_\theta^i, \mathbf{E}_z^i\}$ is

$$\mathbf{r}_i = (r_i + u_i(r_i, \theta_i, z_i, t))\mathbf{E}_r^i + v_i(r_i, \theta_i, z_i, t)\mathbf{E}_\theta^i + w_i(r_i, \theta_i, z_i, t)\mathbf{E}_z^i. \tag{4.3}$$

The velocity of a material point is obtained by the material time derivative of the position vector $\mathbf{r}_i$ that combines: (a) convective velocity because the angle θ_i associated with a material point changes with time, and (b) partial derivatives of elastic deflections with respect to time. As the component rotates with a relative speed $(\Omega_{c_i} - \Omega_C)$, the material point at a given θ_i changes with time as $\partial\theta_i/\partial t = (\Omega_{c_i} - \Omega_C) = \Omega_{c_iC}$. The material time derivatives of the deflection and the reference bases are

$$\frac{du_i}{dt} = \frac{\partial u_i}{\partial t} + \frac{\partial u_i}{\partial r_i}\frac{\partial r_i}{\partial t} + \frac{\partial u_i}{\partial \theta_i}\frac{\partial \theta_i}{\partial t} + \frac{\partial u_i}{\partial z_i}\frac{\partial z_i}{\partial t} = u_{i,t} + \Omega_{c_iC} u_{i,\theta_i}, \tag{4.4a}$$

$$\frac{d\mathbf{E}_r^i}{dt} = \frac{\partial \mathbf{E}_r^i}{\partial t} + \frac{\partial \mathbf{E}_r^i}{\partial \theta_i}\frac{\partial \theta_i}{\partial t} = \Omega_C \mathbf{E}_\theta^i + (\Omega_{c_i} - \Omega_C)\mathbf{E}_\theta^i = \Omega_{c_i}\mathbf{E}_\theta^i, \tag{4.4b}$$

$$\frac{d\mathbf{E}_\theta^i}{dt} = \frac{\partial \mathbf{E}_\theta^i}{\partial t} + \frac{\partial \mathbf{E}_\theta^i}{\partial \theta_i}\frac{\partial \theta_i}{\partial t} = -\Omega_C \mathbf{E}_r^i - (\Omega_{c_i} - \Omega_C)\mathbf{E}_r^i = -\Omega_{c_i}\mathbf{E}_r^i, \tag{4.4c}$$

$$\frac{d\mathbf{E}_z^i}{dt} = 0, \tag{4.4d}$$

where $(\cdot)_{,t}$ and $(\cdot)_{,\theta_i}$ are the partial derivatives with respect to time t and θ_i. The material point velocity from the material time derivative of $\mathbf{r}_i$ is

$$\begin{aligned}\dot{\mathbf{r}}_i = &\left[u_{i,t} + \Omega_{c_iC} u_{i,\theta_i} - \Omega_{c_i} v_i\right]\mathbf{E}_r^i + \left[v_{i,t} + \Omega_{c_iC} v_{i,\theta} + \Omega_{c_i}\left(r_i + u_i\right)\right]\mathbf{E}_\theta^i + \\ &\left[w_{i,t} + \Omega_{c_iC} w_{i,\theta}\right]\mathbf{E}_z^i.\end{aligned} \tag{4.5}$$

The kinetic energy of the central component with cross-sectional area A_i is

$$T_i = \frac{1}{2}\int_{A_i}\int_0^{2\pi} \rho_i \dot{\mathbf{r}}_i \cdot \dot{\mathbf{r}}_i \, r_i \, \mathrm{d}\theta_i \mathrm{d}A_i. \tag{4.6}$$

The relative velocity $\Omega_{c_iC} = 0$ in Eq. (4.5) for the central component C that rotates with speed Ω_C. The non-axisymmetric central component can be defined using three-dimensional Cartesian coordinates. The material velocity of the undeformed point $\mathbf{r}_o = x_c\mathbf{E}_1 + y_c\mathbf{E}_2 + z_c\mathbf{E}_3$ of the central component C in the Cartesian reference frame is

$$\dot{\mathbf{r}}_C = \left[u_{c,t} - \Omega_C(y_c + v_c)\right]\mathbf{E}_1 + \left[v_{c,t} + \Omega_C\left(x_c + u_c\right)\right]\mathbf{E}_2 + w_{c,t}\mathbf{E}_3, \tag{4.7}$$

where u_c, v_c, and w_c are the deflections along the $\{\mathbf{E}_1, \mathbf{E}_2, \mathbf{E}_3\}$ bases. The kinetic energy of the central component with volume V_C is

$$T_C = \frac{1}{2}\int_{V_C} \rho_C \dot{\mathbf{r}}_C \cdot \dot{\mathbf{r}}_C \mathrm{d}V_C. \tag{4.8}$$

4.2.2 Kinetic energy of the substructure

The undeformed position vector of a point on the jth substructure is $\mathbf{r}_o = R_{s_j}\mathbf{e}_r^j + r_j\mathbf{e}_r^j + z_j\mathbf{e}_z^j$, where R_{s_j} is the radial distance of the center of the substructure. In planetary gears, the distance $R_{s_j} = R_s + R_p$, where R_s and R_p are the radii of the sun gear and planet gear, respectively. The position vector of the deformed material point in the substructure basis vectors $\{\mathbf{e}_r^j, \mathbf{e}_\theta^j, \mathbf{e}_z^j\}$ is

$$\begin{aligned}\mathbf{r}_j = R_{s_j}\mathbf{e}_r^j + [r_j + \zeta_j(r_j, \theta_j, z_j, t)]\mathbf{e}_r^j + \eta_j(r_j, \theta_j, z_j, t)\mathbf{e}_\theta^j \\ + \left[z_j + \xi_j(r_j, \theta_j, z_j, t)\right]\mathbf{e}_z^j.\end{aligned} \tag{4.9}$$

The material time derivatives of the displacements and substructure base vectors

are similar to Eq. (4.4). The velocity of the point at an angle θ_j is

$$\dot{\mathbf{r}}_j = \left[\zeta_{j,t} + \Omega_{s_jC}\zeta_{j,\theta_j} - \Omega_{s_j}\eta_j\right]\mathbf{e}_r^j + \left[\eta_{j,t} + \Omega_{s_jC}\eta_{j,\theta} + \Omega_{s_j}\left(R_{s_j} + r_j + \zeta_j\right)\right]\mathbf{e}_\theta^j + \left[\xi_{j,t} + \Omega_{s_jC}\xi_{j,\theta_j}\right]\mathbf{e}_z^j. \tag{4.10}$$

The kinetic energy of the j^{th} substructure with radial cross-sectional area A_j obtained using Eq. (4.10) is

$$T_j = \frac{1}{2}\int_{A_j}\int_0^{2\pi} \rho_j \dot{\mathbf{r}}_j \cdot \dot{\mathbf{r}}_j r_j \mathrm{d}\theta_j \mathrm{d}A_j. \tag{4.11}$$

4.2.3 Strain energies of the central components and substructures

Strain energies of the axisymmetric central components and substructures are obtained from Green's nonlinear strain-displacement relations in the cylindrical basis vectors. Similarly, for a non-axisymmetric central component C, Cartesian basis vectors are used. The strains are expressed as a sum of the linear (L) and nonlinear (NL) terms as

$$\boldsymbol{\epsilon}_k = \{\epsilon_{rr}^k, \epsilon_{\theta\theta}^k, \epsilon_{zz}^k, \gamma_{r\theta}^k, \gamma_{\theta z}^k, \gamma_{rz}^k\}^{\mathrm{T}} = \boldsymbol{\epsilon}_k^{\mathrm{L}} + \boldsymbol{\epsilon}_k^{\mathrm{NL}}, \quad k = c_i, s_i \tag{4.12a}$$

$$\boldsymbol{\epsilon}_C = \{\epsilon_{xx}, \epsilon_{yy}, \epsilon_{zz}, \gamma_{xy}, \gamma_{yz}, \gamma_{xz}\}^{\mathrm{T}} = \boldsymbol{\epsilon}_C^{\mathrm{L}} + \boldsymbol{\epsilon}_C^{\mathrm{NL}}. \tag{4.12b}$$

The general, nonlinear strain-displacement relations [3] are

$$\epsilon_{ij} = \frac{\partial u_i}{\partial x_j} + \frac{\partial u_j}{\partial x_i} + \frac{1}{2}\frac{\partial u_k}{\partial x_i}\frac{\partial u_k}{\partial x_j}, \tag{4.13}$$

where u are the generalized displacements and x are the generalized coordinates. These are not similar to the notations used before to represent displacements and coordinates

of a particular component. The generalized displacements u for the central components and substructures are $\{u, v, w\}$ and $\{\zeta, \eta, \xi\}$, respectively. The generalized coordinates are $x = \{r, \theta, z\}$.

The stresses are obtained from the constitutive relation $\boldsymbol{\sigma} = \mathbf{D}\boldsymbol{\epsilon}$, where $\mathbf{D}$ is the elasticity tensor. The elastic strain energies of the axisymmetric components and the central component C are

$$\Pi_k = \frac{1}{2}\int_{A_k}\int_0^{2\pi} {\boldsymbol{\epsilon}_k}^{\mathrm{T}}\boldsymbol{\sigma}_k r_k \mathrm{d}\theta_k \mathrm{d}A_k, \quad \Pi_C = \frac{1}{2}\int_{V_C} {\boldsymbol{\epsilon}_C}^{\mathrm{T}}\boldsymbol{\sigma}_C \mathrm{d}V_C. \tag{4.14}$$

The nonlinear strain-displacement relations are necessary to obtain the prestress effects due to rotation-induced force, mean torque, and other external forces. The prestress effects are neglected further in the model to reduce complexity. The prestress effects are included by following [144]. In a highly flexible component and at high rotational speeds, the prestress effects become important and should be credited for giving more accurate results.

4.2.4 Discretization and component equations of motion

Axisymmetry of the central components and substructures allows for the semi-analytical finite element discretization of the components only in the radial cross-section. The radial cross-section of a component is divided into finite elements. Because of axisymmetry, the discretization remains same at any angular orientation θ_i of the component and thus, the local shape functions within the elements depend only on r_i and z_i.

The displacement fields are continuous in θ_i and 2π periodic. Thus, Fourier series approximate the θ-dependence of the displacement fields. The radial displacement field for

an axisymmetric component is

$$u_e(r_i, z_i, \theta_i, t) = \boldsymbol{\Psi}_u^{e\,T}(r_i, z_i) \left[\mathbf{U}_0^e(t) + \sum_{n=1}^{\infty} \left(\mathbf{U}_{nc}^e(t) \cos n\theta_i + \mathbf{U}_{ns}^e(t) \sin n\theta_i \right) \right], \tag{4.15}$$

where the vector $\boldsymbol{\Psi}_u^e(r_i, z_i)$ represents the shape functions for the radial displacement field within an element. The time-dependent coefficients $\mathbf{U}_{nc}^e(t)$, $\mathbf{U}_{ns}^e(t)$ are the nth Fourier harmonics of the displacements of the element, also referred to as n nodal diameter components of displacement. The tangential and axial displacement fields are approximated similar to Eq. (4.15).

In the present model, the displacements for all axisymmetric components are represented by Fourier series in the circumferential direction. The coefficients determine the contribution of a particular harmonic to the vibration mode. The zeroth and first harmonics of the displacement fields in Eq. (4.15) describe the rigid body motion of the body. The rigid body motion of the axisymmetric body are not separately included in the displacement fields. For an axisymmetric body, the six rigid body motions are related to the Fourier harmonics as

$$\begin{aligned}
x_r &= \tfrac{1}{2A} \int_A \left[\boldsymbol{\Psi}_u^T(r,z) \mathbf{U}_{1c} + \boldsymbol{\Psi}_v^T(r,z) \mathbf{V}_{1s} \right] \mathrm{d}A, \\
y_r &= \tfrac{1}{2A} \int_A \left[\boldsymbol{\Psi}_u^T(r,z) \mathbf{U}_{1s} + \boldsymbol{\Psi}_v^T(r,z) \mathbf{V}_{1c} \right] \mathrm{d}A, \\
z_r &= \tfrac{1}{A} \int_A \boldsymbol{\Psi}_w^T(r,z) \mathbf{W}_0 \mathrm{d}A, \quad \gamma_{xr} = \tfrac{1}{2A} \int_A \boldsymbol{\Psi}_w^T(r,z) \mathbf{W}_{1s} \mathrm{d}A, \\
\gamma_{yr} &= \tfrac{1}{2A} \int_A \boldsymbol{\Psi}_w^T(r,z) \mathbf{W}_{1c} \mathrm{d}A, \quad \gamma_{zr} = \tfrac{1}{2A} \int_A \boldsymbol{\Psi}_v^T(r,z) \mathbf{V}_0 \mathrm{d}A,
\end{aligned} \tag{4.16}$$

where $\{x_r, y_r, z_r, \gamma_{xr}, \gamma_{yr}, \gamma_{zr}\}$ are the six rigid body degrees of freedom of the body.

The displacement fields from Eq. (4.15) are substituted in the kinetic and strain en-

ergy Eqs. (4.6), (4.8), (4.11), and (4.14) of the components. Applying Lagrange's equations to the energy expressions, the equation of motion of the system is obtained as

$$\mathbf{M}\ddot{\mathbf{q}} + \mathbf{G}\dot{\mathbf{q}} + (\mathbf{K} - \mathbf{C})\mathbf{q} = \mathbf{T} + \mathbf{F}_{\Omega}, \tag{4.17a}$$

$$\mathbf{q} = \left\{ \mathbf{q}_{c_1} \quad ... \quad \mathbf{q}_{c_N} \quad \mathbf{q}_C \quad \mathbf{q}_{s_1} \quad ... \quad \mathbf{q}_{s_P} \right\}^T, \tag{4.17b}$$

$$\mathbf{M} = \mathrm{diag}(\mathbf{M}_{c_1}, ..., \mathbf{M}_{c_N}, \mathbf{M}_C, \mathbf{M}_{s_1}, ..., \mathbf{M}_{s_P}), \tag{4.17c}$$

where $\mathbf{q}_{c_i}$ and $\mathbf{q}_{s_j}$ are the unknown Fourier nodal coefficients for the c_ith central component and s_jth substructure. The vector $\mathbf{q}_C$ are the unknown nodal coefficients of the non-axisymmetric central component. The mass ($\mathbf{M}$), gyroscopic ($\mathbf{G}$), elastic stiffness ($\mathbf{K}$), and centripetal ($\mathbf{C}$) matrices are block diagonal and uncoupled between different elastic bodies in the system. The matrices $\mathbf{G}$, $\mathbf{K}$, and $\mathbf{C}$ have similar form as the mass matrix in Eq. (4.17c).

In systems with identical substructures, the substructure matrix components $\mathbf{M}_{s_j}$ in Eq. (4.17c) are identical. Similarly, the substructure matrix components in $\mathbf{G}$, $\mathbf{C}$, and $\mathbf{K}$ are also identical.

The gyroscopic matrix $\mathbf{G}_{c_i}$ for the c_ith central component is of the form $\mathbf{G}_{c_i} = \Omega_{c_i}\mathbf{G}^i_{c_i} + \Omega_{c_iC}\mathbf{G}^c_{c_i}$. Similarly, the other gyroscopic matrices consist of one part that multiplies with the rotation speed of the component and the other part that multiplies with the relative speed of the component with respect to speed Ω_C of the reference frame. Similarly, the centripetal matrix is a combination of three components given as $\mathbf{C}_{c_i} = \Omega^2_{c_i}\mathbf{C}^i_{c_i} + \Omega^2_{c_iC}\mathbf{C}^c_{c_i} + \Omega_{c_i}\Omega_{c_iC}\mathbf{C}^p_{c_i}$.

For each axisymmetric body, the Fourier harmonics are uncoupled because of orthogonality of the trigonometric functions. The coupling elements, discussed next, may break the axisymmetry of these components resulting in the Fourier harmonic coupling.

4.2.5 Substructure - central components coupling

The coupling between two central components is assumed to be axisymmetric. An asymmetric coupling between the central components that is spatially fixed with respect to the rotating reference frame $\{\mathbf{E}_1, \mathbf{E}_2, \mathbf{E}_3\}$ is allowed. This central component coupling results in constant coefficient equations of motion. An asymmetric coupling that rotates relative to the $\{\mathbf{E}_1, \mathbf{E}_2, \mathbf{E}_3\}$ reference frame would result in time-dependent coefficient equations of motion.

The coupling between the substructures and the central component C can be rigid or flexible. The flexible coupling can model the bearings that couple the planet gears (substructures) to the carrier (central component) in a planetary gear model. It can also model the coupling between the rolling elements (substructures) and the bearing cage.

Multipoint constraints and the stiffness matrix model developed in Chapter 3 models the bearings that couple the substructures to the central component C. Fig. 4.2 shows the schematic of the constraint coupling. The cross-sectional nodes of the s_jth axisymmetric substructure are constrained to the reference node O_{s_j} using constraint Eqs. (3.19). A multipoint constraint Eq. (3.17b) between multiple points on the central component surface (shown by dots) and the reference node O_C constrains the central component. A bearing stiffness matrix $\mathbf{K}_B$ between the two reference nodes models the bearing flexibility. These multipoint constraints and the stiffness matrix couple the degrees of freedom of the substructure ($\mathbf{q}_{s_j}$) to the degrees of freedom of the central component ($\mathbf{q}_C$).

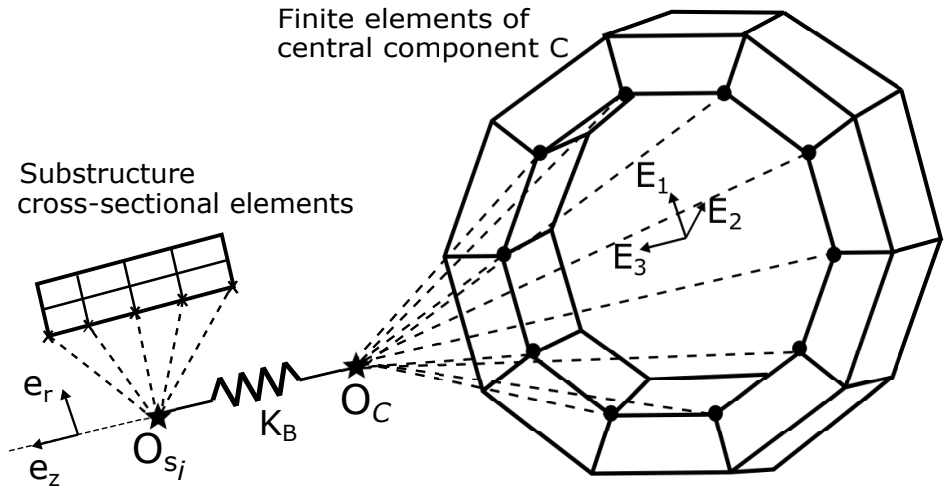

Figure 4.2: Multipoint constraint (dashed lines) between the central component C, substructure s_i and their respective reference nodes O_C and O_{s_i}. A bearing stiffness matrix $\mathbf{K}_B$ couples the reference nodes.

The substructures are coupled to the other central components using stiffness coupling elements. These coupling elements are spatially fixed in the rotating reference frame. The stiffness coupling elements can depend on time and nonlinearly on the displacement of the contact location.

In planetary gears, the mesh stiffness between the planet gear (substructures) and ring/sun gears (central components) models the coupling. The strain energies in the ring-planet ($k_{ri}(t)$) and sun-planet ($k_{si}(t)$) mesh stiffnesses in a helical planetary gear are

$$\Pi_{rp} = \sum_{j=1}^{P} \frac{1}{2} k_{rj}(t) \Delta_{rj}^2, \quad \Pi_{sp} = \sum_{j=1}^{P} \frac{1}{2} k_{sj}(t) \Delta_{sj}^2, \tag{4.18a}$$

$$\begin{aligned} \Delta_{rj} = &\left(u_r \sin\alpha_r + v_r \cos\alpha_r \cos\beta_r + w_r \cos\alpha_r \sin\beta_r\right)|_{\theta_r = \psi_j} \\ &- \left(\zeta_j \sin\alpha_r + \eta_j \cos\alpha_r \cos\beta_r - \xi_j \cos\alpha_r \sin\beta_r\right)|_{\theta_j = 0} \end{aligned} \tag{4.18b}$$

$$\Delta_{sj} = \left(u_s \sin\alpha_s + v_s \cos\alpha_s \cos\beta_s + w_s \cos\alpha_s \sin\beta_s\right)|_{\theta_s=\psi_j}$$
$$- \left(\zeta_j \sin\alpha_s + \eta_j \cos\alpha_s \cos\beta_s - \xi_j \cos\alpha_s \sin\beta_s\right)|_{\theta_j=\pi}, \tag{4.18c}$$

where $\{u_r, v_r, w_r\}$, $\{u_s, v_s, w_s\}$, and $\{\zeta_i, \eta_i, \xi_i\}$ are the displacements of the ring gear, sun gear, and jth planet gear, respectively. The pressure angles and helix angles are α_r, α_s and β_r, β_s, respectively. Δ_{rj} and Δ_{sj} are the deflections in the mesh stiffnesses along the line of contact. The time-varying mesh stiffness can capture the change in the number of teeth in contact between the gears. It can also capture mesh phasing [148] in mesh stiffnesses between a central component (ring/sun gear) and different planet gears.

The coupling between the central components and substructures is captured in the coupling stiffness matrix given as

$$\mathbf{K}_c = \begin{bmatrix} \mathbf{K}^c_{c_1c_1} & \dots & \mathbf{K}^c_{c_1c_N} & \mathbf{K}^c_{c_1C} & \mathbf{K}^c_{c_1s_1} & \dots & \mathbf{K}^c_{c_1s_P} \\ & \dots & & & & & \\ & & \mathbf{K}^c_{c_Nc_N} & \mathbf{K}^c_{c_NC} & \mathbf{K}^c_{c_Ns_1} & \dots & \mathbf{K}^c_{c_Ns_P} \\ & & & \mathbf{K}^c_{CC} & \mathbf{K}^c_{Cs_1} & \dots & \mathbf{K}^c_{Cs_P} \\ & & & & \mathbf{K}^c_{s_1s_1} & \dots & \mathbf{K}^c_{s_1s_P} \\ & & & & & \dots & \\ & & & & & & \mathbf{K}^c_{s_Ps_P} \end{bmatrix}, \tag{4.19}$$

where the coupling matrix components $\mathbf{K}^c_{c_is_j}$ and $\mathbf{K}^c_{c_iC}$ couples the substructures to the c_ith and Cth central components. The matrix components $\mathbf{K}^c_{c_ic_j}$ couple the central components and $\mathbf{K}^c_{s_is_j}$ couples the substructures in the system. In compound planetary gears, a set of planet gears can couple to another set of planet gears, leading to non-zero $\mathbf{K}^c_{s_is_j}$ matrix components.

4.2.6 System equation of motion

The component equations of motion in Eq. (4.17a) and the coupling matrix Eq. (4.19) result in the system equation of motion as

$$\mathbf{M}\ddot{\mathbf{q}} + \mathbf{G}\dot{\mathbf{q}} + (\mathbf{K} + \mathbf{K}_c - \mathbf{C})\mathbf{q} = \mathbf{T} + \mathbf{F}_\Omega. \tag{4.20}$$

The free eigenvalue problem from use of $\mathbf{q} = \boldsymbol{\chi} e^{\lambda t}$ in the system equation of motion Eq. (4.20) is

$$\lambda^2 \mathbf{M}\boldsymbol{\chi} + \lambda \mathbf{G}\boldsymbol{\chi} + (\mathbf{K} + \mathbf{K}_c - \mathbf{C})\boldsymbol{\chi} = \mathbf{0}. \tag{4.21}$$

Cyclically symmetric structures [33, 128] and rotationally periodic systems with unequally spaced substructures [91, 128] have structured modal characteristics. The modal characteristics of cyclically symmetric and rotationally periodic systems are validated using the model developed in Eq. (4.21).

4.3 Modal structure of cyclically symmetric systems

Planetary gears and bearings are examples of the commonly used cyclically symmetric systems. These systems have identical sets of substructures. A compound planetary gear can have multiple sets of substructures, but all substructures in a single set are identical. In planetary gears [27, 68, 90, 91, 148, 155], the identical planet gears (substructures) are equally spaced circumferentially. A cyclically symmetric carrier supports the identical planet gears. In roller/ ball bearings, the rollers/ balls are equally spaced circumferentially in the rotor cage. The inner and outer races are axisymmetric rings.

Cyclic symmetric bodies possess structured modal characteristics. Shi and Parker

[128] categorized the modal properties of general cyclically symmetric systems into translational modes, rotational modes, and substructure modes. The lumped parameter spur planetary gears [27, 90], elastic-discrete spur planetary gears [148, 155], and compound planetary gears [81] all show the structured modal characteristics of cyclic symmetric systems. Refs. [27, 148] proved the modal structure persists for cyclically symmetric spur planetary gears with gyroscopic effects. Three-dimensional cyclic symmetric systems [33, 37] follow the modal properties with the modes categorized as translational-tilting, rotational-axial, and substructure modes.

The modal characteristics of general cyclically symmetric systems [33] are preserved for systems with all flexible bodies. The numerical model in this study considers all bodies to be flexible. Most previous works on this problem obtained structured modal characteristics for systems with lumped mass central components and substructures. The modes of a cyclically symmetric system without gyroscopic effects are characterized into one of the four mode types: translational-tilting, rotational-axial, substructure, and pure component modes. Pure component modes are not a separate modal category in [33] because the pure component modes transition into a rotational-axial mode or a substructure mode with gyroscopic effects. In this case, a separate category of pure component modes is considered for stationary systems. With gyroscopic effects, the transition of pure component modes depends on the coupling models. For three-dimensional systems with coupling elements that couple the displacement degrees of freedom in all three directions, pure component modes transition into rotational-axial or substructure modes. In planar systems, for example, spur planetary gears, pure component modes with out-of-plane vibration are observed. These out-of-plane pure component modes remain pure component modes even with gyroscopic effects. Other rotational effects - centripetal effects and prestress due to rotation induced forces included in the present model change the natural frequency values but do not alter

the mode types.

The eigenvalue problem for a stationary system consists of a self-adjoint mass matrix $\mathbf{M}$ and stiffness matrix $(\mathbf{K}+\mathbf{K}_c)$. This eigenvalue problem results in real-valued vibration modes. All degrees of freedom of the system are either in-phase or 180 degree out-of-phase in a given mode. These modes are called as standing-wave modes. In case of a spinning system, a skew self-adjoint gyroscopic matrix $\mathbf{G}$ results in complex-valued vibration modes. The different degrees of freedom of the system vibrate out-of-phase with each other. The complex-valued eigenmodes result in traveling-wave vibration modes.

The following paragraphs summarizes the key modal properties for each expected mode type.

Rotational-axial modes. For this mode type, the central components have only rotation about the symmetry axis and axial translation. The rotation and axial translation correspond to the rigid body rotation γ_{zr} and translation z_r in Eq. (4.16). The zeroth harmonics of tangential and axial displacements $\mathbf{V}_0$ and $\mathbf{W}_0$ are present in the rotational-axial modes. In addition to the rigid body components, the central component deformations contain only $jN+0$, where $j = 0, \pm1, \pm2, ...$, nodal diameter components. The substructures have identical in-phase motion. The rotational-axial modes are also called type 0 modes.

Rotational-axial modes have distinct natural frequencies for stationary and rotating systems. The properties of the mode type remain the same for stationary and rotating systems, except that the vibration modes are real-valued standing wave modes for stationary systems and complex-valued traveling wave modes for spinning systems with gyroscopic effects.

A planar cyclically symmetric system, for example, a spur planetary gear [148, 155] has negligible axial deflection. Thus, the rotational-axial modes reduce to only rotational

modes.

Translational-tilting modes. The central components contain only in-plane translation and out-of-plane tilting. The in-plane translations and out-of-plane tilting of the rigid body motion of the central component corresponds to $\{x_r, y_r\}$ and $\{\gamma_{xr}, \gamma_{yr}\}$ in Eq. (4.16). The first harmonics of the in-plane displacements $\mathbf{U}_{1c}, \mathbf{U}_{1s}, \mathbf{V}_{1c}, \mathbf{V}_{1s}$ represent the in-plane translations. Similarly, the first harmonics $\mathbf{W}_{1c}$ and $\mathbf{W}_{1s}$ of the axial displacement represents the tilting motion of the vibration mode. In addition to the rigid body motion, the central component deformation contains $jN \pm 1$ nodal diameter components for the stationary system standing-wave modes. For a spinning system with gyroscopic effects, the traveling-wave translational-tilting modes are classified into type 1 modes and type $N-1$ modes. The modal deflections of the central components contain $jN+1$ and $jN-1$ nodal diameters for the type 1 and type $N-1$ traveling-wave mode natural frequencies, respectively. The translational-tilting modes for the stationary system cannot be classified into two sub-types.

The stationary natural frequencies are degenerate with a multiplicity of two for systems for $N \geq 3$. The translational-tilting mode natural frequencies split into two distinct natural frequencies for spinning systems with gyroscopic effects.

Substructure modes. No central components vibrate in a substructure mode. Substructure modes exist for systems with $N \geq 4$ substructures. The substructure modes for a stationary system with $N \geq 5$ are degenerate with multiplicity two. These degenerate mode natural frequencies split into distinct natural frequencies for non-zero rotation speeds. The central component deformation contains $jN \pm d$ nodal diameter components for a d-type standing wave mode, where $d \in \{2, 3, ..., \text{int}((N-1)/2)\}$. Stationary systems with even number of substructures have distinct substructure modes. Distinct substructure modes are associated with an integer $N/2$ and the central component deformation contains $jN +$

$N/2$ nodal diameter components. All substructure modes are distinct for rotating systems. Substructure modes with $(N-3)$ type associated with $d \in \{2, 3, ..., (N-2)\}$ exist for rotating, gyroscopic systems.

Pure component modes. Only one component of the system vibrates in a pure component mode. These pure component modes exist only in stationary systems. The pure component modes are distinct. A pure ring mode [148, 155] contains elastic deflection in the ring only. Pure central component modes are of two types: type 0 and type $N/2$. The type 0 mode contains only $jN + 0$ nodal diameters in the central component, whereas type $N/2$ mode contains only $jN + N/2$ nodal diameters. The type $N/2$ mode exists only for systems with even number of substructures. Spinning systems with gyroscopic effects lead to the transition of the standing-wave type 0 mode and $N/2$ mode into a traveling-wave rotational-axial mode and substructure mode, respectively.

A pure standing-wave substructure component mode has a multiplicity of N. Each pure substructure component mode is associated with a single substructure. The pure substructure component mode evolves into one of the first three mode types on including the gyroscopic effects.

In a planar system (for example, spur planetary gear), pure out-of-plane component modes are observed. Each mode contains a single nodal diameter component. No pattern is observed for these modes. The pure component modes for stationary planar systems remain pure component modes even with gyroscopic effects.

The natural frequencies, vibration modes, and observed mode types of a stationary, three-dimensional, four-planet spur planetary gear are verified with a full three-dimensional model in Nastran. The mode types of a rotating, three-dimensional, four-planet helical planetary gear are then validated with the expected modal structure.

4.3.1 Verification of the model with full three-dimensional model

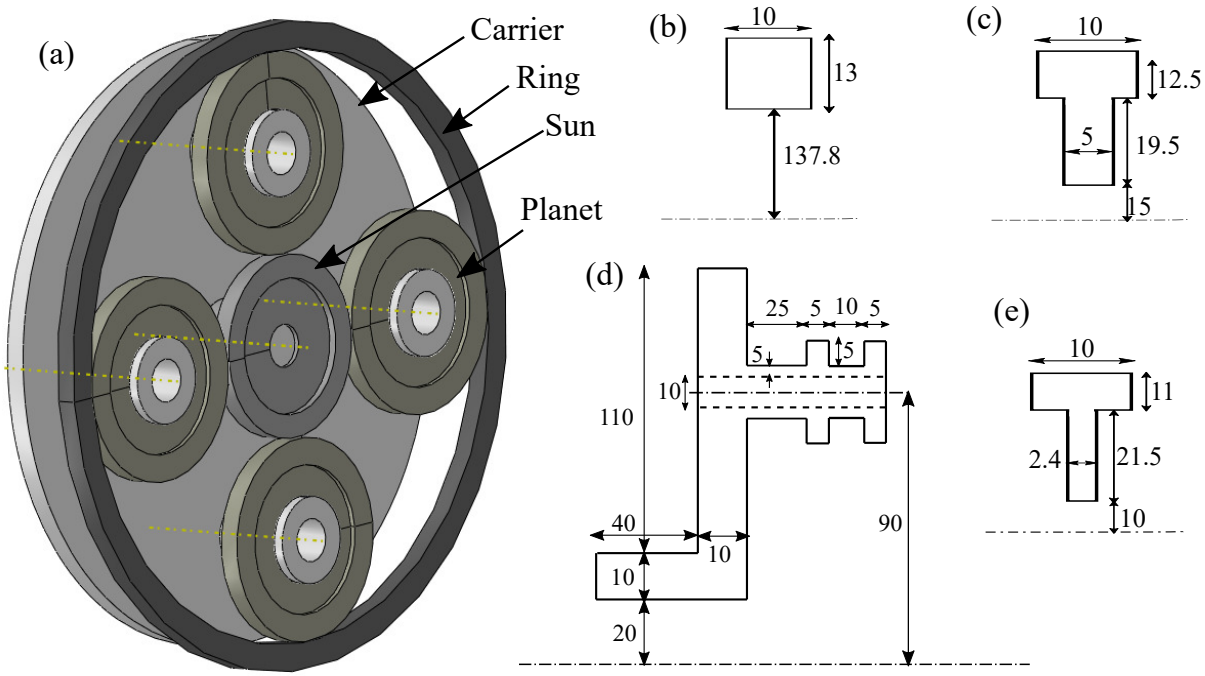

Figure 4.3: (a) Four-planet planetary gear with dimensions in millimeters for (b) ring gear, (c) planet gear, (d) carrier, and (e) sun gear

Table 4.1: Parameters of a four-planet planetary gear.

	Ring	Sun	Planet	Carrier
Young's modulus (GPa)	202.1	202.1	202.1	202.1
Poisson Ratio	0.3	0.3	0.3	0.3
Density (kg/m^3)	7850	7850	7850	7850
Number of Teeth	96	30	33	-
Pressure Angle (deg)	22.5	22.5	22.5	-
Helix Angle (deg)	20	20	20	-
Bearing translational stiffness (N/m)	1×10^9	1×10^9	x, y: 1×10^9 z: 1×10^6	-
Bearing tilting stiffness (Nm/rad)	0	1×10^6	1×10^4	-
Ring-planet mesh stiffness (N/m)	120×10^6			
Sun-planet mesh stiffness (N/m)	90×10^6			

The natural frequencies, vibration modes, and observed mode types for a stationary, cyclic symmetric system obtained using the present model in Eq. (4.21) are validated with a

full three-dimensional Nastran model. Fig. 4.3 shows an equally spaced four-planet system with parameters in Table 4.1. The carrier, sun, and ring gears are the central components and the planet gears are the substructures. The system has axisymmetric ring, sun, and planet gears and cyclically symmetric carrier. The dimensions of the system are given in Fig. 4.3. The validation model in this section is a spur planetary gear with 0 helix angle. The sun-planet and ring-planet mesh stiffnesses couple the central components (sun and ring gears) to the substructures (planets). The deflections in the mesh stiffnesses is given in Eq. (4.18). The out-of-plane motion at the nodes on the outer radius of the ring and inner radius of the sun gear are fixed. The validation spur planetary gear does not include the carrier. Instead, the nodes at the planet gear inner radius are constrained using multi-point constraints from Chapter 3 to a reference node at the center of the planet gears. A bearing stiffness with translational stiffness of 1×10^6 N/μm couples the planet reference node to ground.

Table 4.2: Comparison of natural frequencies between present model and Nastran for the four-planet spur planetary gear in Fig. 4.3 in the absence of the carrier with system parameters in Table 4.1.

Index	Mode type	Present Model (Hz)	Nastran (Hz)	Multiplicity	Difference (%)
1	Pure Ring	382	394	1	3.2
2	Rotational	501	506	1	0.9
3	Translational	613	627	2	2.3
4	Substructure	1151	1082	1	5.9
5	Sun out-of-plane	1178	1230	2	4.5
6	Translational	1194	1148	2	3.9
7	Rotational	1211	1209	1	0.2
8	Planet out-of-plane	1460	1549	8	6.1
9	Pure Ring	2040	2245	1	10
10	Planet out-of-plane	2069	2121	4	2.5
11	Ring out-of-plane	2108	2130	1	1.1
12	Translational	2425	2589	2	6.8
13	Substructure	2823	2940	1	4.1
14	Ring out-of-plane	2943	3042	2	3.6
15	Rotational	3850	3995	1	3.8

The natural frequencies obtained from the eigenvalue problem in Eq. (4.21) compare well with the three-dimensional Nastran model, as shown in Table 4.2. The natural

frequency differences are large for vibration modes with higher nodal diameter components because of a coarse Nastran mesh in the circumferential direction. A finer mesh in Nastran results in the convergence of the Nastran model natural frequencies to the frequencies obtained in the present model.

For the three-dimensional model of a stationary spur planetary gear, four mode types exist: translational, rotational, substructure, and pure component modes. The translational, rotational, and substructure modes follow the modal properties mentioned above. The translational modes have multiplicity 2 and central components consist of $jN \pm 1 = 1, 3, 5, ...$ nodal diameter components. The rotational modes and substructure modes are distinct with $jN = 0, 4, ...$ and $jN \pm 2 = 2, 6, ..$ nodal diameter components in the central components. The substructure modes for a four planet system are type 2 modes.

The pure component modes for a planar system are further subdivided into in-plane pure component modes and out-of-plane pure component modes. The in-plane pure ring modes are described as 'Pure Ring' in Table 4.2. These modes follow the properties described for the pure component modes, i.e., the multiplicity is one. The ring consists of a single nodal diameter (either $jN = 4, 8, ...$ or $jN + N/2 = 2, 6, ...$) for a particular mode. The pure ring mode with frequency index 1 is type 2 ($N/2$) pure component modes with two nodal diameter in the ring, whereas the mode with frequency index 9 is a pure ring mode of type 0 with four nodal diameter component. For the spinning system with gyroscopic effects, the type 2 pure component mode converts to a substructure mode and the type 0 pure component mode converts to a rotational mode. The out-of-plane pure component modes have multiplicity of 2 per component and are single nodal diameter modes. The 5th mode in Table 4.2 is a tilting sun mode. The 11th mode is an axial rigid body ring mode with zero nodal diameter axial Fourier component. These out-of-plane modes for a spur planetary gear are component modes and are unaffected by the cyclic symmetry or coupling

between different components.

4.3.2 Modal structure for a rotating, gyroscopic system

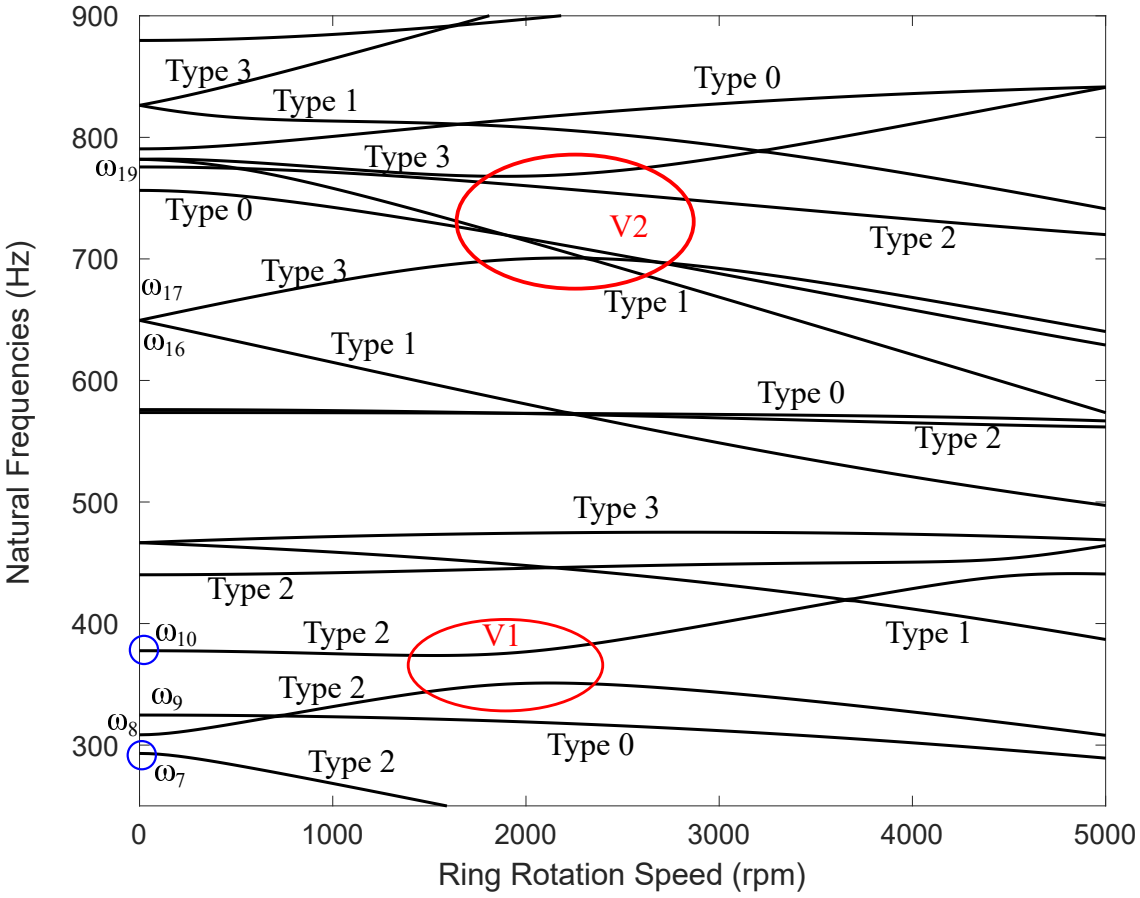

Figure 4.4: Eigenvalue loci of a four-planet helical planetary gear shown in Fig. 4.3 with material parameters in Table 4.1.

Fig. 4.4 shows the eigenvalue loci of the helical planetary gear in Fig. 4.3 with stationary carrier. The parameters of the planetary gear are given in Table 4.1. The axisymmetric ring and sun gears couple to the planets via carrier-fixed ring-planet and sun-planet mesh stiffnesses. The deflections in the mesh stiffnesses along the line of action are given in

Eq. (4.18). The planet gears are supported on the cyclically symmetric carrier shown in Fig. 4.3. The outer surface of the carrier pins that couple to the planet gears is constrained using multi-point constraints in Eq. (3.17) to a reference node at the planet center. Similarly, the surface at the inner radius of the planet is constrained to another reference node at the planet center. The two reference nodes are coupled via a bearing stiffness. The stiffness constants of the bearing are given under "Planet" in Table 4.1.

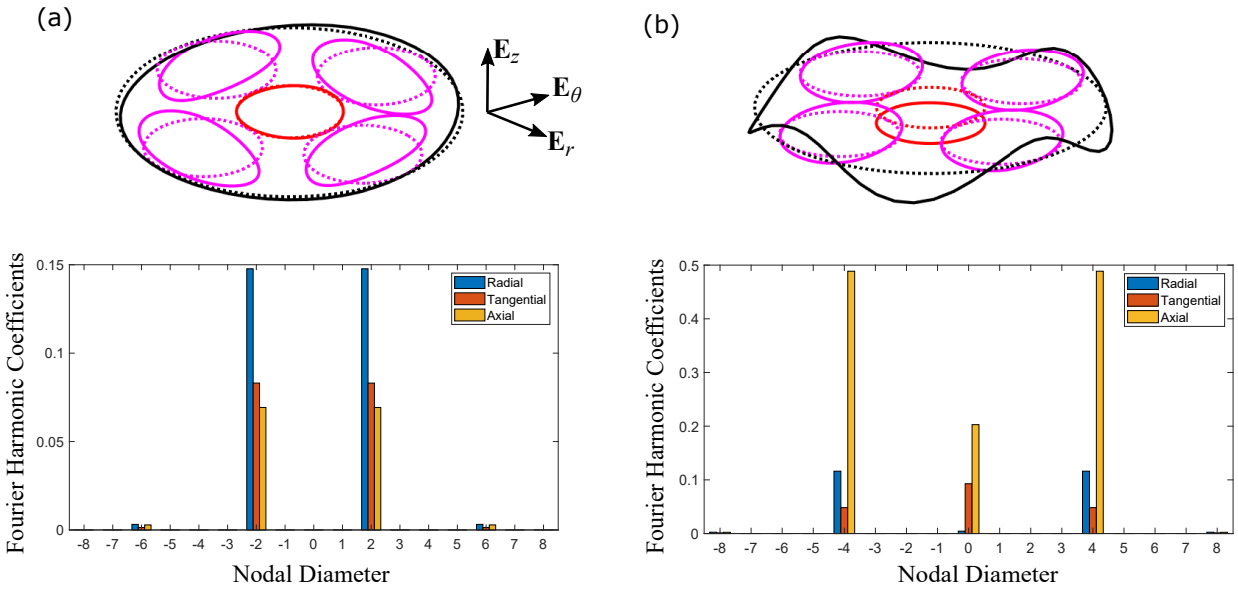

Figure 4.5: (a) Planet mode ω_{19}, and (b) Rotational-axial mode ω_{36} for the stationary, four planet system in Fig. 4.3. The black, red, and magenta dotted and solid lines represent the ring gear, sun gear, and the planet gears undeformed and deformed states. The ring gear Fourier coefficients are shown in the bar plots below the vibration modes.

The mode types for frequencies ω_7 to ω_{25} of the four planet helical planetary gear are marked in Fig. 4.4. Four categories of stationary modes are observed: translational-tilting, rotational-axial, substructure, and pure component modes. Translational-tilting modes have degenerate, stationary natural frequencies and the other three types of modes have distinct natural frequencies. The stationary modes with frequencies ω_7 and ω_{10} (marked with blue circles) are pure ring out-of-plane and pure ring in-plane modes, respectively with two nodal

diameter components. Fig. 4.5 shows a substructure mode ω_{19} and a rotational-axial mode ω_{36} for the stationary system. The Fourier harmonic coefficients for a node on the ring gear are shown. The ring deformation contains $2, 6, \ldots$ nodal diameter components for the substructure mode and $0, 4, 8, \ldots$ nodal diameter components for the rotational-axial mode. Other central components also contain similar nodal diameter components (not shown). The system has coupled in-plane and out-of-plane deformation. The substructure modes (type 2) and rotational-axial modes (type 0) retain their modal characteristics for the spinning system with gyroscopic effects.

Degenerate stationary translational-tilting modes split into distinct type 1 and type 3 modes, as seen for degenerate frequencies ω_{16}, ω_{17} in Fig. 4.4. Fig. 4.6(a) shows the vibration mode and Fourier harmonic components of the ring gear for the stationary translational-tilting mode. The presence of first nodal diameter components for the in-plane (radial and tangential) and out-of-plane (axial) deformation is indicative of the translational and tilting feature of the mode. The other harmonic components follow the $jN \pm 1, j = 0, 1, ...$ rule that is expected for the translational-tilting modes. In the case of a spinning system with gyroscopic effects, the degenerate mode splits into a type 1 mode (Fig. 4.6(b)) and a type 3 mode (Fig. 4.6(c)). The spinning system modes in Fig. 4.6(b) and (c) are at ring rotation speed $\Omega_r = 2000$rpm. The figure shows the real and imaginary components of the vibration mode. The type 1 mode and type 3 mode consist of $jN + 1$ and $jN + 3$, $j = ..., -2, -1, 0, 1, 2, ...$, nodal diameter components in the central components.

In the three-dimensional four-planet helical planetary gear, the stationary, standing pure ring mode transitions into a rotational-axial type 0 or a substructure type 2 mode with gyroscopic effects. Fig. 4.7(a) shows a stationary pure ring mode ω_{10} (marked with a blue circle in Fig. 4.4). The real and imaginary parts of the same mode at ring rotation speed $\Omega_r = 2000$rpm are shown in Fig. 4.7(b). The mode transitions to a planet mode with $2, 6, ...$

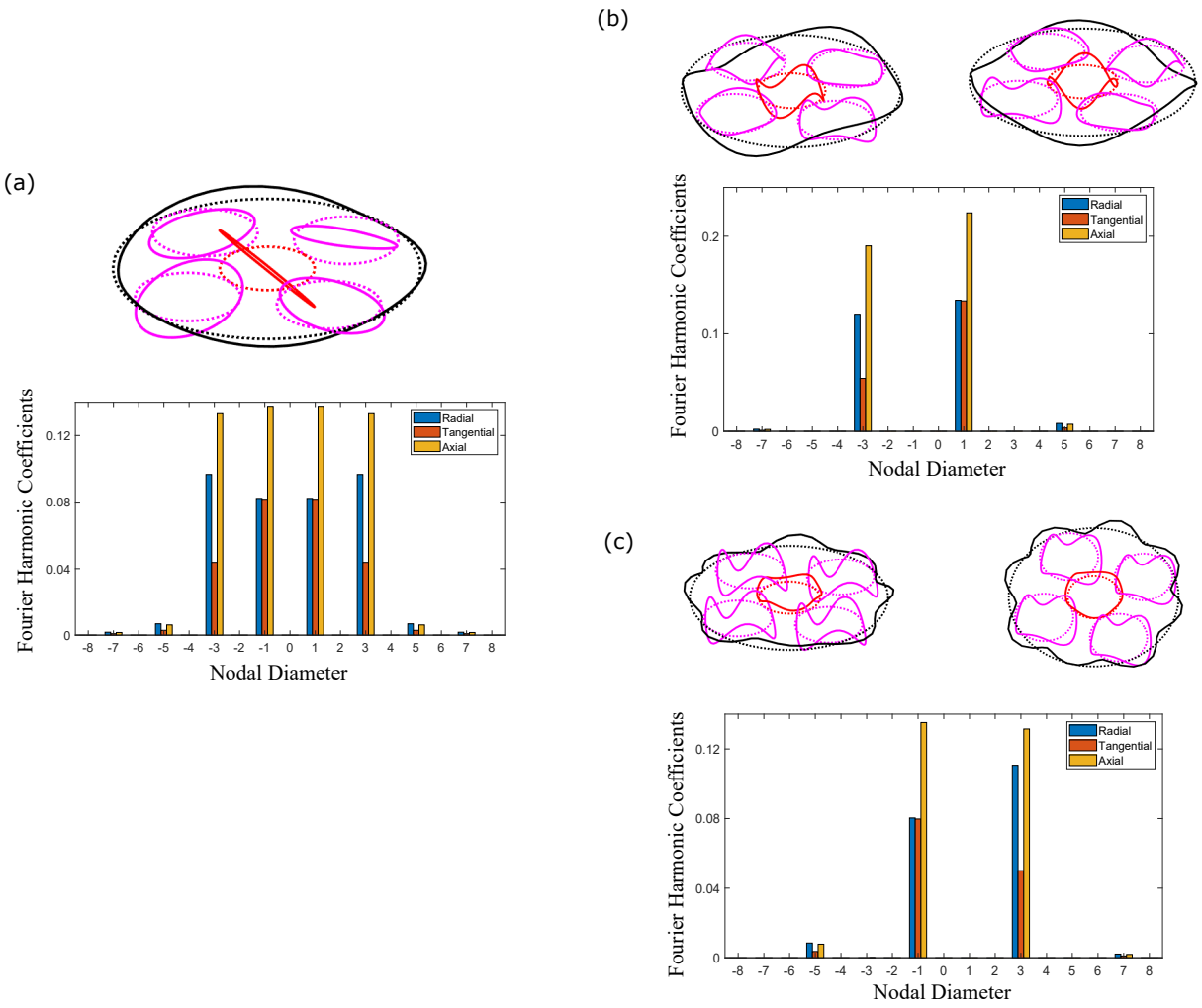

Figure 4.6: (a) Standing-wave, degenerate translational-tilting mode ω_{16}, ω_{17}. (b) Type 1 and (c) Type 3 distinct translational-tilting modes at ring rotation speed $\Omega_r = 2000$rpm and stationary carrier. The carrier displacement is not shown in the vibration modes for simplicity. The real and imaginary parts of the vibration mode for a spinning system are shown in (b) and (c). The Fourier harmonic coefficients for a node on the ring gear are shown for each vibration mode.

nodal diameter components in the central components.

Eigenvalue veering occurs when two eigenvalues approach each other as a parameter is varied but then veer away without crossing [115], as shown by red circles and marked as V1 and V2 in Fig. 4.4. Despite the absence of intersection of the loci, the vibration modes are exchanged between the two loci as the varying parameter increases or decreases across the

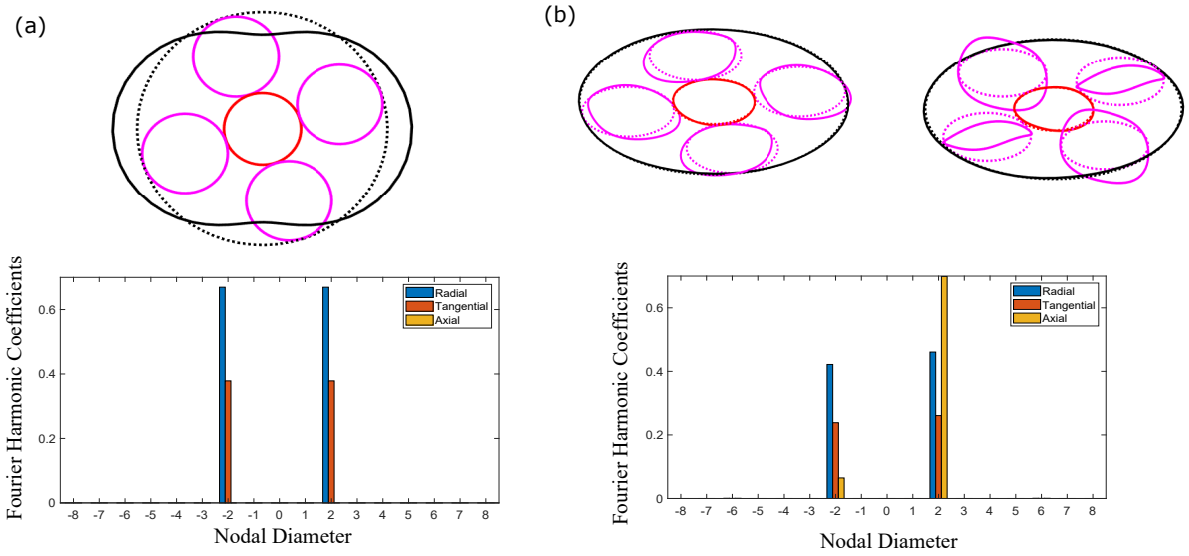

Figure 4.7: (a) Standing wave pure ring mode ω_{10}. (b) The real and imaginary component of the same mode that transitions into a planet mode ω_{10} with gyroscopic effects at ring rotation speed $\Omega_r = 2000$rpm. The Fourier harmonic coefficients of the ring gear are shown by bar plots for each vibration mode.

veering region. If the modes of the two approaching eigenvalues are of the same type with common Fourier harmonic coefficients, then eigenvalue veering occurs. The veering region V1 occurs between substructure modes of type 2 and veering region V2 occurs between two traveling-wave translational modes of type 3. The eigenvalues for two translational modes of different type intersect each other and no veering occurs. Veering cannot occur between two eigenvalues of different mode types.

4.4 Modal structure of unequally spaced substructures

While most rotationally periodic systems have equally spaced substructures, some have unequally spaced substructures due to special applications or assembly constraints. Arbitrarily spaced substructures disrupt the symmetry of the system, resulting in a loss of structured frequency and modes observed for the equally spaced substructures. A diametrically

opposed substructure configuration, however, retains the modal structural properties. The diametrically opposed configuration is statically and dynamically balanced. Lin and Parker [91] characterized the vibration modes of planetary gears with unequally spaced planets into translational, rotational, and planet modes for a lumped-parameter model. In the case of an elastic-discrete planetary gear model with elastic ring gear, Parker and Wu [110] categorized all modes of the system into either translational or rotational modes. No other mode type was identified for the system with diametrically opposed planets. For a three-dimensional system with diametrically opposed substructures, the rotational and translational modes in [110] are rotational-axial and translational-tilting modes, as discussed for the equally spaced substructures.

The diametrically opposed configuration disrupts the cyclic symmetry of the equal spaced configuration. The asymmetry causes all degenerate natural frequencies to split into distinct frequencies resulting in distinct, stationary natural frequencies for the translational-tilting modes of a diametrically opposed substructure system.

In rotational-axial modes for diametrically opposed substructures, the central components have only rotation about the symmetry axis and axial translation with no in-plane translation or out-of-plane tilting. The central components contain only even nodal diameter components. The deflections of all substructures is no longer identical, however, diametrically opposed substructures have identical motion.

The central components in the translational-tilting modes have in-plane translation and out-of-plane tilting with no rotation and axial translation. The central components in the diametrically opposed substructure system contain only odd nodal diameter components in the translational-tilting modes. Only the motion of diametrically opposed substructures are related.

The structured modal characteristics are validated for a four-planet helical planetary gear with unequally spaced planets. The geometry of the sun, planet, and ring gears is similar to Fig. 4.3. The planet gears are constrained to ground through multi-point constraints and the bearing stiffness with parameters in Table 4.1. The carrier is not included in this model. The other system parameters are identical to the four planet system parameters in Table 4.1. The circumferential locations of the four planets are $\Psi = 0°, 70°, 180°$, and $250°$.

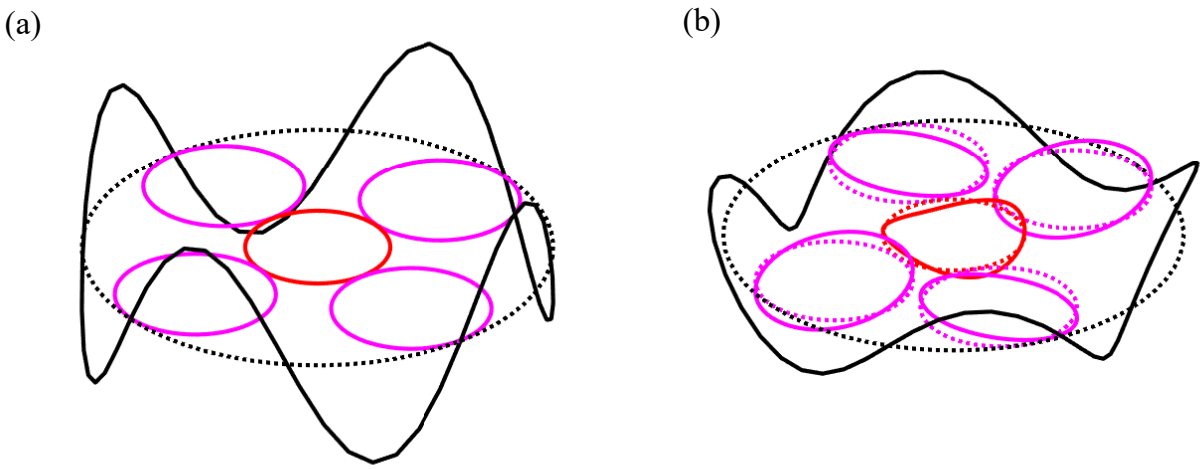

Figure 4.8: Mode comparison of a four-planet planetary gear with: (a) a pure ring mode for equally spaced planets, and (b) corresponding rotational-axial mode for diametrically opposed substructures. The positions of the substructures for the diametrically opposed planets are $\Psi = 0, 70°, 180°, 250°$.

Fig. 4.8 shows the pure ring mode in an equally spaced planetary gear transition to a rotational-axial mode for the diametrically opposed planetary gear. Because the pure ring mode has even numbered (four) nodal diameter components, it transitions into a rotational mode. Similarly, the type 2 planet modes in the four-planet equally-spaced planetary gear that contain $2, 6, ..$ nodal diameter components transition to rotational modes.

The developed model can analyze systems with arbitrary circumferential spacing of the substructures. No known structured modal characteristics exist for such a system.

4.5 Conclusions

The semi-analytical model for rotationally periodic systems include the flexibility of all central components and substructures. The system model is developed in the rotating reference frame of the central component that supports the substructures. This leads to a constant coefficient equation of motion. The coupling elements between the central components and the substructures remain fixed in the rotating reference frame.

A special case of rotationally periodic systems, cyclically symmetric systems, have structured modal characteristics. The modes are categorized into: translational-tilting, rotational-axial, and substructure modes. An additional mode type, a pure component mode, is observed for stationary systems. For three-dimensionally coupled systems, pure component modes transition into substructure or rotational-axial modes with gyroscopic effects. The three-dimensional model of a planar system (spur planetary gears) retains the out-of-plane pure component modes even with gyroscopic effects. The modal properties of cyclically symmetric systems compare well with the analytical models in literature.

Systems with diametrically opposed substructures only possess translational-tilting and rotational-axial mode types. The substructure modes of the equally spaced substructure systems transition to rotational-axial or translational-tilting mode type for diametrically opposed system depending on the presence of even or odd numbered nodal diameters contained in the central components.

Chapter 5

Parametric excitation from coupling elements in coupled rotating systems

5.1 Introduction

Changing contact conditions between a rotating body and other rotating/stationary bodies can lead to large vibration and instabilities. The change in the number of teeth in contact in coupled gears, the change in the contact between rolling elements and bearing races in a bearing, and rotor-stator rub in dual rotor-casing systems are some examples of changing contact conditions. This change in contact is modeled with time-varying coupling elements. They act as a source of parametric excitation in the system. Parametric instabilities occur when a combination of two natural frequencies is near a harmonic of the excitation frequency.

Canchi and Parker [12] analyzed parametric instability of a rotating ring with moving, time-varying springs in a model derived in the rotating reference frame. Liu et al. [93] investigated parametric instability in spinning rings excited by periodically fluctuating discrete, space-fixed stiffnesses. They obtained a closed form expression for the instability boundaries using method of multiple scales. Tai and Shen [137] analyze parametric resonance of a spinning cyclic symmetric rotor coupled to a flexible housing. The instabilities in [137] show combination resonances between a rotor mode and an elastic housing mode. Wang et al. [153] analyzed parametric instabilities in a cracked, anisotropic rotor-bearing

system with the crack modeled as a time-varying stiffness.

Investigation into parametric instabilities in planetary gears can be found in Refs. [23, 92, 111, 148, 158]. Mesh stiffness fluctuation is the main source of parametric excitation in planetary gears. Lin and Parker [92] used a rotational degree of freedom lumped-parameter model to investigate parametric instabilities for different mesh phasing conditions. Parker and Wu [111] derived an instability existence rule that is based on the mesh phasing parameters and the modal properties of the planetary gear mode. Wang and Parker [148] extended the discrete-elastic model to study effects of gyroscopic and centripetal effects on the parametric instability. Zhu et al. [158] analyzed parametric instabilities in a wind turbine planetary gear with mesh stiffness fluctuations. In Chen and Shao [23], tooth root crack modeled as a time-varying stiffness is the source of parametric excitation. Speed fluctuations are the source of parametric instability in planetary gears in Qiu et al. [116].

Roller element bearings also show parametric instabilities because of changing number of rolling elements in contact with the bearing races. Liu et al. [95] show parametric instabilities in a spur gear pair excited by bearing and tooth mesh stiffness fluctuations. Using Hertz contact theory, Yang et al. [157] included varying contact in intershaft roller bearings in the form of external forces. This system can be modified to include the bearing stiffness fluctuation as a parametric excitation instead of an external force. Similarly, blade rotor-casing rub [16, 151, 157] can also be modeled as source of parametric excitations.

This study investigates the parametric instability in coupled systems excited by periodically fluctuating stiffness coupling elements. The general equations of motion for coupled systems obtained in the previous chapters are used. The general form of the equation of motion is similar to the spinning ring coupled to fluctuating stiffness [93] and planetary gears with fluctuating mesh stiffnesses [148]. The closed-form expressions of the instability boundaries are obtained using method of multiple scales [93, 153]. The closed-form expres-

sions results are compared with numerical integration and Floquet theory. The effects of the modal strain energy in the fluctuating coupling element are correlated with the instability bandwidths.

5.2 Analytical Model

The general equation of motion of a system comprising of rotating and stationary bodies coupled via time-varying coupling elements is

$$\mathbf{M}\ddot{\mathbf{q}} + \mathbf{G}(\Omega)\dot{\mathbf{q}} + (\mathbf{K} + \mathbf{K}_c(t) - \mathbf{C}(\Omega^2))\mathbf{q} = \mathbf{0}, \tag{5.1}$$

where $\mathbf{M}$, $\mathbf{G}(\Omega)$, and $\mathbf{C}(\Omega^2)$ are the mass, gyroscopic, and centripetal matrices, respectively. The gyroscopic and centripetal matrices linearly and quadratically depend on the rotation speeds of the bodies. The stiffness matrix $\mathbf{K}$ consists of elastic stiffness and prestress stiffness of the bodies. The matrix $\mathbf{K}_c(t)$ is the time-varying coupling stiffness matrix. The coefficient vector $\mathbf{q}$ consists of the Fourier harmonic nodal coefficients of the rotating bodies and the nodal coefficients of the stationary bodies in the system.

The mass ($\mathbf{M}$), centripetal ($\mathbf{C}$), and stiffness ($\mathbf{K} + \mathbf{K}_c(t)$) matrices are self-adjoint, whereas the gyroscopic ($\mathbf{G}$) matrix is skew-adjoint.

A number of time-varying discrete stiffnesses couple the bodies. Each discrete stiffness can be expanded in a Fourier series as

$$k_{ci}(t) = k_{gi} + \sum_{L=1}^{\infty} \left(k_i^{(L)} \mathrm{e}^{\mathrm{j}L\omega_c t} + \text{c.c.} \right), \tag{5.2}$$

where k_{gi} is the average stiffness over a period, $k_i^{(L)}$ is the Lth Fourier coefficient of the

stiffness, ω_c is the coupling stiffness frequency, and c.c. denotes the complex conjugate.

We define a small perturbation parameter $\epsilon_i = k_{ppi}/k_{gi}$, where k_{ppi} is the peak-to-peak stiffness of the ith coupling stiffness. Using the perturbation parameter, the coupling stiffness in Eq. (5.2) is

$$k_{ci}(t) = k_{gi} + k_{gi}\epsilon \sum_{L=1}^{\infty} \left(\alpha_i^{(L)} \mathrm{e}^{\mathrm{j}L\omega_c t} + \text{c.c.} \right), \quad \alpha_i^{(L)} = k_i^{(L)}/k_{ppi}. \tag{5.3}$$

The coupling stiffness matrix separated into time-varying and time-invariant parts using Eq. (5.3) for N_s discrete stiffnesses is

$$\mathbf{K}_c(t) = \sum_{i=1}^{N_s} \left[\mathbf{K}_{gi} + \epsilon \sum_{L=1}^{\infty} \left(\alpha_i^{(L)} \mathrm{e}^{\mathrm{j}L\omega_m t} + \text{c.c.} \right) \mathbf{K}_{gi} \right], \tag{5.4}$$

where $\mathbf{K}_{gi}$ is the average stiffness matrix.

The unperturbed ($\epsilon \to 0$) eigenvalue problem obtained from Eq. (5.1) is

$$\lambda_k^2 \mathbf{M}\boldsymbol{\phi}_k + \lambda_k \mathbf{G}\boldsymbol{\phi}_k + (\mathbf{K} + \sum_{i=1}^{N_s} \mathbf{K}_{gi} - \mathbf{C})\boldsymbol{\phi}_k = \mathbf{0}, \tag{5.5}$$

where λ_k and $\boldsymbol{\phi}_k$ are the eigenvalue and corresponding eigenvector of kth vibration mode of the system. The eigenvalue is purely imaginary below the first critical speed ($\lambda_k = j\omega_k$) and the eigenvector for the gyroscopic system is complex-valued [99].

The equation of motion Eq. (5.1) with the time-varying coupling matrix Eq. (5.4) is cast into a state space form [99] as

$$\mathbf{A}\dot{\mathbf{p}} + \mathbf{B}\mathbf{p} + \epsilon \sum_{i=1}^{N_s} \sum_{L=1}^{\infty} \left(\alpha_i^{(L)} \mathrm{e}^{\mathrm{j}L\omega_m t} + \text{c.c} \right) \mathbf{D}_i \mathbf{p} = \mathbf{0}, \quad \mathbf{p} = [\dot{\mathbf{q}},\, \mathbf{q}]^T, \tag{5.6a}$$

$$\mathbf{A} = \begin{pmatrix} \mathbf{M} & \mathbf{0} \\ \mathbf{0} & \mathbf{K} + \sum_{i=1}^{N_s} \mathbf{K}_{gi} - \mathbf{C} \end{pmatrix}, \tag{5.6b}$$

$$\mathbf{B} = \begin{pmatrix} \mathbf{G} & \mathbf{K} + \sum_{i=1}^{N_s} \mathbf{K}_{gi} - \mathbf{C} \\ -\left[\mathbf{K} + \sum_{i=1}^{N_s} \mathbf{K}_{gi} - \mathbf{C}\right] & \mathbf{0} \end{pmatrix}, \tag{5.6c}$$

$$\mathbf{D}_i = \begin{pmatrix} \mathbf{0} & \mathbf{K}_{gi} \\ \mathbf{0} & \mathbf{0} \end{pmatrix}. \tag{5.6d}$$

The eigenvalue problem of the state-space form of the equation of motion Eq. (5.6) is

$$\mathrm{j}\omega_k \mathbf{A}\boldsymbol{\psi}_k + \mathbf{B}\boldsymbol{\psi}_k = \mathbf{0}, \quad \boldsymbol{\psi}_k = \left[\mathrm{j}\omega_k \boldsymbol{\phi}_k,\, \boldsymbol{\phi}_k\right]^T. \tag{5.7}$$

The eigenfunctions $\boldsymbol{\psi}_k$ of the state space formulation are orthogonal with respect to $\mathbf{A}$ and $\mathbf{B}$ such that [98]

$$(\boldsymbol{\psi}_l, \mathbf{A}\boldsymbol{\psi}_k) = \delta_{lk}, \quad (\boldsymbol{\psi}_l, \mathbf{B}\boldsymbol{\psi}_k) = -\mathrm{j}\omega_l \delta_{lk}, \tag{5.8}$$

where δ_{lk} is the Kronecker delta and the notation $(\mathbf{p}_1, \mathbf{p}_2)$ is the inner product of two arbitrary functions $\mathbf{p}_1$ and $\mathbf{p}_2$.

The method of multiple scales [101] is used to solve state-space formulation in Eq. (5.6) with ϵ as the perturbation parameter. The perturbation parameter controls the variation of the time-varying coupling component. The method of multiple scales yields closed-form expressions for parametric instability boundaries that identify the regions in the

parametric excitation frequency (ω_m) and amplitude (ϵ) parameter plane where parametric instabilities occur. The details are provided in Liu et al. [93].

A combination parametric instability occurs when a harmonic of the excitation frequency is close to the sum of two natural frequencies, given as

$$L\omega_m = \omega_l + \omega_k + \epsilon\sigma, \quad L = 1, 2, ... \tag{5.9}$$

where $\sigma = \mathrm{O}(1)$ is a real-valued detuning parameter. In this case, both modes experience large vibrations at their natural frequencies. The difference type parametric instability cannot occur for systems with self-adjoint mass and stiffness matrices [121].

The instability boundaries for the two modes $\boldsymbol{\psi}_k$ and $\boldsymbol{\psi}_l$ using the perturbation approach in [93] is

$$\omega_m^{(L,l,k)} = \frac{\omega_l + \omega_k}{L} \pm \frac{2\sqrt{\omega_l\omega_k}}{L}|\epsilon D_L^{lk}|, \tag{5.10a}$$

$$D_L^{lk} = \sum\nolimits_{i=1}^{N_s} k_{gi}\alpha_i^{(L)}\overline{\Delta}_{li}\overline{\Delta}_{ki} \tag{5.10b}$$

where $\omega_m^{(L,l,k)}$ represents the instability region, and Δ_l and Δ_k are the lth and kth modal deflections in the discrete coupling element.

Because the eigenfunctions of the system are complex-valued, there are phase differences between modal deflections at the coupling elements for each mode. Phase differences also exist for the time-varying coupling component. These phase differences change the bandwidth of instability regions. The complex valued terms in Eq. (5.10b) are written as

$$\alpha_i^{(L)} = |\alpha_i^{(L)}|\mathrm{e}^{\mathrm{j}\xi_i^L}, \quad \Delta_{li} = |\Delta_{li}|\mathrm{e}^{\mathrm{j}\xi_{li}}, \quad \Delta_{ki} = |\Delta_{ki}|\mathrm{e}^{\mathrm{j}\xi_{ki}}. \tag{5.11}$$

Substitution of Eqs. (5.11) and (5.10b) in Eq. (5.10a) leads to

$$\omega_m^{(L,l,k)} = \frac{\omega_l + \omega_k}{L} \pm \frac{2\sqrt{\omega_l \omega_k}}{L} \epsilon \left| \sum_{i=1}^{N_s} \left[|k_{gi} \alpha_i^{(L)} \overline{\Delta}_{li} \overline{\Delta}_{ki}| \mathrm{e}^{\mathrm{j}(\xi_i^L - \xi_{li} - \xi_{ki})} \right] \right| . \tag{5.12}$$

The instability bandwidth depends on the modal amplitudes, and the phases of the modal deflections and the coupling stiffness Fourier coefficients.

5.3 Rotating body coupled to fluctuating, space-fixed stiffnesses

We investigate the vibration of a compliant, rotating shaft-disk body coupled to multiple space-fixed, time varying discrete stiffnesses shown in Fig. 5.1. The properties of the body and coupling stiffness elements are given in Table 5.1. Three space-fixed stiffnesses are connected to the rotating body at the same circumferential location. Without loss of generality, the circumferential position of the coupling stiffnesses is $\beta = 0$. The radial location of the stiffnesses on the shaft-disk is $R_o = 100$mm and it is oriented at an angle $\alpha_p = 22.5^\circ$ with respect to $\mathbf{E}_\theta$. The average coupling stiffnesses is given in Table 5.1. The fluctuating component of the coupling stiffnesses is the same for all discrete stiffnesses. Its complex-valued Fourier coefficients are shown in Table 5.2.

Bearings support the shaft at inner radius $R_i = 20$mm and axial location ranges $z = [35, 45]$mm and $z = [130, 140]$mm. The bearings are applied using surface constraints and bearing stiffness given in Eq. (3.22). This results in additional stiffness matrices. The bearing stiffness that couples the shaft surface to the reference node is $\mathbf{k}_{B1} = k_b \, \mathrm{diag}(1, 1, 1, 10^{-5}, 10^{-5}, 0)$ for the first bearing and $\mathbf{k}_{B2} = k_b \, \mathrm{diag}(1, 1, 0, 10^{-5}, 10^{-5}, 0)$ for the second bearing. The value of k_b is given in Table 5.1. In this example, the bearing stiffness matrix and the surface con-

straints are included in the stiffness matrix **K** in Eq. (5.1).

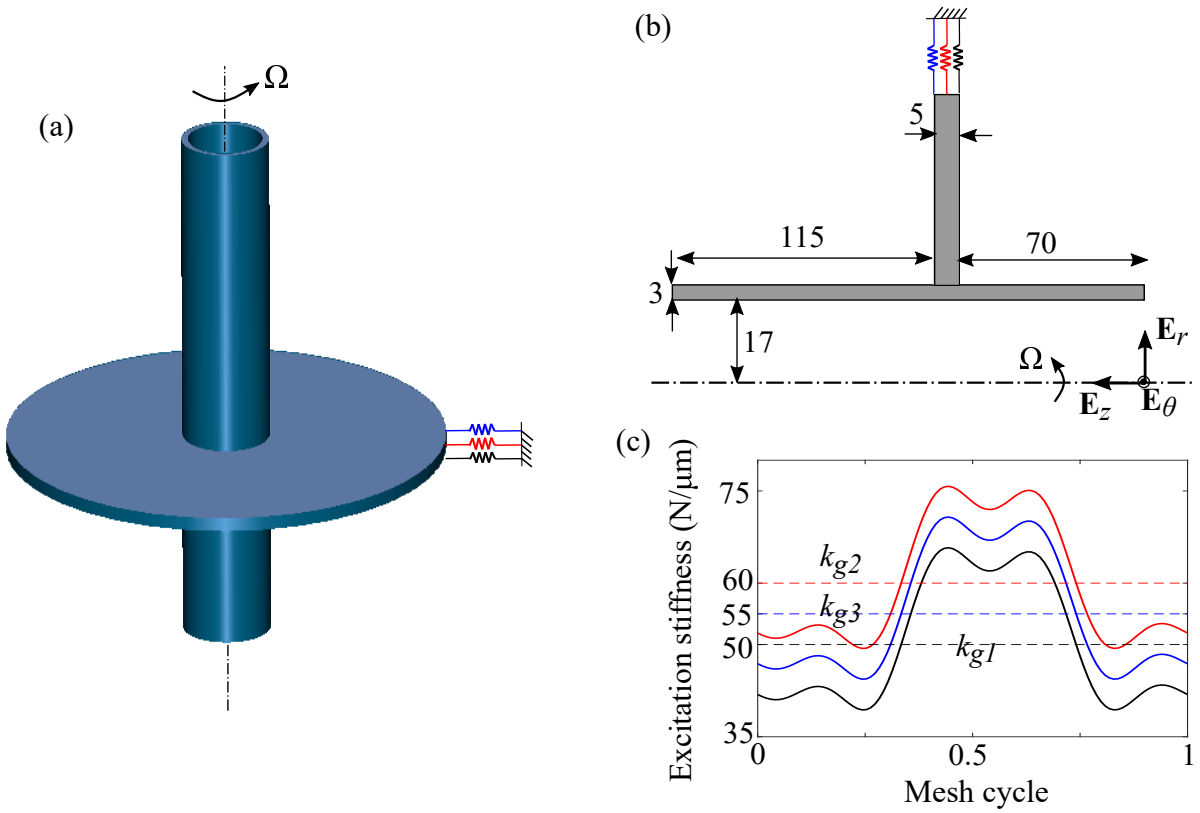

Figure 5.1: (a) Three-dimensional schematic and (b) Two-dimensional radial cross-section of the rotating shaft-disk coupled to space-fixed stiffnesses. The dimensions of the body are in millimeters. (c) Excitation stiffnesses over one mesh cycle.

Table 5.1: Parameters of the rotor-disk system in Fig. 5.1.

Young's modulus (MPa)	211,000
Poisson Ratio	0.3
Density (kg/m^3)	7800
Excitation Relation, Z	100
Orientation Angle, α_p (deg)	22.5
Average coupling stiffness, k_{g1} (N/μm)	50
Average coupling stiffness, k_{g2} (N/μm)	60
Average coupling stiffness, k_{g3} (N/μm)	55
Bearing stiffness, k_b (N/m) or (Nm/rad)	10^9

No phase difference exists between the coupling stiffnesses. The boundaries and

Table 5.2: Fourier coefficients of the fluctuating mesh stiffnesses shown in Fig. 5.1(c).

Harmonic, h	Fourier coefficients, $k_1^{(L)}$ (N/μm)
1	-6.20 + j1.45
2	2.20 - j1.02
3	0.82 - j0.74
4	-0.97 + j1.40

bandwidths of the instability regions (L, l, k) obtained from Eq. (5.12) are

$$\omega_m^{(L,l,k)} = \frac{\omega_l + \omega_k}{L} \pm \frac{2\sqrt{\omega_l \omega_k}}{L} \epsilon \left| \sum_{i=1}^{3} \left[k_{gi} \alpha_i^{(L)} \overline{\Delta}_{li} \overline{\Delta}_{ki} \right] \right|, \tag{5.13a}$$

$$\Delta\omega_m^{(L,l,k)} = \frac{4\sqrt{\omega_l \omega_k}}{L} \epsilon \left| \sum_{i=1}^{3} \left[k_{gi} \alpha_i^{(L)} \overline{\Delta}_{li} \overline{\Delta}_{ki} \right] \right|, \tag{5.13b}$$

$$\Delta_{li} = u_{li}(R_o, Z_i, \beta) \sin \alpha_p + v_{li}(R_o, Z_i, \beta) \cos \alpha_p, \tag{5.13c}$$

where $u_{li}(R_o, Z_i, \beta)$ and $v_{li}(R_o, Z_i, \beta)$ are the modal radial and tangential deflections at the connection location (R_o, Z_i, β) for the ith stiffness.

According to Eq. (5.13b), large deflections in the coupling stiffnesses lead to large instability bandwidths. Large coupling stiffness deflections also corresponds to large strain energy in the coupling stiffnesses. The modal fractional strain energy defined as the ratio of strain energy in the coupling stiffnesses to the total modal strain energy is

$$V_c = \frac{\frac{1}{2}\left(\boldsymbol{\phi}_k, \sum_{i=1}^{N_s} \mathbf{K}_{gi} \boldsymbol{\phi}_k\right)}{\frac{1}{2}\left(\boldsymbol{\phi}_k, \mathbf{K}\boldsymbol{\phi}_k\right) + \frac{1}{2}\left(\boldsymbol{\phi}_k, \sum_{i=1}^{N_s} \mathbf{K}_{gi} \boldsymbol{\phi}_k\right)}, \tag{5.14}$$

where $\mathbf{K}$ and $\mathbf{K}_{gi}$ are the elastic stiffness and ith coupling stiffness matrices from Eq. (5.5), and $\boldsymbol{\phi}_k$ is the kth mode.

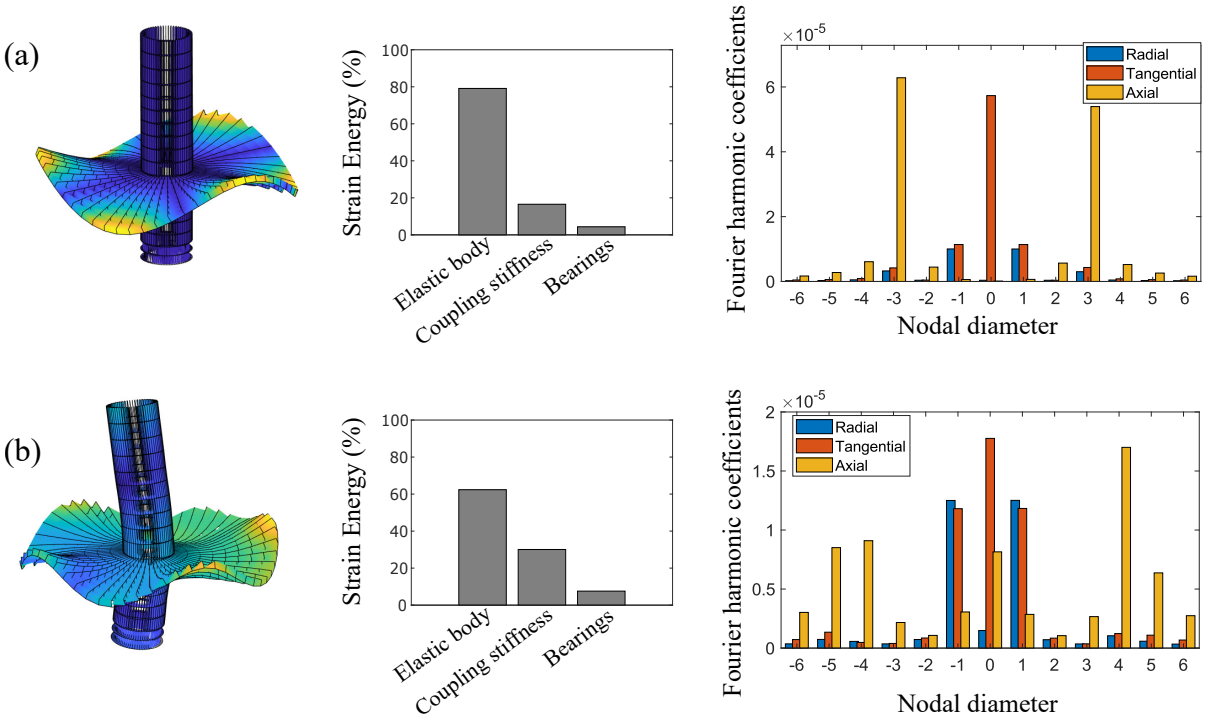

Figure 5.2: Mode shapes, strain energy distribution, and Fourier harmonic coefficients at point $(R_o, Z) = (100, 70)$mm for the (a) 7th mode ($\omega_7 = 1544$Hz) and (b) 12th mode ($\omega_{12} = 3179$Hz) of the rotating shaft-disk coupled to multiple, space-fixed stiffnesses shown in Fig. 5.1. The properties of the body are shown in Table 5.1. The body rotates at $\Omega = 1950$rpm.

Fig. 5.2 shows two vibration modes of the rotating shaft-disk system in Fig. 5.1. These two modes have large modal coupling stiffness energy. Mode 7 and 12 have 16% and 30% of strain energy in the coupling stiffnesses. Few other modes have significant modal coupling energy. Mode 7 has large 3 nodal diameter axial component in the disk coupled to 0th harmonic of the tangential component. The large tangential component increases the modal coupling defection. Similarly, mode 12 has large radial and tangential deflections in the 0th and 1st Fourier harmonics, contributing to large modal coupling deflection. Large coupling stiffness deflections lead to large instability bandwidths.

Fig. 5.3 shows combination instability regions for modes 6 to 8 of the system. The solid lines show the boundaries calculated from Eq. (5.13b) for varying peak-to-peak

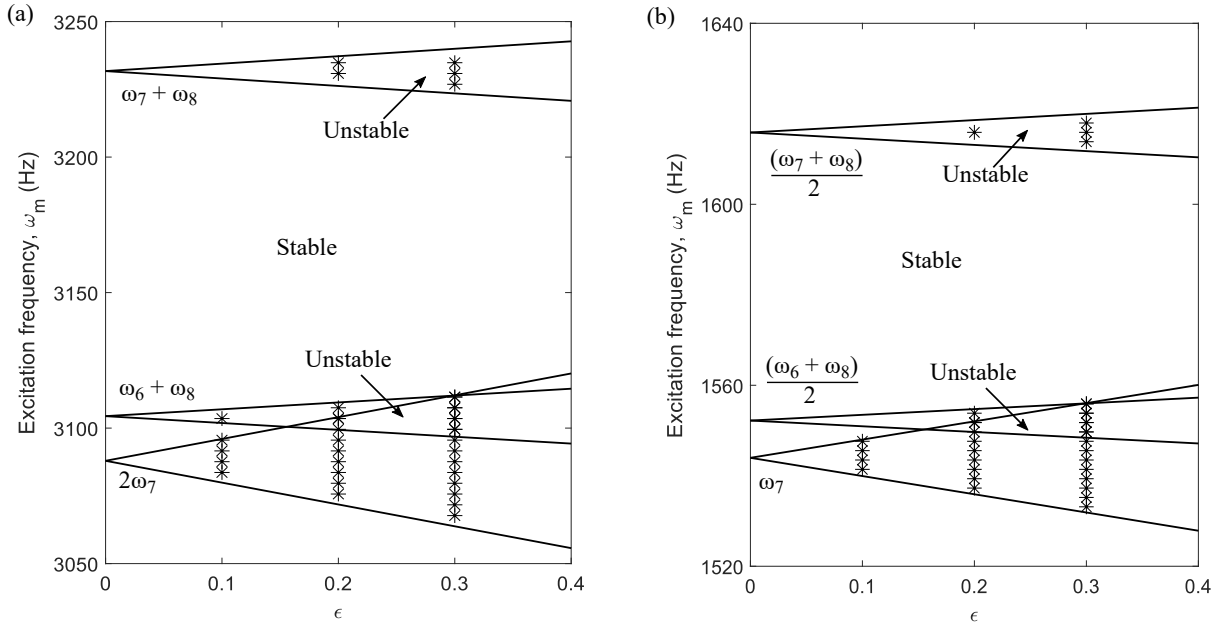

Figure 5.3: Parametric instability regions for shaft-disk system in Fig. 5.1. The body properties are in Table 5.1. The fluctuating coupling stiffness is shown in Fig. 5.1(c) and its Fourier coefficients are given in Table 5.2. The solid lines are perturbation predictions from Eq. (5.13). Floquet theory predictions are shown by asterisks. (a) $L = 1$, (b) $L = 2$.

amplitude of the coupling stiffnesses. The instability region boundaries divide the stable and unstable excitation frequencies ω_m. The response of the system is unbounded when ω_m is within the instability region. Nonlinearities in the system, for example, contact loss in coupled gears, bound the response. Not all instability regions are highlighted in the figure in the excitation frequency range. Modes with large modal coupling energy have larger instability regions. The instability bandwidth of the primary instability region for mode 7 ($\omega_m \approx 2\omega_7$) is larger than the other combination instability regions. Floquet theory is applied to the equation of motion Eq. (5.1) to validate the analytical predictions. The results are shown by asterisks. The numerical results compare well with the analytical expression of the boundaries of instability regions.

Numerical results are used to observe the parametric instabilities. Numerical inte-

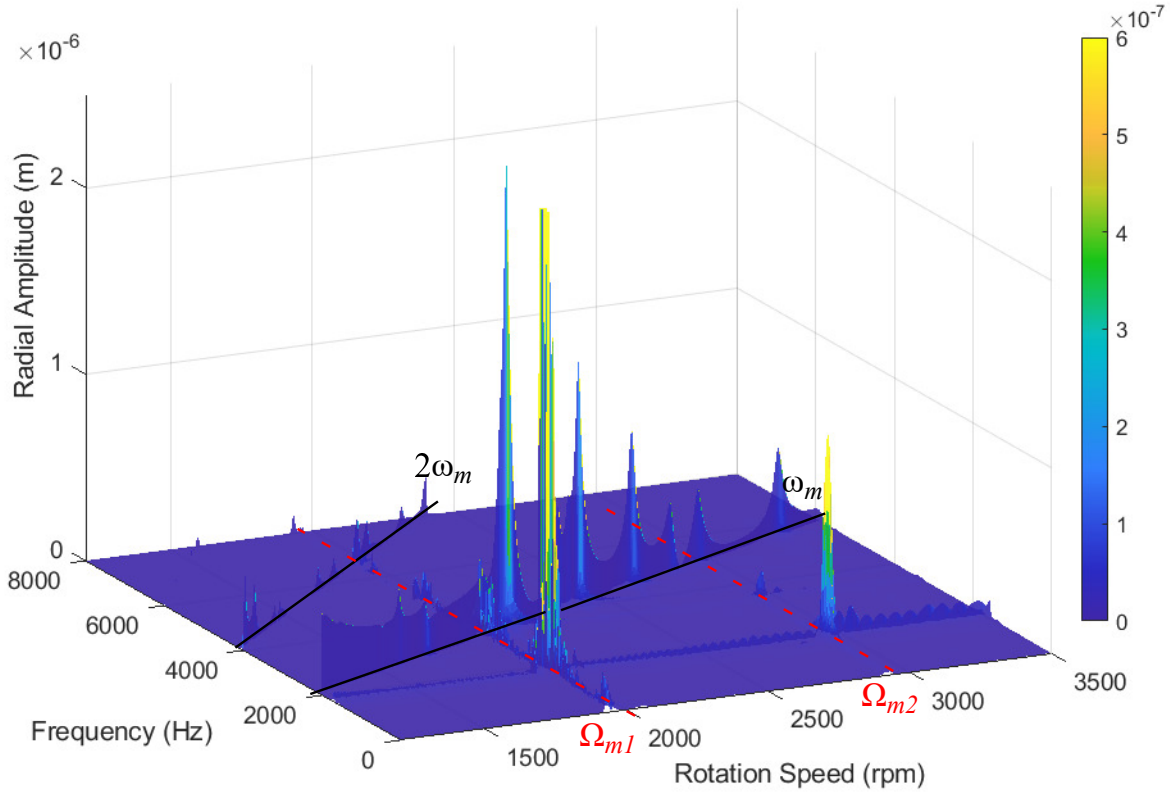

Figure 5.4: Waterfall plot shows the dynamic response of the shaft-disk system with time-varying, coupling stiffnesses in Fig. 5.1. The plot shows radial displacement response at cross-sectional location $(100, 70)$ and angular location $\beta = 0°$. The Fourier harmonics of excitation frequency are marked in black.

gration is performed using the unconditionally stable Newmark-β method at a wide range of shaft-disk rotation speeds. A modal damping of 0.5% is added to remove the transient response. To bound the unbounded response that occurs in the linear system, nonlinear coupling stiffnesses are included to depict the contact loss nonlinearity in gears. The nonlinear coupling stiffness is

$$k_{ci}(\mathbf{q}, t) = \begin{cases} k_{ci}, & \text{if } \Delta_i(\mathbf{q}) > 0; \\ 0, & \text{if } \Delta_i(\mathbf{q}) < 0, \end{cases}, \quad i = 1, 2, 3, \tag{5.15}$$

where Δ_i is the deflection of the ith coupling stiffness, given by Eq. (5.13c). The excitation frequency ω_m is related to the rotation speed as $\omega_m = Z\Omega$, where Z is the excitation frequency relation given in Table 5.1.

Fig. 5.4 shows the radial response of the shaft-disk system with time-varying coupling stiffnesses shown in Fig. 5.1(c). The radial amplitude in Fig. 5.4 is obtained at a cross-sectional location $(100, 70)$ and an angular location $\beta = 0°$. Most resonance vibration occurs when a natural frequency is close to the Fourier harmonics of the excitation frequency, as shown in Fig. 5.4 along lines marked as ω_m and $2\omega_m$. Parametric instability is observed at speeds $\Omega_{m1} = 1945$rpm and $\Omega_{m2} = 2929$rpm, where resonance-like vibration occurs at two natural frequencies that sum to the respective excitation frequency ω_m.

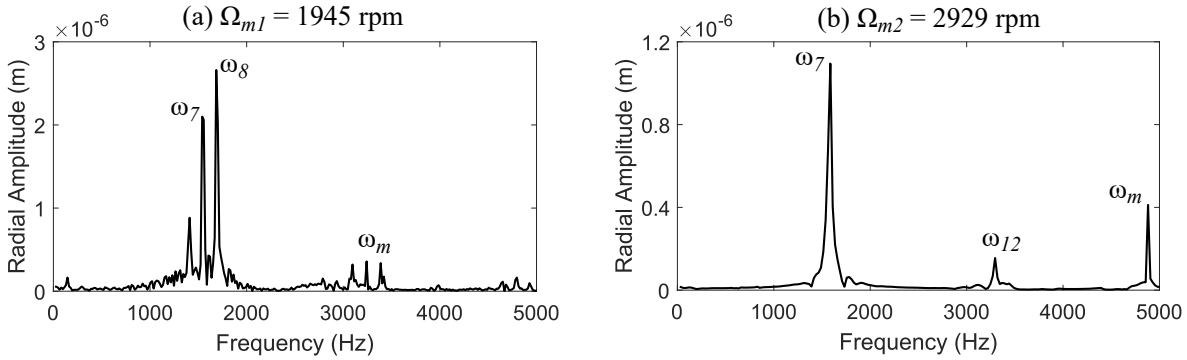

Figure 5.5: Fourier transform of the dynamic response of the shaft-disk with time-varying, space-fixed coupling stiffnesses obtained from Fig. 5.4 at rotation speeds (a) $\Omega_{m1} = 1945$rpm and (b) $\Omega_{m2} = 2929$rpm.

Fig. 5.5 shows the Fourier transform of the radial displacement response at speeds Ω_{m1} and Ω_{m2} in Fig. 5.4. Fig. 5.5(a) and (b) are examples of parametric instabilities that occur when two natural frequencies sum to the excitation frequency or harmonics of the excitation frequency. The excitation frequency at $\Omega_{m1} = 1945$rpm ($\omega_m = 3240$Hz) lies in the parametric instability region of $(\omega_7 + \omega_8)$ in Fig. 5.3(a) for $\epsilon = 1$. Thus, a large amplitude response is observed at the two natural frequencies ω_7 and ω_8, as compared to the excitation frequency in Fig. 5.5(a). Mode 7 has large modal strain energy in the coupling stiffnesses as

shown in Fig. 5.2(a). Mode 8 has 7% modal strain energy in the coupling stiffness. At Ω_{m2} ($\omega_m = 4881$Hz) in Fig. 5.4, the natural frequencies of modes 7 and 12 sum to the excitation frequency as shown in the Fourier transform in Fig. 5.5(b). Both modes 7 and 12 have large coupling modal strain energies, shown in Fig. 5.2. Modes with large modal strain energy in the time-varying coupling element are susceptible to parametric resonance.

5.4 Planetary gears with time-varying mesh stiffnesses

The semi-analytical model of the rotationally periodic system derived in Chapter 4 models planetary gears. The semi-analytical finite element model from Chapter 2 is used for axisymmetric sun, planet, and ring gears. The carrier can be cyclically symmetric. Three-dimensional finite elements are used to model the carrier. The system equations are developed in the carrier-fixed rotating reference frame. Gyroscopic and centripetal effects are included. The equation of motion of the planetary gears has the general conservative, gyroscopic system form given in Eq. (5.1).

In planetary gears, the sun-planet and ring-planet mesh stiffnesses are time-varying because of the changing contact conditions. This stiffness variation is periodic at the mesh frequency. The time-varying mesh stiffnesses are the source of parametric excitation in the planetary gears. Parametric instabilities occur when the mesh frequency or a Fourier harmonic of the mesh frequency is close to the combination of two natural frequencies of the system. Parker and Wu [111] investigated parametric instabilities for stationary planetary gears. Wang and Parker [148] analyzed parametric instabilities for spinning planetary gears with gyroscopic effects. Using the method of multiple scales, they obtained closed-form expressions for parametric instability regions. Because of system symmetry, there exists conditions for when parametric instabilities will occur or will be suppressed.

The sun-planet (ring-planet) mesh stiffnesses for different planets are shifted in time. The mesh phase between the nth and the first sun-planet/ ring-planet meshes is γ_{sn}/ γ_{rn}. The sun-planet and ring-planet mesh stiffnesses for the nth planet are

$$k_{sn}(t) = k_{s1}(t - \gamma_{sn}T_m), \quad k_{rn}(t) = k_{r1}(t - \gamma_{rn}T_m), \tag{5.16a}$$

$$\gamma_{sn} = Z_s\psi_n/(2\pi), \quad \gamma_{rn} = -Z_r\psi_n/(2\pi), \quad \text{for}\, \Omega_c > \Omega_r \tag{5.16b}$$

$$\gamma_{sn} = -Z_s\psi_n/(2\pi), \quad \gamma_{rn} = Z_r\psi_n/(2\pi), \quad \text{for}\, \Omega_c < \Omega_r, \tag{5.16c}$$

where k_{s1} and k_{r1} are sun-planet and ring-planet meshes for the first planet, $T_m = 2\pi/\omega_m$ is the mesh period, ψ_n is the angular location of the nth planet, Z_s and Z_r are the sun and ring gear tooth numbers, and Ω_c and Ω_r are the carrier and ring rotation speeds. The time-varying stiffnesses are similar to Eq. (5.2). The mean stiffnesses are k_{sp} and k_{rp}, and $k_{sn}^{(L)}$ and $k_{rn}^{(L)}$ are the Fourier coefficients for the nth planet.

The parametric instability boundaries obtained using the method of multiple scales is identical to Eq. (5.10a) with D_L^{lk} for planetary gears as in [148]

$$D_L^{lk} = \sum_{n=1}^{N_p} \left[\sum_{i=1}^{N_s} \left(k_{s1i}^{(L)} \overline{\Delta}_{sni}^{\ [l]} \overline{\Delta}_{sni}^{\ [k]} + k_{r1i}^{(L)} \overline{\Delta}_{rni}^{\ [l]} \overline{\Delta}_{rni}^{\ [k]} \right) \mathrm{e}^{-\mathrm{j}2\pi L\gamma_{rn}} \right], \tag{5.17}$$

where Δ_{sn} and Δ_{rn} are the sun-planet and ring-planet mesh deflections, N_s is the number of stiffnesses for a planet, and N_p are the number of planets. The gear mesh deflections for

the nth planet related to the first planet using phase index $d^{[l]}$ of the lth vibration mode are

$$\Delta_{sn_i}^{[l]} = \Delta_{s1_i}^{[l]} e^{\mathrm{j}d^{[l]}\psi_n}, \quad \Delta_{rn_i}^{[l]} = \Delta_{r1_i}^{[l]} e^{\mathrm{j}d^{[l]}\psi_n}. \tag{5.18}$$

Because of system symmetry, structured mode types exist for rotationally periodic systems. The modes of the spinning system with gyroscopic effects fall into one of the following categories: rotational-axial, translational-tilting, and substructure modes. The phase index (d) for rotational-axial modes is 0, translational-tilting modes is 1 or $N_p - 1$, and substructure modes is $d \in \{2, 3, ..., N_p - 2\}$, as described in Chapter 4.

The rotationally periodic (for example, planetary gear) system symmetries result in simple rules for when a particular parametric instability might not occur. Substituting Eq. (5.18) and mesh phase Eq. (5.16) into Eq. (5.17) leads to simple suppression rules. The instability bandwidth $\Delta\omega_m$ between lth and kth modes vanish and the parametric instability is suppressed when [148]

$$(d^{[l]} + d^{[k]} - LZ_r)/N_p \neq \text{integer}, \quad \text{when } \Omega_c > \Omega_r, \tag{5.19a}$$

$$(d^{[l]} + d^{[k]} + LZ_r)/N_p \neq \text{integer}, \quad \text{when } \Omega_c < \Omega_r. \tag{5.19b}$$

We investigate the parametric instability regions for the four-planet, equally-spaced, helical planetary gear shown in Fig. 4.3. The system properties are given in Table 4.1. Fig. 5.6 shows the fluctuating ring-planet and sun-planet mesh stiffnesses. Table 5.3 gives the Fourier coefficients of the mesh stiffnesses.

Fig. 5.7 shows the parametric instability regions for a combinations of natural

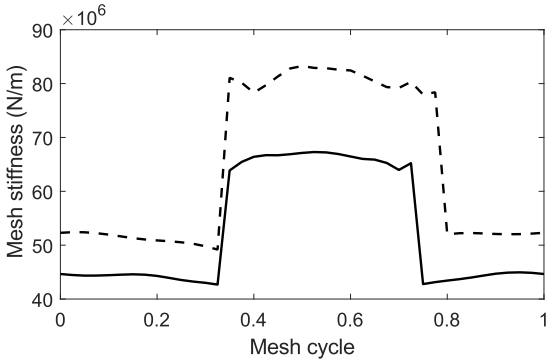

Figure 5.6: Sun-planet (solid line) and ring-planet (dashed line) mesh stiffnesses.

Table 5.3: Fourier coefficients of the fluctuating sun-planet and ring-planet mesh stiffnesses for the first planet shown in Fig. 5.6.

Harmonic, L	$k_{s1}^{(L)}$ (N/μm)	$k_{r1}^{(L)}$ (N/μm)
1	-6.42 + j1.52	-8.51 + j3.67
2	2.30 - j1.03	1.68 - j1.19
3	0.80 - j0.76	0.76 - j2.32
4	-0.99 + j1.46	-0.01 + j1.19
5	0.07 - j 0.02	0.49 + j1.19

frequencies for the four-planet system with $Z_r = 100$ and $Z_s = 40$. Combination instabilities for modes between ω_{34} and ω_{37} are analyzed. Mode 34 is a rotational-axial mode, mode 35 is a substructure mode, and modes 36, 37 are translational-tilting modes. With gyroscopic effects, the degenerate translational-tilting modes split into distinct modes with phase indices 1 and $N_p - 1$. In this case, modes 36 and 37 have phase indices $d = 1$ and $d = 3$, respectively.

In the case with $Z_r = 100$ and $Z_s = 40$, the system is in-phase because Z_r/N_p and Z_s/N_p are integers. For the in-phase system, the suppression rules are independent of the harmonic number. The suppression rule for $\Omega_c < \Omega_r$ predicts that the parametric instability occurs between: two rotational-axial modes, two translational-tilting modes (one with phase index 1 and other with phase index $N_p - 1$), and two substructure modes (with phase indices d and $N_p - d$, where $d = 2$ for four-planet system). Fig. 5.7 shows single mode parametric instabilities occur for a rotational-axial mode (ω_{34}) and a substructure

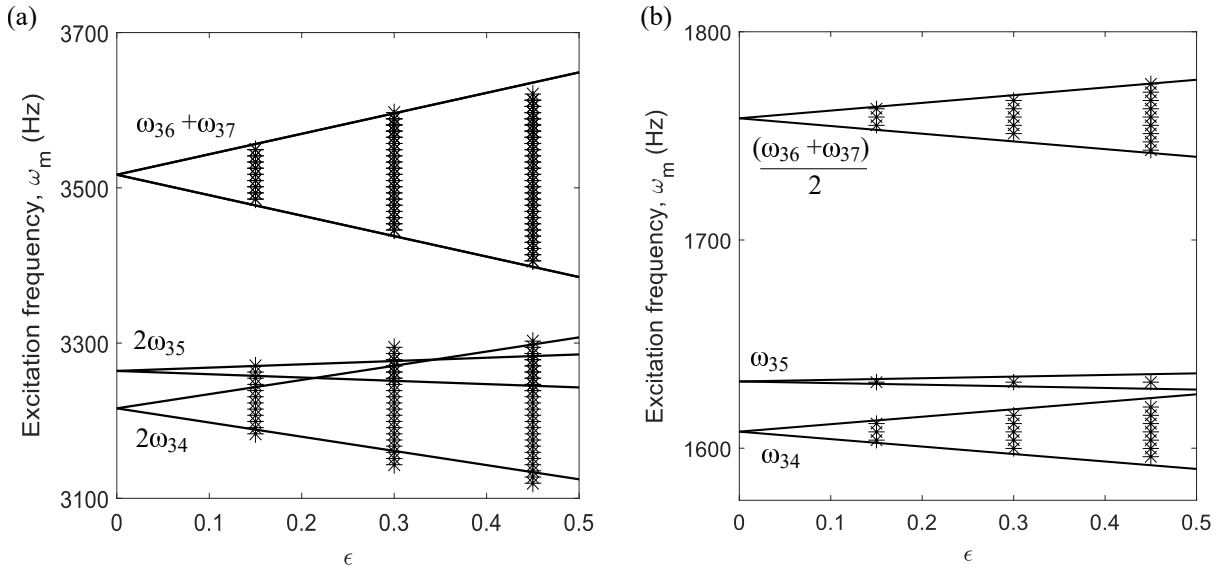

Figure 5.7: Instability regions for four-planet planetary gear in Fig. 4.3 with $Z_r = 100, Z_s = 40$ and at ring rotation speed $\Omega_r = 1000$rpm and stationary carrier for a range of ϵ. The solid lines are perturbation predictions from Eq. (5.13), and the asterisks are the Floquet theory predictions. (a) $L = 1$, (b) $L = 2$.

mode (ω_{35}). A combination instability occurs for two split translational-tilting modes (ω_{36}, ω_{37}) with different phase indices. Other combinations of natural frequencies show negligible instability bandwidths and are neglected in Fig. 5.7 for clarity.

Fig. 5.8 shows parametric instability regions for an out-of-phase four-planet planetary gear with $Z_r = 102$ and $Z_s = 40$. The natural frequencies (ω_{34} to ω_{37}) and mode type of the planetary gear in Fig. 4.3 remain the same, as compared to the in-phase system case. According to the suppression rule Eq. (5.19b), for the first harmonic of mesh stiffnesses ($L = 1$), the parametric instabilities can occur between: a rotational-axial mode and a substructure mode (ω_{34}, ω_{35}), two translational-tilting modes with phase index 1, and two translational-tilting modes with phase index 3, as seen in Fig. 5.8(a). For the second harmonic ($L = 2$) shown in Fig. 5.8(b), the parametric instabilities occur between: two rotational-axial modes (ω_{34}), two substructure modes (ω_{35}), and two translational-tilting

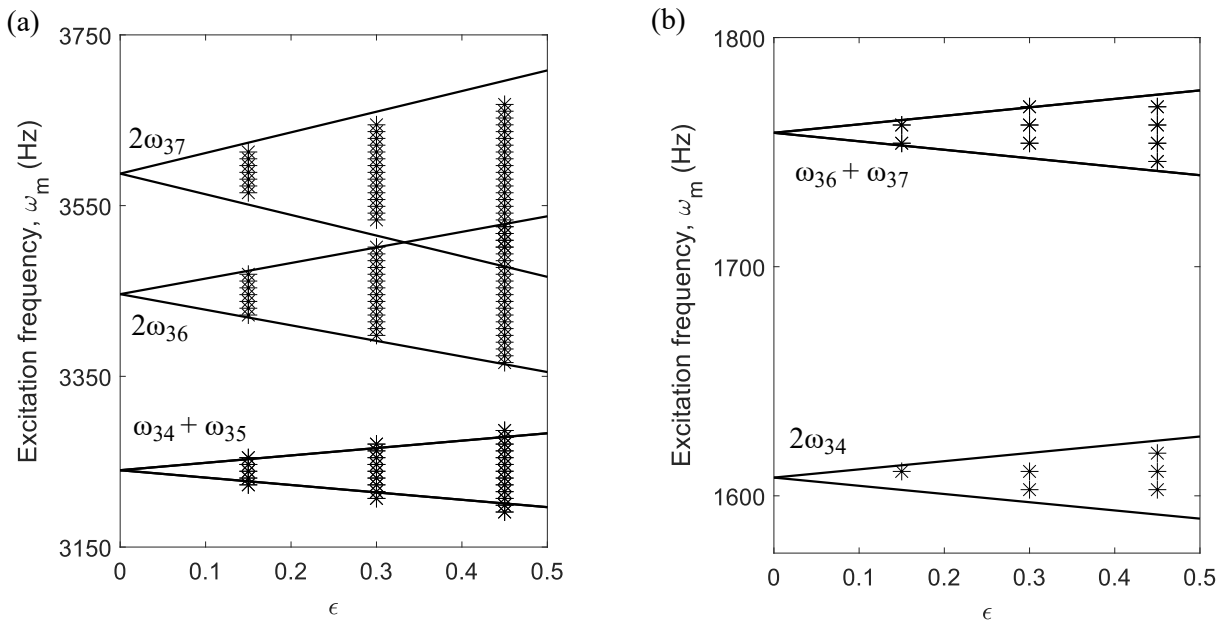

Figure 5.8: Instability regions for four-planet planetary gear in Fig. 4.3 with $Z_r = 102, Z_s = 40$ and at ring rotation speed $\Omega_r = 1000$rpm and a stationary carrier. The solid lines are perturbation predictions from Eq. (5.13), and the asterisks are the Floquet theory predictions. (a) $L = 1$, (b) $L = 2$.

modes, one with phase index 1 (ω_{36}) and other with phase index 3 (ω_{37}). The instability regions obtained using the closed-form analytical expression compare well with numerical integration results from Floquet theory.

Figs. 5.7 and 5.8 show different parametric instability regions even for an identical planetary gear system with small difference in the number of gear teeth. Thus, potential parametric instabilities with large bandwidths can be suppressed by changing the number of gear teeth and with minimal change in the natural frequencies and vibration modes.

5.5 Conclusions

The developed semi-analytical model for spinning, coupled systems and spinning rotationally periodic systems can be used to predict parametric instabilities in coupled rotating systems.

The time-varying coupling elements that act as a source of parametric instability in the system are investigated. Parametric instability regions obtained for a rotating body coupled to space-fixed, time-varying coupling stiffness using the method of multiple scales compares well with numerical results from Floquet theory. The vibration modes with large deflections in the time-varying, coupling element and large modal coupling strain energy lead to large parametric instability bandwidths. These vibration modes are highly susceptible to parametric resonance, where the system vibrates at the two natural frequencies that sum to a Fourier harmonic of the excitation frequency.

The parametric instability regions are also investigated for a rotationally periodic system with equally spaced substructures. The parametric instability boundaries predicted by the analytical expression compare well with Floquet theory predictions. The system symmetry results in suppression rules that define the combination of mode types that can cause parametric instability, and when parametric instability can be suppressed.

Appendices

Appendix A

Chapter 1

A.1 Two-dimensional cross-section elemental matrices

The 0^{th} and n^{th} harmonic nodal coefficients of an element are represented by $\mathbf{q}_{0_e} = \{\mathbf{U}_0^e, \mathbf{V}_0^e, \mathbf{W}_0^e\}$ and $\mathbf{q}_{n_e} = \{\mathbf{U}_{nc}^e, \mathbf{U}_{ns}^e, \mathbf{V}_{ns}^e, \mathbf{V}_{nc}^e, \mathbf{W}_{nc}^e, \mathbf{W}_{ns}^e\}$, respectively. The superscript 'e' in the local shape functions $\mathbf{\Psi}_u^e$, $\mathbf{\Psi}_v^e$, and $\mathbf{\Psi}_w^e$ of Eq. (2.15) are dropped in the following equations.

The mass matrix $\mathbf{m}_e$ of an element for all harmonics is $\mathbf{m}_e = \text{diag}(\mathbf{m}_e^0, \mathbf{m}_e^1, ..., \mathbf{m}_e^n)$, where

$$\mathbf{m}_e^0 = \text{diag}(\mathbf{m}_{uu}^0, \mathbf{m}_{vv}^0, \mathbf{m}_{ww}^0),$$
$$\mathbf{m}_e^n = \text{diag}(\mathbf{m}_{uu}^n, \mathbf{m}_{uu}^n, \mathbf{m}_{vv}^n, \mathbf{m}_{vv}^n, \mathbf{m}_{ww}^n, \mathbf{m}_{ww}^n), \tag{A.1}$$

$$\mathbf{m}^0_{uu} = 2\pi\int_{A_e}\rho\boldsymbol{\Psi}^T_u\boldsymbol{\Psi}_u r\mathrm{d}A_e, \qquad \mathbf{m}^0_{vv} = 2\pi\int_{A_e}\rho\boldsymbol{\Psi}^T_v\boldsymbol{\Psi}_v r\mathrm{d}A_e,$$
$$\mathbf{m}^0_{ww} = 2\pi\int_{A_e}\rho\boldsymbol{\Psi}^T_w\boldsymbol{\Psi}_w r\mathrm{d}A_e,$$
$$\mathbf{m}^n_{uu} = \pi\int_{A_e}\rho\boldsymbol{\Psi}^T_u\boldsymbol{\Psi}_u r\mathrm{d}A_e, \qquad \mathbf{m}^n_{vv} = \pi\int_{A_e}\rho\boldsymbol{\Psi}^T_v\boldsymbol{\Psi}_v r\mathrm{d}A_e,$$
$$\mathbf{m}^n_{ww} = \pi\int_{A_e}\rho\boldsymbol{\Psi}^T_w\boldsymbol{\Psi}_w r\mathrm{d}A_e.$$

The gyroscopic matrix of an element is $\mathbf{g}_e = \mathrm{diag}(\mathbf{g}^0_e, \mathbf{g}^1_e, ..., \mathbf{g}^n_e)$, where

$$\mathbf{g}^0_e = \begin{bmatrix} \mathbf{0} & \mathbf{g}^0_{uv} & \mathbf{0} \\ -\mathbf{g}^{0\ T}_{uv} & \mathbf{0} & \mathbf{0} \\ \mathbf{0} & \mathbf{0} & \mathbf{0} \end{bmatrix}, \ \mathbf{g}^n_e = \begin{bmatrix} \mathbf{0} & \mathbf{g}^n_{uu} & \mathbf{0} & \mathbf{g}^n_{uv} & \mathbf{0} & \mathbf{0} \\ -\mathbf{g}^{n\ T}_{uu} & \mathbf{0} & -\mathbf{g}^n_{uv} & \mathbf{0} & \mathbf{0} & \mathbf{0} \\ \mathbf{0} & \mathbf{g}^{n\ T}_{uv} & \mathbf{0} & \mathbf{g}^n_{vv} & \mathbf{0} & \mathbf{0} \\ -\mathbf{g}^{n\ T}_{uv} & \mathbf{0} & -\mathbf{g}^{n\ T}_{vv} & \mathbf{0} & \mathbf{0} & \mathbf{0} \\ \mathbf{0} & \mathbf{0} & \mathbf{0} & \mathbf{0} & \mathbf{0} & \mathbf{g}^n_{ww} \\ \mathbf{0} & \mathbf{0} & \mathbf{0} & \mathbf{0} & -\mathbf{g}^{n\ T}_{ww} & \mathbf{0} \end{bmatrix}, \quad \text{(A.2)}$$

$$\mathbf{g}^0_{uv} = -4\pi\int_{A_e}\rho\boldsymbol{\Psi}^T_u\boldsymbol{\Psi}_v r\mathrm{d}A_e,$$
$$\mathbf{g}^n_{uu} = 2\pi\int_{A_e}\rho n\boldsymbol{\Psi}^T_u\boldsymbol{\Psi}_u r\mathrm{d}A_e, \qquad \mathbf{g}^n_{uv} = -2\pi\int_{A_e}\rho\boldsymbol{\Psi}^T_u\boldsymbol{\Psi}_v r\mathrm{d}A_e,$$
$$\mathbf{g}^n_{vv} = 2\pi\int_{A_e}\rho n\boldsymbol{\Psi}^T_v\boldsymbol{\Psi}_v r\mathrm{d}A_e, \qquad \mathbf{g}^n_{ww} = 2\pi\int_{A_e}\rho n\boldsymbol{\Psi}^T_w\boldsymbol{\Psi}_w r\mathrm{d}A_e.$$

The centripetal matrix of an element is $\mathbf{c}_e = \mathrm{diag}(\mathbf{c}_e^0, \mathbf{c}_e^1, ..., \mathbf{c}_e^n)$, where

$$\mathbf{c}_e^0 = \mathrm{diag}(\mathbf{c}_{uu}^0, \mathbf{c}_{vv}^0, \mathbf{c}_{ww}^0),$$

$$\mathbf{c}_e^n = \begin{bmatrix} \mathbf{c}_{uu}^n & \mathbf{0} & \mathbf{c}_{uv}^n & \mathbf{0} & \mathbf{0} & \mathbf{0} \\ \mathbf{0} & \mathbf{c}_{uu}^n & \mathbf{0} & \mathbf{c}_{uv}^n & \mathbf{0} & \mathbf{0} \\ \mathbf{c}_{uv}^{n\ T} & \mathbf{0} & \mathbf{c}_{vv}^n & \mathbf{0} & \mathbf{0} & \mathbf{0} \\ \mathbf{0} & \mathbf{c}_{uv}^{n\ T} & \mathbf{0} & \mathbf{c}_{vv}^n & \mathbf{0} & \mathbf{0} \\ \mathbf{0} & \mathbf{0} & \mathbf{0} & \mathbf{0} & \mathbf{c}_{ww}^n & \mathbf{0} \\ \mathbf{0} & \mathbf{0} & \mathbf{0} & \mathbf{0} & \mathbf{0} & \mathbf{c}_{ww}^n \end{bmatrix}, \tag{A.3}$$

$$\mathbf{c}_{uu}^0 = 2\pi \int_{A_e} \rho \mathbf{\Psi}_u^T \mathbf{\Psi}_u r \mathrm{d}A_e, \qquad \mathbf{c}_{vv}^0 = 2\pi \int_{A_e} \rho \mathbf{\Psi}_v^T \mathbf{\Psi}_v r \mathrm{d}A_e,$$
$$\mathbf{c}_{uu}^n = \pi \int_{A_e} \rho(1+n^2) \mathbf{\Psi}_u^T \mathbf{\Psi}_u r \mathrm{d}A_e, \qquad \mathbf{c}_{uv}^n = -2\pi \int_{A_e} \rho n \mathbf{\Psi}_u^T \mathbf{\Psi}_v r \mathrm{d}A_e,$$
$$\mathbf{c}_{vv}^n = \pi \int_{A_e} \rho(1+n^2) \mathbf{\Psi}_v^T \mathbf{\Psi}_v r \mathrm{d}A_e, \qquad \mathbf{c}_{ww}^n = \pi \int_{A_e} \rho n^2 \mathbf{\Psi}_w^T \mathbf{\Psi}_w r \mathrm{d}A_e.$$

The rotation-induced constant centripetal acceleration vector of an element is $\mathbf{F}_\Omega = (\mathbf{f}_\Omega^0, \mathbf{0}, ..., \mathbf{0})^{\mathrm{T}}$, where

$$\mathbf{f}_\Omega^0 = (\mathbf{f}_u^0, \mathbf{0}, \mathbf{0}), \tag{A.4}$$
$$\mathbf{f}_u^0 = 2\pi \int_{A_e} \rho \mathbf{\Psi}_u r^2 \mathrm{d}A_e.$$

The deformation matrix components $\mathbf{B}_e$, $\mathbf{S}_e(\mathbf{q}_e)$, and $\boldsymbol{\beta}_e$ for an element in Eq.

(2.21) with $c_n = \cos n\theta$ and $s_n = \sin n\theta$ are

$$\mathbf{B}_e = \text{diag}(\mathbf{B}_e^0, \mathbf{B}_e^1, ..., \mathbf{B}_e^n), \quad \mathbf{B}_e^n = \mathbf{B}_e^{nc} c_n + \mathbf{B}_e^{ns} s_n, \tag{A.5}$$
$$\boldsymbol{\beta}_e = \text{diag}(\boldsymbol{\beta}_e^0, \boldsymbol{\beta}_e^1, ..., \boldsymbol{\beta}_e^n),$$

$$\mathbf{B}_e^0 = \begin{bmatrix} \frac{\partial \boldsymbol{\Psi}_u}{\partial r} & \mathbf{0} & \mathbf{0} \\ \frac{\boldsymbol{\Psi}_u}{r} & \mathbf{0} & \mathbf{0} \\ \mathbf{0} & \mathbf{0} & \frac{\partial \boldsymbol{\Psi}_w}{\partial z} \\ \mathbf{0} & \left(\frac{\partial \boldsymbol{\Psi}_v}{\partial r} - \frac{\boldsymbol{\Psi}_v}{r}\right) & \mathbf{0} \\ \mathbf{0} & \frac{\partial \boldsymbol{\Psi}_v}{\partial z} & \mathbf{0} \\ \frac{\partial \boldsymbol{\Psi}_u}{\partial z} & \mathbf{0} & \frac{\partial \boldsymbol{\Psi}_w}{\partial r} \end{bmatrix}, \tag{A.6}$$

$$\mathbf{B}_e^{nc} = \begin{bmatrix} \frac{\partial \boldsymbol{\Psi}_u}{\partial r} & \mathbf{0} & \mathbf{0} & \mathbf{0} & \mathbf{0} & \mathbf{0} \\ \frac{\boldsymbol{\Psi}_u}{r} & \mathbf{0} & -\frac{n\boldsymbol{\Psi}_v}{r} & \mathbf{0} & \mathbf{0} & \mathbf{0} \\ \mathbf{0} & \mathbf{0} & \mathbf{0} & \mathbf{0} & \frac{\partial \boldsymbol{\Psi}_w}{\partial z} & \mathbf{0} \\ \mathbf{0} & \frac{n\boldsymbol{\Psi}_u}{r} & \mathbf{0} & \left(\frac{\partial \boldsymbol{\Psi}_v}{\partial r} - \frac{\boldsymbol{\Psi}_v}{r}\right) & \mathbf{0} & \mathbf{0} \\ \mathbf{0} & \mathbf{0} & \mathbf{0} & \frac{\partial \boldsymbol{\Psi}_v}{\partial z} & \mathbf{0} & \frac{n\boldsymbol{\Psi}_w}{r} \\ \frac{\partial \boldsymbol{\Psi}_u}{\partial z} & \mathbf{0} & \mathbf{0} & \mathbf{0} & \frac{\partial \boldsymbol{\Psi}_w}{\partial r} & \mathbf{0} \end{bmatrix},$$

$$\mathbf{B}_e^{ns} = \begin{bmatrix} \mathbf{0} & \frac{\partial \boldsymbol{\Psi}_u}{\partial r} & \mathbf{0} & \mathbf{0} & \mathbf{0} & \mathbf{0} \\ \mathbf{0} & \frac{\boldsymbol{\Psi}_u}{r} & \mathbf{0} & -\frac{n\boldsymbol{\Psi}_v}{r} & \mathbf{0} & \mathbf{0} \\ \mathbf{0} & \mathbf{0} & \mathbf{0} & \mathbf{0} & \mathbf{0} & \frac{\partial \boldsymbol{\Psi}_w}{\partial z} \\ -\frac{n\boldsymbol{\Psi}_u}{r} & \mathbf{0} & -\left(\frac{\partial \boldsymbol{\Psi}_v}{\partial r} - \frac{\boldsymbol{\Psi}_v}{r}\right) & \mathbf{0} & \mathbf{0} & \mathbf{0} \\ \mathbf{0} & \mathbf{0} & -\frac{\partial \boldsymbol{\Psi}_v}{\partial z} & \mathbf{0} & -\frac{n\boldsymbol{\Psi}_w}{r} & \mathbf{0} \\ \mathbf{0} & \frac{\partial \boldsymbol{\Psi}_u}{\partial z} & \mathbf{0} & \mathbf{0} & \mathbf{0} & \frac{\partial \boldsymbol{\Psi}_w}{\partial r} \end{bmatrix},$$

$$\mathbf{S}_e(\mathbf{q}_e) = \begin{bmatrix} \mu_{ru} & \mu_{rv} & \mu_{rw} & 0 & 0 & 0 & 0 & 0 & 0 \\ 0 & 0 & 0 & \mu_{\theta u} & \mu_{\theta v} & \mu_{\theta w} & 0 & 0 & 0 \\ 0 & 0 & 0 & 0 & 0 & 0 & \mu_{zu} & \mu_{zv} & \mu_{zw} \\ \mu_{\theta u} & \mu_{\theta v} & \mu_{\theta w} & \mu_{ru} & \mu_{rv} & \mu_{rw} & 0 & 0 & 0 \\ 0 & 0 & 0 & \mu_{zu} & \mu_{zv} & \mu_{zw} & \mu_{\theta u} & \mu_{\theta v} & \mu_{\theta w} \\ \mu_{zu} & \mu_{zv} & \mu_{zw} & 0 & 0 & 0 & \mu_{ru} & \mu_{rv} & \mu_{rw} \end{bmatrix}, \tag{A.7}$$

$$\begin{gathered} \mu_{ru} = \tfrac{\partial u_e}{\partial r}, \quad \mu_{rv} = \tfrac{\partial v_e}{\partial r}, \quad \mu_{rw} = \tfrac{\partial w_e}{\partial r}, \\ \mu_{\theta u} = \tfrac{1}{r}\left(\tfrac{\partial u_e}{\partial \theta} - v_e\right), \quad \mu_{\theta v} = \tfrac{1}{r}\left(\tfrac{\partial v_e}{\partial \theta} + u_e\right), \quad \mu_{\theta w} = \tfrac{1}{r}\tfrac{\partial w_e}{\partial \theta}, \\ \mu_{zu} = \tfrac{\partial u_e}{\partial z}, \quad \mu_{zv} = \tfrac{\partial v_e}{\partial z}, \quad \mu_{zw} = \tfrac{\partial w_e}{\partial z}, \end{gathered} \tag{A.8}$$

$$\boldsymbol{\beta}_e^0 = \begin{bmatrix} \frac{\partial \boldsymbol{\Psi}_u}{\partial r} & \mathbf{0} & \mathbf{0} \\ \mathbf{0} & \frac{\partial \boldsymbol{\Psi}_v}{\partial r} & \mathbf{0} \\ \mathbf{0} & \mathbf{0} & \frac{\partial \boldsymbol{\Psi}_w}{\partial r} \\ \mathbf{0} & -\frac{\boldsymbol{\Psi}_v}{r} & \mathbf{0} \\ \frac{\boldsymbol{\Psi}_u}{r} & \mathbf{0} & \mathbf{0} \\ \mathbf{0} & \mathbf{0} & \mathbf{0} \\ \frac{\partial \boldsymbol{\Psi}_u}{\partial z} & \mathbf{0} & \mathbf{0} \\ \mathbf{0} & \frac{\partial \boldsymbol{\Psi}_v}{\partial z} & \mathbf{0} \\ \mathbf{0} & \mathbf{0} & \frac{\partial \boldsymbol{\Psi}_w}{\partial z} \end{bmatrix}, \tag{A.9}$$

$$\boldsymbol{\beta}_e^n = \begin{bmatrix} \frac{\partial \boldsymbol{\Psi}_u}{\partial r} c_n & \frac{\partial \boldsymbol{\Psi}_u}{\partial r} s_n & \mathbf{0} & \mathbf{0} & \mathbf{0} & \mathbf{0} \\ \mathbf{0} & \mathbf{0} & -\frac{\partial \boldsymbol{\Psi}_v}{\partial r} s_n & \frac{\partial \boldsymbol{\Psi}_v}{\partial r} c_n & \mathbf{0} & \mathbf{0} \\ \mathbf{0} & \mathbf{0} & \mathbf{0} & \mathbf{0} & \frac{\partial \boldsymbol{\Psi}_w}{\partial r} c_n & \frac{\partial \boldsymbol{\Psi}_w}{\partial r} s_n \\ -\frac{n\boldsymbol{\Psi}_u}{r} s_n & \frac{n\boldsymbol{\Psi}_u}{r} c_n & \frac{\boldsymbol{\Psi}_v}{r} s_n & \frac{\boldsymbol{\Psi}_v}{r} c_n & \mathbf{0} & \mathbf{0} \\ \frac{\boldsymbol{\Psi}_u}{r} c_n & \frac{\boldsymbol{\Psi}_u}{r} s_n & -\frac{n\boldsymbol{\Psi}_v}{r} c_n & \frac{n\boldsymbol{\Psi}_v}{r} s_n & \mathbf{0} & \mathbf{0} \\ \mathbf{0} & \mathbf{0} & \mathbf{0} & \mathbf{0} & -\frac{n\boldsymbol{\Psi}_w}{r} s_n & \frac{n\boldsymbol{\Psi}_w}{r} c_n \\ \frac{\partial \boldsymbol{\Psi}_u}{\partial z} c_n & \frac{\partial \boldsymbol{\Psi}_u}{\partial z} s_n & \mathbf{0} & \mathbf{0} & \mathbf{0} & \mathbf{0} \\ \mathbf{0} & \mathbf{0} & -\frac{\partial \boldsymbol{\Psi}_v}{\partial z} s_n & \frac{\partial \boldsymbol{\Psi}_v}{\partial z} c_n & \mathbf{0} & \mathbf{0} \\ \mathbf{0} & \mathbf{0} & \mathbf{0} & \mathbf{0} & \frac{\partial \boldsymbol{\Psi}_w}{\partial z} c_n & \frac{\partial \boldsymbol{\Psi}_w}{\partial z} s_n \end{bmatrix}.$$

A.2 One-dimensional cross-section elemental stiffness matrices

Substitution of the displacement field approximations of Eq. (2.52) into the strain-displacement relations of an axisymmetric shell Eq. (2.47) leads to matrix forms of the

relation with $c_n = \cos n\theta$ and $s_n = \sin n\theta$ as

$$\boldsymbol{\epsilon}_e = \mathbf{B}_e\mathbf{q}_e + \tfrac{1}{2}\mathbf{S}_e(\mathbf{q}_e)\boldsymbol{\beta}_e\mathbf{q}_e, \quad \boldsymbol{\kappa} = \mathbf{B}_{\kappa_e}\mathbf{q}_e, \tag{A.10}$$

$$\mathbf{B}_e = \mathrm{diag}(\mathbf{B}_e^0, \mathbf{B}_e^1, ..., \mathbf{B}_e^n), \quad \mathbf{B}_e^n = \mathbf{B}_e^{nc}c_n + \mathbf{B}_e^{ns}s_n,$$

$$\mathbf{B}_{\kappa e} = \mathrm{diag}(\mathbf{B}_{\kappa e}^0, \mathbf{B}_{\kappa e}^1, ..., \mathbf{B}_{\kappa e}^n), \quad \mathbf{B}_{\kappa e}^n = \mathbf{B}_{\kappa_e}^{nc}c_n + \mathbf{B}_{\kappa_e}^{ns}s_n,$$

$$\boldsymbol{\beta}_e = \mathrm{diag}(\boldsymbol{\beta}_e^0, \boldsymbol{\beta}_e^1, ..., \boldsymbol{\beta}_e^n), \quad \boldsymbol{\beta}_e^n = \boldsymbol{\beta}_e^{nc}c_n + \boldsymbol{\beta}_e^{ns}s_n.$$

The deformation matrices in Eq. (A.10) are

$$\mathbf{B}_e^{nc} = \begin{bmatrix} \frac{1}{A_\alpha}\frac{\partial \boldsymbol{\Psi}_u}{\partial \alpha} & \mathbf{0} & \mathbf{0} & \mathbf{0} & \frac{\boldsymbol{\Psi}_w}{R_\alpha} & \mathbf{0} \\ \frac{\boldsymbol{\Psi}_u}{A_\alpha A_\theta}\frac{\partial A_\theta}{\partial \alpha} & \mathbf{0} & -\frac{n\boldsymbol{\Psi}_v}{A_\theta} & \mathbf{0} & \frac{\boldsymbol{\Psi}_w}{R_\theta} & \mathbf{0} \\ \mathbf{0} & \frac{n\boldsymbol{\Psi}_u}{A_\theta} & \mathbf{0} & \frac{1}{A_\alpha}\frac{\partial \boldsymbol{\Psi}_v}{\partial \alpha} - \frac{\boldsymbol{\Psi}_v}{A_\alpha A_\theta}\frac{\partial A_\theta}{\partial \alpha} & \mathbf{0} & \mathbf{0} \end{bmatrix}, \tag{A.11a}$$

$$\mathbf{B}_e^{ns} = \begin{bmatrix} \mathbf{0} & \frac{1}{A_\alpha}\frac{\partial \boldsymbol{\Psi}_u}{\partial \alpha} & \mathbf{0} & \mathbf{0} & \mathbf{0} & \frac{\boldsymbol{\Psi}_w}{R_\alpha} \\ \mathbf{0} & \frac{\boldsymbol{\Psi}_u}{A_\alpha A_\theta}\frac{\partial A_\theta}{\partial \alpha} & \mathbf{0} & -\frac{n\boldsymbol{\Psi}_v}{A_\theta} & \mathbf{0} & \frac{\boldsymbol{\Psi}_w}{R_\theta} \\ -\frac{n\boldsymbol{\Psi}_u}{A_\theta} & \mathbf{0} & -\frac{1}{A_\alpha}\frac{\partial \boldsymbol{\Psi}_v}{\partial \alpha} + \frac{\boldsymbol{\Psi}_v}{A_\alpha A_\theta}\frac{\partial A_\theta}{\partial \alpha} & \mathbf{0} & \mathbf{0} & \mathbf{0} \end{bmatrix}, \tag{A.11b}$$

$$\mathbf{B}_{\kappa_e}^{nc} = \begin{bmatrix} \frac{1}{A_\alpha}\frac{\partial}{\partial \alpha}\left(\frac{\boldsymbol{\Psi}_u}{R_\alpha}\right) & \mathbf{0} & \mathbf{0} & \mathbf{0}... \\ & & -\frac{1}{A_\alpha}\frac{\partial}{\partial \alpha}\left(\frac{1}{A_\alpha}\frac{\partial \boldsymbol{\Psi}_w}{\partial \alpha}\right) & \mathbf{0} \\ \frac{\boldsymbol{\Psi}_u}{A_\alpha A_\theta R_\alpha}\frac{\partial A_\theta}{\partial \alpha} & \mathbf{0} & -\frac{n\boldsymbol{\Psi}_v}{A_\theta R_\theta} & \mathbf{0}... \\ & & -\frac{1}{A_\alpha^2 A_\theta}\frac{\partial A_\theta}{\partial \alpha}\frac{\partial \boldsymbol{\Psi}_w}{\partial \alpha} + \frac{n^2\boldsymbol{\Psi}_w}{A_\theta^2} & \mathbf{0} \\ \frac{\boldsymbol{\Psi}_u}{R_\alpha A_\theta} & -\frac{n\boldsymbol{\Psi}_u}{2A_\theta}\left(\frac{1}{R_\theta} - \frac{1}{R_\alpha}\right) & \mathbf{0} & \frac{\boldsymbol{\Psi}_v}{A_\alpha R_\theta} - \frac{\boldsymbol{\Psi}_v}{A_\alpha A_\theta R_\theta}\frac{\partial A_\theta}{\partial \alpha} + \frac{1}{2A_\alpha A_\theta}\frac{\partial (A_\theta \boldsymbol{\Psi}_v)}{\partial \alpha}... \\ & & -\frac{1}{A_\alpha A_\theta}\frac{\partial \boldsymbol{\Psi}_w}{\partial \alpha} & \frac{n\boldsymbol{\Psi}_w}{A_\alpha A_\theta}\left(-1 + \frac{1}{A_\theta}\frac{\partial A_\theta}{\partial \alpha}\right) \end{bmatrix} \tag{A.11c}$$

$$\mathbf{B}^{ns}_{\kappa_e} = \begin{bmatrix} \mathbf{0} & \frac{1}{A_\alpha}\frac{\partial}{\partial\alpha}\left(\frac{\boldsymbol{\Psi}_u}{R_\alpha}\right) & \mathbf{0} & \mathbf{0}... \\ & & \mathbf{0} & -\frac{1}{A_\alpha}\frac{\partial}{\partial\alpha}\left(\frac{1}{A_\alpha}\frac{\partial\boldsymbol{\Psi}_w}{\partial\alpha}\right) \\ \mathbf{0} & \frac{\boldsymbol{\Psi}_u}{A_\alpha A_\theta R_\alpha}\frac{\partial A_\theta}{\partial\alpha} & \mathbf{0} & \frac{n\boldsymbol{\Psi}_v}{A_\theta R_\theta}... \\ & & \mathbf{0} & -\frac{1}{A_\alpha^2 A_\theta}\frac{\partial A_\theta}{\partial\alpha}\frac{\partial\boldsymbol{\Psi}_w}{\partial\alpha} + \frac{n^2\boldsymbol{\Psi}_w}{A_\theta^2} \\ \frac{n\boldsymbol{\Psi}_u}{2A_\theta}\left(\frac{1}{R_\theta} - \frac{1}{R_\alpha}\right) & \frac{\boldsymbol{\Psi}_u}{R_\alpha A_\theta} & -\frac{\boldsymbol{\Psi}_v}{A_\alpha R_\theta} + \frac{\boldsymbol{\Psi}_v}{A_\alpha A_\theta R_\theta}\frac{\partial A_\theta}{\partial\alpha} - \frac{1}{2A_\alpha A_\theta}\frac{\partial(A_\theta\boldsymbol{\Psi}_v)}{\partial\alpha} & \mathbf{0}... \\ & & \frac{n\boldsymbol{\Psi}_w}{A_\alpha A_\theta}\left(1 - \frac{1}{A_\theta}\frac{\partial A_\theta}{\partial\alpha}\right) & -\frac{1}{A_\alpha A_\theta}\frac{\partial\boldsymbol{\Psi}_w}{\partial\alpha} \end{bmatrix} \tag{A.11d}$$

$$\boldsymbol{\beta}^{nc}_e = \begin{bmatrix} -\frac{\boldsymbol{\Psi}_u}{R_\alpha} & \mathbf{0} & \mathbf{0} & \mathbf{0} & \frac{1}{A_\alpha}\frac{\partial\boldsymbol{\Psi}_w}{\partial\alpha} & \mathbf{0} \\ \mathbf{0} & \mathbf{0} & \mathbf{0} & -\frac{\boldsymbol{\Psi}_v}{R_\theta} & \mathbf{0} & \frac{n\boldsymbol{\Psi}_w}{A_\theta} \\ \mathbf{0} & -\frac{n\boldsymbol{\Psi}_u}{2A_\theta} & \mathbf{0} & \frac{1}{2A_\alpha}\frac{\partial\boldsymbol{\Psi}_v}{\partial\alpha} + \frac{\boldsymbol{\Psi}_v}{2A_\alpha A_\theta}\frac{\partial A_\theta}{\partial\alpha} & \mathbf{0} & \mathbf{0} \end{bmatrix}, \tag{A.11e}$$

$$\boldsymbol{\beta}^{ns}_e = \begin{bmatrix} \mathbf{0} & -\frac{\boldsymbol{\Psi}_u}{R_\alpha} & \mathbf{0} & \mathbf{0} & \mathbf{0} & \frac{1}{A_\alpha}\frac{\partial\boldsymbol{\Psi}_w}{\partial\alpha} \\ \mathbf{0} & \mathbf{0} & \frac{\boldsymbol{\Psi}_v}{R_\theta} & \mathbf{0} & -\frac{n\boldsymbol{\Psi}_w}{A_\theta} & \mathbf{0} \\ \frac{n\boldsymbol{\Psi}_u}{2A_\theta} & \mathbf{0} & -\frac{1}{2A_\alpha}\frac{\partial\boldsymbol{\Psi}_v}{\partial\alpha} + \frac{\boldsymbol{\Psi}_v}{2A_\alpha A_\theta}\frac{\partial A_\theta}{\partial\alpha} & \mathbf{0} & \mathbf{0} & \mathbf{0} \end{bmatrix}, \tag{A.11f}$$

$$\mathbf{S}_e(\mathbf{q}_e) = \begin{bmatrix} \mu_1 & 0 & \mu_3 \\ 0 & \mu_2 & \mu_3 \\ \mu_2 & \mu_1 & 0 \end{bmatrix}, \tag{A.11g}$$

$$\mu_1 = \frac{1}{A_\alpha}\frac{\partial w_e}{\partial\alpha} - \frac{u_e}{R_\alpha}, \quad \mu_2 = \frac{1}{A_\theta}\frac{\partial w_e}{\partial\theta} - \frac{v_e}{R_\theta}, \quad \mu_3 = \frac{1}{2A_\alpha A_\theta}\left(\frac{\partial A_\theta v_e}{\partial\alpha} - \frac{\partial A_\alpha u_e}{\partial\theta}\right). \tag{A.11h}$$

The displacement approximations u_e, v_e, and w_e in Eq. (2.52) are substituted into Eqs. (A.11g) and (A.11h).

The linear elastic stiffness matrix obtained from the strain energy in Eq. (2.48) is $\mathbf{k}_e = \text{diag}(\mathbf{k}_e^0, \mathbf{k}_e^1, ..., \mathbf{k}_e^n)$, where

$$\mathbf{k}_e^n = \int_\alpha \int_0^{2\pi} \left(h\mathbf{B}_e^{nT}\mathbf{D}\mathbf{B}_e^n + \frac{h^3}{12}\mathbf{B}_{\kappa_e}^{n\ T}\mathbf{D}\mathbf{B}_{\kappa_e}^n \right) r \mathrm{d}\theta \mathrm{d}\alpha. \tag{A.12}$$

The nonlinear stiffness term $\mathbf{n}_e(\mathbf{q}_e)$ for a shell is analogous to Eq. (2.21b).

Bibliography

[1] V. Abousleiman and P. Velex. A hybrid 3D finite element/lumped parameter model for quasi-static and dynamic analyses of planetary/epicyclic gear sets. *Mechanism and Machine Theory*, 41(6):725–748, 2006.

[2] V. Abousleiman, P. Velex, and S. Becquerelle. Modeling of Spur and Helical Gear Planetary Drives With Flexible Ring Gears and Planet Carriers. *Journal of Mechanical Design*, 129(1):95–106, 2007.

[3] M. Amabili. *Nonlinear vibrations and stability of shells and plates*. Cambridge University Press, 2008.

[4] M. Amabili and A. Rivola. Dynamic analysis of spur gear pairs: Steady-state response and stability of the SDOF model with time-varying meshing damping. *Mechanical Systems and Signal Processing*, 11(3):375–390, 1997.

[5] V. K. Ambarisha and R. G. Parker. Nonlinear dynamics of planetary gears using analytical and finite element models. *Journal of Sound and Vibration*, 302(3):577–595, 2007.

[6] A. C. Antoulas, C. A. Beattie, and S. Gugercin. *Interpolatory Methods for Model Reduction*. Computational Science and Engineering 21, SIAM, 2020.

[7] N. K. Arakere and C. Nataraj. Vibration of high-speed spur gear webs. *Journal of Vibration and Acoustics*, 120(July 1998):791–800, 1998.

[8] I. Babuška. The Finite Element Method with Penalty. *Mathematics of Computation*, 27(122):221–228, 1973.

[9] Klaus-Jürgen Bathe. *Finite element procedures*. Klaus-Jurgen Bathe, 2006.

[10] C. W. Bert and T. L. C. Chen. On vibration of a thick flexible ring rotating at high speed. *Journal of Sound and Vibration*, 61(4):517–530, 1978.

[11] M. Botman. Epicyclic Gear Vibrations. *Journal of Engineering for Industry*, 98(3): 811–815, 1976.

[12] Vangipuram Canchi and R. G. Parker. Parametric Instability of a Rotating Circular Ring With Moving, Time-Varying Springs. *Journal of Vibration and Acoustics*, 128 (2):231, 2006.

[13] E. Carrera and M. Filippi. Vibration analysis of thin/thick, composites/metallic spinning cylindrical shells by refined beam models. *Journal of Vibration and Acoustics*, 137(3):031020, 2015.

[14] G. Chen. A new rotor-ball bearing-stator coupling dynamics model for whole aero-engine vibration. *Journal of Vibration and Acoustics*, 131:1–9, 2009.

[15] G. Chen. Vibration modelling and verifications for whole aero-engine. *Journal of Sound and Vibration*, 349:163–179, 2015.

[16] G. Chen. Simulation of casing vibration resulting from blade-casing rubbing and its verifications. *Journal of Sound and Vibration*, 361:190–209, 2016.

[17] G. Chen, C. G. Li, and D. Y. Wang. Nonlinear dynamic analysis and experiment verification of rotor-ball bearings-support-stator coupling system for aeroengine with rubbing coupling faults. *Journal of Engineering for Gas Turbines and Power*, 132:1–9, 2010.

[18] J. S. Chen. Stability Analysis of a Spinning Elastic Disk Under a Stationary Concentrated Edge Load. *Journal of Applied Mechanics*, 61:788–792, 1994.

[19] J. S. Chen. Parametric Resonance of a Spinning Disk Under Space- Fixed Pulsating Edge Loads. *Journal of Applied Mechanics*, 64:139–143, 1997.

[20] J.-S. Chen and J.-L. Jhu. On the in-plane vibration and stability of a spinning annular disk. *Journal of Sound and Vibration*, 195(4):585–593, 1996.

[21] J. S. Chen and C. C. Wong. Vibration and stability of a spinning disk in contact with evenly-spaced stationary load systems. *Journal of Vibration and Acoustics*, 120(1): 301–302, 1998.

[22] Y. Chen, H. B. Zhao, Z. P. Shen, I. Grieger, and B. H. Kroplin. Vibrations of high speed rotating shells with calculations for cylindrical shells. *Journal of Sound and Vibration*, 160(1):137–160, 1993.

[23] Z. Chen and Y. Shao. Dynamic simulation of planetary gear with tooth root crack in ring gear. *Engr. Failure Analysis*, 31:8–18, 2013.

[24] Ö. Civalek. An efficient method for free vibration analysis of rotating truncated conical shells. *International Journal of Pressure Vessels and Piping*, 83(1):1–12, 2006.

[25] R. W. Clough and Y. Rashid. Finite analysis of axi-symmetric solids. *Journal of Engineering Mechanics Division*, 91(1):71– 86, 1965.

[26] R. D. Cook, D. S. Malkus, M. E. Plesha, and R. J. Witt. *Concepts and Applications of Finite Element Analysis*. John Wiley & Sons, Inc., USA, 2007. ISBN 0470088214.

[27] C. G. Cooley and R. G. Parker. Vibration properties of high-speed planetary gears with gyroscopic effects. *Journal of Vibration and Acoustics*, 134(6):061014–1–11, 2012.

[28] C. G. Cooley and R. G. Parker. Vibration of high-speed rotating rings coupled to space-fixed stiffnesses. *Journal of Sound and Vibration*, 333(12):2631–2648, 2014.

[29] C. G. Cooley and R. G Parker. Vibration of high-speed compliant gear pairs. In *ASME 2016 International Design Engineering Technical Conferences and Computers and Information in Engineering Conference*, pages V008T10A042–V008T10A042. American Society of Mechanical Engineers, 2016.

[30] C. G. Cooley, R. G. Parker, and S. M. Vijayakar. An efficient finite element solution for gear dynamics. *IOP Conference Series: Materials Science and Engineering*, 10: 1–10, 2010.

[31] F. Cunliffe, J. D. Smith, and D. B. Welbourn. Dynamic Tooth Loads in Epicyclic Gears. *Journal of Engineering for Industry*, 95(May):578–584, 1974.

[32] C. D'Angelo. *Vibration and aeroelastic stability of a disk rotating in a fluid*. PhD thesis, University of California Berkeley, 1991.

[33] B. Dong and R.G. Parker. Modal properties of cyclically symmetric systems with central components vibrating as three-dimensional rigid bodies. *Journal of Sound and Vibration*, 435:350–371, 2018.

[34] T. M. Ericson and R.G. Parker. Planetary gear modal vibration experiments and correlation against lumped-parameter and finite element models. *Journal of Sound and Vibration*, 332(9):2350–2357, 2013.

[35] T. Eritenel and R. G. Parker. An investigation of tooth mesh nonlinearity and partial contact loss in gear pairs using a lumped-parameter model. *Mechanism and Machine Theory*, 56:28–51, 2012.

[36] T. Eritenel and R. G. Parker. Three-dimensional nonlinear vibration of gear pairs. *Journal of Sound and Vibration*, 331(15):3628–3648, 2012.

[37] T. Eritenel and R.G. Parker. Modal properties of three-dimensional helical planetary gears. *Journal of Sound and Vibration*, 325:397–420, 2009.

[38] J. Fayos, L. Baeza, F. D. Denia, and J. E. Tarancon. An eulerian coordinate-based method for analysing the structural vibrations of a solid of revolution rotating about its main axis. *Journal of Sound and Vibration*, 306:618–635, 2007.

[39] M. Filippi and E. Carrera. Dynamic analyses of axisymmetric rotors through three-dimensional approaches and high-fidelity beam theories. *Journal of Vibration and Acoustics*, 139(6):061008, 2017.

[40] R. D. Firouz-Abadi, M. A. Torkaman-Asadi, and M. Rahmanian. Whirling frequencies of thin spinning cylindrical shells surrounded by an elastic foundation. *Acta Mechanica*, 224:881–892, 2013.

[41] M Friswell, JET Penny, and SD Garvey. Model reduction for structures with damping and gyroscopic effects. In *Proceedings of the international seminar on modal analysis*, volume 3, pages 1151–1158. KU Leuven; 1998, 2001.

[42] M. I. Friswell, S. D. Garvey, and J. E. T. Penny. Model reduction using dynamic and iterated irs techniques. *Journal of Sound and Vibration*, 186(2):311–323, 1995.

[43] M. I. Friswell, J. E. T. Penny, S. D. Garvey, and A. W. Lees. *Dynamics of rotating machines*. Cambridge University Press, 2010.

[44] G. Genta. *Dynamics of Rotating System*. Springer, 2005.

[45] G. Genta and A. Tonoli. A Harmonic Finite Element for the Analysis of Flexural, Torsional and Axial Rotordynamic Behavior of Discs. *Journal of Sound and Vibration*, 196(1):19–43, 1996.

[46] M. Geradin and N. Kill. A new approach to finite element modelling of flexible rotors. *Engineering Computations*, 1(1):52–64, 1984.

[47] D. Guo and Z. Zheng. Vibration analysis of a prestressed rotating cylindrical shell under stationary point load. *International Journal of Structural Stability and Dynamics*, 6(4):527–539, 2006.

[48] D. Guo, Z. C. Zheng, and F. L. Chu. Vibration analysis of spinning cylindrical shells by finite element method. *International Journal of Solids and Structures*, 39(3):725–739, 2002.

[49] Y. Guo and R. G. Parker. Stiffness matrix calculation of rolling element bearings using a finite element/contact mechanics model. *Mechanism and Machine Theory*, 51:32–45, 2012.

[50] Q. Han and F. Chu. Effect of rotation on frequency characteristics of a truncated circular conical shell. *Archive of Applied Mechanics*, 83(12):1789–1800, 2013.

[51] J. Heilig and J. Wauer. Stability of a nonlinear brake system at high operating speeds. *Nonlinear Dynamics*, 34:235–247, 2003.

[52] T. Hidaka, Y. Terauchi, and K. Ishioka. Dynamic behavior of planetary gear: 2nd report, displacement of sun gear and ring gear. *Bulletin of JSME*, 19(138):1563–1570, 1976.

[53] T. Hidaka, Y. Terauchi, M. Nohara, and J.-I. Oshita. Dynamic behavior of planetary gear: 3rd report, displacement of ring gear in direction of line of action. *Bulletin of JSME*, 20(150):1663–1672, 1977.

[54] T. Hidaka, T. Ishida, Y. Zhang, M. Sashara, and Y. Tanioka. Vibration of a strain-wave

gearing in an industrial robot. *1990 International Power Transmission and Gearing Conference*, pages 789–794, 1990.

[55] A. Hmida, A. Hammami, M. T. Khabou, F. Chaari, and M. Haddar. Effect of elastic coupling on the modal characteristics of spur gearbox system. *Applied Acoustics*, 144: 71–84, 2019.

[56] D. Hochlenert, G. S. Korspeter, and P. Hagedorn. Friction induced vibration in moving continua and their application to brake squeal. *Journal of Applied Mechanics*, 74(3): 542–549, 2007.

[57] L. Hu and A. Palazzolo. An enhanced axisymmetric solid element for rotor dynamic model improvement. *Journal of Vibration and Acoustics*, 141:051002:1–13, 2019.

[58] L. Hua and K. Y. Lam. Frequency characteristics of a thin rotating cylindrical shell using the generalized differential quadrature method. *International Journal of Mechanical Sciences*, 40(5):443–459, 1998.

[59] L. Hua and K. Y. Lam. The generalized differential quadrature method for frequency analysis of a rotating conical shell with initial pressure. *International Journal for Numerical Methods in Engineering*, 48(12):1703–1722, 2000.

[60] J. Huang, C.M. Krousgrill, and A. K. Bajaj. An efficient approach to estimate critical value of friction coefficient in brake squeal analysis. *Journal of Applied Mechanics*, 74 (3):534–541, 2007.

[61] S. C. Huang and B. S. Hsu. Theory of receptance applied to modal analysis of a spinning disk with interior multi-point supports. *Journal of Vibration and Acoustics*, 114(4):468–476, 1992.

[62] S. C. Huang and B. S. Hsu. Modal analysis of a spinning cylindrical shell with interior point or circular line supports. *Journal of Vibration and Acoustics*, 115(4):535–543, 1993.

[63] S. C. Huang and B. S. Hsu. Vibrations of a spinning annular plate with multi-circular line guides. *Journal of sound and vibration*, 164(3):535–547, 1993.

[64] Shyh-Chin Huang and Werner Soedel. Effects of coriolis acceleration on the free and forced in-plane vibrations of rotating rings on elastic foundation. *Journal of sound and vibration*, 115(2):253–274, 1987.

[65] S. G. Hutton, S. Chonan, and B. F. Lehmann. Dynamic response of a guided circular saw. *Journal of Sound and Vibration*, 112(3):527–539, 1987.

[66] W. D. Iwan and T. L. Moeller. The stability of a spinning elastic disk with a transverse load system. *ASME Journal of Applied Mechanics*, 43(3):485–490, 1976.

[67] G. Jacquet-Richardet, M. Torkhani, P. Cartraud, F. Thouverez, T. Nouri Baranger, M. Herran, C. Gibert, S. Baguet, P. Almeida, and L. Peletan. Rotor to stator contacts in turbomachines. review and application. *Mechanical Systems and Signal Processing*, 40:401– 420, 2013.

[68] A. Kahraman. Planetary Gear Train Dynamics. *Journal of Mechanical Design*, 116 (3):713–720, 1994.

[69] A. Kahraman and R. Singh. Nonlinear dynamics of a spur gear pair. *Journal of Sound and Vibration*, 142(1):49–75, 1990.

[70] A. Kahraman and R. Singh. Non-linear dynamics of a spur gear pair. *Journal of sound and vibration*, 142(1):49–75, 1990.

[71] A. Kahraman and R. Singh. Interactions between time-varying mesh stiffness and clearance non-linearities in a geared system. *Journal of Sound and Vibration*, 146(1): 135–156, 1991.

[72] A. Kahraman, A. A. Kharazi, and M. Umrani. A deformable body dynamic analysis of planetary gears with thin rims. *Journal of Sound and Vibration*, 262(3):752–768, 2003.

[73] B. Kang. Dynamic stability of a spinning thick disk under nonconservative traction. *International Journal of Structural Stability and Dynamics*, 12(5):1–45, 2012.

[74] J. Kang. Squeal analysis of gyroscopic disc brake system based on finite element method. *International Journal of Mechanical Sciences*, 51:284–294, 2009.

[75] J. Kang, C. M. Krousgrill, and F. Sadeghi. Dynamic instability of a thin circular plate with friction interface and its application to disc brake squeal. *Journal of Sound and Vibration*, 316:164–179, 2008.

[76] J. Kang, C. M. Krousgrill, and F. Sadeghi. Comprehensive stability analysis of disc brake vibrations including gyroscopic, negative friction slope and mode-coupling mechanisms. *Journal of Sound and Vibration*, 324:387–407, 2009.

[77] C. W. Kennedy and J. P. Desai. Modeling and control of the mitsubishi pa-10 robot arm harmonic drive system. *IEEE/ASME Trasactions on Mechatronics*, 10(3), 2005.

[78] R. M. H. Khorasany and S. G. Hutton. Large displacement analysis of elastically constrained rotating disks with rigid body degrees of freedom. *International Journal of Mechanical Sciences*, 54(1):1–11, 2012.

[79] R. M. H. Khorasany and S. G. Hutton. Vibration Characteristics of Rotating Thin

Disks—Part II: Analytical Predictions. *Journal of Applied Mechanics*, 79(4):041007, 2012.

[80] Y. J. Kim and J. S. Bolton. Effects of rotation on the dynamics of a circular cylindrical shell with application to tire vibration. *Journal of Sound and Vibration*, 275:605–621, 2004.

[81] D. R. Kiracofe and R.G. Parker. Structured vibration modes of general compound planetary gear systems. *Journal of Vibration and Acoustics*, 129:1–16, 2007.

[82] J. Kirkhope and G. J. Wilson. Vibration and stress analysis of thin rotating discs using annular finite elements. *Journal of Sound and Vibration*, 44(4):461–474, 1976.

[83] L. Komzsik and A. Vollan. *Computational techniques of rotor dynamics with the finite element method*. CRC Press, 2012.

[84] E. Kramer. *Dynamics of rotors and foundations*. Springer-Verlag, New York, 1993.

[85] S. Kung, G. Stelzer, V. Belsky, and A. Bajer. Brake squeal analysis incorporating contact conditions and other nonlinear effects. *SAE Technical Report*, 2003-01-3343, 2003.

[86] K. Y. Lam and L. Hua. Vibration analysis of a rotating truncated circular conical shell. *International Journal of Solids and Structures*, 34(17):2183–2197, 1997.

[87] K.Y. Lam and L. Hua. Influence of Boundary Conditions on the Frequency Characteristics of a Rotating Truncated Circular Conical. *Journal of Sound and Vibration*, 223(2):171–195, 1999.

[88] T. H. Lee. A Dynamic Analysis for Elastic Structures Interacting with Rotating Machinery. *Journal of Aircraft*, 10(1):45–51, 1973.

[89] K. M. Liew, Y. G. Hu, T. Y. Ng, and X. Zhao. Dynamic stability of rotating cylindrical shells subjected to periodic axial loads. *International Journal of Solids and Structures*, 43(25-26):7553–7570, 2006.

[90] J. Lin and R. G. Parker. Analytical Characterization of the Unique Properties of Planetary Gear Free Vibration. *Journal of Vibration and Acoustics*, 121(3):316, 1999.

[91] J. Lin and R. G. Parker. Structured vibration characteristics of planetary gears with unequally spaced planets. *Journal of Sound and Vibration*, 233:921–928, 2000.

[92] J. Lin and R. G. Parker. Planetary gear parametric instability caused by mesh stiffness variation. *Journal of Sound and Vibration*, 249(1):129–145, 2002.

[93] C. Liu, C. G. Cooley, and R. G. Parker. Parametric instability of spinning elastic rings excited by fluctuating space-fixed stiffnesses. *Journal of Sound and Vibration*, 400: 533–549, 2017.

[94] G. Liu and R. G. Parker. Nonlinear dynamics of idler gear systems. *Nonlinear Dynamics*, 53:345–367, 2008.

[95] G. Liu, J. Hong, and R. G. Parker. Influence of simultaneous time-varying bearing and tooth mesh stiffness fluctuations on spur gear pair vibration. *Nonlinear Dynamics*, 97 (2):1403–1424, 2019.

[96] H. Ma, X. Zhao, Y. Teng, and B. Wen. Analysis of dynamic characteristics for a rotor system with pedestal looseness. *Shock and Vibration*, 18:13–27, 2011.

[97] L. Meirovitch. *Methods of Analytical Dynamics*. McGraw-Hill Book Company, United States, 1970.

[98] L. Meirovitch. A new method of solution of the eigenvalue problem for gyroscopic systems. *AIAA*, 12:1337–1342, 1974.

[99] L. Meirovitch. *Principles and techniques of vibrations*. Prentice-Hall Inc., 1997.

[100] MSC Nastran. Basic dynamic analysis user's guide. *MSC. Software Corporation. US A*, 2004.

[101] Ali H Nayfeh. *Perturbation methods*. John Wiley & Sons, 2008.

[102] H. D. Nelson and S. H. Crandall. Effect of elastic coupling on the modal characteristics of spur gearbox system. *Applied Acoustics*, 144:71–84, 2019.

[103] V. V. Novozhilov. *Thin Shell Theory*. Springer, Netherlands, 1964.

[104] B. Olson, S. W. Shaw, C. Shi, C. Pierre, and R.G. Parker. Circulant matrices and their application to vibration analysis. *Applied Mechanics Review*, 66:040803, 2014.

[105] K. Ono, J. S. Chen, and D. B. Bogy. Stability Analysis for the Head- Disk Interface in a Flexible Disk. *Journal of Applied Mechanics*, 58:1005–1014, 1991.

[106] H. Ouyang, J. E. Mottershead, M. P. Cartmell, and M. I. Friswell. Friction-induced parametric resonances in discs: effect of a negative friction-velocity relationship. *Journal of Sound and Vibration*, 209(2):251–264, 1998.

[107] H. Ouyang, W. Nack, Y. Yuan, and F. Chen. Numerical analysis of automotive disc brake squeal: a review. *International Journal of Vehicle Noise and Vibration*, 1:207–231, 2005.

[108] J. Padovan. Natural frequencies of rotating prestressed cylinders. *Journal of Sound and Vibration*, 31(4):469–482, 1973.

[109] R. G. Parker. On the eigenvalues and critical speed stability of gyroscopic continua. *Journal of Applied Mechanics*, 65(1):134–140, 1998.

[110] R. G. Parker and X. Wu. Vibration modes of planetary gears with unequally spaced planets and an elastic ring gear. *Journal of Sound and Vibration*, 329:2265–2275, 2010.

[111] R. G. Parker and X. Wu. Parametric Instability of Planetary Gears Having Elastic Continuum Ring Gears. *Journal of Vibration and Acoustics*, 134(4):041011–1–11, 2012.

[112] R. G. Parker, V. Agashe, and S. M. Vijayakar. Dynamic Response of a Planetary Gear System Using a Finite Element/Contact Mechanics Model. *Journal of Mechanical Design*, 122(3):304–310, 2000.

[113] R. G. Parker, S. M. Vijayakar, and T. Imajo. Non-linear dynamic response of a spur gear pair: modelling and experimental comparisons. *Journal of Sound and Vibration*, 237(3):435–455, 2000.

[114] L. E. Penzes and H. Kraus. Free vibration of prestressed cylindrical shells having arbitrary homogeneous boundary conditions. *AIAA Journal*, 10(10):1309–1313, 1972. doi: 10.2514/3.6605.

[115] N. C. Perkins and C. D. Mote Jr. Comments on curve veering in eigenvalue problems. *Journal of Sound and Vibration*, 106(3):451–463, 1986.

[116] X. Qiu, Q. Han, and F. Chu. Investigation of parametric instability of the planetary gear under speed fluctuations. *Shock and Vibration*, 2017.

[117] J. S. Rao. *History of rotating machinery dynamics*, volume 20. Springer Science & Business Media, 2011.

[118] E. S. Reddy and W. B. Rickford. On the in-plane vibrations of a rotating ring with equi-spaced spokes. *Journal of Sound and Vibration*, 103(4):533–544, 1985.

[119] Junuthula Narasimha Reddy. *An introduction to the finite element method*. McGraw-Hill, Inc., New York, 1993.

[120] Garth M Reese, Timothy F Walsh, and Manoj K Bhardwaj. Salinas–theory manual version 4.22. *SAND2011-8272, Sandia National Laboratories, Albuquerque, NM*, 2011.

[121] A. A. Renshaw. Determining stability boundaries using gyroscopic eigenfunctions. *Journal of Vibration and Acoustics*, 125:405–407, 2003.

[122] A. A. Renshaw and C. D. Mote. A perturbation solution for the flexible rotating disk: 26 non-linear equilibrium and stability under transverse loading. *Journal of Sound and Vibration*, 183(2):309–326, 1995.

[123] A. A. Renshaw and C. D. Mote Jr. Local stability of gyroscopic systems near vanishing eigenvalues. *Journal of Applied Mechanics*, 63(1):116–120, 1996.

[124] J. L. Sanders Jr. Nonlinear theories for thin shells. *Quarterly of Applied Mathematics*, 21(1):21–36, 1963.

[125] S. Sarkheil and M. S. Foumani. Free vibrational characteristics of rotating joined cylindrical-conical shells. *Thin-Walled Structures*, 107:657–670, 2016.

[126] I. Y. Shen and Y. Song. Stability and Vibration of a Rotating Circular Plate Subjected to Stationary In-Plane Edge Loads. *Journal of Applied Mechanics*, 63:121–127, 1996.

[127] J.-Y Shen, C. W. Tseng, and I. Y. Shen. Vibration of rotating disk / spindle systems with flexible housing / stator assemblies. *Journal of Sound and Vibration*, 271:725–756, 2004.

[128] C. Shi and R.G. Parker. Vibration mode structure and simplified modelling of cyclically symmetric or rotationally periodic systems. *Proceedings of the Royal Society A*, 471: 20140672, 2014.

[129] K. R. Sivadas. Vibration Analysis of Pre-Stressed Rotating Thick Circular Conical Shell. *Journal of Sound and Vibration*, 186:99–109, 1995.

[130] Michael Smith. *ABAQUS/Standard User's Manual, Version 6.9*. Dassault Systèmes Simulia Corp, United States, 2009.

[131] G. Spelsberg-Korspeter, D. Hochlenert, O. N. Kirillov, and P. Hagedorn. In- and Out-of-Plane Vibrations of a Rotating Plate With Frictional Contact: Investigations on Squeal Phenomena. *Journal of Applied Mechanics*, 76(4):041006, 2009.

[132] G. W. Stewart. A krylov–schur algorithm for large eigenproblems. *SIAM Journal on Matrix Analysis and Applications*, 23(3):601–614, 2001.

[133] S. Sun, S. Chu, and D. Cao. Vibration characteristics of thin rotating cylindrical shells with various boundary conditions. *Journal of Sound and Vibration*, 331(18):4170–4186, 2012.

[134] S. Sun, D. Cao, and S. Chu. Free vibration analysis of thin rotating cylindrical shells using wave propagation approach. *Archive of Applied Mechanics*, 83(4):521–531, 2013.

[135] K. S. Surana. Transition finite elements for axisymmetric stress analysis. *International Journal for Numerical Methods in Engineering*, 15:809–832, 1980.

[136] A. T. Tadeo and K. L. Cavalca. A comparison of flexible coupling models for updating in rotating machinery response. *Journal of the Brazilian Society of Mechanical Sciences and Engineering*, 25(3):235–246, 2003.

[137] W. C. Tai and I. Y. Shen. Parametric resonances of a spinning cyclic symmetric rotor assembled to a flexible stationary housing via multiple bearings. *Journal of Vibration and Acoustics*, 135:051030–1–9, 2013.

[138] S. Theodossiades and S. Natsiavas. Non-linear dynamics of gear-pair systems with periodic stiffness and backlash. *Journal of Sound and vibration*, 229(2):287–310, 2000.

[139] J. Tian and S. G. Hutton. Self-excited vibration in flexible rotating disks subjected to various transverse interactive forces: A general approach. *Journal of Applied Mechanics*, 66:800–805, 1999.

[140] G. V. Tordion and R Gauvin. Dynamic Stability of a Two-Stage Gear Train Under the Influence of Variable Meshing Stiffnesses. *Journal of Engineering for Industry*, 99: 785–791, 1977.

[141] C. W. Tseng, J.-Y. Shen, H. Kim, and I. Y. Shen. A Unified Approach to Analyze Vibration of Axisymmetric Rotating Structures with Flexible Stationary Parts. *Journal of Vibration and Acoustics*, 127(2):125, 2005.

[142] J. G. Tseng and J. A. Wickert. Nonconservative stability of a friction loaded disk. *Journal of Vibration and Acoustics*, 120(4):922–929, 1998.

[143] T. D. Tuttle and W. Seering. Modeling a harmonic drive gear transmission. In *[1993] Proceedings IEEE International Conference on Robotics and Automation*, pages 624–629 vol.2, 1993. doi: 10.1109/ROBOT.1993.291889.

[144] K. S. Vaidya and R. G. Parker. Space-fixed formulation for the vibration of rotating, prestressed, axisymmetric bodies and shells. *Journal of Sound and Vibration*, 495, 2021.

[145] E. Ventsel and T. Krauthammer. *Thin plates and shells*. Marcel Dekker, Inc, 2001.

[146] S. M. Vijayakar. A combined surface integral and finite element solution for a three-dimensional contact problem. *International Journal for Numerical Methods in Engineering*, 31:525–545, 1991.

[147] C. Wang and R. G. Parker. Dynamic modeling and mesh phasing-based spectral

analysis of quasi-static deformations of spinning planetary gears with a deformable ring. *Mechanical Systems and Signal Processing*, 136:106497, 2020.

[148] C. Wang and R. G. Parker. Modal properties and parametrically excited vibrations of spinning epicyclic/planetary gears with a deformable ring. *Journal of Sound and Vibration*, 494:115828, 2021.

[149] J. Wang, Y. Cao, and G. Lin. Vibration analysis of high-speed rotating conical shell with arbitrary boundary conditions. *Proc. Mtgs. Acoust.*, 29, 2016.

[150] J. Wang, Z. Wan, Z. Dong, and Z. Li. Research on performance test system of space harmonic reducer in high vacuum and low temperature environment. *Machines*, 9, 2021.

[151] N. Wang, C. Liu, D. Jiang, and K. Behdinan. Casing vibration response prediction of dual-rotor-blade-casing system with blade-casing rubbing. *Mechanical Systems and Signal Processing*, 118:61–77, 2019.

[152] Nanfei Wang, Dongxiang Jiang, and Hongzhi Xu. Dynamic characteristics analysis of a dual-rotor system with inter-shaft bearing. *Proceedings of the Institution of Mechanical Engineers, Part G: Journal of Aerospace Engineering*, 233(3):1147–1158, 2019.

[153] S. Wang, C. Bi, J. Li, and C. Zheng. Parametric instability of anisotropic rotor-bearing systems with a transverse crack. *Journal of Sound and Vibration*, 443:253–269, 2019.

[154] E. L. Wilson. Structural Analysis of Axisymmetric Solids. *AIAA Journal*, 3(12): 2269–2274, 1965.

[155] X. Wu and R. G. Parker. Modal Properties of Planetary Gears With an Elastic Continuum Ring Gear. *Journal of Applied Mechanics*, 75(3):031014/1–12, 2008.

[156] Y. Yang, D. Cao, D. Wang, and G. Jiang. Fixed-point rubbing characteristic analysis of a dual-rotor system based on the lankarani-nikravesh model. *Mechanism and Machine Theory*, 103:202–221, 2016.

[157] Y. Yang, H. Ouyang, Y. Yang, D. Cao, and K. Wang. Vibration analysis of a dual-rotor-bearing-double casing system with pedestal looseness and multi-stage turbine blade-casing rub. *Mechanical Systems and Signal Processing*, 143:106845, 2020.

[158] C. C. Zhu, X. Y. Xu, T. C. Lim, X. S. Du, and M. Y. Liu. Effect of flexible pin on the dynamic behaviors of wind turbine planetary gear drives. *Proc. Inst. Mech. Eng., Part C*, 227:74–86, 2013.

[159] O. C. Zienkiewicz and R. L. Taylor. *The Finite Element Method Volume 2: Solid Mechanics*, volume 2. Butterworth Heinemann, 2000.